DISSERTATION

SUBMITTED TO THE

COMBINED FACULTIES OF THE NATURAL SCIENCES AND MATHEMATICS

OF THE RUPERTO-CAROLA-UNIVERSITY OF HEIDELBERG, GERMANY

FOR THE DEGREE OF

DOCTOR OF NATURAL SCIENCES

PUT FORWARD BY:

TOBIAS ALBERTSSON

BORN IN VÄNERSBORG, SWEDEN

ORAL EXAMINATION: JANUARY 15, 2014

Deuterium fractionation in the interstellar medium

REFEREES:

PROF. DR. THOMAS HENNING

PROF. DR. RALF KLESSEN

ABSTRACT

To date more than 170 species have been identified in interstellar space, and the chemical processes that govern their formation and destruction are driven by thousands of reactions connecting hundreds of atomic and molecular species. The study of these species give us essential information on the physical and chemical processes of astrophysical environments. Studies of deuterated species give us important clues also on the chemical ages and thermal history of these environments. As we enter a new exciting era with highly sensitive measurements of the chemical cosmos provided by ALMA, there is a need for new sophisticated models to analyze the forthcoming wealth of data.

The purpose of this thesis is to develop a sophisticated chemical model for studying the deuterium chemistry, benchmark it and its uncertainties and to utilize it to model increasingly more complex star-formation environments. We benchmark the deuterium chemistry model by comparing the calculated to observed D/H ratios of a variety of mono-, doubly-, and triply-deuterated species in distinct astrophysical environments. Uncertainties in abundances and D/H ratios are quantified by a sensitivity analysis, and the most problematic reactions are also identified to aid future laboratory experiments.

Ortho−para chemistry has been found to have a profound effect on the pace of deuterium fractionation. The *ortho−para* model is developed and used successfully to study the para-fractions in diffuse clouds where we improve our understanding of the underlying chemistry of H_3^+ and H_2. Finally, high-temperature reactions are added to the network and used in a study of the origin of Earth's ocean water and the water in primitive bodies of the Solar system (comets and asteroids).

ZUSAMMENFASSUNG

Bis heute wurden im interstellaren Raum mehr als 170 verschiedene Atome und Moleküle identifiziert. Die chemischen Prozesse, die deren Entstehung und Vernichtung regulieren, werden dabei durch tausende Reaktionen bestimmt, die wiederum hunderte verschiedene Atom- und Molekülsorten umfassen. Die Erforschung dieser Moleküle gibt uns wesentlichen Aufschluss über die physikalischen und chemischen Prozesse in astrophysikalischen Umgebungen. Die Erforschung deuterierter Moleküle gibt uns zudem wichtige Hinweise über das chemische Alter und die thermische Geschichte in diesen Umgebungen. Mit dem Eintritt in eine neue, spannende Ära hochpräziser Messungen des chemischen Kosmos durch ALMA, besteht die Notwendigkeit der Entwicklung neuer, ausgefeilter Modelle, um die bevorstehende Fülle an Daten zu analysieren.

Das Ziel dieser Arbeit ist es, ein fortgeschrittenes chemisches Modell zu entwickeln um die Deuteriumchemie zu erforschen, dieses zu testen und dessen Unsicherheiten abzuschützen und es dazu zu benutzen, sukzessive immer komplexere Sternentstehungsregionen zu modellieren. Wir testen und bewerten dieses Modell, indem ich die damit bestimmten D/H-Verhältnisse einer Vielzahl einfach, doppelt und dreifach deuterierter Moleküle mit beobachteten Verhältnissen aus verschiedenen astrophysikalischen Umgebungen vergleiche. Unsicherheiten in den Häufigkeiten und den D/H-Verhältnissen werden dabei durch eine Sensitivitätsanalyse quantifiziert. Als Hilfestellung für zukünftige Laborexperimente werden zudem die problematischsten Reaktionen identifiziert.

Dabei hat sich herausgestellt, dass die ortho-para-Chemie einen beträchtlichen Effekt auf die Geschwindigkeit der Deuteriumsfraktionierung hat. Das ortho-para-Model wurde entwickelt und erfolgreich angewendet, um den para-Anteil in diffusen Wolken zu erforschen. Dabei konnten wir das Verständnis der hierbei zugrundeliegenden H_3^+- und H_2-Chemie vertiefen. Zum Abschluss wurden dem Netzwerk Hochtemperaturreaktionen hinzugefügt und zur Erforschung des Ursprungs des Ozeanwassers auf der Erde, sowie des Wassers in Kometen und Asteroiden des Sonnensystems, verwendet.

PUBLICATIONS

Some of the ideas and work described in this thesis have previously appeared in the following publications:

New extended deuterium fractionation model: assessment at dense ISM conditions and sensitivity analysis, Albertsson, Semenov, Vasyunin, Henning, Herbst, 2013, The Astrophysical Journal: Supplement series, vol. 207, pp. 27

Chemo-dynamical deuterium fractionation in the early solar nebula: The origin of water on Earth, in asteroids and comets, Albertsson, Semenov, Henning, 2014, The Astrophysical Journal, Submitted

First time-dependent study of H_2 and H_3^+ ortho−para chemistry in the diffuse ISM, Albertsson, Indriolo, Kreckel, Semenov, Crabtree, Henning, 2014, The Astrophysical Journal, in prep.

CONTENTS

LIST OF FIGURES

LIST OF TABLES

ACRONYMS

VLT Very Large Telescope

JWST James Webb Space Telescope

CoRoT COnvection, ROtation & planetary Transits

CRIRES CRyogenic high-resolution InfraRed Echelle Spectrograph

ISO Infrared Space Observatory

HARPS High Accuracy Radial Velocity Planet Searcher

ALMA Atacama large millimeter/submillimeter array

SMA Submillimeter Array

VLA Very Large Array

PdB Plateau de Bure

SKA Square Kilometer Array

LHB Late Heavy Bombardment

ODE ordinary differential equation

VODE Variable-coefficient ODE solver

DVODPK Differential Variable-coefficient Ordinary Differential equation solver with the Preconditioned Krylov method Generalized Minimal RESidual method (GMRES) for the solution of linear systems

GMRES Generalized Minimal RESidual method

ISM interstellar medium

CRP cosmic-ray particles

DC dark clouds

PPD proto-planetary disk

IRDC infrared dark clouds

HMPO high-mass protostellar objects

KIDA Kinetic database for Astrochemistry

UMIST University of Manchester Institute of Science and Technology

LTE local thermal equilibrium

CDMS Cologne Database of Molecular Spectroscopy

MMR mean motion resonances

FWHM full width half-maximum

LSR local standard of rest

ICR Ion Cyclotron Rresonances

FA Flowing Afterglow

TPD Temperature Programmed Desorption

SIFT Selected Ion Flow Tube

CRESU Reaction Kinetics in Uniform Supersonic Flow

DR Dissociative recombination

EA electron attachment

RA radiative association

UV ultraviolet

IR infrared

UHV ultrahigh vacuum

1 INTRODUCTION

"The history of astronomy is a history of receding horizons"

— Edwin P. Hubble, Realm of the Nebulae, 1936

Mankind has always been intrigued by the carpet of light floating above our heads, but we have come a long way since our ancestors first began studying the motion of the stars. We are the generation to have witnessed the discovery of the first extra-solar planet, henceforth referred to as an exoplanet. Even more interesting, today, almost three decades after this discovery, we have taken the first sniffs of a few distant worlds and have been able to characterize a handful of planets as potentially habitable. Many more are to follow as we are currently the spectators of an intense race to find other habitable planets outside our Solar System. But in order to truly understand these distant worlds, we first need to understand the formation of these bodies and this is a question that is still today one of the most important questions in science.

As our understanding about planet formation has deepened, the science has grown so far in complexity that it requires the combined effort of astronomy, chemistry and also biology. Alongside the evolution of the smallest pebbles into rocky and gas giant planets, an equally complex evolution of the chemistry takes place, starting from atomic elements and simple diatomic molecules, such as H_2 and CO, and eventually forming complex and pre-biotic organics, such as methanol and formic acid.

To date more than 170 molecules[1] have been observed in space. Most of them have been detected in the interstellar medium (ISM), which has been revealed to be surprisingly active and even the most dilute environments found to be rich in molecular complexity, containing everything from simple atomic to complex organics and fullerenes such as C_{60} and C_{70}.

Some molecules play an active role in physical processes, such as H_2O and CO, by cooling the gas and allowing for a contraction of the medium. More importantly, molecules can be utilized to probe certain physical and chemical processes that govern the interstellar cycle of material, and have been utilized for a long time as probes of physical parameters, and can also give us additional information on the age of these environments. Due to the sheer number of hydrogen-dominated molecules, and their presence in the majority of reactions, the chemistry of deuterium, hydrogen with one neutron in the nucleus, is also recognized as an essential ingredient in the cosmic chemistry.

In this thesis, we have evaluated and applied an extended chemical model intended for studying the deuterium chemistry in inter- and circum-stellar space. The chapters in this thesis will follow the development of this new, extensive chemical model for deuterium chemistry, and its application to the different

1 see http://www.astro.uni-koeln.de/cdms/molecules for up-to-date information

stages of the ISM. The chemistry considered begins with the molecular clouds which collapse to form a protostar. Together these lay the chemical foundations for the final stage considered; the proto-planetary disk (PPD), where the genesis of alien worlds, and life itself, takes place. In the remainder of this introduction we will review the concepts of planet and star formation in connection with astrochemistry, as well as the fundamentals of astrochemistry itself, in order to put this work into context.

1.1 EXTRA-SOLAR WORLDS

It is only recently, thanks to modern observing space telescopes such as Herschel (Pilbratt et al. 2010), COnvection, ROtation & planetary Transits (CoRoT) (Baglin 2003) and Kepler (Borucki et al. 2010) space telescopes, and ground-based facilities such as the Very Large Telescope (VLT), Subaru telescope, Keck telescopes, High Accuracy Radial Velocity Planet Searcher (HARPS) instrument, and Atacama large millimeter/submillimeter array (ALMA), that we have begun pushing sensitivities towards planets with masses similar to that of Earth. With their help we are entering a new dawn in our pursuit of habitable rocky exoplanets. With the imminent results from GAIA (Perryman et al. 2001), and the predicted launch of the James Webb Space Telescope (JWST) (Gardner et al. 2006) in 2018 we are about to enter a new epoch of exoplanet detection. Additional capabilities of these instruments will allow transient spectroscopy of exoplanet atmospheres (for a review see Seager & Deming 2010).

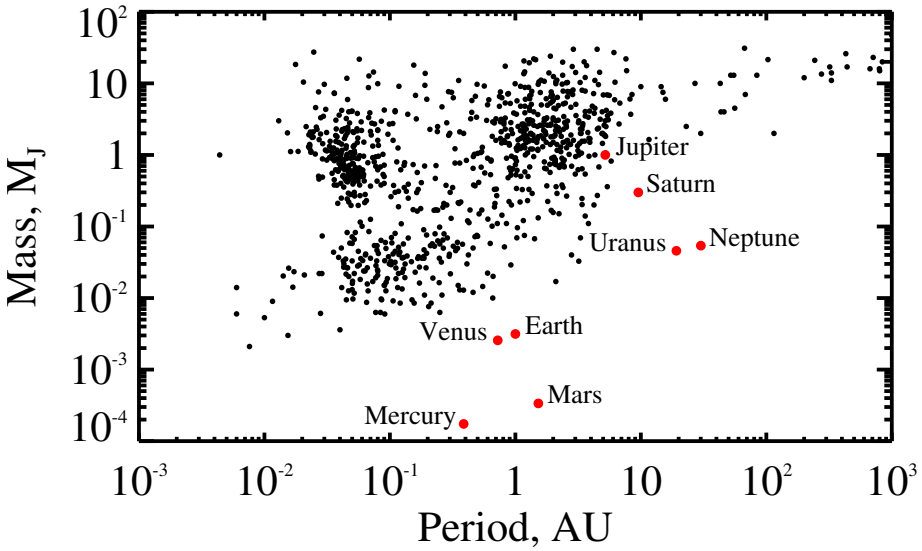

Figure 1.1: Orbital period plotted against estimated (minimum) mass of confirmed exoplanets. Data on confirmed exoplanets taken from `exoplanet.eu`. The Solar System planets are added for comparison.

Ever since the observation of the first exoplanet orbiting a main-sequence star by Mayor & Queloz (1995), our encyclopedia of distant worlds has experienced an explosive growth and has revealed a diversity of planetary system

configurations (see Figure 1.1), with Howard (2013) providing a comprehensive review. To date more than 1 000 exoplanets have been observed outside our Solar System in more than 170 planetary systems[2]. On top of these, there are several thousands of planet candidates which require further analysis before they can be confirmed as exoplanets.

From the hundreds of observed planetary systems we have come to find that the Solar System is unique in its composition of planets. However, as our cosmochemical studies are limited to Solar System objects (meteorites, comets, planets, satellites, etc.) we are somewhat restrained in our ability to test planet formation and evolution theories.

1.1.1 *Solar system*

For centuries the long-term stability and co-planar configuration of the bodies in the Solar System with near-circular orbits was taken as evidence that the planets formed *in situ* by accreting material from the young solar nebula. However, as we uncovered more details about the Solar system, several features were discovered which the general formation theory could not reproduce. Geological studies of rocks on the moon suggest that a cataclysmic event took place $\sim$ 700 Myr after the planets formed, judging by a spike in the cratering rate which is often referred to as the Late Heavy Bombardment (LHB) (Hartmann et al. 2000). It is believed to have been caused by a high flux of scattered asteroids that originated from the outer disk ($\sim$ 10 AU), beyond the snow line where many volatiles freeze onto the grains, and points to a more dynamically unstable period of the Solar System's evolution. Furthermore, heavily populated mean motion resonances (MMR) in the Kuiper belt suggest that the planets have migrated at some point between their formation and the present. Furthermore, the current belt mass (< 0.1 M_{Earth}) is orders of magnitude too small to have grown by binary accretion on short timescale, inferring a substantial mass loss as it should have been 100 to 1000 times larger (Stern & Colwell 1997; Kenyon & Luu 1998).

The NICE model, presented in a series of three papers (Tsiganis et al. 2005; Gomes et al. 2005; Morbidelli et al. 2005), was developed as the up-to-date model for the formation of our Solar System, and showed great success in reproducing several of its unexplained observed features. It concentrates on the evolution of the four giant planets after their formation, before the terrestrial planets have been formed and the inner regions is largely made up of large-sized planetesimals. In the scenario of the NICE model, the four giant planets are proposed to have formed (about 4.5 Gyrs ago) in a much more compact configuration than observed today in circular orbits inside a large disk of icy debris, with Jupiter and Saturn initiated in orbits close to their 1:2 MMR. By accretion or scattering of planetesimals the two planets began to migrate by exchange of angular momentum, including also effects on the orbits of Neptune and Uranus, such as a flip in orbits between Neptune and Uranus in 50% of their models (Tsiganis et al. 2005).

2 see http://exoplanet.eu/ for up-to-date information

As Jupiter and Saturn crossed the 1:2 MMR, interactions between the planets increase in intensity. As a result of this, nearby formed asteroids experienced a chaotic period in which Jupiter captured its trojans that are present today. The trojans trail Jupiter in its orbit in co-orbital motion, and the resulting population from the NICE model is able to reproduce their total mass and orbital distributions. Furthermore, they found that the trojans can have formed in the outer regions and were later captured, explaining their deficiency in water and organics (Morbidelli et al. 2005). This event generated a high flux of planetesimals being thrown towards the inner regions of the solar nebula, initiating a scenario similar to the LHB (Gomes et al. 2005). Finally, as the interactions between Jupiter and Saturn were damped by dynamical friction, where any increase in eccentricity and inclinations is suppressed as the planets interact with the remaining material in the disk, the system stabilizes again and the four giant planets settle in their current observed orbital configurations (Tsiganis et al. 2005).

The NICE model however fails to explain the low mass of Mars. Mars should have ended up much more massive due to the high surface density of material in the inner disk and which increases towards the inner radii of the solar nebula (Raymond et al. 2009). One possible way of reducing the mass of Mars is to reduce the amount of available material in the inner region, before Mars grows too big. Hansen (2009) reflected on this idea by truncating the solar nebula with an outer edge at 1.0 AU, which resulted in a much smaller mass of Mars.

Walsh et al. (2011) improved on this idea by looking for a formation scenario that can reproduce the truncated disk. In their scenario the giant planets begin migrating inwards before the terrestrial planets have formed, much as in the NICE model, and on their way they interact with the planetesimals and debris consisting mostly of volatile-poor bodies (similar to S-type asteroids). This theory is supported by hydrodynamical simulations that have shown that Jupiter and Saturn can undergo a two-staged inward followed by outward migration (Masset & Snellgrove 2001; Morbidelli & Crida 2007; Pierens & Nelson 2008). However, in this scenario Jupiter reaches further into the inner regions of the solar nebula, to a distance of $\sim$1.5 AU from the Sun. At this point Saturn catches up with Jupiter and the two become locked in a 1:2 MMR, causing the giant planets to begin moving outwards again, until they reach their current orbits. Uranus and Neptune also migrated inwards during this scenario and around 3.8 Gyrs ago they initiated a scenario resembling the LHB as they moved through the disk and interacted with the planetesimals they meet on their way. Bottke et al. (2012) also proposed that before this inward migration, the asteroid belt could have extended much closer to Mars' orbit ($\sim$ 1.7 AU) resulting in the LHB lasting much longer than previously thought. A longer LHB allows for more lunar impacts, agreeing with the predicted number of craters. These impactors are also thought to have played a part in the delivery of complex organics (see e.g. Anders 1989) and Earth's water, whereas Earth is believed to have formed dry owing to its proximity to the Sun (see Chapter 5).

The molecules that exist on Earth and other bodies of the Solar System are much similar to the molecules that we are built up from, such as water, carbon

monoxide and various complex organics. These molecules are formed from atoms and simple molecules that exist in the cradles of star formations: interstellar clouds. Their chemical evolution is governed by thousands of reactions which create a chemical diversity characteristic of both the local environment and the present molecular abundances. Therefore, the chemical diversity is stipulated both by the conditions under which it is formed, but also on the chemical history of the environment, which is continuously changing as processes are reacting to the evolving environment. Next we will review both the physical and chemical evolution taking places as we grow the dust in the diffuse interstellar clouds, into the fundaments for planetary systems; the PPDs.

1.2 THE EVOLUTION OF INTERSTELLAR MATTER

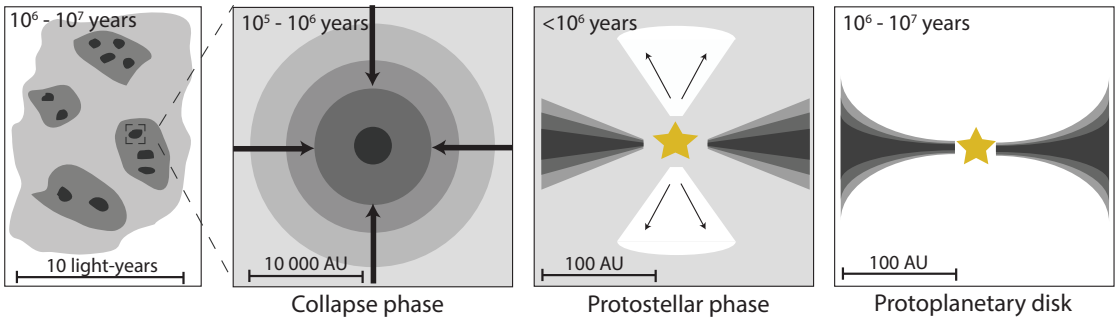

Figure 1.2: Schematic illustration of low-mass star formation.

The birth of a planetary system begins in the stellar nurseries of the ISM in diffuse clouds and involves several stages, each with characteristic physical and chemical processes (see Figure 1.2). These environments can span several light-years in size and typically have gas temperatures up to about 80 K and low densities of $\sim$ 10-100 cm^{-3} (Snow & McCall 2006a). Hence, they are heavily radiated by ultraviolet (UV) fields and were for long thought to be devoid of molecules. But ever since the first detections of CN, CH and CH^+ in the diffuse ISM (McKellar 1940; Adams 1941; Douglas & Herzberg 1941), a wealth of molecules have been detected in these sparse environments, from simple molecules such as H_2 (Carruthers 1970; Smith 1973; Spitzer et al. 1973) and CO (Wilson et al. 1970), to more complex molecules such as NH_3, H_2CO (Cheung et al. 1968; Snyder et al. 1969), as well as exotic species, such as $HC_{11}N$ (Bell et al. 1997), and even fullerenes, such as C_{60} and C_{70} (Werner et al. 2004; Sellgren et al. 2007, 2010; Cami et al. 2010).

Initiated by external forces, such as those exerted by stellar winds or supernova explosions, regions of the clouds begin fragmenting, collapsing and form individual, gravitationally-bound clumps inside the cloud. These clumps have low temperatures of $\sim$ 10 K and densities $\gtrsim 10^4$ cm^{-3} (Snow & McCall 2006a; Bergin & Tafalla 2007). At this stage the environment is enriched with molecules as the dense clouds become shielded from UV radiation which, along with the higher densities, increases the rate of the chemical evolution. Due to the low temperatures, however, most of these molecules freeze-out onto

(sub-)μm-sized dust grains, and the gas remains largely void of molecules, with the exception being H_2, HD and D_2. Sites on the grains act as catalysts and a rich surface chemistry takes place, supplying the environments with essential molecules such as H_2O and CO_2 (Cheung et al. 1969; D'Hendecourt & Jourdain de Muizon 1989). It is also on the grain surfaces that the formation of H_2 takes place, as the radiative association (RA) of two H atoms has a very low rate of $\sim 10^{-29}$ cm^3 s^{-1}. The efficiency of surface formation of H_2 is still heavily debated, and many uncertainties remain regarding the effects of such processes such as quantum tunneling. However, the importance of surface chemistry on the formation of H_2 is well documented (see review by Vidali 2013).

The central parts of these clumps continue to contract and can become dense enough to overcome magnetic and gas pressures, eventually forming a prestellar core. This forms the seed that eventually will become a star, with low temperatures of 8-15 K, and moderate densities, $10^4 - 10^6$ cm^{-3} (André et al. 2009; Launhardt et al. 2010), and essentially the same chemistry taking place as in the surrounding environment. The prestellar core manages to sustain itself from further collapse for another $10^4 - 10^6$ years by the energy that is released during the contraction. Here, the chemistry begins to interact and play an important role in the cooling of the physical environment by radiating away energy via infrared (IR) radiation, which can freely escape the cloud. This allows the core to collapse, eventually forming a protostar.

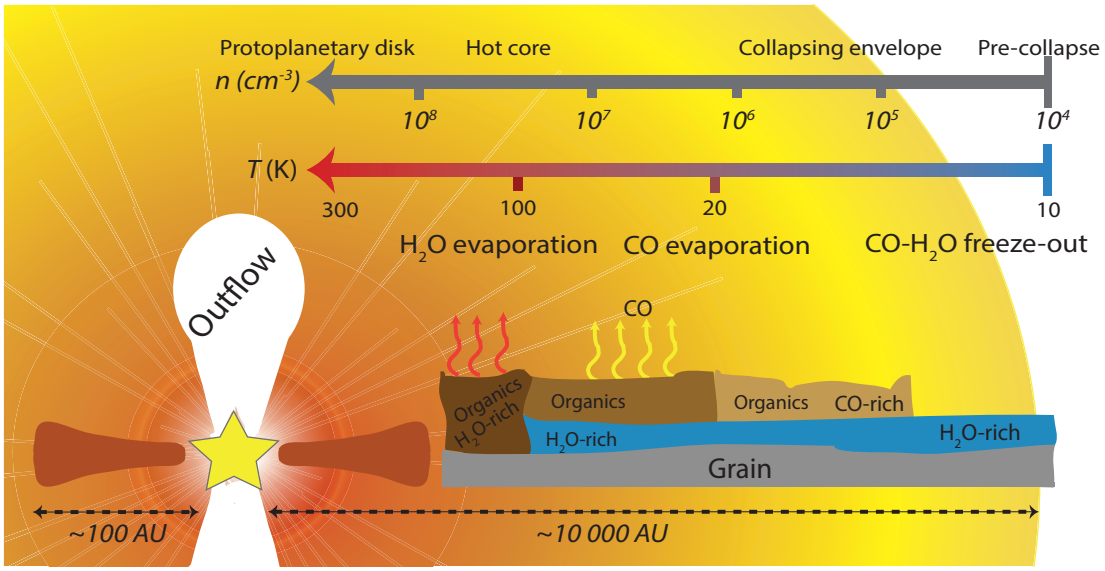

Figure 1.3: Schematic representation of low-mass star formation and some of the essential chemistry involved, adopted from Herbst & van Dishoeck (2009).

This protostellar object is initially deeply embedded in its surrounding material, which it heats up, reaching temperatures of several hundred K close to the central protostar and high densities of $\gtrsim 10^8$ cm^{-3} (van Dishoeck 2009). These environments drive a rich and greatly varying chemistry owing to the ranges of temperatures and densities (see Figure 1.3). The gradual warm-up

of the environment, as well as accretion shocks, cause volatile species, such as CO, H_2O and N_2, to slowly evaporate from the grains. As the temperature increases, a rich surface chemistry involving heavy radicals becomes active due to the increased mobility allowing complex organic species such as HCOOH and $HCOOH_3$ to be formed (e.g. Garrod & Herbst 2006; Garrod et al. 2008; Öberg et al. 2009a; Herbst & van Dishoeck 2009).

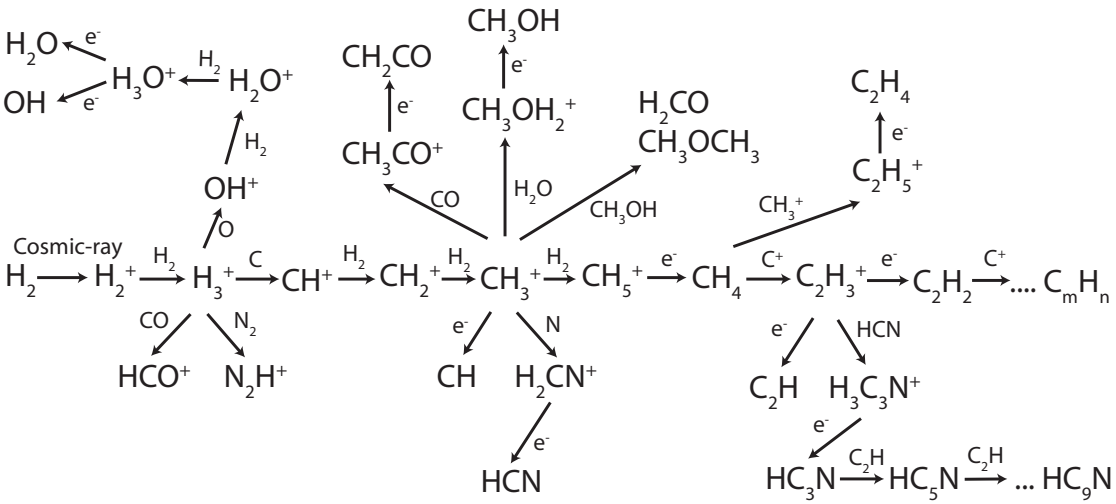

Figure 1.4: Schematics of the essential pathways related to the H_3^+ chemistry.

Additionally, the increasing temperature creates an environment favorable for driving a rich gas-phase chemistry initiated by H_3^+. Owing to its very low proton affinity, H_3^+ can transfer one of its protons to most neutral atoms and molecules, with the exception being N and O_2 (see Figure 1.4). Of these CO is the most essential coreactant, and to some lesser extent N_2. H_3^+ is formed in the gas-phase by ionization of H_2 via cosmic-ray particles (CRP), as direct photoionization is not energetic enough to overcome the H_2 ionization potential of 15.4 eV. The produced ion H_2^+ reacts further with H_2 to form H_3^+ (and atomic H). Because this is an exothermic reaction the H_3^+ abundance quickly increases, as it is dependent upon the rate of the ionization of H_2. As the temperature increases CO, and eventually also N_2, is released into the gas-phase which initiates a cascade of chemical processes through molecules such as HCO^+, N_2H^+, HCN and more. Eventually this leads to the formation of large species through a second explosion in the chemical complexity via the CH_3^+ ion (see Figure 1.4). This highly efficient chemical pathway is also active in the previous evolutionary stages. However, due to the low temperatures, CO and other neutral simple molecules that can react with H_3^+ to form larger molecules, are largely depleted onto the grains, reducing the efficiency much below the value found in the protostellar (and subsequent) evolutionary stages.

While the protostellar envelope continues to collapse by ejecting mass through bipolar outflows, the rotation of the envelope increases due to conservation of the angular momentum and flattens out the nebula, eventually forming a disk. Inside these PPDs, the temperature and density varies greatly and typically consists of four chemically divided regions: the warm inner regions and

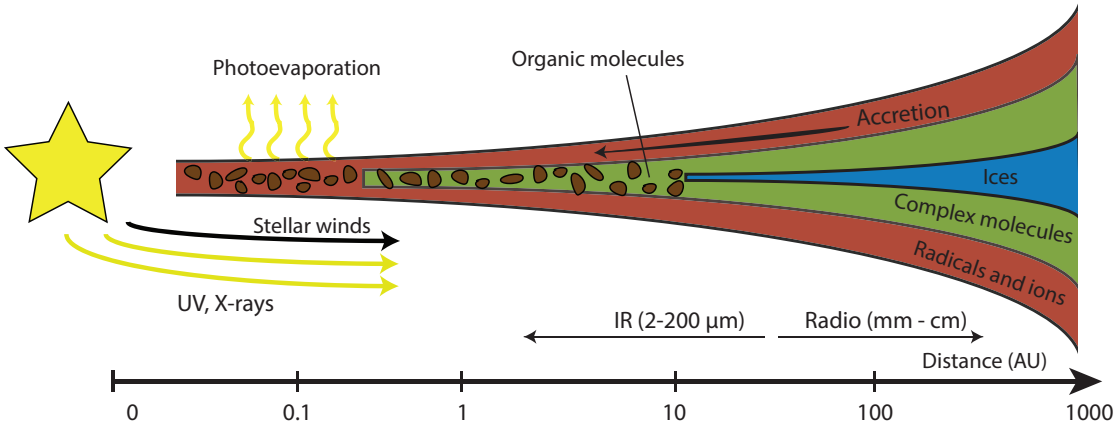

Figure 1.5: Sketch of physical and chemical structure of proto-planetary disks. Adopted from Semenov (2010).

the three layers of the outer disk (see Figure 1.5). The cold midplane with temperatures 10−20 K and high densities is opaque to UV and X-ray radiation, leaving the medium essentially neutral. Owing to the cold temperatures, ices dominate these regions, while dynamical interaction with other layers and CRP-driven processes allow for some gas-phase chemistry initiated by rapid ion-molecule reactions.

Above this layer temperatures are higher, typically 30−100 K, and the environment is only partly shielded from UV and X-ray radiation. The increased temperature allows for some volatiles to be desorbed, and together with the dissociation and ionization of the gas by photons, allows for a rich chemistry with high molecular abundances. For this reason the layer is typically referred to as the molecular layer.

At the top layer of the outer disk, often referred to as the disk atmosphere, the medium is heavily irradiated with high temperatures > 100 K and low densities. The dominating photochemistry and dissociation processes do not allow for significant amounts of molecules, mostly only smaller radicals and simple ions.

Finally, in the warm inner regions, typically with temperatures $\gtrsim 50$ K, gas-phase reactions, including neutral-neutral reactions with barriers, dominate the chemistry. Here, dissociative and ionization processes driven by stellar X-ray radiation are efficient, and densities are also high enough ($\gtrsim 10^{10}$ cm^{-3}) for three-body reactions to play a role (Aikawa & Herbst 1999b).

The protostar continues to accrete the surrounding material and increases in temperature, eventually reaching a similar surface temperature to that of a main-sequence star, at which point it is classified as a T Tauri star. The surrounding disk eventually disperses, due mainly to the ignition of fusion in the core injecting energy into the disk, but also through accretion and photo-evaporation processes. This signals the birth of a main-sequence star. The PPD that is left orbiting the disk is then heavily irradiated by stellar far-UV and X-ray radiation. For a low-mass star this system will eventually evolve into a

planetary system similar to our own, but for high-mass stars the evolution is not yet fully understood. It has been suggested that it is an up-scaled version of low-mass evolution, however it is also likely that other mechanisms are at work (Zinnecker & Yorke 2007).

Throughout the evolution from gas into stars, the dust also grow slowly in size by aggregation during the pre-disk stage. The essential evolution into planets begins in the protoplanetary stage. At this stage of the evolution dust particles grow into kilometer-sized, self-gravitating bodies called planetesimals. These bodies continue to grow gravitationally through accretion and collisions with other planetesimals, eventually forming planets. This process of grain evolution has been observationally confirmed in PPDs (see e.g. van Boekel et al. 2004, 2005; Sicilia-Aguilar et al. 2006; Rodmann et al. 2006; Natta et al. 2007; Cortes et al. 2009; Birnstiel et al. 2010b; Ricci et al. 2010; Ubach et al. 2012). Details on the grain growth up until planets are however still unclear as there are many difficulties to surpass in achieving the necessary size of dust particles, with several competing theories for overcoming these obstacles (e.g., Nakagawa et al. 1981; Dullemond et al. 2001; Dullemond & Dominik 2004, 2005; Watanabe 2005; Brauer et al. 2007, 2008; Cazaux et al. 2008; Okuzumi et al. 2009; Birnstiel et al. 2010a; Kalvans & Shmeld 2011; Okuzumi & Hirose 2012; Windmark et al. 2012). For reviews see e.g. Chambers (2004), Nagasawa et al. (2007), and Raymond (2008).

1.3 ASTROCHEMISTRY

The chemistry evolve alongside the formation of stars and their planets, and an immense number of reactions compete over the available material to form molecules of increasing complexity. Throughout this evolution the chemistry in the gas and dust reacts to the changing physical conditions of the environment. This is the fundaments of molecular astrochemistry, combining laboratory, theoretical and observational studies to advance the field (in Chapter 4 we present such a collaboration).

To date we have observed the chemical heritage throughout all stages of star and planetary formation. Using modern ground-based observing facilities such as ALMA, VLT, Very Large Array (VLA), Square Kilometer Array (SKA), Keck, Subaru, Plateau de Bure (PdB) and Submillimeter Array (SMA), as well as space telescopes such as Herschel, Infrared Space Observatory (ISO) and Spitzer, we are continuously pushing our knowledge into new frontiers by providing, or have provided, us with new data to be understood. In order to identify molecules amongst the forest of spectral lines that are observed, correct line frequencies and molecular properties need to be determined in laboratories with spectroscopic studies. In order to understand what we might learn from the extracted abundances of these observations, results are to be compared to theoretically predicted abundances from astrochemical models. For these theoretical studies, modelers need rates of the chemical reactions that take place in these environments, which can either be determined through laboratory experiments or by theoretical studies. While laboratory experiments

Table 1.1: Different types of reactions and their equivalent reaction rate equations.

Reaction type	Example					Rate
photodissociation	CO	+ $h\nu$	⇒	C	+ O	$k_{\rm PD}$
photoionization	H	+ $h\nu$	⇒	H^+	+ e^-	$k_{\rm PD}$
ζ dissociation	H_2	+ $\zeta_{\rm CRP}$	⇒	H^+	+ H^-	$k_{\rm CRP}$
ζ ionization	H_2	+ $\zeta_{\rm CRP}$	⇒	${H_2}^+$	+ e^-	$k_{\rm CRP}$
ion - neutral	${H_3}^+$	+ CO	⇒	HCO^+	+ H_2	$k_{\rm kooji}$
neutral - neutral	CH_2	+ N	⇒	HCN	+ H	$k_{\rm kooji}$
charge - transfer	OH	+ C^+	⇒	OH^+	+ C	$k_{\rm kooji}$
Dissociative recombination	${H_3}^+$	+ e^-	⇒	H_2	+ H	$k_{\rm kooji}$
radiative association	C^+	+ H_2	⇒	CH_2^+	+ $h\nu$	$k_{\rm kooji}$
radiative recombination	H_2CO^+	+ e^-	⇒	H_2CO	+ $h\nu$	$k_{\rm kooji}$
electron attachment	C_6H	+ e^-	⇒	C_6H^-	+ $h\nu$	$k_{\rm kooji}$
mutual neutralization	HCO^+	+ H^-	⇒	H_2	+ CO	$k_{\rm kooji}$
third-body assisted reactions	H + H	+ H	⇒	H_2	+ H	k_{3-body}
adsorption	H_2O		⇒	$H_2O_{\rm ice}$		$k_{\rm ads}$
desorption	$H_2O_{\rm ice}$		⇒	H_2O		$k_{\rm des}$
grain-surface hydrogenation	$O_{\rm ice}$	+ $H_{\rm ice}$	⇒	$OH_{\rm ice}$		$k_{\rm surface}$
grain surface, radical-radical	$OH_{\rm ice}$	+ $H_{\rm ice}$	⇒	$H_2O_{\rm ice}$		$k_{\rm surface}$

$k_{\rm PD}$ [s^{-1}] = $\alpha\, e^{-\gamma A_V}$ - A_V visual extinction

$k_{\rm CRP}$ [s^{-1}] = $\alpha\,\zeta$ - ζ H_2 cosmic-ray ionization rate

$k_{\rm kooji}$ [$cm^3\ s^{-1}$] = $\alpha\,(T/300)^{\beta}\, e^{-\gamma/T}$ - α, β, γ laboratory rate coefficients

$k_{3-\rm body}$ [$cm^6\ s^{-1}/cm^3\ s^{-1}$] - e.g. Anicich (1993) uses complex density dependence

$k_{\rm ads} = \sigma_d \langle v_{th}(i) \rangle\, n_d$ - σ_d dust cross-setion, v_{th} species thermal velocity, n_d grain density

$k_{\rm des}$ — see e.g. Leger et al. (1985) and Semenov et al. (2010a)

$k_{\rm surface}$ — see e.g. Hasegawa et al. (1992)

and observational studies are often time-consuming, experimentalists and observers receive input from models to identify the important molecules that needs to be further investigated. It is through this collaborative effort that we can determine the physical and chemical structure of these distant environments, such as temperature, density, ionization rates, as well as evolutionary age.

In Table 1.1 the groups of reactions used in modern chemical networks are listed, where the majority of reactions are ion-neutral, followed by dissociative recombination and neutral-neutral reactions. Because ion-neutral reactions almost always are exothermic, they typically have high rate coefficients, $\sim 10^{-9}$ s^{-1}, increasing with low temperatures (e.g. Dalgarno & Black 1976). Dissociative recombination usually have higher rates increased by Coulomb attraction of a charged species and an electron, $\sim 10^{-7}$ cm^3 s^{-1} while neutral-neutral reactions have lower reactions rates, $\sim 10^{-12}$ cm^3 s^{-1}, and are less significant in the cold ISM owing to large energy barriers. The importance is more clear in environments of high-temperatures, such as in hot cores or the inner regions of PPDs, where reactions with large barriers become active. Dissociative recombination (DR) and radiative recombination helps neutralize the medium and regulate the ionization degree by removing essential ions such as H_3^+ and HCO^+. Furthermore, as we will discuss in Chapter 4, DR plays a particularly vital role in the ortho-para chemistry of diffuse clouds.

Finally, it has become clear that gas-phase processes alone can not explain the richness and variety of the chemistry found in the ISM, the importance of gas-grain processes has ignited a surge of experimental and theoretical studies on these reactions. The surfaces of grains act as catalysts where accreted species meet and react, and excess reaction energy can be donated to the grain, in a process called the Langmuir-Hinshelwood mechanism. The grain surface topology, the presence of high- and low-energy binding sites, grain sizes and shapes are all separate parameters that may severely impact the chemistry. An accurate study of this impact will require a detailed treatment of the microscopic physics of molecules on various solid surfaces, see e.g. Perets & Biham (2006); Cuppen et al. (2009); Vasyunin & Herbst (2013a,b), where some of these issues are already addressed. The rate of reactions is set by the rate of adsorption (and desorption) of species, and the surface migration rate at which they move around on the surface. The energy required for moving species over the surface increases with mass, and therefore larger molecules often need to wait for a more mobile co-reactant. Because hydrogen atoms are very abundant and light, so that they are very mobile on the grain surface, the process of hydrogenation is very effective in the cold ISM. A typical example of this is the formation of water, where first an O and H atom meet to form OH, and after which water is formed after another H atoms meets OH and react (Dulieu et al. 2010). Details of surface chemistry are not clear and can depend on dust properties such as porosity and surface structure (see e.g. Hornekær et al. 2003; Perets et al. 2005).

1.3.1 *Laboratory experiments*

Laboratory experiments are a pivotal ingredient in astrochemistry, as they contribute the detailed knowledge required in order to study the fundamentals of the chemistry that takes place in the ISM. However, physical conditions are very different in space from that on Earth. Foremost, in space collisional time scales are long, typically in the range of hours, days, or months for densities $\sim 10^4$ cm^{-3}. Temperatures are also much lower to those ubiquitous on Earth, but using cryogenic cooling or supersonic expansions, temperatures down to a few K have been achieved using swarm techniques, beam methods, and traps (e.g. Luine & Dunn 1985; Rowe & Marquette 1987; Gerlich & Horning 1992; Smith 1998; Smith & Rowe 2000). In the last decade, scientists have been able to reach high-vacuums equivalent to number densities $\sim 10^{16}$ cm^{-3}, and even ultra-high vacuums of $\sim 10^{13}$ cm^{-3}, but values also depends on temperature.

Laboratory experiments and theoretical calculations provide us with two essential types of information to help us better understand the chemistry in interstellar space. The first is the reaction rate k, or $k(T)$ to stress its temperature dependence, which is expressed in different ways depending on the nature of the reaction (see Table 1.1). For bimolecular processes the rate coefficient is defined from the rate of change in concentration with time, for species A and B as:

$$-d\,[A]/d\,t = k(T)[A][B] \tag{1.1}$$

It is common to express this rate coefficient in terms of three variables, the so-called Arrhenius equation or Kooji formulation:

$$k(T) = \alpha(T/300)^{\beta} e^{-\gamma/T}, \tag{1.2}$$

where α has the same unit as $k(T)$, cm^2 s^{-1}, β is unitless and describes the temperature dependence of the rate and γ is an energy barrier expressed in Kelvin. Secondly, we can learn more about the nature of the products, more specifically their observable frequencies, the branching ratios of two or more different sets of products and which products are not possible, or highly unlikely, to form.

Because the nature of reaction groups is different, various techniques need to be adopted in order to study them in detail. A list of essential laboratory experiment techniques and methods are summarized in Table 1.2 and briefly discussed below.

The two most important techniques for laboratory experiments before the 1980s were the Ion Cyclotron Rresonances (ICR) and Flowing Afterglow (FA) techniques for studying ion-neutral reactions. In the ICR method the ions are stored using a combination of electric and magnetic fields and, after the introduction of a neutral coreactant, the ions are transferred through an analysis region after a specific time delay. Many of the reactions their early models of Prasad & Huntress (1980a,b) for the ISM contributed greatly from results of the ICR method. In the FA method ions are diluted by a buffer gas, usually He or Ar, and then transported into a flow tube, where the neutral coreactant can

be introduced and the resulting products are then analyzed downstream in the instrument using a mass spectrometer. One of the drawback with the FA method is the possibility for multiple reactant ions, however it was overcome by allowing mass selection of the reactant ion, known as Selected Ion Flow Tube (SIFT). Another development of flow methods is the Reaction Kinetics in Uniform Supersonic Flow (CRESU) technique. It uses a nozzle, expanding the gas or mixture of gases from a high pressure reservoir into a vacuum chamber, changing the gas into a supersonic beam that is essentially collision free. The advantage is that the nozzle can be chosen to produce a specific temperature between $\sim$ 10 K and room temperature. By crossing the gas flow with an electron beam, and subsequently study rates and products by redirecting the resulting flow into a mass analyzer. With modifications neutral-neutral, RA and electron attachment (EA) reactions can also be studied (Smith 2008). Another important use of the CRESU technique has been to show the temperature dependence of reactions at low temperatures, where a reduction in temperature could generate an increase in rate constant (Smith 2011).

Because DR reactions are usually highly exothermic several channels may be energetically available and it is important to study also the branching ratios between the channels as well as the reaction rates. FA methods were long used to measure reaction rates but a problem with the ions existing in various excited states as they merged with the electron beam caused ion storage rings to be developed (Larsson 1995; Geppert & Larsson 2008). Ions are stored in a ultrahigh vacuum (UHV) system and using magnetic focusing elements such as dipole magnets the ions are stored in a ring structure for up to 30 s, allowing any vibrationally excited ions to radiate excess energy before reactions are allowed. The advantage of the method is that it gives also knowledge on branching ratios of all channels (the importance of understanding these branching ratios is discussed in Chapter 4).

For surface chemistry, Temperature Programmed Desorption (TPD) is one of the most commonly used experimental technique today. The surface temperature on a sample is increased with time and desorbed molecules are studied as a function of time (and temperature). Analysis of reactions is done by knowing both the available material before the thermalization is initiated and the observed desorbed species.

1.3.2 *Observations*

The abundances and column densities derived by observations are an essential ingredient to learn more about the distant space environments. There is a difficulty in observing certain molecules, such as H_2O, O_2 and CO_2, using ground-telescopes, owing to absorption in the Earth atmosphere of these lines. This is solved by deploying space telescopes in orbit around the Earth, which also have the added advantage of avoiding seeing effects caused by turbulent stirring of the atmosphere, however can not be made as large as ground-based facilities due to transport limitations.

Table 1.2: The different types of laboratory experiments and the targeted group of reactions. Unless otherwise states, reactions are gas-phase. The methods in parenthesis are not discussed in detail but given for completeness.

Reactions	Experiment technique
Ion-neutral	FA, ICR, SIFT, CRESU, Ion storage rings
Neutral-neutral	(Flow tube), CRESU
Radiative association	(Ion traps), CRESU
Dissociative recombination	FA, (Merged beam), SIFT, Ion storage rings
Electron attachment	CRESU
Photo-ionization	(Absorption spectroscopy)
Surface	TPD

The observations of molecules can typically be divided into three regimes, depending on energy of a transition: studies of rotational, vibrational and electronic transitions. While linear molecules usually have regularly distributed levels, polyatomic molecules have much more complicated spectra, where transitions are also caused by bending, twisting and stretching of bonds, making analyses more difficult. Observations of various transitions and in different wavelength regimes are summarized in Table 1.3.

Rotational spectra corresponds to transitions in the microwave region (millimeter wavelengths). Because intermolecular interactions hinder rotation in the liquid or solid phases, observations of rotational spectra are purely done in the gas-phase. Furthermore, some molecules are non-polar, meaning they posses an even distribution of positive and negative charges, such as symmetrical molecules like H_2, C_2 and CH_4, and need to be observed by other methods. For molecules lacking polarity, their vibrational frequencies, resulting from vibrational motion of the molecular bonds, can instead be identified using IR spectroscopy. The downside with this method however is that a background IR source is needed, supplying the environment with the photons characteristic of the structures of these molecules. This means that we can only gather information along these line of sights, but has the advantage that both symmetric and solid-phase molecules can be observed. Electronic transitions are caused by a restructure of electron distributions in the shells, as caused by for example excitation or after recombination of an ion where the electron recombines into a high energy state. These transition are often in the UV and because they are blocked in the Earth atmosphere, have to be observed from space. However, studies of electronic transitions do not reach the same high sensitivity as rotational transitions.

1.3.3 *Theoretical models*

Models take the input from laboratory experiments, their measured rate coefficients, in order to study the formation and destruction of molecules. Numer-

Table 1.3: The different types of observational wavelength regimes and examples of typical telescopes and targeted molecules.

Transition	Wavelength	Telescopes, e.g.
Electronic	UV/optical	Hubble, VLT, Keck
Vibrational	IR	VLT, Spitzer
Rotational	IR/sub-mm	Herschel, SMA, PdB, ALMA

Wavelengths	Environment	Molecules, e.g.
UV/Visible absorption	Diffuse clouds	H, C^+, CO, CN
mm absorption	Diffuse clouds	HCO^+, OH, C_2H
IR absorption	Diffuse clouds	CO, H_2, HD, H_3^+, H_2O (ice)
Radio emission	Dense clouds	CO, NH_3, H_2O, H_2CO
IR absorption	Dense clouds	Ices
IR emission	Protostars, inner PPDs	OH, H_2O, H_2
mm emission	Protostars, outer PPDs	CS, HCN, H_2CO, HC_3N

ically, the rate of change in the absolute concentration of any molecule x is calculated by adding up the formation and destruction pathways as:

$$\frac{\mathrm{d}n_x}{\mathrm{d}t} = \sum R_{\text{production}} - \sum R_{\text{destruction}}, \tag{1.3}$$

where n_x is the density of species x and $R_{\text{production}}$ and $R_{\text{destruction}}$ are the rate for individual formation and destruction reactions respectively. The rates R have units $\mathrm{cm}^{-3}\ \mathrm{s}^{-1}$ and are calculated from the rate coefficient (see Table 1.1), then multiplied by the density of the reactant, or reactants, of the reactions. This means the rate is $R = k\,n_i$ for first order-kinetics, $R = k\,n_i\,n_j$ for second-order kinetics, and $R = k\,n_i\,n_j\,n_m$ for third-order kinetics. Considering the types of reactions listed in Table 1.1, processes such as cosmic-ray ionization and photodissociation belong to the first-order kinetics (the other reactant being a photon), while ion-neutral and dissociative recombination belong to second-order kinetics. As is also listed in Table 1.1, the rate k differs depending on the type of reaction.

This large number of reactions form a ordinary differential equation (ODE) system which needs to be solved in order to determine the densities, or abundances, of a set of species. The simplest way is to assume a chemical equilibrium as the derivative of all molecules densities are set to zero, and solving the corresponding algebraic system of equations. This can be explained through a simple example for the adsorption and desorption of any species, with rates k_{ads} and k_{des} respectively:

$$\begin{cases} \mathrm{d}n_{\text{gas}}/\mathrm{d}t = \sum R_{\text{ice}} - \sum R_{\text{gas}} = k_{\text{des}} n_{\text{ice}} - \mathrm{k}_{\text{ads}} n_{\text{gas}} \\ \mathrm{d}n_{\text{ice}}/\mathrm{d}t = \sum R_{\text{gas}} - \sum R_{\text{ice}} = k_{\text{ads}} n_{\text{gas}} - \mathrm{k}_{\text{des}} n_{\text{ice}} \end{cases} \tag{1.4}$$

This works perfectly for a static environment, but one has to make sure the environment in question can reach steady-state abundances within its lifetime.

Otherwise the equations have to be solved time-dependently, using an integration package such as the Variable-coefficient ODE solver (VODE) (Brown et al. 1989) or Differential Variable-coefficient Ordinary Differential equation solver with the Preconditioned Krylov method GMRES for the solution of linear systems (DVODPK), all available in ODEPACK[3], a collection of ODE solvers. This is especially important if physical conditions change on time scales shorter than the chemical time scales, such as core collapse or PPD models.

Typical chemical networks consist of thousands of reactions connected by hundreds of molecules, and there exist two major chemical networks today for chemical studies throughout star formation; the Kinetic database for Astrochemistry (KIDA)[4] and the University of Manchester Institute of Science and Technology (UMIST) database[5]. Agundez & Wakelam (2013) analyzed differences between the models for dark cloud and pre-stellar core conditions and found that the calculated abundances between the networks are comparable, agreeing within an order of magnitude. The largest discrepancies, over an order of magnitude, are for larger carbon-rich molecules such as CH_3CHO, CH_3C_2H as well as H_2 and NS. Although it is difficult to trace the exact sources of the discrepancies, the fact that many neutral-neutral reactions involved in the chemistry of these molecules are mere estimations and that all their formation pathways may not have yet been fully explored is a likely cause. McElroy et al. (2013a) also discussed differences between the two networks. They found an agreement for most species, but for species such as CH_3CHO, C_3H_6 and HCOOH they found significant differences where calculated abundances using UMIST is in better agreement with observed abundances. These differences can be traced to newly measured rate coefficients included in UMIST but not yet in KIDA.

As our knowledge of both the physical and chemical processes break through new barriers, new theoretical models are developed. The most significant evolution of the chemistry in astrochemical models are the treatment of the surface chemistry. While many models consider grains to only consist of the surface, it has the consequence that all species can interact with one another. In reality, the icy surfaces of grains are ordered into layers, where only the few topmost layers can interact with one another, and species in the lower layers can only react through the slower process of surface diffusion or bombardment of high-energy photons such as cosmic rays. Cuppen et al. (2009) demonstrated the importance of correct treatments of layers by following the positions of individual species, and showing that the common rate equation methods can overestimate effects from variations in gas-phase abundances, and cause fluctuations in surface abundances. Therefore it has been introduced in a few studies of surface chemistry (e.g. Hasegawa & Herbst 1993; Fayolle et al. 2011; Taquet et al. 2012b; Garrod 2013).

A different way to account for the multi-layered nature of icy grains is using microscopic Monte Carlo method. The models follow the exact position

3 http://www.netlib.org/odepack/
4 kida.obs.u-bordeaux1.fr
5 udfa.net

of species on the grain, and because only species in the proximity of each other can react, it automatically takes into account the multilayered nature of icy grains. Unfortunately, this method is computationally expensive and often chemistry has to be reduced to smaller networks, and can not be modeled for long time scales. In macroscopic Monte Carlo methods, only the number density, rather than the exact positions, are tracked with time (Charnley 1998, 2001). Recently a Monte Carlo model handling multiple phases of the ice mantle has been developed (Vasyunin & Herbst 2013a). A unification between macroscopic and microscopic Monte Carlo methods has also been developed (Chang & Herbst 2012).

A simpler way, which is faster and easier to couple to the gas chemistry, is using the Master equation method as it handle both gas and surface kinetics in a similar way. In it, each possible configuration of species is considered and for each configuration a separate rate equation is constructed. With large number of species this leads to an infinite number of possibilities, but selective cut-offs can be used to remove high-order terms if their probability is small enough (Lipshtat & Biham 2004; Barzel & Biham 2007). Models available for handling large chemical networks has been developed, where the Master equation method is only applied when the accretion limit is reached for a species (Du & Parise 2011). A modified approach to the rate equation method have been developed where modifications to the rate equations mimic the stochastic behavior of the surface chemistry (Caselli et al. 1998; Garrod 2008) and has been shown to give excellent results in agreement with macroscopic Monte Carlo methods (Garrod et al. 2009).

Several physical processes have been added to astrochemical models in the past decade. Dynamics, in the form of transport of material has been included in a few models of protostellar and protoplanetary disk studies. This has successfully been used to study the chemistry during the warm-up of the ISM as it evolves into a protostellar environment (e.g. Visser et al. 2009, 2011). Furthermore, the effects on the chemistry through the transport in protoplanetary disks has been studied (e.g. Gail 2002; Wehrstedt & Gail 2002; Ilgner et al. 2004; Boss 2004; Ilgner & Nelson 2006; Semenov et al. 2006; Willacy et al. 2006; Aikawa 2007; Turner et al. 2007; Tscharnuter & Gail 2007; Hersant et al. 2009; Heinzeller et al. 2011b; Semenov & Wiebe 2011; Jacquet & Robert 2013; Furuya et al. 2013, see also Chapter 5). Detailed hydrodynamical codes have also been employed, but have mostly been restricted to simple chemistry due to computational restrictions (see e.g. Aikawa et al. 2008, 2012b). The transportation in protoplanetary disks is especially important in the search for Earth's origin as Earth is believed to have formed wet and, at least the majority, of its water is believed to have been delivered subsequently through collisions of comets and/or asteroids (see Chapter 5). The evolution of grains affects the cross sections of grains, as well as the rate of surface chemistry, and has been observed to effectively reducing the effects of processes such as ionization by UV and X-ray photons (see e.g. van Boekel et al. 2004, 2005; Sicilia-Aguilar et al. 2006; Rodmann et al. 2006; Natta et al. 2007; Cortes et al. 2009; Ricci et al. 2010; Ubach et al. 2012). It has been employed in a few studies of protoplanetary disks (e.g. Vasyunin et al. 2011).

1.4 STRUCTURE OF DISSERTATION

In this thesis we aim to further the advancement of our chemical understanding of the Universe, enlightening us on important clues and insights that we can learn from the study of the deuterium chemistry throughout the evolution from dark pre-stellar cores and till the onset of planet formation in PPDs. For this we have developed an extensive chemical network for the study of deuterium chemistry in these environments and this thesis follows the advancement of the chemical network through additions of high-temperature reactions and nuclear spin states, implemented in environments from the relatively simple structure of dark and diffuse clouds to the dynamically evolving structures of PPDs.

This thesis is divided into four separate chapters. First we will assess the reliability of our new up-to-date, extended, multi-deuterated network by modeling the deuterium chemistry in various phases of the ISM and comparing it with observed D/H ratios of a variety of mono-, doubly-, and triply-deuterated species in distinct astrophysical environments. Dominant pathways for a few essential molecules are analyzed and discussed, to compare the chemistry with previous studies. Finally, we also make predictions for observable deuterated species with ALMA in dark clouds (DC), warm infrared dark clouds (IRDC) and high-mass protostellar objects (HMPO).

Because there are many uncertainties associated with cloning our chemical network, in the second chapter we conduct a study on the propagation of uncertainties throughout the chemical evolution of gas-phase deuterated molecules in environments of DCs and warm IRDCs.

In the third chapter the chemical network is extended to include the nuclear spin states of H_2, H_2^+ and H_3^+, which has been found to have a profound effect on deuterium fractionation. This extended network is adopted in the first time-dependent study of the ortho-para chemistry in the diffuse ISM.

In the fourth, and final, chapter high-temperature reactions are added in order to study in detail the deuterium fractionation in the inner regions of protoplanetary disks. We adopt this network do investigate the chemical evolution of deuterated water in the young Solar nebula, emphasizing on the study of the origin of Earth's oceans.

2

NEW EXTENDED DEUTERIUM FRACTIONATION MODEL: ASSESSMENT AT DENSE ISM CONDITIONS

Adapted from Albertsson, Semenov, Vasyunin, Henning & Herbst (2013), ApJS, Vol. 207, p. 27 [1]

2.1 ABSTRACT

Observations of deuterated species are useful in probing the temperature, ionization level, evolutionary stage, chemistry, and thermal history of astrophysical environments. The analysis of data from ALMA and other new telescopes requires elaborate models for deuterium fractionation, however, the majority of reactions in deuterium chemistry have unknown reaction rates, and previous studies have often utilized limited chemical models for this reason. In this chapter we present a publicly available chemical network with multi-deuterated species and an extended, up-to-date set of gas-phase and surface reactions. We study how recent updates to reaction rates affect calculated D/H ratios. To test this network, we simulate deuterium fractionation at dense interstellar conditions, where D/H ratios are calculated for a range of temperatures and densities, and compared to the extensive list of observations in dense interstellar environments. We find that many multiply-deuterated species produced at 10 K retain enhanced D/H ratios at temperatures $\lesssim$ 100 K and calculated D/H ratios agree to observations within an order of magnitude, and for some species, such as HCN, HNC, DCN, DNC, our understanding of the chemistry compared to previous studies has improved in recent years. To further study the robustness of the chemical model we identify the dominant pathways for a selection of species, and find that pathways agree with the commonly accepted pathways for species such as H_3^+, HCO^+, HCN, H_2O, and including their isomers and isotopes. The long-term evolution of a selection of representative species are studied, and species that are dominantly formed on grains show significant variations in abundances at times $> 10^8$ years. Two cases of initial abundances are considered: (i) atomic except for H_2 and HD, and (ii) molecular from a prestellar core, and species are sorted according to their sensitivity to temperature gradients and initial abundances. Finally, in preparations for ALMA data, we list potentially observable deuterated species that are predicted to be abundant in low- and high-mass star-formation regions.

1 The results and text in this chapter was all done by me, but I received much help from Dmitry Semenov with identifying the dominant chemical pathways in Tables A.3 – A.7.

2.2 INTRODUCTION

As a large number of molecules and reactions are hydrogen-dominated, the importance of deuterium chemistry becomes clear. It mainly involves the study of the relative abundances between the deuterated and the un-deuterated analogue (hence on referred to as D/H ratio). There is an observed elemental D/H ratio $\sim 1.5 \times 10^{-5}$ in the ISM (Linsky 2003). However, a variety of deuterated species have been detected in various astrophysical environments with enhanced D/H ratios compared to the elemental ratio, including molecular clouds: DCO^+ (van der Tak et al. 2009; Guelin et al. 1977), DNC (van der Tak et al. 2009; Turner & Zuckerman 1978), H_2D^+(Parise et al. 2011; Stark et al. 1999), HDCO (Loren & Wootten 1985), D_2CO (Turner 1990), HD_2^+ (Parise et al. 2011), HDO (Phillips et al. 1973); pre-stellar cores: D_2CO (Bacmann 2004), H_2D^+ (Caselli et al. 2003; Vastel et al. 2006a; Caselli et al. 2008), HD_2^+ (Vastel et al. 2012), N_2D^+ (Miettinen et al. 2012), NH_3D^+ (Cernicharo et al. 2013), NHD_2 (Roueff et al. 2000); hot cores/corinos: D_2CO, HDCO (Bergman et al. 2011), $DCOOCH_3$ (Demyk et al. 2010; Margulès et al. 2010), HD_2^+ (Vastel et al. 2004), HDO, NH_2D (Jacq et al. 1990); warm protostellar envelopes: DCO^+, HDCO (Parise et al. 2009), HDO (Jørgensen & van Dishoeck 2010; Liu et al. 2011), OD (Parise et al. 2012); PPDs: DCN (Qi et al. 2008), DCO^+ (van Dishoeck et al. 2003; Guilloteau et al. 2006; Qi et al. 2008), H_2D^+ (Ceccarelli et al. 2004), HD (Bergin et al. 2013) and comets: CH_3D (Bonev et al. 2009; Gibb et al. 2012), HDCO (Kuan et al. 2008), HDO (Villanueva et al. 2009; Hartogh et al. 2011; Gibb et al. 2012). For comprehensive reviews, see Roueff & Gerin (2003) and Bergin et al. (2007).

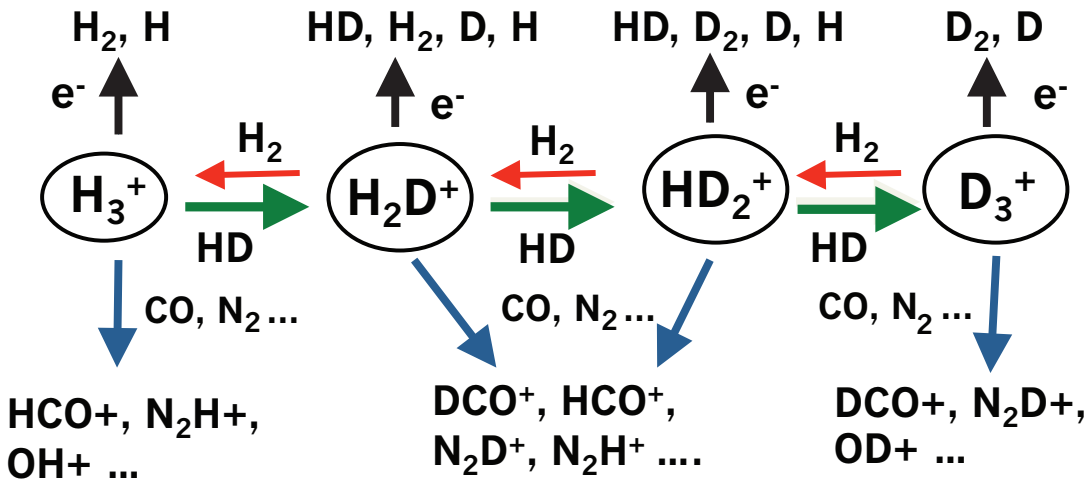

Figure 2.1: The chemistry of deuterium fractionation, beginning with H_3^+, and proceeding in a similar fashion, redistributing deuterium. Green arrows signify exothermic reactions, red endothermic and blue the essential pathways furthering the chemical complexity. Adopted from H. Roberts.

This enhanced D/H ratio has been found to be a result of the isotopic fractionation. The redistribution of elemental deuterium, initially locked mainly in HD, is initiated by fast ion-molecule reactions with polyatomic ions, such as H_3^+, H_2D^+, HD_2^+ and D_3^+ (see Figure 2.1). Due to zero-point vibrational energy differences between modes with D and H, and the lack of a ground rotational state for H_3^+, the backward reactions between H_2 and H_3^+ isotopologues are endothermic, with barriers of $\sim 100 - 300$ K, leading to the initial enrichment of the H_3^+ isotopologues at $\lesssim 20 - 30$ K. In a similar way, other ions such as CH_2D^+ and C_2HD^+ allow deuterium fractionation to proceed effectively at warmer temperatures of $\lesssim 30 - 80$ K because of the larger endoergicities for the backward reactions (e.g., Millar et al. 1989; Roueff et al. 2005; Parise et al. 2009). These deuterated ions react further with abundant molecules such as CO and N_2, transferring deuterium atoms to new molecules similar to H_3^+ in Figure 1.4. These findings have been proven both observationally and theoretically (see, e.g., Bacmann et al. 2002, 2003; Roberts et al. 2003; van der Tak 2006; Roberts & Millar 2006; Caselli et al. 2008). The initial gas-phase deuterium enrichment of H_3^+ is even more pronounced in cold, dense regions, where some destructive neutral species, especially CO, become severely depleted onto dust grain surfaces. The dissociative recombination of abundant H_3^+ isotopologues leads to a high flux of D atoms ($\lesssim 10 - 30\%$ compared to H) sticking to dust grains. This leads to further reactions with surface species such as CO forming abundant multi-deuterated complex (organic) ices such as formaldehyde and methanol. These molecules can later desorb into the gas-phase due to non-thermal desorption or due to the gradual warm-up of the environment by a forming protostar.

It is these properties that cause the study of the deuterium chemistry to have been long employed as constraints of similar parameters compared to their undeuterated analogues, such as the the ionization fraction, density and thermal history of the ISM and PPDs (e.g., Geiss & Reeves 1981; Turner 1990; Aikawa & Herbst 2001; Crapsi et al. 2005; Willacy 2007; Öberg et al. 2012). Furthermore the chemical age and thermal history of the environment can also be probed (Chen et al. 2011).

With the ALMA observing facilities now in full use we are entering a new era of high-sensitivity observing facilities where we will be able to test theories and gain a wider understanding of the formation and evolution in low- and high-mass star-formation regions. In order to analyze these rich observational data, new astrochemistry models including isotope-exchange reactions and state-to-state processes will be required.

The implementation of deuterium chemistry is a challenging task though because of a limited number of accurately determined rate coefficients of relevant reactions, and the sheer number of hydrogen-dominated reactions in astrochemical networks. Previous studies used the available limited set of reaction data, substituted with "educated guesses" for missing reaction rates, and cloned data from similar reactions involving hydrogen-bearing species (e.g., Herbst 1982; Brown et al. 1988; Rodgers & Millar 1996; Charnley et al. 1997; Turner 2001; Aikawa et al. 2003, 2012b; Sipilä et al. 2013a). In many cases only mono- and double-deuterated species were considered.

Because of the exothermicity of the reactions responsible for the redistribution of deuterium, temperature plays a vital role in the deuterium chemistry, as does density because of its effects on many physical processes, as well as the rate of reactions. But, not only are the current physical properties of the environment important for chemical evolution, but also is the evolutionary history. Taquet et al. (2012a) have considered a two-stage model to study deuterium chemistry in prestellar cores, with a gas-phase steady-state phase followed by the formation and evolution of grain mantles and surface deuterium fractionation. With such a simple approach they have reproduced high observed abundances of the isotopologues of formaldehyde and methanol. Taquet et al. (2012a) have concluded that D and H abstraction and substitution reactions on dust surfaces are crucial for attaining the observed high D/H ratios. The role of abstraction reactions for deuterium fractionation has been intensively investigated in the laboratory (see e.g., Nagaoka et al. 2005; Hidaka et al. 2009; Hama et al. 2012).

Cazaux et al. (2011) have studied the chemistry of formaldehyde and water by modeling the formation of ices in translucent clouds, and later following the chemical evolution as the cloud collapses to eventually form a Class I protostellar object. Their results show that the degree of deuteration of formaldehyde is sensitive to the initial D/H ratios of gaseous molecules attained before the collapse phase, while the degree of deuteration of water depends strongly on the dust temperature during the water ice formation. Intriguingly, Coutens et al. (2012) have observed deuterated water vapor in the low-mass protostar IRAS 16293-2422 and found that the water D/H ratio is lower than for other deuterated species detected in the same source. This observational trend continues toward more evolved hot cores/corinos (e.g., Parise et al. 2004; Bacmann et al. 2012) and suggests that the water may have formed relatively early, in a warm dilute ISM environment, while the depletion of CO at a later, cold and dense dense core stage allows for efficient surface synthesis of highly deuterium-enriched complex ices. An alternative explanation could be efficient abstraction and substitution reactions of H atoms by D atoms for organic ices like formaldehyde and methanol during cold prestellar cloud phase, which would not be as effective for water ice. A detailed one-dimensional chemical-hydrodynamical model of the prestellar core collapse and the formation of a protostar, coupled to the gas-grain chemistry and deuterium fractionation, has been developed by Aikawa et al. (2012b). They have found that due to initially high D/H ratios accumulated in the cold phase, large (organic) molecules and carbon chains remain strongly deuterated even at later, warmer conditions.

While physical properties, such as temperature and density, and surface chemistry can have a significant effect on deuterium fractionation, smaller effects can derive from other global properties such as metallicity and ionization fields. In order to understand the influence of metallicity and ionization one needs to study deuterated species on a more global scale. Bayet et al. (2010) have conducted an observational survey of deuterated species in extragalactic star-forming regions, studying the influence of density, temperature, far-UV radiation field, cosmic-ray ionization and metallicity on the D/H ratios for $\sim$20 deuterated species. Without modeling any particular source, they have com-

pared the predicted column densities with those derived from the limited set of observational data in external galaxies with reasonable agreement.

ALMA is a truly revolutionary observational facility not only for extragalactic and cosmological studies, but also for observations of the Milky Way ISM. With the high-sensitive, high-resolution ALMA being operational we have the possibility to, for the first time, detect and spatially resolve emission lines of numerous new complex and rare-isotope molecules. In order to analyze these rich observational data, new astrochemistry models including isotope-exchange reactions and state-to-state processes will be required and in this chapter we provide a new extended, public deuterium fractionation model, and explore its validity and accuracy. We assess the reliability of our deuterium chemistry model by modeling the deuterium fractionation in various phases of the ISM and comparing the results with observed D/H ratios of a variety of mono-, doubly-, and triply-deuterated species in distinct astrophysical environments. A list of the most promising, deuterated species potentially detectable with ALMA in the local Milky Way ISM is provided and the new deuterium network is freely available on the Internet[2].

The remainder of this chapter is structured as follows. In Section 2.3 we present the new deuterium chemistry model. We give a detailed description of the construction of our deuterium network and our choice of relevant reaction rates and branching ratios, as well as investigate the effects of recent updates to reaction rates. In Section 2.4 we discuss results in general trends of D/H distributions over our 2D-parameter space, the long-term chemical evolution of a few species, analyze the dominant chemical pathways for a assortment of essential species and finally compare our calculated D/H ratios to assorted observations and make predictions for observable deuterated species with ALMA. Added and updated reaction reactions to non-deuterated and deuterated reactions are listed in Tables A.1 and A.2.

2.3 MODEL

2.3.1 *Parameter space*

In this chapter we are primarily concerned with providing a new extended deuterium network and assessing its capacity to model chemistry under both static cold and warm conditions in the ISM. We do not consider evolutionary models such as those pertaining to low-mass and high-mass star formation separately, although the static conditions we consider arise from evolutionary processes. We concentrate on the evolutionary stages ranging from a cold molecular cloud to the warm envelopes of protostars, choosing a wide parameter space with a grid of 1 000 points covering temperatures between $5-150$ K and densities of $10^3 - 10^{10}$ cm^{-3}, and assume the standard ISM dust and a fixed $A_V = 10$ mag, meaning that the photochemistry is only driven by secondary UV photons. Assuming a fixed A_V reduces the problem to two dimensions, which is easier to analyze and visualize.

2 http://mpia.de/PSF/codes.php

2.3.2 *Chemical model*

I have utilized the gas-grain chemical model "ALCHEMIC" developed by Semenov et al. (2010b), where a detailed description of the code and its performance is presented, but a few features of the "ALCHEMIC" model are summarized below.. The code is optimized for modeling the time-dependent evolution of large chemical networks, including both gas-phase and surface species.

The self-shielding of H_2 from photodissociation was calculated using Equation (37) from Draine & Bertoldi (1996). The shielding of CO by dust grains, H_2, and its self-shielding was calculated using the precomputed table of Lee et al. (1996, Table 11). We consider CRP as the only external ionizing source, using a CRP ionization rate for H_2, $\zeta_{CR} = 1.3 \times 10^{-17}$ s^{-1} (Herbst & Klemperer 1973), appropriate for molecular cloud environments and which has been utilized in several previous studies (such as Wakelam et al. 2006b; Vasyunin et al. 2008b; Druard & Wakelam 2012). The gas-grain interactions include DR and neutralization of ions on charged grains, sticking of neutral species and electrons to uniformly-sized 0.1 μm dust grains with a sticking coefficient of 1 and release of ices by thermal, CRP-, and UV-induced desorption, such that at high temperatures the surface population will be low as thermal desorption takes over. We do not allow H_2 and its isotopologues to stick to grains. We assume a UV photodesorption yield of 10^{-3} (e.g., Öberg et al. 2009a,b). With our fixed visual extinction, the photon field derives from secondary electron excitation of molecular hydrogen followed by fluorescence.

We assume that each 0.1μm spherical silicate grain provides $\approx 1.88 \times 10^6$ sites (Biham et al. 2001) for surface recombination that proceeds solely through the classical Langmuir-Hinshelwood mechanism (e.g. Hasegawa et al. 1992). Upon a surface recombination, we assume there is a 5% probability for the products to leave the grain due to the conversion of some of the exothermicity of reaction into breaking the surface-adsorbate bond (Garrod et al. 2007). We do not find significant differences (less than a factor of 2) in D/H ratios and abundances of essential species, such as H_3^+, water, ammonia from varying this probability between 1−10%. However, we found a significant variation in ice abundances of formaldehyde and methanol of up to a factor of 6 at lower temperatures ($\lesssim$ 25 K) when considering higher desorption probabilities $\gtrsim$ 5%. Interestingly, ice abundances increase with the desorption probability and we find that this is due to a much more efficient formation of formaldehyde and methanol at intermediate times. Due to more intense gas-grain interactions precursor species of H_2CO and CH_3OH are able to form more readily in the gas phase and later stick to grains. Consequently, formaldehyde and methanol are formed faster via surface processes. Following experimental studies on the formation of molecular hydrogen on dust grains by Katz et al. (1999), we adopt the standard rate equation approach to the surface and ice chemistry without quantum-mechanical tunneling through the potential walls of the surface sites. We also do not consider competition kinetics between activation and diffusive barriers (Garrod & Pauly 2011).

A typical run, with relative and absolute tolerances of 10^{-5} and 10^{-25}, utilizing the original gas-grain network without deuterium chemistry (∼7 000

Table 2.1: Initial abundances for the Primordial model with respect to n_{H}.

Species	H_2	H	HD	He	C
	0.499	2.00×10^{-3}	1.50×10^{-5}	9.75×10^{-2}	7.86×10^{-5}
Species	N	O	S	Si	Na
	2.47×10^{-5}	1.80×10^{-4}	9.14×10^{-8}	9.74×10^{-9}	2.25×10^{-9}
Species	Mg	Fe	P	Cl	
	1.09×10^{-8}	2.74×10^{-9}	2.16×10^{-10}	1.00×10^{-9}	

Table 2.2: Initial abundances of major species for the "Evolution" model with respect to n_{H}.

Species	H_2	He	H	HD	C
	0.500	9.76×10^{-2}	2.32×10^{-4}	9.57×10^{-6}	1.02×10^{-8}
Species	N	O	S	Si	Na
	8.75×10^{-8}	1.45×10^{-6}	2.00×10^{-9}	7.00×10^{-11}	6.37×10^{-11}
Species	Mg	Fe	P	Cl	H_2O (ice)
	3.70×10^{-10}	6.07×10^{-11}	5.72×10^{-12}	1.64×10^{-10}	9.90×10^{-5}
Species	CO (ice)	CO	CH_4 (ice)	NH_3 (ice)	O_2
	3.91×10^{-5}	1.85×10^{-5}	1.66×10^{-5}	1.30×10^{-5}	7.04×10^{-6}
Species	N_2	O_2 (ice)	D	N_2 (ice)	HDO (ice)
	3.78×10^{-6}	2.29×10^{-6}	1.81×10^{-6}	1.26×10^{-6}	1.08×10^{-6}
Species	C_3H_2 (ice)	HNO (ice)	D_2		
	7.68×10^{-7}	7.25×10^{-7}	7.07×10^{-7}		

reactions, $\sim$ 700 species) takes 1–5 s for 1 Myr of evolution with a Xeon 3.0 GHz CPU. With our new, almost tenfold larger deuterium network, the same run takes approximately an order of magnitude longer to calculate. The linear dependence of the CPU time vs. species number in the model is due to the advanced numerical scheme implemented in the ALCHEMIC code, which generates and uses sparse Jacobi matrices.

2.3.3 *Initial abundances*

As input data, reaction rate coefficients and physical properties need to be specified, as do initial abundances. We have chosen to implement two different initial abundance sets and calculate the chemical evolution with the new deuterium network for 1 Myr.

For the first set, hereafter referred to as the "Primordial" model, we utilized the "low metals" abundances of Graedel et al. (1982) and Lee et al. (1998a). Initially all deuterium is located in HD, with $\mathrm{D/H} = 1.5 \times 10^{-5}$ (Stancil et al. 1998; Linsky 2003), see Table 2.1. The abundances in the second set, the "Evolution" model, were calculated with our deuterium chemistry model, assuming

a TMC1-like environment: $T = 10$ K and $n_H = 10^4$ cm^{-3}, at $t = 1$ Myr. Under such conditions elemental deuterium from HD is efficiently redistributed to other molecules, leading to their high initial D/H fractionation. These final abundances at 1 Myr are used as input in the "Evolution" model (see Table 2.2). The "Evolution" model serves as a simple example of a two-stage chemical model with physical conditions that can change dramatically at 1 Myr, unless the evolutionary model is run strictly under TMC-1 conditions.

2.3.4 *Deuterium model*

As a first step toward creating a consistent network with deuterium fractionation, we undertook a thorough search in the literature for updates to the reaction rates of the original non-deuterated network. We utilized the latest osu.2009 gas-phase chemical network and incorporated all essential updates as of April 2013, adopted from Horn et al. (2004), Chabot et al. (2010), Hamberg et al. (2010a), Wakelam et al. (2010b), Laas et al. (2011), as well as those reported in the KInetic Database for Astrochemistry (KIDA)[3]. Further, to allow for the synthesis of the few complex molecules in our network such as methanol (CH_3OH), methyl formate ($HCOOCH_3$), and dimethyl ether (CH_3OCH_3), an extended list of surface reactions and photodissociation of ices was adopted from Garrod & Herbst (2006). Several tens of gas-phase photoreaction rates were updated using the new calculations of van Dishoeck et al. (2006)[4].

Next, we applied a cloning routine to this updated network (as described in Rodgers & Millar 1996), and added all additional primal isotope exchange reactions for H_3^+ as well as CH_3^+ and $C_2H_2^+$ from Roberts & Millar (2000b); Gerlich et al. (2002); Roberts et al. (2004); Roueff et al. (2005). In this cloning routine all reactions bearing hydrogen atoms are considered to have deuterated analogues, and "cloned" accordingly (assuming the same rate coefficient if no laboratory data are available). In cases where the position of the deuterium atom is ambiguous, we apply a statistical branching approach. In the resulting network we do not yet distinguish between the ortho/para states of molecules, and leave this for a separate paper.

A typical example of the outcome of the cloning procedure is presented for the reaction between C^+ and CH_3:

$$C^+ + CH_3 \rightarrow C_2H^+ + H_2 \Rightarrow \begin{cases} C^+ + CHD_2 \rightarrow C_2D^+ + HD \\ C^+ + CHD_2 \rightarrow C_2H^+ + D_2 \end{cases} \tag{2.1}$$

The single ion-molecule reaction of C^+ with CH_3 is cloned into two separate channels for CHD_2. Moreover, the branching of these two new channels is not equal. To visualize this, we label the two deuterium atoms in CHD_2 D_a and D_b. For the first reaction, which forms C_2D^+, D_a can be placed on either product and D_b on the other, hence we have two possibilities: $C_2D_a{}^+ + HD_b$ or $C_2D_b{}^+ + HD_a$. For the second channel, which forms C_2H^+, both deuterons have to be

3 http://kida.obs.u-bordeaux1.fr/ as of [2013-4-13]
4 http://www.strw.leidenuniv.nl/~ewine/photo/

Table 2.3: Species showing variations in D/H ratios by more than a factor of 5 due to the updates in the reaction network. Only species with fractional abundances $> 10^{-25}$ are considered.

Species	R(D/H)	Species	R(D/H)	Species	R(D/H)
HD_2O^+	24.3	HD_2CS^+	5.4	H_2DO^+	5.9
CH_2D_2	8.5	CHD_3	8.5	D_2CS	5.3
CH_4D^+	7.9	CH_3D	8.1		
CD_4	7.0	$C_2H_2D_2$	7.3		

placed on D_2 and we only have one possibility. This analysis assumes that the deuterons on D_2 are indistinguishable, which is in agreement with the Pauli Exclusion Principle. Alternatively, we could initially assume that they are distinguishable, but because half of the D_2 rotational-nuclear spin states are missing, the simple argument about $2/3$ and $1/3$ branching ratios remains valid.

Full tables of added and updated reactions are found in Tables A.1 and A.2. The resulting chemical network consists of $\sim$ 62 000 reactions connected by $\gtrsim$ 1 900 species, to our knowledge the most extended network for deuterium chemistry to date[5].

2.3.5 *Analysis of reaction updates*

It is of interest to characterize the influence of the reaction rate updates on the calculated abundances and the D/H ratios. This may help us to highlight the significance of recent laboratory astrochemistry activities, both for deuterated and un-deuterated species, in providing more accurate astrochemical data to the community.

First, we studied the effects of introducing deuterium chemistry into our model on abundances of un-deuterated species by comparing abundances throughout the parameter space to a non-deuterated version of the network. We found that species with relative abundance $> 10^{-25}$ show mean values in abundance variations between the two networks within a factor 0.95 - 1.05. Since we did not find any particularly large variations in abundances for H-bearing species, we conclude that the results from our updated analysis are a pure effect of updated reaction rates and not caused by the additional pathways created by the cloning routine.

In order to separate the effect that recent updates have had on abundances, we generated an additional network by cloning an outdated network restricted to the reaction rate updates up until 2005. We then studied the impact of updated reaction rate coefficients by comparing the calculated time-dependent abundances between the "old" chemical network and the "new" network in the 2D-parameter space discussed in Sect. 2.3.1. In addition to the D/H abundance ratios, we will emphasize the differences in these ratios between the

5 Publicly available at: http://mpia.de/PSF/codes.php

models, which we calculated by dividing the respective D/H ratios in the updated 2013 network by those from the outdated 2005 network, and will denote this ratio as $R(\mathrm{D/H})$. The results have been obtained with the Primordial model only. In this comparison, we have excluded minor species with relative abundances below 10^{-25}. It should be noted that the $R(\mathrm{D/H})$ ratios may remain unchanged when absolute abundances of species and their isotopologues in the updated and outdated networks increase in unison.

We list in Table 2.3 the arithmetic mean value calculated over the parameter grid ($T = 5 - 150$ K, $n_{\mathrm{H}} = 10^3 - 10^{10}$ cm^{-3}) of R(D/H) ratios for all species with fractional abundances $\geq 10^{-25}$ for which the mean value of R(D/H) ratios have changed by more than a factor of 5. Among the listed species, we find light hydrocarbons (e.g., CHD_3, CH_2D_2), ions (CH_4D^+, HD_2O^+), and simple organic molecules (e.g. DCOOH, D_2CO), as well as key molecules such as doubly-deuterated water and ammonia. Multi-deuterated species appear to be more affected by the updates than their singly-deuterated analogues, as there are more intermediate pathways involved in their chemistry, as is most evident by comparing HD_2O^+ and H_2DO^+ in Table 2.3.

There are also several species affected by the abundances that do no show any variance in D/H ratios, i.e. both deuterated and undeuterated species are similarly affected by updates. The abundances of CH_2D^+ and $CHD_2{}^+$ provide good examples of such behavior. These species show a coherent increase (within a factor of 1.1 between un-deuterated species and isotopologues) in their gas-phase abundances at 1 Myr and at high temperatures ($\gtrsim 100$ K) and densities ($n_{\mathrm{H}} \gtrsim 10^7$ cm^{-3}). As a result, their $R(\mathrm{D/H})$ values remain close to unity. We identified the coherent increase in abundance as originating from an update taken from KIDA in the rate coefficient for the slow radiative association reaction forming $CH_5{}^+$ via $CH_3{}^+$ colliding with H_2. The rate coefficient of this reaction was lowered by almost two orders of magnitude, from 1.30 $\times 10^{-14}$ cm^3 s^{-1} to 4.10 $\times 10^{-16}$ cm^3 s^{-1} (at room temperature; see Wakelam et al. 2010b). We note that the older value was based on a misinterpretation of the original literature, which used 300 K in the formula for the rate coefficient but was intended only for temperatures up to 50 K (Herbst 1985). The same D/H ratio variation is transferred to HD_2O^+ and H_2DO^+ through the ion-neutral reaction with $CH_5{}^+$ and its isotopologues reacting with free oxygen atoms. The abundances of the CH_4 isotopologues derive from the dissociative recombination of $CH_5{}^+$ (and its isotopologues) as well as from ion-molecule reactions with CO, so CH_4 is directly affected by the updated reaction rate. It then transfers its D/H ratio variation into $C_2H_2D_2$ through CH_2D_2 reacting with CH. Another route involves the intermediary reaction between CH_2D_2 and S^+ to form HD_2CS^+, which later dissociatively recombines into D_2CS, which in turn reacts with CH_2D_2.

On the other hand, the deuterated analogue of this radiative association reaction does not occur; instead CH_3^+ + HD produces CH_2D^+ and H_2, and the corresponding rate constant is the same in the outdated and new networks (Millar et al. 1989). This slows down production of the key ion, CH_5^+, while deuterated isotopologues of CH_3^+ and CH_5^+ are produced with almost the same rate, consequently affecting D/H ratios of the gas-phase species listed

Table 2.4: Species showing strong dependences on initial abundances or temperature.

Initial abundances	Temperatures	
	~ 30 K	~ 80 K
C_2HD, C_3HD, C_6D, CD, CD_2, CD_3OH, CH_2D_2, CH_2DCN, CH_2DOH, CHD_2OH, CHDCO, D_2CO, D_2CS, DC_3N, DC_5N, $DCOOCH_3$, DCOOH, DCS^+, DNCO, H_2DO^+, HDCO, HDO, HDS, ND, NH_2D, NHD_2, OD	C_2D_2, C_2HD^+, CD_4, CHD, CHD_3, N_2D^+, D_2O, D_2S, D_3^+, D_3O^+, DCN, DCO^+, DNC, DOC^+, H_2D^+, HD_2^+, HD_2O^+, N_2D^+, ND_3	C_2HD^+, CH_2D^+ CHD_2^+

in Table 2.3. It does not affect abundant organic species such as methanol and formaldehyde however, as they are mainly formed by surface hydrogenation of CO ice.

We find that there is a particularly large variance in abundances for the two sulphur-bearing species, C_2S and C_2S^+, which show an increase in abundance by a factor of 187 and 26, respectively, compared with the non-deuterated network. We are not concentrating on the chemistry of sulphur-bearing molecules in this study because their chemistry is still poorly understood and often restricted to a few pathways. But the additional pathways that the cloning routine generates has a stronger effect on these two species as pathways reducing their abundances proceed much slower than their formation pathways.

2.4 RESULTS

2.4.1 *General trends in D/H distributions*

In this section, we discuss general trends in the modeled D/H ratios in our 2D-parameter space (see Section 2.3.1). The computed D/H fractionation ratios at the final time of 1 Myr are shown in Figure 2.2 for the "Primordial" (left panels of each separate block) and "Evolution" model (right panels of each separate block), which were introduced in Section 2.3.3, as functions of density and temperature for the following key gaseous molecules: H_2DO^+, H_2D^+, HDO, D_2O, ND, ND_3, DCOOH and DCN. For most species, the D/H ratios can reach high values of $\gtrsim 10^{-3}$ at $T \lesssim 30 - 80$ K. At higher temperatures, $\gtrsim$ 100 K, the computed D/H ratios begin to approach the elemental ratio of $\approx 1.5 \times 10^{-5}$. The higher D/H ratios of $\gtrsim 0.1$ have been observed for many species in the ISM, such as CH_2DOH, D_2CO (Ceccarelli 2002), D_2O (Butner et al. 2007), H_2D^+ (Caselli et al. 2003), HDO (Liu et al. 2011), NH_2D (Hatchell 2003; Roueff et al. 2005), NHD_2 (Roueff et al. 2005). For comparison of our model results with observations, see Section 2.4.4.

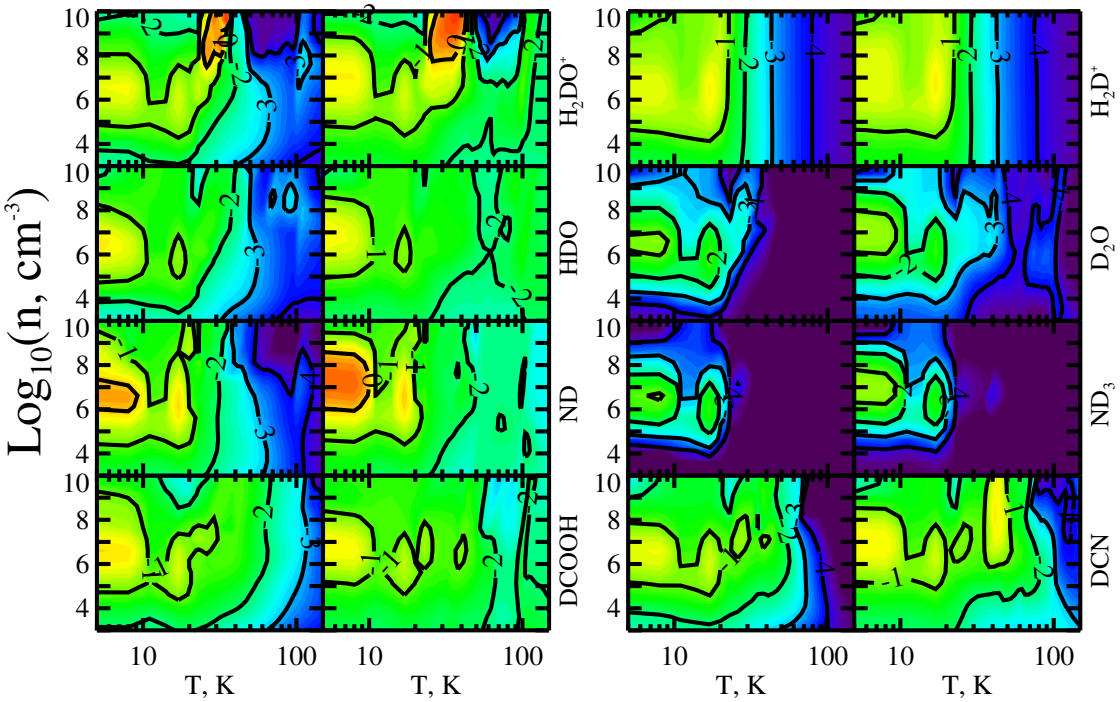

Figure 2.2: Plots of the D/H distributions at 1 Myr for our models. Each panel is a contour plot displaying the distribution of specific logarithmic D/H ratios. In the online version, fractionation levels with elemental (low), intermediate, and high D/H fractions are indicated with a continuous scale starting with dark blue ($\leq 10^{-5}$), green (10^{-2}), yellow (10^{-1}), and red (≥ 1) colors. Columns 1 and 2 show ratios with significant differences from the norm in their strong dependence on initial abundance and Columns 3 and 4 show species with an unusually strong dependence on temperature. Columns 1 and 3 show results from the "Primordial" model while columns 2 and 4 show results from the "Evolution" model.

We isolate species that are either mostly sensitive to kinetic temperature or initial abundances, the former referring to the standard temperature dependence for deuterium fractionation, and the latter referring to the difference between the initial abundances in the primordial and evolutionary models. We note that usually species for which D/H ratios depend more strongly on the initial abundances also show (a weaker) temperature dependence, because the release of CO and other radicals decreases the abundances of the H_3^+ isotopologues which lowers the efficiency of transferring D atoms to other species. These two groups are listed in Table 2.4. The temperature-dependent species can be further divided into two subgroups by the temperature where D/H ratios decrease most sharply, and hence where deuterium fractionation becomes less pronounced: (1) at low temperatures, $T \sim 20 - 40$ K (related to the fractionation via H_3^+ isotopologues) and (2) at higher temperatures $T \sim 80$ K (related to the fractionation via CH_2D^+ and C_2HD^+).

The left two columns of Figure 2.2 show species that demonstrate a strong dependence of D/H ratios on the initial abundances while the right two columns show species with a strong temperature gradient for D/H ratios and no distinct dependence on initial abundances. We define here a strong dependence on the initial abundance as an overall variation by a factor of 5 in D/H ratios at temperatures > 100 K for the final time step. For the case of HDO in Figure 2.2, D/H ratios are approximately 2 orders of magnitude higher in the "Evolution" model compared to the "Primordial" model at temperatures > 100 K and hence its D/H ratios are considered to depend strongly on the initial abundance. Frozen molecules show D/H distributions similar to their gas-phase analogues as we do not specifically consider selective substitution of H by D in surface species (yet we do consider production of deuterated molecules by surface chemistry). Therefore, we do not discuss the distribution of D/H for ices separately.

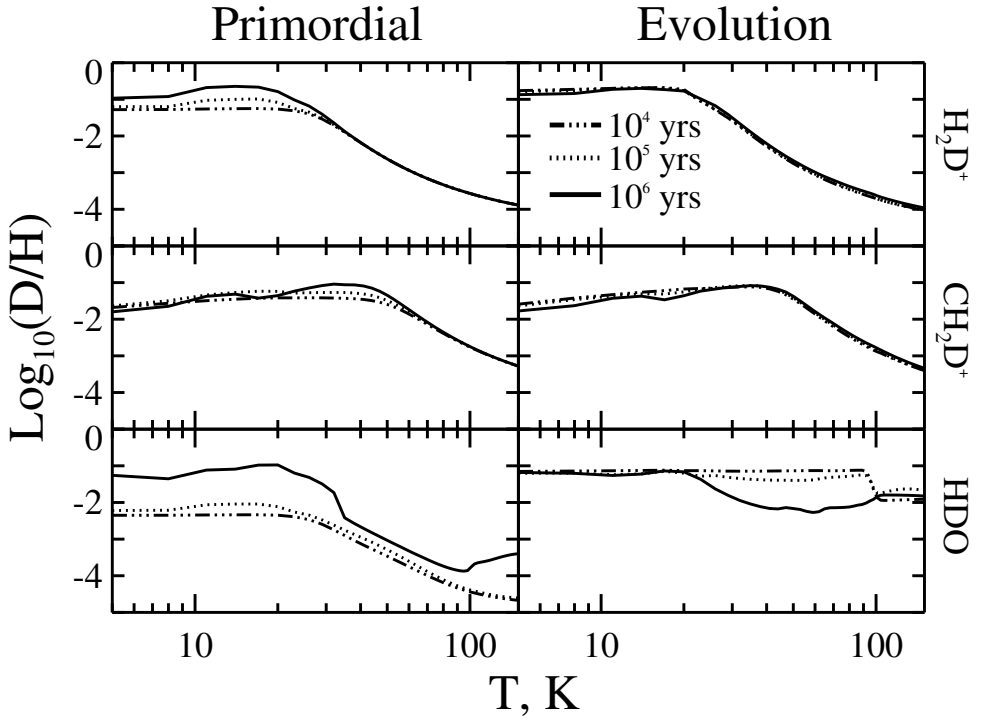

Figure 2.3: D/H ratios for H_2D^+, CH_2D^+ and HDO as a function of temperature at a density $n_H = 10^4$ cm^{-3} and for three specific times: $10^4, 10^5, 10^6$ years.

The placement of species in different groups can be explained by the relative pace of their chemical evolution. If steady-state abundances are reached by 1 Myr in the primordial stage, then they remain at steady state throughout the evolutionary model unless the physical conditions are changed. In Figure 2.3 we show the evolution of D/H ratios at three separate times of $10^4, 10^5, 10^6$ years, and at a density $n_H = 10^4$ cm^{-3} as a function of temperature for H_2D^+, CH_2D^+ and HDO. We discuss the specific case for the evolution of HDO later and begin with the two ions (two top panels) which are highly reactive, with fast chemical timescales associated with ion-neutral reactions and dissociative

recombinations. Thus, the chemical "memory" of the pristine state of the fast-evolving deuterated species is completely lost at the final considered time of 1 Myr, with no apparent differences between abundances computed with the two distinct initial abundance sets.

We find that the majority of neutral species, which includes several H-, C-, O-, N- and S-bearing species, show a dependence on the initial abundance as their evolution is significantly slower compared to ions. These are predominantly neutral species unless they are strongly associated with one of the major ions (such as H_3^+, CH_3^+, HCO^+ and their isotopologues). This is illustrated in Figure 2.3 for HDO (bottom panel), where we see differences in D/H ratios of ~ 3 orders of magnitude between the two models at higher temperatures approaching 100 K. In the "Primordial" model we start with atomic abundances and the water D/H ratios are lower for ices than for gas vapor because. This is because the formation of key ingredients for HDO ice through OD + H or OH + D is slower gas-phase fractionation via ion-molecule processes. In contrast, the "Evolution" model starts with high abundances and D/H ratios of water, mostly frozen onto grains. At low temperatures < 30 K water quickly reach the steady-state abundances while at higher temperatures, because gas-phase fractionation is not efficient, the D/H ratios of water vapor decreases with increasing temperature. Desorption play an important role at temperatures above $20 - 30$ K where, even in highly obscured regions, CRP-driven desorption occurs. At temperatures $\gtrsim 100$ K we see a drop in D/H ratios down to similar values of water ice because desorption replenishes the water vapor constantly and the water vapor also inherits the same D/H ratios as the ice ($\sim 10^{-2}$).

H_2DO^+ was the only ion we found showing a significant difference in the distribution between the two sets of initial abundances, which is related to the protonation of HDO by H_3^+ and which thus behaves chemically similar to HDO (see above). Complex neutral species, which are not a direct outcome of fast dissociative recombination reactions, evolve more slowly via neutral-neutral and surface processes, and thus show a dependence on the adopted initial abundances. The high initial abundances of deuterated species accumulated at 10 K in the "Evolution" model enable rich deuterium chemistry during the entire time span of 1 Myr even at warm temperatures of $T \lesssim 50 - 100$ K. As a result, some species show almost uniformly high D/H ratios of $\gtrsim 10^{-3}$ at $T = 10 - 150$ K (see Figure 2.2, left column). On the other hand, the same species in the "Primordial" model (with only HD available initially) show a significant decrease in the final D/H ratios toward warmer temperatures ($\gtrsim 40 - 80$ K). The effect is strong for saturated species that are at least partly formed on dust surfaces, and thus are sensitive to the choice of the initial abundances (and temperature), such as water or ammonia isotopologues. Also, most multiply-deuterated species, whose formation involves several isotope exchange reactions, show strong dependence on the initial abundances.

Ions constitute the majority of species for which calculated D/H ratios are only dependent on temperature (see Figure 2.2, right two columns). Species such as the H_3^+ isotopologues that are sensitive to freeze-out (or specifically, the freeze-out of CO), "daughter" molecules such as DCO^+, as well as (ion-

ized) light hydrocarbons related to CH_2D^+ and C_2HD^+, all show a strong temperature dependence. From the exact gas kinetic temperature, labeled the critical temperature, at which the D/H ratios start to approach the elemental value, we can separate these species into two subgroups. The deuterated species formed via low-temperature fractionation channels involving isotopologues of H_3^+ have a critical temperature of $20 - 30$ K, whereas other deuterated species synthesized via high-temperature fractionation channels involving CH_2D^+ and C_2HD^+ show a higher critical temperature of ~ 80 K (Parise et al. 2009). Most multi-deuterated species belong exclusively to the low-temperature group as do the majority of ions, which inherit the temperature dependence from the $H_3{}^+$ isotopologues via proton/deuteron transfer reactions. The best example of such species is H_2D^+, shown in Figure 2.2. It shows a D/H turnover point at 20 K, after which the fractionation ratios decrease smoothly and reach levels of $\sim 10^{-5}$ at temperatures of $\sim$100 K.

There are only a few species that show a dependence on temperature where deuterium fractionation is reduced at $T \sim 80$ K. Those are directly synthesized from deuterated light hydrocarbon ions such as CH_2D^+, which retain high D/H ratios at elevated temperatures, e.g. DCN and CH_2D_2. HDCS is unique in showing no clear difference between the two models at least within our defined temperature range, as its chemical evolution depends almost equally on the two distinct deuterium fractionation routes (via H_3^+ and light hydrocarbon isotopologues) via the formation of the ion H_2DCS^+,

Also, we find that the overall sensitivity of the calculated D/H ratios to density is weak, except for species sensitive to the freeze-out of CO and other radicals, i.e. H_2D^+, HD_2^+, and their direct dissociative recombination products. These species experience a rapid decrease in fractionation ratios toward lower densities of $< 10^4$ cm^{-3}, at which CO cannot severely deplete onto the dust grains even after 1 Myr of evolution. However, if we would follow the evolution of our chemical model beyond 1 Myr, at some moment the CO depletion can become severe enough for low-density regions to allow high D/H ratios for the H_3^+ isotopologues (if the adopted non-thermal desorption rate is not too high).

2.4.2 *Long-term evolution*

Concerning the deuterium fractionation, time is an important factor, and as such it can also be used to determine the evolutionary stage of the observed environment. While we have so far only discussed abundances up until and at the time of 1 Myr of evolution, we will next discuss the long-term abundances of molecules, and the time it takes for certain groups of species to, possibly, reach a steady-state. We allow our models to run for 100 Myr and consider steady-state abundances to have been reached if abundances change by $< 1\%$ over a time frame equal to 1% of the already elapsed time. Because the "Evolution" model is initiated with high abundances, and hence most likely would only result in molecules reaching steady-state abundances faster, we only consider the "Primordial" model for determining the long-term chemical evolu-

tion. For this analysis we have chosen six characteristic species to study; H_3^+, CH_3^+, H_2O (gas and solid), CH_3OH (gas and solid), N_2H^+ and H_2S. Due to the low abundances for multi-deuterated species, we consider only up to triply-deuterated species.

In Figure 2.4 we present the evolution of abundances with time at a temperature of 10 K and density 10^4 cm^{-3}, other model parameters are the same as in our previous models, i.e. dark conditions. It is clear that many of the species reach a steady state abundance after approximately $10^5 - 10^6$ years, with only small changes in abundances thereafter. Important to note here is that most molecules do not show variations of D/H ratios at $\gtrsim 10^6$ years because abundances of the minor and major isotopologues of a species behave similarly with time.

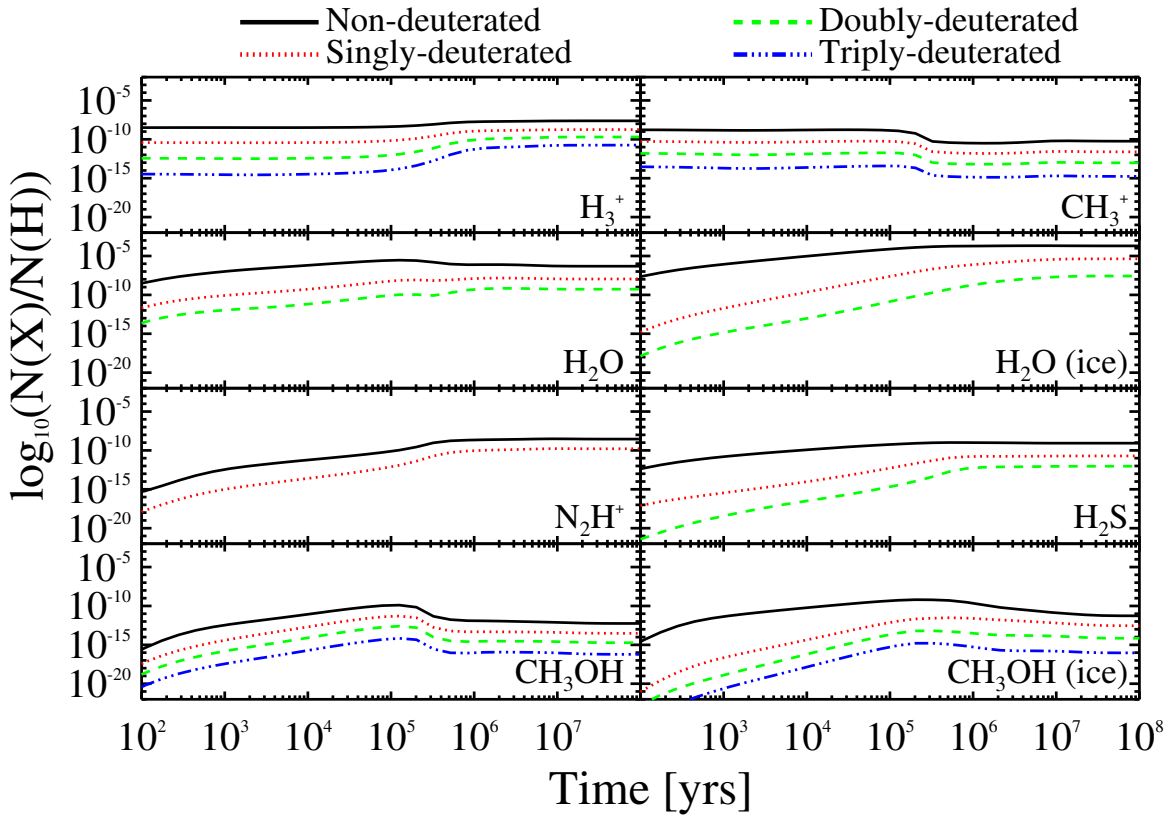

Figure 2.4: Time evolution for the abundances of six species; H_3^+, CH_3^+, H_2O (gas and solid), N_2H^+, H_2S, CH_3OH (gas and solid), and their up to triply-deuterated analogues. Analysis for temperature 10 K and density 10^4 cm^{-3}. Non-deuterated species are shown in solid lines, singly-deuterated in dotted lines, doubly-deuterated in dashed and triply-deuterated in dot-dashed lines.

After approximately 10^5 years H_3^+ abundances increases to its peak and steady state abundances of $n(H_3^+/n(H)) \sim 10^{-8}$ and this increase coincide well with the freeze-out time scales of CO ($\sim 10^5$ years). The increase in abundance of H_3^+ and its isotopologues just prior to 1 Myr is reflected in the

evolution of most other molecules, and subsequent changes in D/H ratios are instead resulting from other chemical processes such as DR.

The isotopologues of H_3^+ reach their steady state abundances on the same time scales as H_3^+ but there they experience a significantly larger increase in abundances compared to H_3^+. As soon as singly-deuterated species become abundant, we see a response in abundances of multi-deuterated species, as a step-wise redistribution of deuterium atoms takes places, transferring D atoms to create multi-deuterated isopotologues. H_2D^+ abundance increase from 10^{-11} to 10^{-9}, HD_2^+ from 10^{-13} to 10^{-10} and D_3^+ from 10^{-15} to 10^{-11}. This means that D/H ratios also increase from $\sim$ 1% to $\sim$ 10% for all of the isotopologues.

CH_3^+ experiences a drop in abundances, also around $\sim 10^5$ years, dropping it from a steady abundance of 10^{-8} down to 10^{-11}. This is caused by the freeze-out of C atoms which hinders the formation of CH_3^+ through H_3^+ reacting with C to form CH^+, and subsequent addition of H atoms through H_2. The isotopologues follow the same evolution with D/H ratios of $\sim$ 5%.

Water is strongly dependent on the surface chemistry, but can also form in appreciable abundances in the gas-phase. Gas-phase H_2O reaches a peak abundance of $\sim 10^{-5}$ at $\sim 10^5$ years, then drops in response to the increase in deuterium fraction while the abundances of its isotopologues continues to increase until they reach their peak abundances of $\sim 10^{-8}$ and 10^{-9}, for HDO and D_2O respectively. Re-processing of water ice is limited in these environments, and hence the abundance evolution shows a steady increase until the steady-state abundance of $\sim 10^{-4}$ is reached after $\sim 10^6$ years. As surface processes is relatively slow compared to gas-phase processes, the deuteration processes takes time and therefore the increase of D/H ratios, and hence steady-state abundance of water ice isotopologues, requires longer times, typically $\sim 10^7$ years with D/H ratios of $\sim$ 5% for HDO ice.

N_2H^+ show a similar increase in abundance as gaseous water, with small variations caused by the CO freeze-out that otherwise destroys small amounts of N_2H^+, forming HCO^+ and H_2. Its formation is more strongly dependent on N_2 which does not significantly adsorb onto grains at 10 K, therefore it steadily increases by H_3^+ reacting with N_2 until it reaches steady-state abundances of $\sim 5 \times 10^{-9}$ after $\sim 10^6$ years. N_2D^+ follows a similar evolution abundances, but as soon as N_2H^+ reaches its steady-state abundance, D/H ratios increase from $\sim$ 1% to $\sim$ 10%.

H_2S is not strongly affected by H_3^+ and its abundance increases steadily until it reaches steady-state at $\sim 10^5 - 10^6$ years, peaking at $\sim 10^{-9}$. Its formation is instead strongly related to surface chemistry through the hydrogenation of sulphur on the grains, after which H_2S is chemisorbed. H_2S is also protonated at later times $\gtrsim 10^5$ years by reacting with H_3^+. However, the DR of H_3S^+ is efficient enough to reform H_2S without significant changes being visible.

Methanol, and other complex organics such as formaldehyde, are also strongly affected by the increase in H_3^+ abundance. After reaching its peak abundance of $\sim 10^{-10}$ at 10^5 years, it is dissociated by H_3^+ as:

$$\begin{aligned} H_3^+ + CH_3OH \quad \Rightarrow \quad & CH_3^+ + H_2O + H_2 \\ & H_3CO^+ + H_2 + H_2 \end{aligned} \tag{2.2}$$

The dissociation of methanol does not allow it to be reformed through DR and instead methanol reaches a steady state abundance of $\sim 5 \times 10^{-12}$ after $> 10^6$ years. Methanol ice show a similar behavior to the gaseous methanol, albeit somewhat slower due to the slow pace of surface processes. It reaches peak abundances of $\sim 10^{-9}$ after almost 10^6 years which then decreases to steady-state abundances $\sim 10^{-12}$ after $\sim 10^8$ years as it is dissociated by H_3^+. Important to note is that the D/H ratio of CH_2DOH ice therefore increases from $\sim$ 1% to $\sim$ 10% between 10^6 and 10^8 years. The slow gradual drop in methanol ice abundances is in response to the decreased gas-phase abundances of methanol, and adsorption is no longer efficient enough to counteract the photodissociation of methanol ice by CRP-driven UV photons:

$$\begin{aligned} CH_3OH(ice) + h\nu \quad \Rightarrow \quad & H_2CO(ice) + H_2(ice) \\ & CH_3(ice) + OH \end{aligned} \tag{2.3}$$

In Figure 2.5 we show the time evolution for the same set of species but for temperature 75 K and density 10^8 cm^{-3}. At these higher temperatures the $H_3{}^+$ isotopologues become de-fractionated because of backward reactions which lower abundances of the isotopologues and the D/H ratios. H_3^+ retains a steady-state abundance of $\sim 10^{-11}$ throughout the modeled time, but its isotopologues shows significantly decreased abundances with H_2D^+ D/H ratios $\sim 10^{-5}$, typical cosmic values reflecting the high temperatures. HD_2^+ and D_3^+ have D/H ratios of 10^{-10} and 10^{-14} respectively. However, at later times $\sim 5 \times 10^7$ years there is an increase in abundances for both HD_2^+ and D_3^+ which is caused by the increased abundances of D_2 which requires long timescales to form in appreciable amounts. D_2 react with H_3^+ and H_2D^+ to form HD_2^+ and D_3^+, causing the significant increase in abundance. D/H ratios still remains too low however for it to be the primary fractionation pathway.

Instead, the deuterium fractionation is governed by the $CH_3{}^+$ isotopologues, which show a significantly higher degree of fractionation $\sim$ 10%. CH_3^+ quickly reach peak abundances of $\sim 10^{-10}$ but experience a drop in abundances after $> 10^3$ years owing to reactions with atomic elements such as O, C and N, which drops abundances down to 10^{-13}. D/H ratios for CH_2D^+ is 1% throughout the time span of the model, and an order of 100 and 10 000 lower for CHD_2^+ and CD_3^+, respectively. The final increase in abundances for all the isotopologues after $> 5 \times 10^7$ years is due to a small overproduction of CH_3^+ due to an increase of atomic carbon, which is caused by the slow destruction of CO reacting with ions such as H_3^+ and He^+.

Both gas and ice water show a similar evolution as for 10 K. However, owing to the lower D/H ratios of CH_3^+ the water D/H ratios are lower, dropping from 10% to 1%. More importantly, the water ice abundances increase much faster

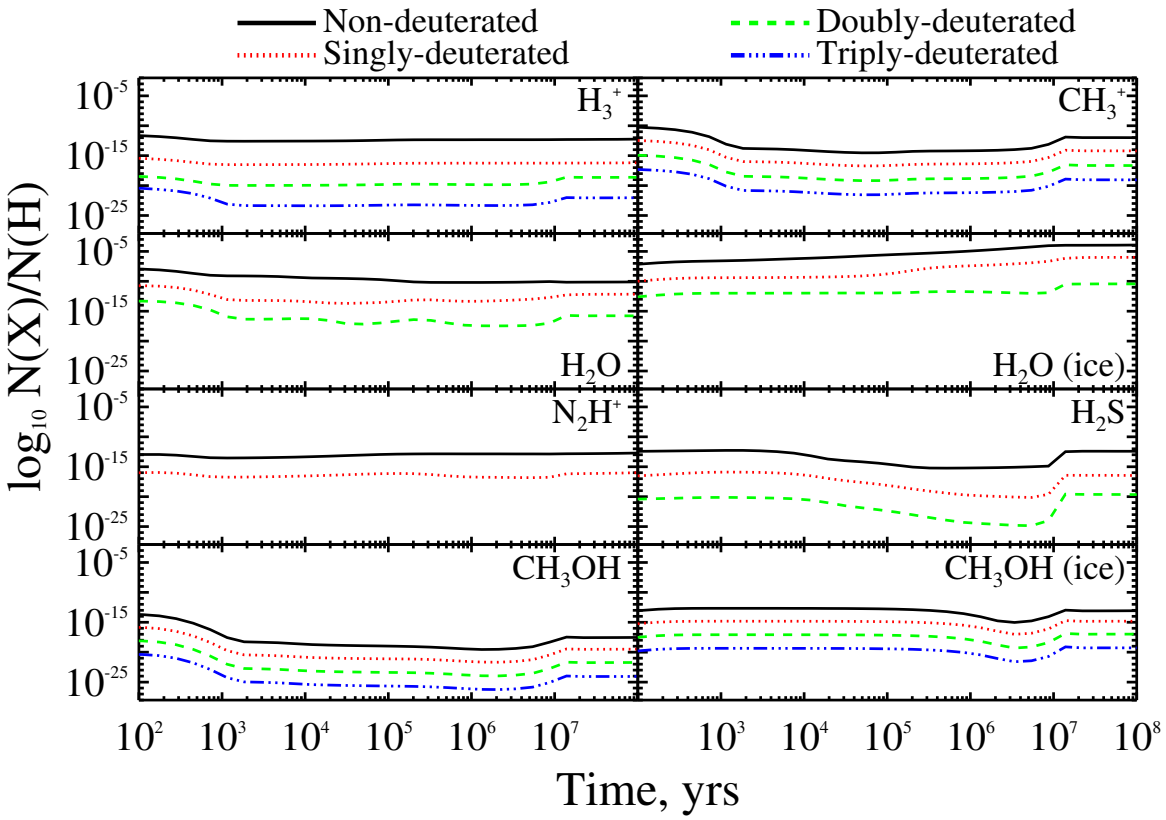

Figure 2.5: Time evolution for the abundances for six species; H_3^+, CH_3^+, H_2O (gas and solid), N_2H^+, H_2S, CH_3OH (gas and solid), and their up to triply-deuterated analogues. Analysis for temperature 75 K and density 10^8 cm^{-3}. Non-deuterated species are shown in solid lines, singly-deuterated in dotted lines, doubly-deuterated in dashed and triply-deuterated in dot-dashed lines.

due to the increased mobility on the grains. This is further aided by the higher density which also cause freeze-out to be more efficient, hence the abundance of gaseous water is typically lower than at cold temperatures, $10^{-9} - 10^{-7}$. The same reason for lower abundances goes also for its isotopologues.

N_2H^+ quickly reaches its steady-state abundance of 10^{-13} after ~ 100 years, after which there is a small drop in abundance of almost an order of magnitude as CO becomes abundant enough to destroy N_2H^+ by significant amounts. N_2H^+ is strongly linked to H_3^+ but due to N_2H^+ reacting with D atoms the D/H ratios is somewhat higher, 10^{-3} relative to 10^{-5} for H_3^+. There are small variations in N_2D^+ which can be explained by variations in atomic D abundances which is predominantly produced by various small $C_nD_m^+$ ions reacting with C and H_2.

H_2S also experiences a similar evolution with time, reaching peak abundances of $\sim 10^{-12}$ at $\sim 10^4$ years and then slowly dropping down to $\sim 10^{-16}$ after $\sim 10^6$ years. Much as for HCN, H_2S abundances decrease as ions, most prominently C^+ and S^+, slowly become abundant enough to effectively remove H_2S. Finally, after $\sim 5 \times 10^7$ years, abundances increase again up to

$\sim 10^{-13}$ due to the increase in electron abundance, which reforms H_2S by charge-transfer of H_2S^+ reacting with H^+.

Methanol reaches its peak gas abundance of $\sim 10^{-14}$ after $\sim 10^3$ years, after which it drops slowly as freeze-out times scales become significant and much of it is depleted onto the grains, decreasing abundances down to 10^{-18} after $\sim 10^5$ years. This adsorption increase the abundances for methanol ice, reaching its peak of $\sim 10^{-12}$ at $\sim 10^4 - 10^5$ years, after which photodissociation begins to reduce abundances again until gas-phase abundances increases again at $\sim 5 \times 10^7$ years due to DR reactions of protonated methanol and $H_5C_2O_2^+$.

At low temperatures, it is clear that most species, especially at low temperatures, have reached at least semi-steady state abundances within 10^6 years. Complex organics and molecules predominantly formed on surface, such as methanol and water, can experience small but significant variations in abundances, as well as D/H ratios, after 10^6 years before the steady-state abundances are reached. Most species at low temperatures, $T < 20 - 30$ K, reach a quasi-steady state within 10^6 years.

At higher temperatures ($\sim$ 75 K), species on grains are more mobile while desorption rates also are higher. This significantly reduces the available reactants for the surface chemistry, but allows the formation of heavier molecules owing to the increased mobility. The late increase in abundance of many molecules at $\sim 5 \times 10^7$ years is due to the increased ionization degree of the environment, which allow the reformation of many molecules through DR or charge-transfer reactions.

For hot cores/corinos the situation is more complex than what we have modeled here, as initial abundances are not atomic. However, one should bear in mind that time scales for clouds and, especially, protostellar environments (see Figure 1.2), are much shorter than the time of $\sim 10^8$ years needed to reach steady-state abundances. Therefore, steady-state chemical models of protostellar environments are not able to accurately predict abundances for larger molecules and other species that are predominantly formed on grains.

2.4.3 *Detailed chemical analysis for assorted species*

To understand in more detail the differences between the evolution of deuterated molecules, we have analyzed the chemistry of several key isotopologues. We included representative ions (isotopologues of H_3^+, DCO^+), simple molecules (DCN), complex organics (isotopologues of CH_3OH) and water (HDO, D_2O) for this analysis.

We analyze the evolution of these representative species in four distinct astrophysical environments: densities of 10^4 and 10^8 cm^{-3}, and temperatures of 10 and 80 K for both the "Primordial" and "Evolution" models. Using our robust "Chemical Analyzer" (CHAN) tool, we isolate the most important formation and destruction pathways for each of these species. Reactions with a net abundance flux $> 20\%$ are considered dominant even if for a short time frame. Other reactions need to retain a net abundance flux of $> 10\%$ for $> 10\%$ of the elapsed time, i.e. for a time > 0.1 x $t_{\rm dominant}/t_{\rm elapsed}$. Groups of reactions

of similar types, i.e. H_3^+ + C/He/O/N, are considered, even though their individual contribution might not surpass the critical flux limit 10%, if their combined contribution is well above the limit ($\gtrsim$ 20%). In the Appendix Tables A.3 – A.7 we include a complete listing of dominant formation and destruction pathways for the assorted species and their main reactants. These agree with the generally accepted pathways and we briefly discuss key pathways below.

2.4.3.1 H_3^+ *isotopologues*

The isotopologues of H_3^+ have been observed extensively; e.g. H_2D^+ (Caselli et al. 2008; Cernicharo et al. 2007; Harju et al. 2006) and HD_2^+ (Parise et al. 2011; Vastel et al. 2004). While observations of the ortho- or para-states of these isotopologues have been successful, we have not considered it in our model. The fully deuterated D_3^+ is symmetric and not observable in the sub-mm range, the same goes for H_3^+, making it hard to determine fractionation ratios for the species directly. H_3^+ can instead be detected using IR/optical absorption of its rovibrational transitions towards warm environments (Goto et al. 2008). The chemistry of isotopologues of H_3^+ has also been target of extensive investigation, most recently by Roberts & Millar (2006), Sipilä et al. (2010); Vastel (2007); Vastel et al. (2006b); van der Tak (2006), and Roberts et al. (2003). There is a great interest in these isotopologues as they serve as the starting point for ion-molecule chemistry. H_3^+ and its isotopologues is formed through CRP ionization of H_2 (see Figure 1.4). Next, isotopologues of H_3^+ could be subsequently formed via ion-molecule reactions with HD (at appropriately low temperatures). This reaction chain is listed below together with temperature barriers for fractionation channels of the H_3^+ isotopologues:

$$H_2 + \mathrm{CRP} \Rightarrow H_2^+ + e^- \tag{2.4}$$
$$H_2^+ + H_2 \Rightarrow H_3^+ + H_2 \tag{2.5}$$

$$H_3^+ + HD \Leftrightarrow H_2D^+ + H_2 \quad (220\mathrm{K}) \tag{2.6}$$
$$H_2D^+ + HD \Leftrightarrow HD_2^+ + H_2 \quad (251\mathrm{K}) \tag{2.7}$$
$$HD_2^+ + HD \Leftrightarrow D_3^+ + H_2 \quad (341\mathrm{K}) \tag{2.8}$$

Then, H_3^+ isotopologues are destroyed by dissociative recombination or by ion-molecule reactions with abundant radicals like CO. Thus, the chemistry of H_3^+ and its deuterated isotopologues is sensitive to freeze-out of relevant molecules and thus to temperature (and, to a lesser extent, to density). A complete list of dominant formation and destruction pathways for the H_3^+ isotopologues is available in Table A.3.

In our parametric study all the H_3^+ isotopologues show clear dependence on temperature, and partly on density, as can be seen in Figure 2.6. In general, the fractionation ratios reach values above 10^{-3}, and only at temperatures $\gtrsim$ 30 K does it go lower, when backward de-fractionation reactions become competitive. The decrease is noticeable as a clear fractionation boundary towards the higher temperatures, which is more pronounced for the multi-deuterated isotopes. At lower temperatures ($\sim$ 10 K) there is a weak dependency on den-

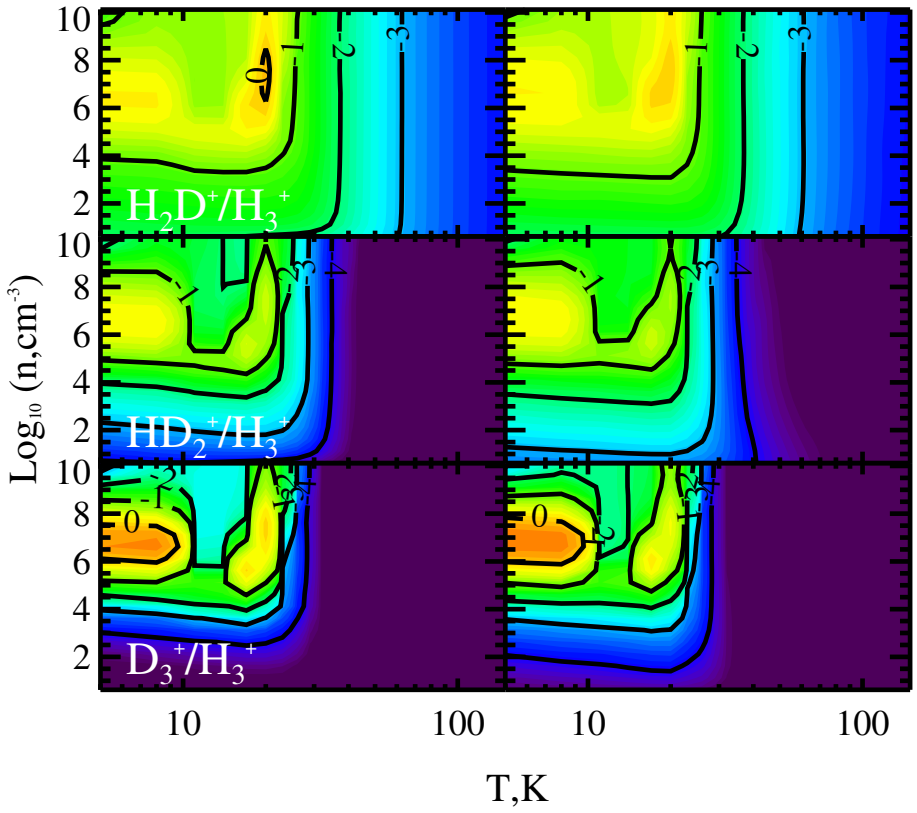

Figure 2.6: Distribution of the D/H fractionation ratios over the investigated parameter space, for the three isotopologues of H_3^+ and the two sets of the initial abundances.

sity with higher fractionation ratios ($\gtrsim 10^{-1} - 1$) achieved at higher densities ($\gtrsim 10^5$ cm^{-3}) due to more severe molecular depletion and thus less efficient propagation of high D/H into other complex species.

D_3^+ show significantly higher D/H fractionation ratios at low temperatures ($\sim$ 10 K) compared to the other isotopologues, increasing with density, up to values as high as $10 - 20$, while other H_3^+ isotopologues reach values of $10^{-1} - 1$ at most. At $T \lesssim 20$ K fractionation proceeds fast because the main destruction channel via the ion-molecule reaction with CO is absent due to all CO being locked in grain icy mantles (Vastel et al. 2006b; Bacmann et al. 2003). Since D_3^+ is a final product of the H_3^+ fractionation, it reaches the highest D/H fractionation of all the H_3^+ isotopologues.

This agrees with the calculations of Roberts (2005) at the limit where CO is entirely depleted onto grains at T $\lesssim$ 20 K (see Figure 2.7). D_3^+ can theoretically reach the D/H values of $\sim$ 20, while H_2^+ and HD_2^+ reach levels of unity, in agreement with our results. Finally, the drop of the D/H ratios for the H_3^+ isotopologues at densities exceeding 10^8 cm^{-3} is due to steady removal of the elemental deuterium in the gas-phase in deuterated ices, such as HDO, D_2O, CH_3D, NH_2D, etc., by surface processes. This reduces the pace of the deuterium fractionation via H_3^+ as abundances of HD and other gas-phase deuterated species drops, whereas abundances of H_3^+ increase, thus decreasing

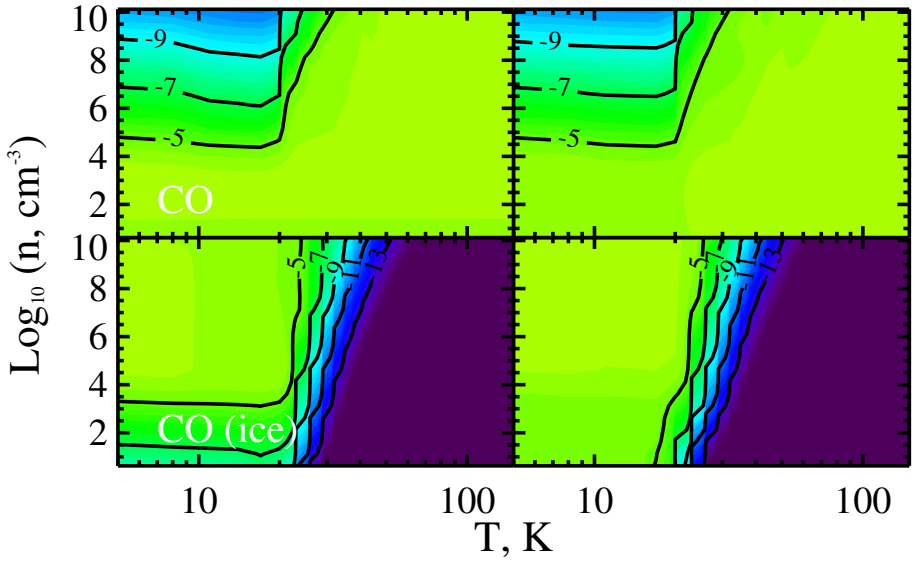

Figure 2.7: Relative abundances at 1 Myr of the CO molecule, both in gas-phase and ices for the "Primordial" (left panel) and "Evolution" (right panel) models.

the corresponding D/H ratios. Long timescales associated with these surface processes require high densities ($\gtrsim 10^5$ cm^{-3}) to have profound effect on the H_3^+ abundances during the considered 1 Myr evolutionary time span.

2.4.3.2 *DCO^+ / DOC^+*

DCO^+ is an important molecular ion, used as a tracer of deuterium fractionation and ionization fraction, and has an isotopomer DOC^+ that has not been detected so far. We have distinguished between these isotopomers in our chemical network, but found that they share reaction pathways in many cases. The D/H fractionation ratios over the investigated parameter space are plotted in Figure 2.8, for both DCO^+ and DOC^+.

Major formation and destruction reactions are listed for both isotopomers as well as key reactants in the online material. The key formation channels are given below:

$$H_3^+ + C \Rightarrow CH^+ + H_2 \quad (2.9)$$
$$CH^+ + H_2 \Rightarrow CH_2^+ + H \quad (2.10)$$
$$CH_2^+ + H_2 \Rightarrow CH_3^+ + H \quad (2.11)$$
$$CH_3^+ + HD \Rightarrow CH_2D^+ + H \quad (2.12)$$

$$CH_2D^+ + O \Rightarrow DCO^+/DOC^+ + H_2 \quad (2.13)$$
$$H_2D^+/D_3 + CO \Rightarrow DCO^+/DOC^+ + H_2/D_2 \quad (2.14)$$
$$HCO^+ + D \Rightarrow DCO^+ + H \quad (2.15)$$
$$DOC^+ + H_2 \Rightarrow DCO^+ + H_2 \quad (2.16)$$
$$DCO^+ + e^- \Rightarrow CO + D \quad (2.17)$$

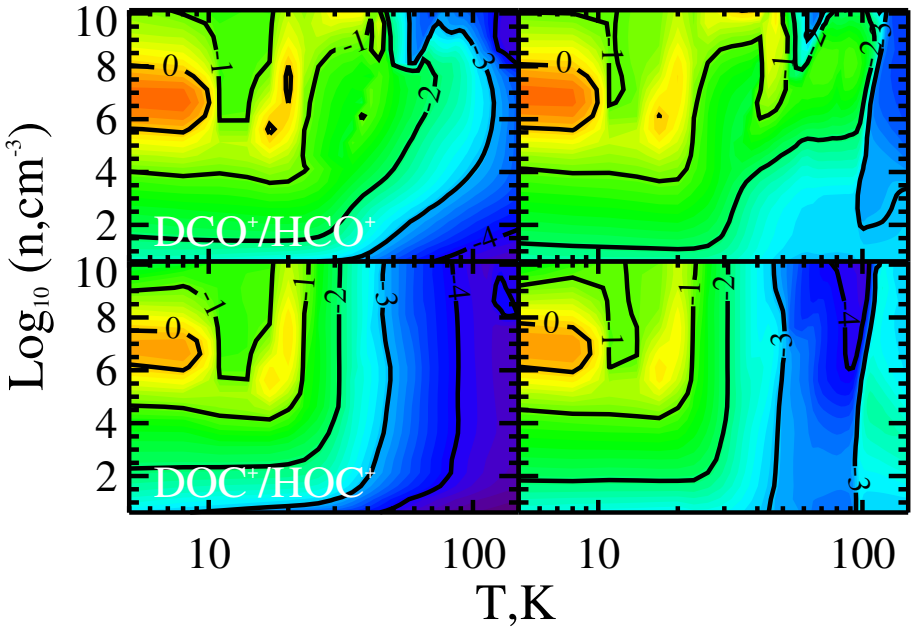

Figure 2.8: Distribution of fractionation ratios for DOC^+ and DOC^+ in both models.

At early times, $\leq 10^3$ years, free oxygen atoms reacting with CH_2D^+ ions (reaction 2.13) dominates the formation of both isotopomers. DOC^+ shows a well defined temperature barrier, whereas DCO^+ shows signs of the same barrier but with extended features toward higher densities ($\gtrsim 10^6$ cm^{-3}). The temperature barrier arise because DCO^+ and DOC^+ both are daughter species of the H_3^+ isotopologues that reacts with CO (reaction 2.14). H_2D^+ is more abundant at early times ($\lesssim 10^4$ years), but at later times D_3^+ constitute the dominant reaction pathway, while HD_2^+ is never abundant enough at intermediate times to be significant.

The isotopomers show similar D/H distributions up to ~30 K, after which the gradient with temperature differ between the isotopomers. This is because DOC^+ is largely formed through the H_3^+ isotopologues alone, while the formation of DCO^+ is also contributed by reactions 2.13 and 2.14. The difference between the two isomers is that formation of DCO^+ is aided by the substitution reaction 2.15, as well as preferred formation of DCO^+ over DOC^+ with reaction 2.16, causing the slight differences for their D/H distributions in the "Primordial" and "Evolution" models. Removal of DOC^+ is dominantly only by reaction 2.16, while DCO^+ is also removed by dissociative recombination (reaction 2.17) that replenish the environment with CO. Since CO is the most common reactant to form the isotopomers, it will contribute to the reformation of the isomers through reaction 2.14.

2.4.3.3 *DCN/DNC*

Observations of HCN and HNC have been used extensively as probes of dense molecular gas (Boger & Sternberg 2005). The HCN/HNC ratio is well-known

to vary with temperature (e.g Schilke et al. 1992). But theoretical studies of the deuterated isomers suggest that the same ratio should be close to unity (Herbst et al. 2000) and agrees with results from laboratory studies (Hiraoka et al. 2006).

In Figure 2.9 we plot the calculated HCN/HNC and DCN/DNC. We find a good agreement to the DCN/HCN ratios with temperature and density when comparing our results to the model of Schilke et al. (1992), but the agreement is worse for HCN/HNC. Our model shows a flat distribution with HCN/HNC ratio close to unity, only reaching 10 at high densities, $\gtrsim 10^8$ cm^{-3}, while Schilke et al. (1992) predicted that the HCN/HNC ratio can reach $> 10^2$ in the same environments. We have traced back these discrepancies to the studies of Dumouchel et al. (2010) and Sarrasin et al. (2010) who studied the collisional rates of HCN/HNC with He and their results showed that the collision rate at low temperatures ($\sim$ 10 K) is larger for HNC than HCN. The conclusion is that using HCN rates to interpret HNC observations in DCs, as was the case prior to these studies, may lead to underestimation of the HCN/HNC ratio.

The DCN/DNC ratio varies stronger over the parameter space in our models, with higher ratios $\sim$ 10 at high densities ($\gtrsim 10^8$ cm^{-3}) and low temperatures ($<$ 40 K), and a gradient of decreasing ratios with increasing temperature. There is a peculiar feature for DCN/DNC at high densities ($\gtrsim 10^5$ cm^{-3}) and temperatures ($\gtrsim$ 70 K) in our models ($\gtrsim 10^5$ cm^{-3}, $\gtrsim$ 60 K), where the ratio rapidly drops to $\sim 10^{-2}$. From a detailed chemical analysis we see that the HNC chemistry is limited to a smaller set of reactions, especially in the solid phase and an important reaction missing in the original network was added, with HNC/DNC reacting with free D/H atoms:

$$\mathrm{HNC + D} \Rightarrow \mathrm{DNC + H} \tag{2.18}$$

$$\mathrm{DNC + H} \Rightarrow \mathrm{HNC + D} \tag{2.19}$$

We implemented the same reaction data for DCN, with the reactions rate of 1.0 x 10^{-10} cm^3 s^{-1}, $\beta = 0.5$ and $\gamma = 500$ K. We plot the corresponding ratios of DCN/DNC for the "Primordial" and "Evolution" model in Figure 2.10, which shows fractionation ratios $\sim 1 - 10$ at high densities ($\gtrsim 10^5$ cm^{-3}) and temperatures ($\gtrsim$ 70 K) as predicted by previous studies. Reactions 2.18 and 2.19 are important when studying rich molecular environments at high temperatures such as inner envelopes of protostars or hot cores, and to fully understand the evolution of HNC and DNC we require better estimates of the reaction parameters.

In Figure 2.11 the fractionation ratios of DCN and DNC are shown. The corresponding D/H ratios reach levels $\gtrsim$ 10% until the temperature barrier of $\sim$ 80 K is reached, at which it drops down to the cosmic level ($\sim 10^{-5}$). This high temperature barrier is related to deuterium fractionation that begins with the deuterated light hydrocarbon ions such as CH_2D^+ and C_2HD^+, and

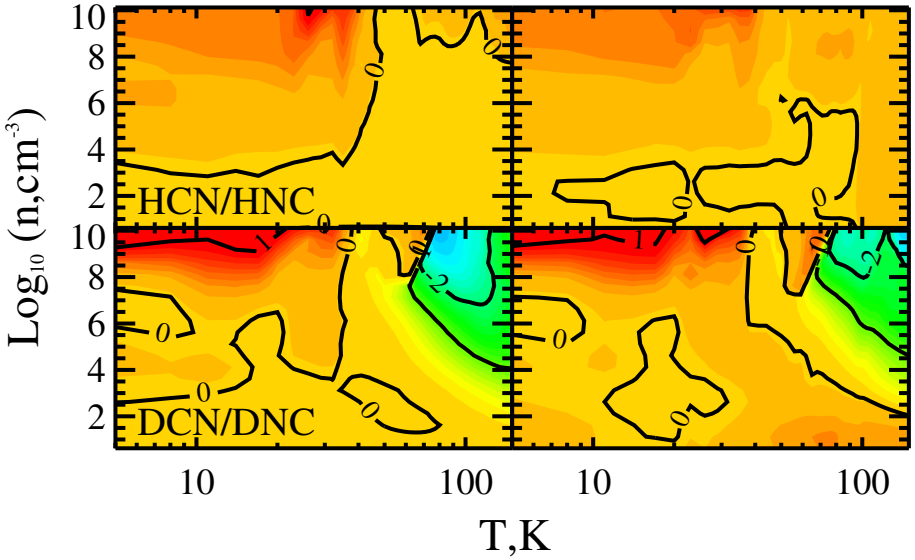

Figure 2.9: The HCN/HNC and DCN/DNC ratios are shown.

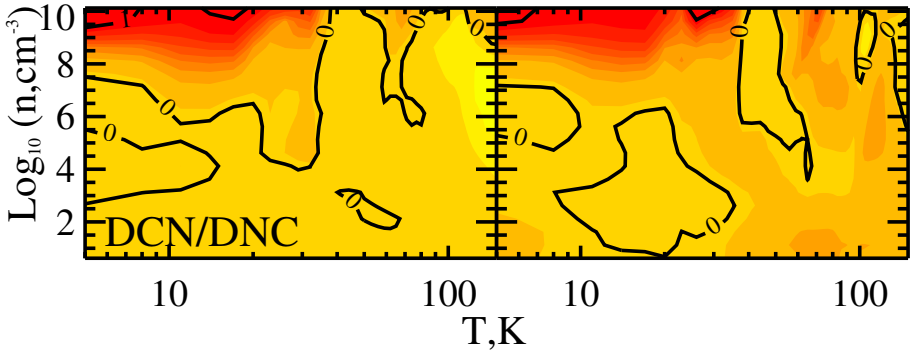

Figure 2.10: The DCN/DNC ratio computed with the additional reactions 2.18 and 2.19.

not the H_3^+ isotopologues as for other discussed species. The key reaction pathways for DCN/DNC are:

$$DCN^+ + H_2 \Rightarrow HDCN^+ + CO \quad (2.20)$$
$$DCO^+ + HCN/HNC \Rightarrow HDCN^+ + H \quad (2.21)$$
$$CH_2D^+ + N \Rightarrow HDNC^+ + H \quad (2.22)$$

$$HDCN^+ + e^- \Rightarrow DCN/DNC + H \quad (2.23)$$
$$HDNC^+ + e^- \Rightarrow DNC + H \quad (2.24)$$
$$D_2CN^+ + e^- \Rightarrow DCN/DNC + D \quad (2.25)$$
$$ND(ice) + C(ice) \Rightarrow DCN/DNC(ice) \quad (2.26)$$
$$CN(ice) + D(ice) \Rightarrow DCN/DNC(ice) \quad (2.27)$$
$$DCN/DNC + H_3^+ \Rightarrow H_2CN^+/HDCN^+ + HD/H_2 \quad (2.28)$$
$$DCN/DNC + D_3^+ \Rightarrow D_2CN^+ + D_2 \quad (2.29)$$

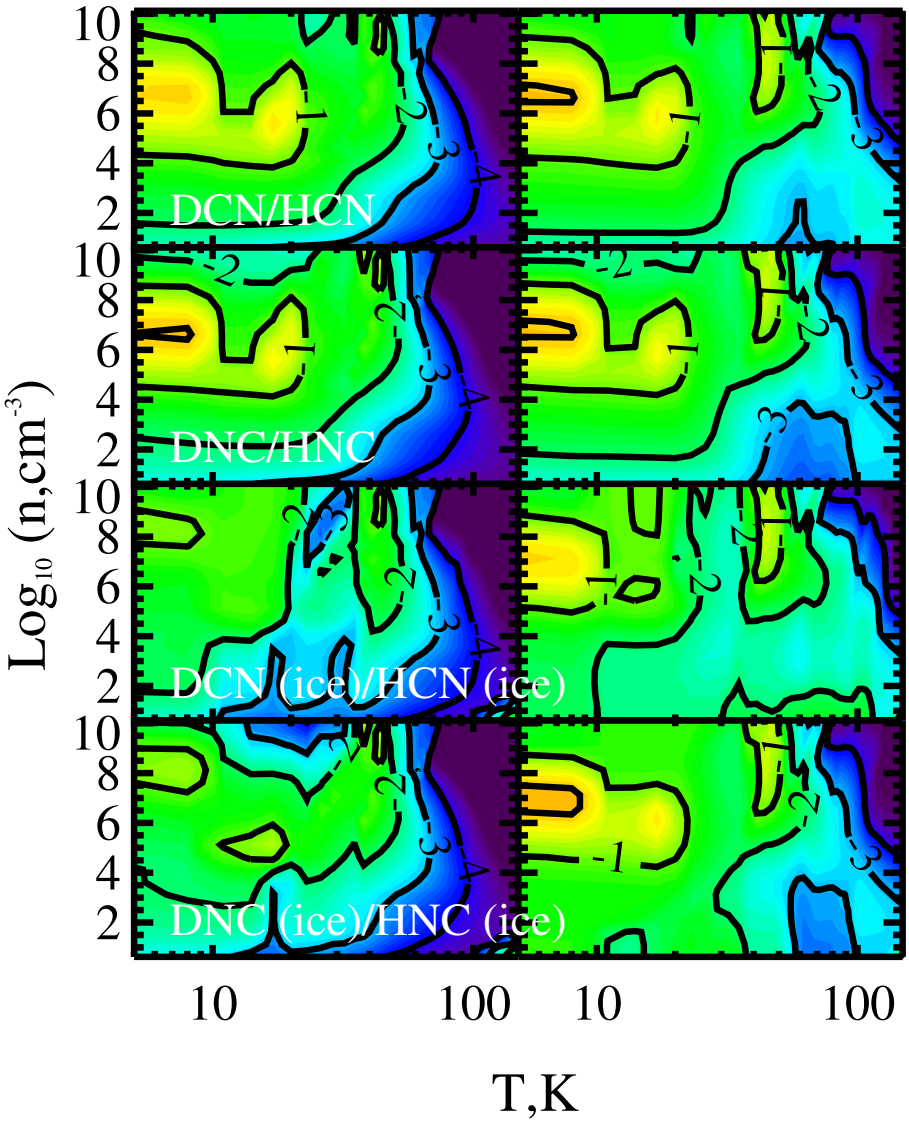

Figure 2.11: The DCN/HCN and DNC/HNC ratios are shown.

Reaction 2.23 is a dominant pathway for both isomers, but is especially strong for DNC, also aided by reaction 2.24, while DCN has a stronger contribution from desorption. Reaction 2.25 is especially significant in the "Evolution" model for both isomers, but only marginally significant in the "Primordial" model. At temperatures $\lesssim$ 60 K, DCN isotopologues are formed on grains through reactions 2.26-2.27 while DNC desorption is only marginally significant in environments of high density ($\gtrsim 10^8$ cm^{-3}) and temperature ($\gtrsim$ 80 K).

The dominant destructive pathway for both isomers is by reacting with H_3^+ or D_3^+(reactions 2.28-2.29), which replenishes the environment with the H_2CN^+ isotopologues that essentially will reform the isomers. Freeze-out of species only has a minor affect at early times ($\lesssim 10^4$ yrs) of the "Evolution" model.

2.4.3.4 *Water isotopologues*

Water is one of the most essential molecule in the context of planet habitability and the evolution of complex lifeforms, and is gaining a lot of interest in the light of new Herschel results (e.g. van Dishoeck et al. 2011; van der Tak et al. 2011; Hartogh et al. 2011). A lot of effort is put on understanding the presence of water throughout the evolution of the interstellar medium and protoplanetary disks (Boogert & Ehrenfreund 2004; Najita et al. 2011). In this context, we perform analysis of the chemical evolution of the deuterated isotopologues of water and deduce essential reaction pathways. The key formation channels of the water isotopologues are given below:

$$H_2{}^+ + O \Rightarrow OD^+ + H_2 \quad (2.30)$$
$$OD^+ + H_2 \Rightarrow HDO^+ + H \quad (2.31)$$
$$H_3^+ + OD \Rightarrow HDO^+ + H_2 \quad (2.32)$$
$$HDO^+ + H_2 \Rightarrow H_2DO^+ + H \quad (2.33)$$

$$H_3O^+ + e^- \Rightarrow H_2O + H \quad (2.34)$$
$$H_3O^+ + HCN/HNC \Rightarrow H_2O + H_2CN^+ \quad (2.35)$$
$$H_2DO^+/HD_2O^+ + e^- \Rightarrow HDO/D_2O + H \quad (2.36)$$
$$H_2DO^+/HD_2O^+ + HCN/HNC \Rightarrow HDO/D_2O + H_2CN^+ \quad (2.37)$$
$$OH/OD(ice) + H(ice) \Rightarrow H_2O/HDO(ice) \quad (2.38)$$
$$OH/OD(ice) + D(ice) \Rightarrow HDO/D_2O(ice) \quad (2.39)$$

Water and its deuterated analogues are formed by dissociative recombination of H_3O^+ (reactions 2.34, 2.36) at low densities ($\lesssim 10^6$ cm^{-3}) which essentially remains dominant throughout the 1 Myr of evolution. In turn, H_3O^+ is produced by subsequent proton transfer via ion-molecule reaction of H_2 with OH_n^+ ($n = 0 - 2$) radicals. At higher densities the H_3O^+ isotopologues also react with HCN/HNC via a proton-transfer reaction (reactions 2.35 and 2.37). However, the significance of these reactions drops below the critical limit after $\sim 10^3 - 10^4$ years. Reactions with different ions such as $H_3{}^+$, HCO^+, N_2H^+ as well as their isotopologues, while individually less important, combined make a significant contribution to removing water.

Freeze-out removes the water isotopologues from the gas at high densities ($\gtrsim 10^6$ cm^{-3}) and is more dominant throughout the "Evolution" model. Surface chemistry is only active at temperatures $\lesssim 100$ K, where various isotopologues of OH and H form deuterated water ice (reactions 2.38 - 2.39). However, only insignificant amounts of it is released back into the gas phase while CRP photons can dissociate the molecule on the surfaces. At higher temperatures desorption becomes significant, which links the evolution of gaseous and solid water.

The D/H ratios for deuterated water, both gaseous and solid, are shown in Figure 2.12. The highest modeled D/H ratio for HDO and D_2O is $\gtrsim 10\%$, achieved at temperatures below $\sim$ 20 K and moderate densities of $10^6 - 10^8$ cm^{-3}. Both isotopologues are able to retain enhanced fractionation ratios ($\sim$

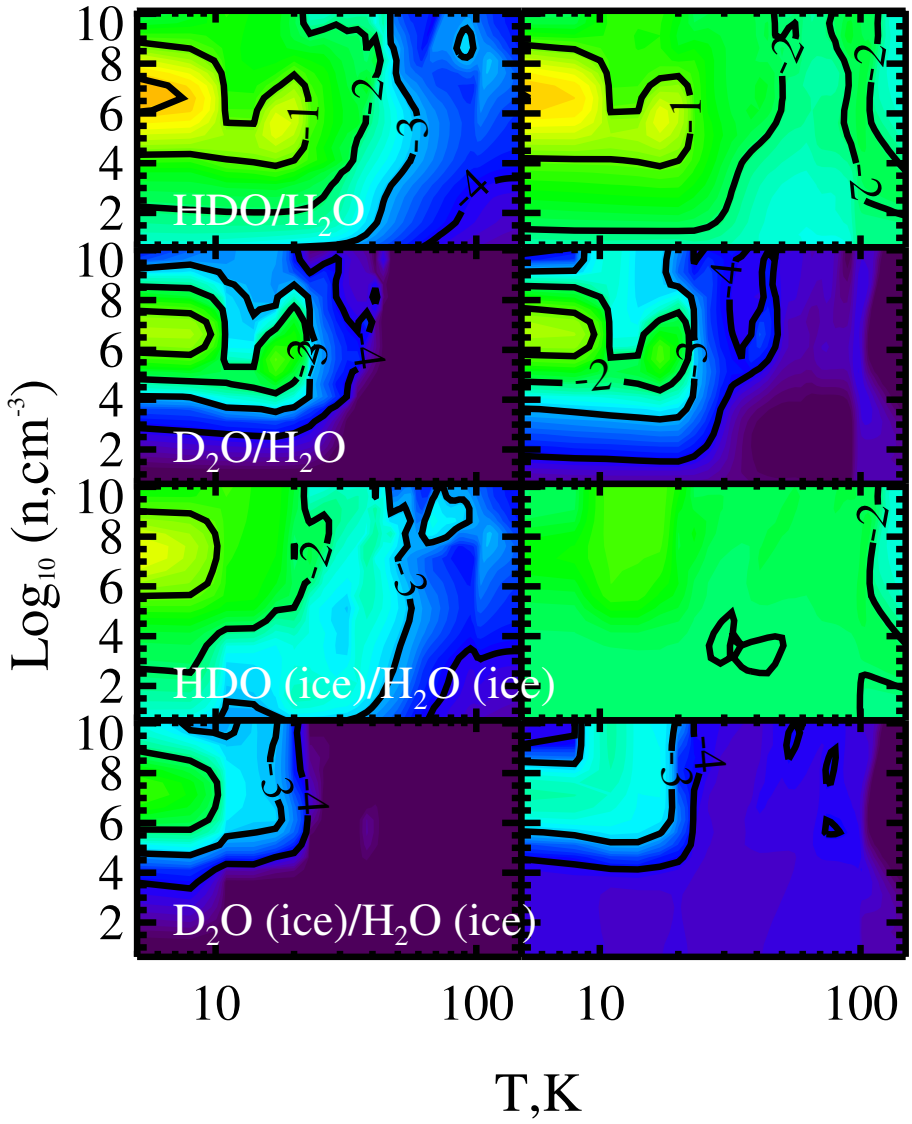

Figure 2.12: Distribution of the fractionation ratios for the isotopologues of H_2O.

10^{-3}) in the gas-phase at low temperatures ($\sim$ 10 K). At higher temperatures only HDO can retain the same enhanced levels, while D_2O reaches levels of $\lesssim 10^{-4}$. This is because the evolution of HDO is mainly linked to H_2D^+, whereas the chemistry of D_2O is more dependent on that of HD_2^+ and D_3^+.

A temperature barrier is present for both isotopologues at $\sim$30 K, just as the case for H_3^+, however not as clearly defined. The main reactants H_2DO^+ and HD_2O^+ are dependent on the isotopologues of H_3^+ through the intermediate formation of HDO^+, which dilutes the barrier boundary.

In the "Evolution" model, HDO has an almost constant fractionation ratio over the whole parameter space, both in the gas-phase and on grains. The HDO abundances are quickly accumulated in the previous cold evolutionary phase used as an input for the "Evolution" model. Since the mass difference between HDO and H_2O is only 5%, both these species stick to and desorb from

dust grains at similar physical conditions. Consequently, their abundance ratio remains nearly constant at a wide range of T and $n_{\rm H}$, particularly for water ices. While HDO is able to retain a high fractionation ratio ($\gtrsim 10^{-3}$), even at high temperatures in the "Evolution" model, D_2O shows only a slightly increased D/H ratio at temperatures $\lesssim 20$ K. It comes as no surprise that D_2O is harder to produce, as most multi-deuterated species have lower abundances compared to their singly-deuterated analogues.

2.4.4 *Observations*

We now discuss how our model results compare with assorted observations. van Dishoeck et al. (1995) observed several deuterated species towards the protobinary source IRAS 16293, namely, DCO^+, DCN, C_2D, HDS, HDCO, NH_2D, detected in the different regions around the protostar. The first region is the warm and dense inner core ($T \gtrsim 80$ K, $n_{\rm H} \sim 10^7$ cm^{-3}) found to be rich with organic molecules, the second is the circumbinary envelope with $T \sim 40$ K and $n_{\rm H} \sim 10^6 - 10^7$ cm^{-3}, where molecules such as DCO^+ and HDCO where found, and the third is the colder, low-density outer part of the envelope with $T \sim 10 - 20$ K and $n_H \sim 10^4 - 10^5$ cm^{-3} with radicals such as CN, C_2H, C_3H_2. We find good agreement between our calculated values and those derived for all observed species. As an example, HDCO shows a D/H ratio of 0.13 in our "Evolution" model compared with the observed value of 0.14, and for DCN the D/H ratio is 0.027 compared with the observed ratio of 0.013. The worst agreement we find is for C_2D and DCO^+ with a difference of a factor of ~ 5 in the D/H ratios, which is still acceptable agreement.

Caselli et al. (2003) detected ortho-H_2D^+ towards the prestellar core L1544, with derived abundances of 7.2 $\times 10^{-10}$ and 3.2 $\times 10^{-10}$ at the peak and off-peak positions, respectively. For our "Primordial" model with a core density $n_{\rm H_2} = 10^6$ cm^{-3}, a temperature 7 K, and an appropriate equilibrium o/p ratio of 3:1 taken from Walmsley et al. (2004a), we find reasonable agreement with calculated abundances of $0.7 - 4.8 \times 10^{-10}$ in the core (peak position) and $2.3 - 4.2 \times 10^{-10}$ at the off-peak position, with a lower density, assuming a density of $10^4 - 10^5$ cm^{-3}. We however find a higher abundance at the off-peak position; there are several possible reasons for the discrepancy such as incorrect treatment of the ortho-para species in the network or the lack of a detailed physical model. A detailed study is not within the scope of this paper but we note that abundances are within a factor of 2-3 of observed abundances.

Stark et al. (2004) observed H_2D^+, DCO^+, HCO^+, HDO and H_2O toward the protobinary source IRAS 16293 (A and B) as well as the cold prestellar object IRAS 16293 E. They measured the H_2D^+ abundance to be 2 $\times 10^{-9}$ in the cold, outer envelope with $n_{\rm H_2} = 10^4 - 10^5$ cm^{-3} and $T < 20$ K, where our "Evolution" model predicts a similar abundance of $\sim 10^{-9}$. In the inner envelope the temperature is higher, depleting the H_3^+ isotopologues as CO returns to the gas phase, and the abundance decreases to $\sim 10^{-12}$ cm^{-3}. The temperature in the inner envelope is not well constrained, but with a central density of $\sim 10^6$ cm^{-3} we find the best agreement at $T \approx 30$ K, with an abundance of 1.2 $\times 10^{-12}$,

and the agreement worsens if the temperature is increased, as more CO returns into the gas phase and the overall deuterium fractionation ceases. DCO^+ and HCO^+ were observed with abundances 2×10^{-11} and $< 1 \times 10^{-9}$ respectively, which agree with our model values from $17 - 26$ K with DCO^+ abundances 8.4 $\times 10^{-11} - 8.2 \times 10^{-11}$ and HCO^+abundances 4.7 $\times 10^{-10} - 1.1 \times 10^{-9}$, leading to a D/H ratio of 0.078 − 0.18. HDO and H_2O were observed with abundances 3×10^{-10} and $3 \times 10^{-7} - 4 \times 10^{-9}$ respectively, which agree reasonably well with our modeled abundances of 5.9 $\times 10^{-12} - 6.3 \times 10^{-11}$ and 9.9 $\times 10^{-10} - 1.7 \times 10^{-8}$, respectively. Lastly, HDO, DCO^+ and HCO^+ were also observed in the prestellar core object IRAS 16293 E. From estimated T $\sim$ 16 - 25 K and densities $1.1 - 1.6 \times 10^6$ cm^{-3} we estimate DCO^+ abundances to be 7.0 $\times 10^{-11} - 2.9 \times 10^{-9}$ and HCO^+abundances 8.9 $\times 10^{-11} - 1.10 \times 10^{-9}$, leading to a D/H ratio 0.26 − 0.79. This agrees well with the observed abundances of 5.0×10^{-11} and 1.0×10^{-10} for DCO^+ and HCO^+ with a D/H ratio 0.5. We find the same agreement for HDO with observed abundance 2×10^{-10} comparable to our modeled values of 3.0 - 7.5 $\times 10^{-10}$.

Coutens et al. (2012) observed multiple lines of HDO and $H_2{}^{18}O$ towards IRAS 16293A with an estimated D/H $\sim$ 0.034 in the hot corino region and D/H$\sim$ 0.005 in the outer envelope, utilizing a standard isotopic ratio of $H_2{}^{18}O$/ $H_2{}^{16}O$ = 500. In order to reproduce observed line emission, Coutens et al. (2012) added an outer absorbing layer with an H_2O column density of 1.23 $\times 10^{13}$ cm^{-2}. Depending on the exact choice of density and temperatures, our models give for the cold envelope ($n_H \sim 10^5$ cm^{-3}, T $\lesssim$ 30 K) D/H ratios of $\sim 0.01 -$ 0.1, for both sets of initial abundances, in agreement with observations. For hot cores ($n_H \sim 10^8$ cm^{-3}, T $\sim$ 150 K) the "Primordial" model estimates the D/H ratio to be $0.0001 - 0.001$, while the "Evolution" model predicts that the D/H ratio is $\sim 0.0001 - 0.01$. Although our evolutionary model is a poor solution and does not account for the gradual warm-up of the environment, our predicted D/H ratios from the "Evolution" model are in agreement with those estimated by Coutens et al. (2012), albeit only with upper limits of our estimates.

The radical OD was observed for the first time outside of the Solar system by Parise et al. (2012) along the line of sight towards the low-mass protostar IRAS 16293A. They also observed HDO and found a high OD/HDO ratio of $\sim 10 - 100$. Parise et al. (2012) compared their observations to the modeled values of OH/H_2O and found their calculated values to be too low. The agreement was slightly better when they implemented a simple evolutionary model with increasing temperature with time, but the result was still lower than observations, with the highest modeled values reaching 5.7. Studying the chemical evolution in our "Primordial" model for temperatures $T < 30$ K and densities $n_H = 10^4 - 10^6$ cm^{-3}, we find that the large OD/HDO ratio is mainly due to the efficient reaction OH + D $\longrightarrow$ OD + H, as originally suggested by Millar et al. (1989). Via this reaction, the OD/HDO ratios can reach values approximately one order of magnitude larger than OH/H_2O. Furthermore, toward temperatures $\sim$ 30 K the OD/HDO ratios can even be as high as two orders of magnitude. Thus, our model is in agreement with the observed OD/HDO ratios from Parise et al. (2012), without the need for a warm-up phase.

2.4.5 *Predictions for ALMA*

We have listed in Tables 2.5-2.7 the most abundant, (potentially) observable deuterated species with ALMA in DC, IRDC, and HMPO, respectively. In order to predict the observability of molecules in these different environments we use the Cologne Database of Molecular Spectroscopy (CDMS) by Müller et al. (2001, 2005) to calculate line fluxes under local thermal equilibrium (LTE) conditions for various deuterated molecules with transitions observable by ALMA. For these estimates we assume the following parameters for the different environments: for DCs temperature 10 K, number density 10^4 cm^{-3} and H_2 column density 10^{22} cm^{-2} (Launhardt et al. 2013), for warm IRDCs 25 K, 10^5 cm^{-3} and H_2 column density 10^{24} cm^{-2} (e.g. Rathborne et al. 2008), and for HMPOs 75 K, 10^5 cm^{-3} and column density 10^{24} cm^{-2} (e.g. Beuther et al. 2007; Rodón et al. 2008). There are known differences in H_2 column densities between interferometry and single-dish observations (Vasyunina et al. 2009). While we concentrate here on the higher end of column densities for our calculations, the calculated line fluxes can be adopted to the lower column densities by simply dividing them by 10.

For DCs and warm IRDCs we implement the atomic initial abundances, while for HMPOs we implemented instead the "Evolution" model (with initially high D/H ratios). Line intensities for a few molecules (e.g. DCO^+) can also be estimated using the non-LTE molecular radiative transfer tool RADEX (van der Tak et al. 2007). Because RADEX and our calculations using CDMS gave different results we scaled our CDMS calculations to match RADEX values for linear molecules (e.g. DCO^+). We look for transitions in bands 3 - 9 for ALMA (84 - 720 GHz with gaps between bands, see `science.nrao.edu/facilities/alma/observing`) and consider a line sensitivity limit of 1 mK for all bands. In Tables 2.5-2.7 are only the three strongest transitions listed, while a full list is available upon request from the authors.

Table 2.5: Observable deuterated species with the Atacama large millimeter/-submillimeter array in dark clouds.

Species	n(x)/n(H_2) [$\times 10^{-11}$]	Line	Frequency [GHz]	Line flux [mK]	Band
D_2CO	1.05	3 0 3 → 2 0 2	174.413	33.48	5
		4 0 4 → 3 0 3	231.410	28.48	6
		5 0 5 → 4 0 4	287.486	14.99	7
D_2O	53.6	1 1 0 → 1 0 1	316.800	1899.80	7
		2 0 2 → 1 1 1	468.247	853.66	8
		2 1 1 → 2 0 2	403.562	198.18	8
D_2S	0.0634	2 2 0 → 1 1 1	669.787	1.40	9
DCN*	5.21	1 → 0	115.271	6648.00	3
		2 → 1	230.538	5272.00	6
		3 → 2	345.796	3860.00	7
DCO^+	16.04	2 → 1	144.077	2196.40	4
		4 → 3	288.144	2054 .53	7
		5 → 4	360.170	801.50	7
DNC	11.01	2 → 1	152.610	1047.68	4

Species	n(x)/n(H_2) [$\times 10^{-11}$]	Line	Frequency [GHz]	Line flux [mK]	Band
		4 → 3	305.207	866.60	7
		6 → 5	457.776	66.33	8
H_2DO^+	29.93	1 0 1 1 → 2 1 1 0	250.914	9.84	6
HDCO	24.69	4 0 4 → 3 0 3	256.586	616.96	6
		2 0 2 → 1 0 1	128.813	513.23	4
		3 1 2 → 2 1 1	201.341	313.03	5
HDCS	0.7897	5 0 5 → 4 0 4	154.885	4.12	4
		3 0 3 → 2 0 2	92.982	3.12	3
		6 0 6 → 5 0 5	185.693	3.01	5
HDS	1.630	2 0 2 → 1 0 1	477.764	25.62	8
		1 0 1 → 0 0 0	244.556	18.22	6
		1 1 0 → 1 0 1	195.559	9.05	5
ND	27.03	1 0 1 2 → 0 1 2 3	491.934	294.70	8
		1 0 1 2 → 0 1 1 2	491.969	124.38	8
		1 0 1 1 → 0 1 2 2	491.917	123.84	8
ND_3	0.96	2 0 0 → 1 0 1	614.933	73.05	9
		2 1 1 → 1 1 0	618.125	60.59	9
		2 1 0 → 1 1 1	614.968	59.74	9
NH_2D	296.70	1 1 0 1 → 0 0 0 0	494.455	10000.00	8
		1 1 1 0 → 1 0 1 1	85.926	870.34	3
		1 0 1 1 → 0 0 0 1	332.782	732.35	7
NHD_2	14.60	2 1 1 0 → 1 0 1 1	699.224	874.07	9
		2 1 1 1 → 1 0 1 0	709.350	456.67	9
		1 1 1 0 → 0 0 0 0	335.514	40.68	7

The table is limited to species with relative abundances $> 10^{-12}$.
Species previously detected in DCs are marked in boldface.
Parameters for line flux calculations: 10 K, 10^4 cm^{-3}, 10^{22} cm^{-2}
* DCN should be observable but is not listed in CDMS or RADEX, instead RADEX values for HCN are listed

Table 2.6: Observable deuterated species with the Atacama large millimeter/-submillimeter array in infrared dark clouds.

Species	n(x)/n(H_2) [$\times 10^{-11}$]	Line	Frequency [GHz]	Line flux [mK]	Band
C_4D	0.039	11 12 → 10 11	97.140	2.36	3
		12 13 → 11 12	105.971	2.35	3
		10 11 → 9 10	88.308	2.25	3
CH_2D^+	0.045	2 1 2 → 1 1 1	490.012	44.05	8
		1 0 1 → 0 0 0	278.692	10.68	7
		2 1 1 → 2 1 2	201.754	1.62	5
CH_2DCN	0.0038	9 0 9 → 8 0 8	156.281	7.47	4
		10 0 10 → 9 0 9	173.639	6.73	5
		6 0 6 → 5 0 5	104.198	6.00	3
D_2CO	0.011	5 0 5 → 4 0 4	287.486	63.48	7
		6 0 6 → 5 0 5	342.522	48.67	7
		3 0 3 → 2 0 2	174.413	45.25	5
D_2O	3.10	1 1 0 → 0 0 0	317.800	30000.00	7
		2 0 2 → 1 0 1	468.247	30000.00	8

Species	n(x)/n(H_2) [$\times 10^{-11}$]	Line	Frequency [GHz]	Line flux [mK]	Band
		2 1 1 → 1 0 0	403.562	24681.37	8
DCN*	0.38	1 → 0	88.634	21800.00	3
		2 → 1	177.258	20590.00	5
		3 → 2	265.886	19040.00	6
DCO^+	47.09	5 → 4	360.170	30000.00	7
		3 → 2	216.113	30000.00	6
		6 → 5	432.189	30000.00	8
DNC	0.81	3 → 2	228.910	24216.75	6
		6 → 5	457.776	14474.58	8
		2 → 1	152.610	11600.74	4
DOC^+	0.00062	3 → 2	229.149	15.36	6
		5 → 4	318.885	15.26	7
		6 → 5	458.237	9.15	8
H_2DO^+	3.39	1 0 1 1 → 2 1 1 0	250.914	2582.00	6
		3 3 1 0 → 2 2 1 1	649.653	368.10	9
		3 3 0 0 → 2 2 0 1	632.902	342.59	9
HDCO	0.10	5 0 5 → 4 0 4	319.770	629.27	7
		3 0 3 → 2 0 2	192.893	502.15	5
		4 1 3 → 3 1 2	268.292	426.06	6
HDCS	0.0065	7 0 7 → 6 0 6	216.662	6.88	6
		5 0 5 → 4 0 4	154.885	6.46	4
		8 0 8 → 7 0 7	247.488	5.69	6
HDS	0.018	1 1 1 → 0 0 0	389.041	70.17	8
		2 0 2 → 1 0 1	477.764	62.06	8
		3 0 3 → 2 0 2	691.498	45.74	9
ND	0.16	1 0 1 2 → 0 1 2 3	491.934	357.79	8
		1 0 1 2 → 0 1 1 2	491.969	150.99	8
		1 0 1 1 → 0 1 2 2	491.917	150.36	8
ND_3	0.0080	2 1 1 → 1 1 0	618.125	125.84	9
		2 1 0 → 1 1 1	614.968	124.41	9
		1 0 1 → 0 0 0	309.909	68.34	7
NH_2D	27.15	1 1 0 1 → 0 0 0 0	494.455	30000.00	8
		2 0 2 1 → 1 0 1 1	649.916	17102.87	9
		1 1 1 0 → 1 0 1 1	85.926	16766.37	3
NHD_2	0.45	1 1 0 1 → 0 0 0 0	388.652	4199.24	8
		2 1 1 1 → 1 0 1 0	709.350	3793.42	9
		2 0 2 0 → 1 1 0 1	410.491	296.35	8

The table is limited to with relative abundances $> 10^{-12}$.

Species previously detected in warm IRDCs are marked in boldface.

Parameters for line flux calculations: 25 K, 10^5 cm^{-3}, 10^{24} cm^{-2}

* DCN should be observable but is not listed in CDMS or RADEX, instead RADEX values for HCN are listed

Table 2.7: Observable deuterated species with the Atacama large millimeter/-submillimeter array in high-mass protostellar objects.

Species	n(x)/n(H_2) [$\times 10^{-11}$]	Line	Frequency [GHz]	Line flux [mK]	Band
C_4D	0.95	23 24 → 22 23	203.104	28.13	5
		22 23 → 21 22	194.275	27.98	5
		24 25 → 23 24	211.932	27.96	6
C_6D	0.018	42 -1 43 → 41 1 42	112.462	1.97	3
		41 -1 42 → 40 1 41	109.856	1.97	3
		41 1 42 → 40 -1 41	109.816	1.97	3
D_2CO	0.0017	8 0 8 → 7 0 7	499.596	2.44	8
		11 0 11 → 10 0 10	605.672	2.21	9
D_2O	1.87	2 1 1 → 2 0 2	403.562	5768.78	8
		4 2 2 → 3 1 1	692.244	3398.71	9
		2 0 2 → 1 0 1	468.247	3334.45	8
DCN*	0.21	1 → 0	88.634	71760.00	3
		2 → 1	177.258	70430.00	5
		3 → 2	265.886	68680.00	6
DCO^+	23.91	9 → 8	648.193	75000.00	9
		6 → 5	432.189	75000.00	8
		5 → 4	360.170	75000.00	7
DCS^+	0.0023	12 → 11	432.338	5.49	8
		10 → 9	360.307	5.27	7
		13 → 12	468.347	5.23	8
DNC	0.41	9 → 8	686.553	7042.88	9
		6 → 5	457.776	6233.04	8
		4 → 3	305.206	3003.38	7
H_2DO^+	2.27	3 3 1 0 → 2 2 1 1	649.653	2352.22	9
		3 3 0 0 → 2 2 0 1	632.902	2258.85	9
		4 1 3 0 → 3 0 3 1	716.959	1629.36	9
HDCO	0.093	10 0 10 → 9 0 9	625.688	136.82	9
		7 0 7 → 6 0 6	444.229	134.73	8
		8 1 8 → 7 1 7	491.937	129.31	8
HDCS	0.56	13 0 13 → 12 0 12	400.766	151.96	8
		11 0 11 → 10 0 10	339.646	148.23	7
		14 0 14 → 13 0 13	431.218	145.25	8
ND	3.70	1 0 1 2 → 0 1 2 3	491.934	911.92	8
		1 0 1 2 → 0 1 1 2	491.969	384.82	8
		1 0 1 1 → 0 1 2 2	491.917	383.23	8
ND_3	0.0031	2 1 1 → 1 0 0	618.125	4.24	9
		2 1 0 → 1 0 0	614.968	4.20	9
NH_2D	25.07	1 1 0 1 → 0 0 0 0	494.455	8876.12	8
		3 3 0 0 → 3 2 2 1	618.142	5010.99	9
		2 2 0 1 → 2 1 2 0	475.890	4998.31	8
NHD_2	0.37	2 1 1 1 → 1 0 1 0	709.350	301.28	9
		1 1 0 1 → 0 0 0 0	388.652	158.40	8
		3 1 2 1 → 2 2 0 0	672.370	40.29	9

The table is limited to species with relative abundances $> 10^{-12}$.

Species previously detected in HMPOs are marked in boldface.

Parameters for line flux calculations: 75 K, 10^5 cm^{-3}, 10^{24} cm^{-2}

* DCN should be observable but is not listed in CDMS or RADEX, instead RADEX values for HCN are listed

Amongst these listed species are tracers (through D/H ratios) of initial abundances (e.g. D_2CO, HDO, NH_2D, CH_2D^+) and temperature (D_2O, DCO^+, DCN, D_2S) as we have listed in Table 2.4. A few ions are observable with ALMA, such as DCO^+, H_2DO^+, CH_2D^+. We find that the tracer of ionization in the cold ISM regions with high depletion, H_2D^+ and $HD_2{}^+$, will be hard to detect with ALMA, as found by Chapillon et al. (2011) for PPDs. We note that all isotopologues of ammonia are easily observable in the all three ISM environments. The metastable doublet lines of NH_3 are used to constrain gas temperature (e.g. Ho & Townes 1983; Maret et al. 2009). We think that using the relative abundances of the minor NH_3 isotopologues one could also discern the previous temperature history of the environment. We determine that several sulphur-bearing species, such as HDCS, D_2CS, HDS, should be observable by ALMA, and as sulphur chemistry is not well understood yet, observations of these species could serve as proxies for future studies. Finally we note that the HDO lines are expected to be observable with ALMA, but it is not included into CDMS, and we could not calculate its line intensities assuming LTE. On the other hand, water has a complex level structure, with some of the lines that are masing and many that become highly optically thick, and the escape probability non-LTE method of RADEX is not capable of modeling its line intensities reliably. For estimation of the water line fluxes one has to perform a full line radiative transfer modeling for each individual object.

For deuterated ices we only list the most abundant species in Table 2.8 and do not try to predict their observability. Amongst the deuterated ices we find several polyynes (C_nH_2, with $n > 4$) are abundant, especially at temperatures > 10 K. These species have been observed in the Solar system such as in Titan's atmosphere (e.g. Teanby et al. 2009), but should also be abundant in ices in interstellar space. Several organics such as deuterated formic acid and hydroxylamine (both singly- and doubly-deuterated) are abundant, even among the most abundant at higher temperatures ($\gtrsim 25$ K). Also both ammonia and water (singly- and doubly-deuterated) show high abundances.

2.5 EARLIER MODELS

Roberts & Millar (2000b) and Roberts & Millar (2000a) have investigated the chemical evolution with deuterium fractionation for temperatures 10−100 K and densities $3 \times 10^3 - 3 \times 10^8$ cm^{-3} on a less resolved grid, consisting of only 100 points. They used a time-dependent chemical gas-phase model based on the UMIST'95 database (Millar et al. 1997). Their resulting network consists of $\sim$ 300 species linked by $>$5 000 reactions, but only includes singly-deuterated species and limited surface chemistry for H_2 and HD. We compared the results between our models for a number of species, including DCO^+, HDCO, DCN, DNC and DC_5N, looking at the distribution of D/H fractionation ratios and time-dependent abundances at 10^5 yr, and we found good agreement between our models. We also studied the molecular abundances under conditions typical of the TMC-1 environment in our "Primordial" model and under these

Table 2.8: Fractional abundances and D/H ratios: deuterated ices. The table is limited for each environment to 10 species or species with relative abundances $> 10^{-12}$.

Species	Abundance	D/H ratio
DCs – 10 K, 10^4 cm^{-3}		
HDO	3.90×10^{-7}	4.26×10^{-3}
CH_3D	1.41×10^{-7}	8.70×10^{-3}
NH_2D	6.75×10^{-8}	6.14×10^{-3}
C_3HD	5.38×10^{-9}	9.61×10^{-3}
CH_2D_2	1.89×10^{-9}	1.17×10^{-4}
DNO	1.72×10^{-9}	1.06×10^{-1}
D_2O	1.05×10^{-9}	1.15×10^{-5}
HDS	6.72×10^{-10}	1.15×10^{-2}
NHD_2	2.48×10^{-10}	2.25×10^{-5}
DCN	1.73×10^{-10}	5.90×10^{-3}
Warm IRDCs – 25 K, 10^5 cm^{-3}		
HDO	6.77×10^{-8}	2.94×10^{-3}
HDO_2	4.06×10^{-9}	1.78×10^{-3}
NH_2D	2.48×10^{-9}	7.40×10^{-3}
C_3HD	6.62×10^{-10}	7.75×10^{-4}
D_2O	4.68×10^{-10}	1.15×10^{-5}
CHDCO	2.77×10^{-10}	1.83×10^{-3}
DCN	2.30×10^{-10}	1.04×10^{-3}
DCOOH	1.72×10^{-10}	4.31×10^{-2}
DNC	1.57×10^{-10}	1.11×10^{-2}
CH_3D	1.53×10^{-10}	1.09×10^{-1}
HMPOs – 75 K, 10^5 cm^{-3}		
HDO	8.68×10^{-7}	1.27×10^{-2}
NHDOH	1.73×10^{-7}	9.25×10^{-2}
NH_2D	1.68×10^{-7}	2.21×10^{-2}
D_2O	1.11×10^{-8}	1.63×10^{-4}
HDO_2	5.01×10^{-9}	7.95×10^{-2}
ND_2OH	3.14×10^{-9}	1.68×10^{-3}
NHD_2	2.65×10^{-9}	3.29×10^{-4}
C_5HD	2.45×10^{-9}	1.25×10^{-2}
C_6HD	9.96×10^{-10}	1.72×10^{-2}
D_2O_2	8.15×10^{-10}	1.29×10^{-2}

Table 2.9: Comparison of D/H ratios for a TMC1-like environment (T = 10 K, $n_H = 10^4$ cm^{-3}) between our model and Roberts & Millar (2000b).

Species	Our model	Roberts & Millar	Ratio
NH_2D	1.4×10^{-2}	8.4×10^{-2}	0.17
HDCO	1.7×10^{-2}	4.2×10^{-2}	0.40
DCN	2.4×10^{-2}	0.9×10^{-2}	2.7
DNC	2.6×10^{-2}	1.5×10^{-2}	1.7
C_2D	1.1×10^{-2}	1.1×10^{-2}	1.0
C_4D	1.6×10^{-2}	0.4×10^{-2}	4.0
DCO^+	3.9×10^{-2}	1.9×10^{-2}	2.1
N_2D^+	8.6×10^{-3}	2.5×10^{-2}	0.34
C_3HD	1.3×10^{-2}	0.6×10^{-2}	2.2
C_3H_3D	1.6×10^{-2}	8.3×10^{-2}	0.19
DC_3N	9.6×10^{-3}	0.7×10^{-2}	1.4
DC_5N	1.2×10^{-2}	2.3×10^{-2}	0.52
HDCS	1.8×10^{-2}	4.0×10^{-2}	1.4

conditions we found that the quantitative agreement in the D/H ratios is better than an order of magnitude for all species, with the worst agreement for NH_2D where the ratio between the two models is 0.14. The comparison for D/H values is shown in Table 2.9. The intrinsic uncertainty in the abundance of DC_5N as predicted in our sensitivity analysis is very large, $\sim 1 - 1.5$ orders of magnitude, and is comparable to the difference between our and Roberts' & Millar's model. We note however that our modeled D/H ratios show a better agreement with the observations of DC_5N and HC_5N in TMC-1 by MacLeod et al. (1981) than calculated values by Roberts & Millar. In Roberts & Millar (2000a) expanded their study to include doubly-deuterated species, allowed species to freeze onto grains and looked at a different selection of species. We compared their predictions with our results for singly- and doubly- deuterated isotopologues of NH_3, H_2O, H_2CO, and found reasonably good agreement for all singly-deuterated species. In our model, NH_2D shows enhanced D/H ratios ($\sim 10^{-3} - 10^{-1}$) up to temperatures of $30 - 40$ K, while the enhanced D/H ratios in the model of Roberts & Millar only appear up to $20 - 30$ K. For the doubly-deuterated species D_2O, NHD_2 and D_2CO we predict similar D/H ratios to Roberts & Millar up to temperatures of ~ 50 K, with values $\sim 10^{-3} - 10^{-1}$, while at larger temperatures our models diverge. Our model predicts a strong decrease in the respective D/H ratios to $\sim 10^{-5}$, while the D/H ratios of Roberts & Millar decrease more smoothly and do not reach the same value until at ~ 100 K.

In the study of Roberts et al. (2004), the chemical evolution in a sample of prestellar cores using two subsets of the Rate'99 and osu.2003 chemical networks was compared. With the networks limited to include species with six

or fewer carbon atoms and no surface chemistry, Roberts et al. (2004) used the chemical models to successfully explain observations of the CO depletion, and its relevance to the D_2CO and HDCO fractionation ratios. If we compare the calculated fractionation ratios between the steady state abundances of Roberts et al. (see their Table 5) and our models for a TMC-1 environment, the D/H ratios for the majority of key species such as H_2D^+, N_2D^+, DCO^+ and HDO agree reasonably well. However, we found significant discrepancies for D_2O, $HD_2{}^+$, $D_3{}^+$ and NHD_2. The reason why our D/H ratios for doubly-deuterated species differ from those of Roberts et al. (2004) appears to be twofold. First, they have not considered surface chemistry and assumed that all atomic D that freezes out is immediately returned to the gas as HD. In contrast, in our model, the accreted deuterium atoms are incorporated in surface species and do not easily return to the gas phase. Second, they use only steady-state abundances while we use time-dependent abundances at 1 Myr.

Walmsley et al. (2004a) studied steady-state chemistry in a completely depleted, low-mass prestellar core, with an emphasize on explaining observations of ortho-H_2D^+ towards L1544 by Caselli et al. (2003). While our model does not yet include nuclear-spin state chemistry, we compared the calculated abundances of the $H_3{}^+$ isotopologues at densities of $n_H = 10^5, 10^6, 10^7$ cm^{-3}, $T = 10$ K assuming a cosmic ray ionization rate $\zeta = 3 \times 10^{-17}$ s^{-1} (Note that at such conditions para-H_2 will be the dominant form of molecular hydrogen and thus fractionation will proceed with a high efficiency as assumed in our model). For both the "Primordial" and "Evolution" models we found good overall agreement for the D/H ratios of the $H_3{}^+$ isotopologues and the electron abundances. The only difference occurs at high densities of $\sim 10^7$ cm^{-3}, where the $HD_2{}^+$ and $D_3{}^+$ abundances are one and two orders of magnitude lower in our model, respectively. We could not find out whether this difference increases at higher densities. The likely reason for such a discrepancy is the lack of surface chemistry and the assumption of complete freeze-out in the Walmsley et al. (2004a) model. Even at such high densities and 10 K, the depletion is not complete in our model, so that the H_3^+ isotopologues can still be destroyed by ion-molecule reactions in addition to dissociative recombination with electrons or negatively charged grains. Moreover, in our model, atomic D released upon dissociative recombination can stick to a grain and be incorporated in the surface molecules. At $n_H \gtrsim 10^7$ cm^{-3} and after 1 Myr of evolution, a substantial fraction of the gas-phase reservoir of the elemental D can be chemically 'transferred' to ices, unable to directly come back to the gas phase. Consequently, it will increase surface fractionation and abundances of deuterated ices.

2.6 CONCLUSIONS

Modern observing facilities such as ALMA will perform observations of the chemistry in interstellar with unprecedented accuracies, and there is a need for new modern chemical models if we are to decipher the wealth of information they provide us. We present in this chapter an extended, publicly avail-

able chemical network for deuterium fractionation, with the most up-to-date reaction rate coefficients from laboratory measurements and theoretical studies, including gas-phase and surface reactions. The new deuterium chemistry model has in this chapter been tested for dense ISM environments in a benchmarking study of deuterium chemistry by comparing observed D/H ratios for dense ISM environments and comparing identified dominant pathways for a subset of essential species to previous studies.

Comparisons to previous theoretical studies illustrates the robustness of our model and quantify the effect that new experimental measurements has had on our chemical understanding of the early phases of the stellar evolution. Amongst the list of species showing a change in D/H ratios by more than a factor of 5, are light hydrocarbons (e.g. CH_2D_2, CHD_3), ions (CH_4D^+, HD_2O^+), simple organics molecules (DCOOH, D_2CO), and key species such as D_2O and NHD_2. Also several species, such as CH_2D^+ and CHD_2^+, show a coherent increase in abundances of deuterated and un-deuterated isotopologues, and hence they are affected by the updates although their D/H remain the same.

A list of deuterated species separated by the dependence of their D/H ratios on temperature or initial abundance show that many late-stage species and multi-deuterated species are strongly affected by initial abundances. The majority of smaller molecules and reactive ions are instead sensitive to temperature with energy barriers of $\sim$ 30 K, and only isotopologues of CH_3^+ and $C_2H_2^+$ show sensitivity for higher temperatures of $\sim$ 80 K.

Finally, the long-term evolution of a few representative species are studied, and molecules that are dominantly formed on grains, such as water and methanol, show significant variations in abundances beyond 10^6 years, while other species reach steady-state at $\sim 10^5$ years. This shows the importance of adopting time-dependent chemical models.

3

ERROR PROPAGATION IN DEUTERIUM FRACTIONATION CHEMISTRY UNDER DARK, COLD INTERSTELLAR CONDITIONS

Adapted from Albertsson, Semenov, Vasyunin, Henning & Herbst (2013), ApJS, Vol. 207, p. 27[1]

3.1 ABSTRACT

The chemical network intended for the study of deuterium chemistry throughout the stellar evolution is accompanied by large uncertainties due to the the use of the cloning routine to include educated guesses on unknown reactions in the deuterium chemistry. These uncertainties will propagate through the chemical evolution, and cause uncertainties in both predicted abundances and D/H ratios. Also, we report a detailed sensitivity analysis to understand and to quantify the intrinsic error bars in calculated abundances of deuterated species in several representative astrophysical environments. We find that uncertainties are typically lower in DC environments, and that the size of the molecule, and number of D-atoms, increases uncertainties. In order to aid future studies of reactions rates I isolate the most problematic gas-phase reactions with uncertain rate coefficients to be studied in the laboratory or theoretically, and quantify the associated uncertainties in modeled abundances.

3.2 INTRODUCTION

Modern astrochemical databases contain thousands of reactions, connected by hundreds of species. Many reactions are still poorly understood and accompanied by larger uncertainties, which will propagate through the chemical kinetics and affect predicted abundances. The deuterium network presented in this thesis is accompanied by large errors from adopting the cloning routine to make educated guesses for unknown reactions in the deuterium chemistry. With the advent of powerful observing facilities such as ALMA breaking new limits in the observational studies of the chemical cosmos, we are entering a new era which will require new sophisticated chemical models in order to reconstruct the evolutionary history of chemical throughout the stellar evolution.

Uncertainties of most reactions are typically a factor of 2 and larger but for the rate coefficients for reactions such as RA, uncertainties are typically considered to be on the order of a magnitude (see e.g. Vasyunin et al. 2008b). For other reactions, such as dissociative recombination, reactions can be accurately

1 Simulations for the sensitivity analysis of this study were done by Anton Vasyunin, everything else of this chapter has been written, analyzed and produced by me.

determined (see e.g. Florescu-Mitchell & Mitchell 2006), but instead branching ratios between different channels are not known precisely (see e.g. Millar et al. 1988; Geppert et al. 2005, 2006; Hamberg et al. 2010b, as well as discussion in Chapter 4). These uncertainties conjugate as the chemistry forms larger and more complex molecules, with their uncertainties propagating through the reaction pathways.

Owing to the time-consuming effort of determining rate coefficients of reactions, experimentalists benefit greatly from sensitivity studies of chemical networks, as it aids in identifying the most problematic reactions that require more accurately determined rate coefficients. Vasyunin et al. (2004) studied the influence of rate uncertainties in dense and diffuse clouds. They found abundance uncertainties of simple molecules are typically limited to an order of magnitude, while uncertainties for larger species increase substantially with the size of the molecule, reaching more than three orders of magnitude for complex molecules with long carbon chains.

Wakelam et al. (2005) studied the uncertainties of gas-phase molecules in hot cores, and found that at times $\leq 10^4$ years the modeled uncertainties are reasonable in comparisons to observations, but at later times, $\geq 10^4$ years, the uncertainties for important species are much higher, for species such as H_2CO and CH_3OH they can be as large as 4 orders of magnitude at times $\sim 10^5$ years. However, it is likely that the hot core has ceased to exist at this age, and uncertainties would never become so large. In both cases however, it is crucial to take into account these uncertainties in comparisons with observations. Wakelam et al. (2006a) concentrated on uncertainties in the chemistry of dense clouds, in particular for the well-studied sources TMC-1CP and L134N, but also took uncertainties in physical parameters into account. They further proved that the best agreement is for early times at $\sim 10^5$ years, but their results also indicated that a static picture of physical considerations, without the inclusion of grain surface interaction, is not enough for a complete, accurate understanding of the chemistry. In Wakelam et al. (2006b) this study was expanded to show that there is a bistability in abundances of many molecules sensitivity to the adopted cosmic-ray ionization rate of helium relative to hydrogen. Vasyunin et al. (2008b) expanded the uncertainty studies to PPDs, and found that typical uncertainties of molecular column densities typically do not exceed a factor of 3-4, even for the largest key molecules, and they determined the need for more accurately determined rate coefficients for approximately a hundred reactions. Finally, Wakelam et al. (2010a) varied individual parameters, such as rate coefficients, temperature, density and cosmic-ray ionization rates, and found that at times $< 4 \times 10^5$ years the dominant uncertainty, averaged over all species, is the rate coefficients, and at later times the physical parameters play a larger role in the uncertainties.

On top of the typical uncertainties in rate coefficients, deuterium chemistry is not at all as well studied as the hydrogen-dominated chemistry, and, as I have shown in Chapter 2, models for studying the deuterium chemistry often have to make educated guesses for the reactions rates, which is prone to include larger uncertainties. It is therefore important to study the impact of uncertainties in reaction rate coefficients on the resulting chemical abundances,

and how they propagate throughout the chemical evolution. It will aid us in understanding where the largest uncertainties in chemical networks are, and which specific pathways should be prioritized in upcoming experimental or theoretical studies.

The aim of this chapter therefore is to identify the most problematic reactions for assortment of essential deuterated molecules, and to quantify intrinsic uncertainties in modeled abundances of deuterated molecules, and D/H ratios. The analytical model for conducting the sensitivity analysis is discussed in Section 3.3, and the resulting uncertainties are discussed in Section 2.6. Finally, in Section 3.4.1 we present and discuss the list of identified problematic reactions.

3.3 ERROR PROPAGATION MODEL

Two separate environments were chosen for this study, representing DCs (T = 10 K, $n_{\mathrm{H}} = 10^4$ cm^{-3}; Nielbock et al. 2012) and lukewarm IRDCs (T = 25 K, $n_{\mathrm{H}} = 10^5$ cm^{-3}; Vasyunina et al. 2012). In these, and all subsequent runs mentioned in this chapter, we use the Primordial initial conditions unless stated to the contrary. We chose to concentrate on the uncertainties of the rate coefficients of the gas-phase reactions. Including variations in surface chemistry rates is a tricky problem as these depend on surface mobility, binding and diffusion energies of reactants, and properties of the surface itself (porosity, irregularities, etc.). Recently, Taquet et al. (2012a) have studied the importance of deuterium fractionation on dust surfaces, using a multi-layered ice mantle model and quantified some of the associated errors in the calculated abundances due to the uncertainties in the surface chemistry, so we do not repeat such a study here.

Our analysis is based on the same method as employed by Dobrijevic & Parisot (1998), Wakelam et al. (2005), Vasyunin et al. (2004) and Vasyunin et al. (2008b). We performed computations for a large set of models, using identical physical conditions and initial abundances, and the same chemical network, but with randomly varied rate coefficients within their uncertainty limits. The rate uncertainties were taken from the KIDA database, and for any unlisted values we adopted a high uncertainty of a factor of 2. Most of the reactions with deuterated species were created by the cloning procedure, and hence have unknown uncertainties. For these reactions we adopted a standard error value with a normal logarithmic error distribution of a factor of 2.

With this method, we generated 10 000 networks with the new rate coefficients $k_r(T)$ for reaction r randomly distributed as follows:

$$k_r(T) = \exp(\ln k_{r,0}(T) + \ln F \times N[0,1]), \tag{3.1}$$

where $k_{r,0}(T)$ is the measured, calculated, or estimated rate coefficient at temperature T for reaction r, F is the statistical distribution of the uncertainty, and $N[0,1]$ is a random value drawn from a standard Gaussian distribution with mean $\mu = 0$ and variance 1. The time needed for a full run consisting of 10 000 networks for a specified temperature and density takes approximately one day

of computational time on a Xeon 3.0 GHz CPU (with relative and absolute tolerances of 10^{-4} and 10^{-20}, respectively).

The huge size of our new deuterium chemical network makes it a challenging task to find a very precise correlation between the rate uncertainties and uncertainties in the molecular abundances of a particular species. Since for many deuterated species the set of primal pathways easily exceeds several reactions, the relative contribution of each individual reaction to the final uncertainty is likely to be small, $\lesssim 10\%$. To isolate the most problematic reactions for several key observed species, we conducted a sensitivity analysis using the same cross-correlation method as implemented by Vasyunin et al. (2008b). We selected a handful of molecules, including their isotopologues and isomers; namely, H_3^+, H_2O, HCN, HCO^+, and CH_3OH, and for each of these species we calculated time-dependent linear correlation coefficients between the abundances and the rate coefficients for all the 10 000 network realizations and for each of our 30 logarithmically taken time steps. The linear correlation coefficients $c_L(i,j,t)$ at specific density, i, and temperature, j, points and at time t are calculated by:

$$c_L(i,j,t) = \frac{\Sigma_l \ (x_l^s(i,j,t) - \overline{x^s(i,j,t)}) \ \ (\alpha_l^j - \overline{\alpha^j})}{\Sigma_l \ (x_l^s(i,j,t) - \overline{x^s(i,j,t)})^2 \ \ \Sigma_l (\alpha_l^j - \overline{\alpha^j})^2} \tag{3.2}$$

with $x_s^l(i,j,t)$ being the molecular abundance for species s and iteration l, and $\overline{x_s^l(i,j,t)}$ and $\overline{\alpha^j}$ signifying the standard (mean) abundances and rate coefficients for species s, respectively. Because key reactions can vary through time evolution, we calculate and use cumulative correlation coefficients in our results, for which we integrated the absolute values of time-dependent linear correlation coefficients over the 30 logarithmic taken time steps taken over 1 Myr. In our results in the next section, we restrict discussion to the cumulative correlation coefficients, designated as c.

3.4 SENSITIVITY ANALYSIS

We have determined that 10 000 realizations of the network may not be adequate for results of our sensitivity analysis to fully converge. For correlation coefficients $c < 0.1$ we sometimes still see small variations when we compare our results with a model containing only 9 000 realizations. Therefore, we also ran a separate set of simulations with 20 000 realizations for a DC environment, but found the same result with only minor deviations for the reactions with low correlation coefficients, $c < 0.1$. All correlation coefficients should stop fluctuating with size as soon as the number of the network realizations exceeds the number of reactions in the network, which is $\sim 50\,000$. Running the sensitivity analysis code with so many realizations, however, would be prohibitively time consuming. Therefore, below we consider reactions with $c > 0.1$ in our discussion.

After calculating time-dependent abundances for all the realizations of the chemical network with varied reaction rate coefficients, and for each considered physical model, we fit Gaussians to the resulting abundance distributions

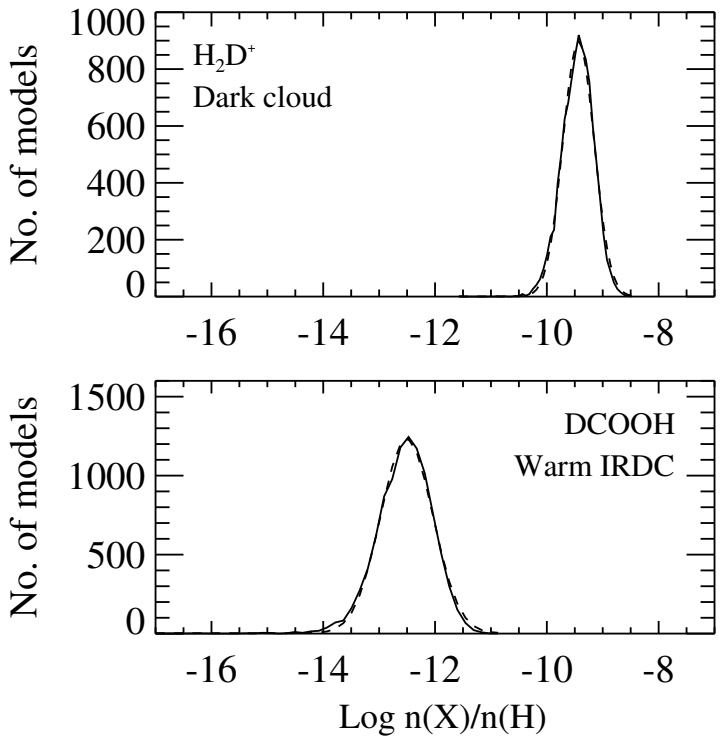

Figure 3.1: Distributions of abundances from 10 000 chemical runs for H_2D^+ in dark clouds (top) and DCOOH in warm infrared dark cloudss (bottom). Plots also show fitted Gaussian distributions (dashed lines).

at 1 Myr for all species. We carefully checked that such an approximation could be applied to the abundance distributions and found it to be the case for almost all species. In Figure 3.1, we show examples of abundance distributions, with their Gaussian fits, for H_2D^+ and DCOOH in DC and warm IRDC environments, respectively, both showing good fits. From the Gaussian fits, we then determined the full width half-maximum (FWHM), 2.35σ, of these distributions and used the 1σ values to quantify the spread in abundances, which we henceforth refer to as the abundance uncertainties. We also applied the same procedure for the calculated D/H ratios, and show examples of the resulting D/H ratio distributions in Figure 3.2 for water and formic acid in the same two regions. We find good fits to all these distributions with estimated 1σ values of factors of 1.9 and 2.9 for the abundance distribution of water and formic acid, respectively, while the values for D/H ratios are a factor of 1.4 and 3.2, respectively.

In Figure 3.3, we plot the 1σ abundance uncertainties for deuterated species with up to three D-atoms at 1 Myr as a function of the number of atoms for both environments. There are two major trends visible in this plot. First, the abundance uncertainties are in general lower in the case of the IRDCs models compared with cold DCs.

At such a low temperature ($10 - 20$ K) many reactions with barriers cannot proceed, lowering the overall chemical complexity and thus the cumulative rate uncertainties. One would expect uncertainties to be the lowest for DCs, but

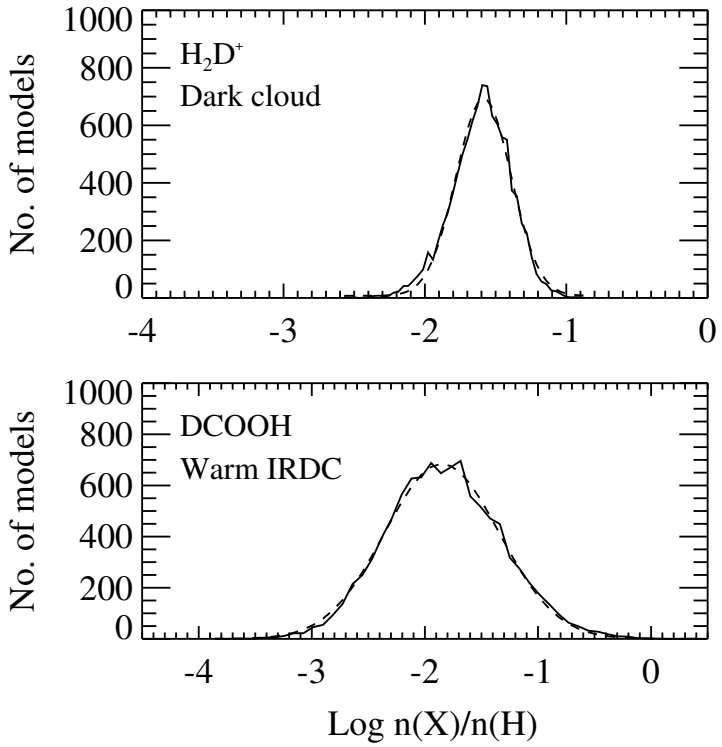

Figure 3.2: Distributions of D/H ratios from 10 000 chemical runs for H_2D^+ in dark clouds (top) and DCOOH in warm infrared dark cloudss (bottom). Plots also show fitted Gaussian distributions (dashed lines).

we suggest that as D/H ratios and abundances of deuterated species are also higher in colder environments, more reactions can occur to increase uncertainties. Second, there is a strong trend of increasing abundance uncertainties with the number of atoms in species. This is obvious as the more atoms a species has, the more reaction pathways lead to its production and destruction from initial composition, and thus the higher is the accumulating effect of their uncertainties on modeled abundances (see also the discussion in Vasyunin et al. 2008b).

In general, using the 1σ confidence level, the abundances and column densities of species made of $\lesssim 3$ atoms (e.g., CO, HCO^+, DCO^+) are uncertain by factors $1.5-5$, those for species made of $4-7$ atoms are uncertain by a factor of $1.5-7$, and those for more complex species made of >7 atoms are uncertain by a factor of $2-10$. The uncertainties for D- and H-bearing species are very similar in DC environments. In warm IRDCs the typical uncertainties of larger H-bearing species (>4 atoms) are approximately a factor of two lower compared to D-bearing species, as de-fractionation begins at these elevated temperatures (25 K). Our estimates for the abundance uncertainties for deuterated species are comparable to the abundance uncertainties of un-deuterated species in protoplanetary disks (Vasyunin et al. 2008b), as well as diffuse and dark dense clouds (e.g., Vasyunin et al. 2004; Wakelam et al. 2006a, 2010a). Chemically simple species containing Mg, Na, and Si tend to have high uncertainties reaching up to 3 orders of magnitude in abundances because their

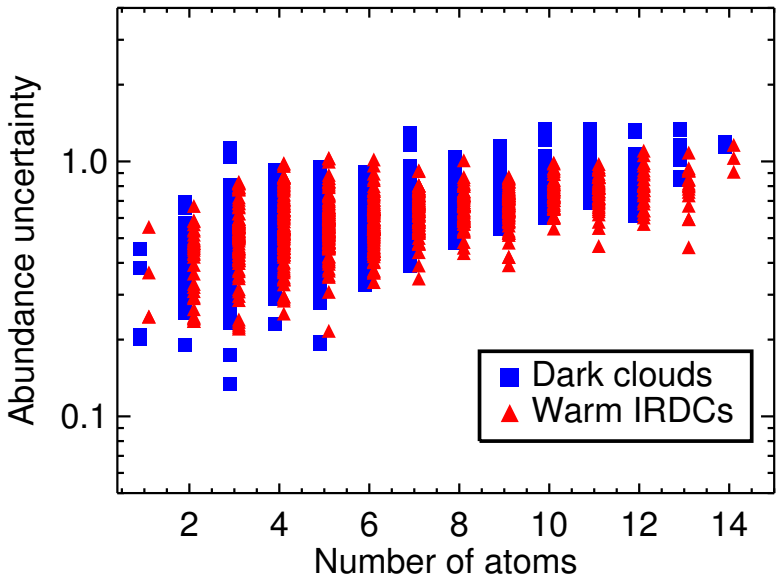

Figure 3.3: The 1σ abundance uncertainties in orders of magnitude for up to triply-deuterated species as a function of the number of atoms in a molecule. The dark clouds model results are denoted by squares and the warm infrared dark clouds model by triangles. A colored version of the plot is available in the online version.

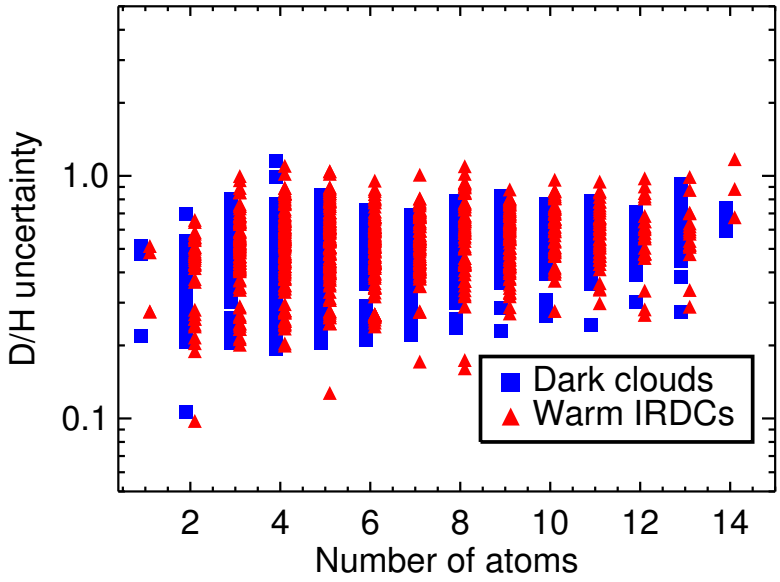

Figure 3.4: The 1σ uncertainties of the calculated D/H ratios in orders of magnitude for up to triply-deuterated species as a function of the number of atoms in a molecule. The dark clouds model results are denoted by squares and the warm infrared dark clouds model by triangles. A colored version of the plot is available in the online version.

chemical pathways remain poorly investigated. Also large molecular species, be they rather abundant hydrocarbons (C_nH_m with n, m $\gtrsim$ 4), with fractional abundances up to $10^{-9} - 10^{-7}$, or complex and less abundant organic species (e.g. methyl formate, dimethyl ether), have large error bars in the computed abundances. For this latter group, the uncertainties can reach more than one order of magnitude.

In addition to the abundance uncertainties, we also determine uncertainties in the resulting D/H ratios, as shown in Figure 3.4. Overall, the uncertainties in D/H ratios are lower when compared with the uncertainties of the corresponding H- and D-bearing isotopologues. This is because abundances of the individual isotopologues are often affected by the rate uncertainties in the same way, given that a majority of the deuterium fractionation processes are cloned, thus inheriting the rate of the "ancestor" reaction. We find the same trends as for the abundance uncertainties, but only a hint of increasing uncertainties with number of atoms. Uncertainties for D/H ratios are generally about half of one order of magnitude, but may vary between a factor of 2 and 10. As in the case of the abundance uncertainties, we find the largest D/H uncertainties for large hydrocarbons (C_nH_m, with $n, m \gtrsim 4$), complex organics and species containing Mg, Na, and Si.

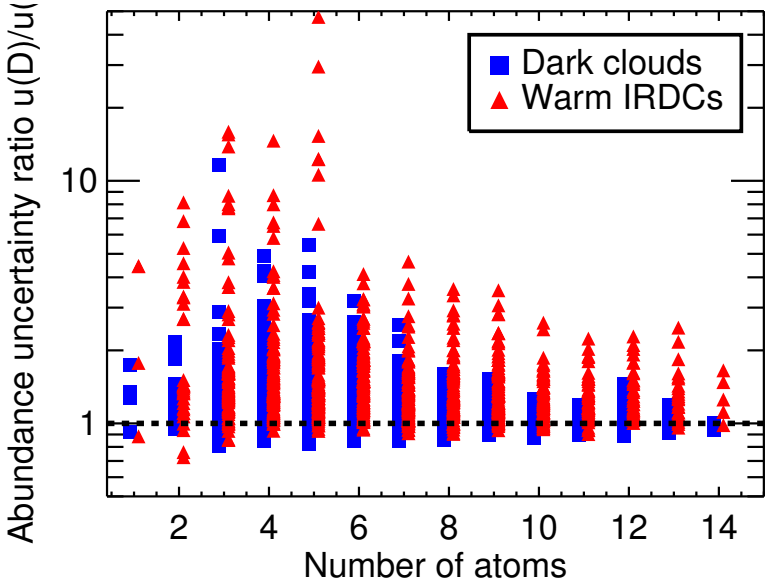

Figure 3.5: Ratios of abundance uncertainties between un-deuterated and deuterated species with up to three D-atoms, as a function of the number of atoms in a molecule. The dark clouds model results are denoted by squares and the warm infrared dark clouds model results by triangles. The dashed line is added to identify where ratios are close to unity. A colored version of the plot is available in the online version.

The question remains how the uncertainties compare between deuterated and un-deuterated species. To illustrate the overall relative uncertainties be-

tween deuterated species and their un-deuterated analogues, we plot in Figure 3.5 the ratios of abundance uncertainties of up to triply-deuterated species and their un-deuterated analogues as a function of the number of atoms. Note that these relative uncertainties are not the same as the uncertainties in D/H ratios; the former can be labeled as u(D)/u(H), while the latter can be labeled as u(D/H), where u stands for uncertainty. Hence, the u(D)/u(H) ratio allows us to compare the relative errors between deuterated and un-deuterated species.

A majority of deuterated species show larger abundance uncertainties with respect to their un-deuterated analogues. There are two major reasons for this behavior. First, the majority of reactions with deuterated species originate from our cloning procedure, and thus have larger assumed uncertainties. Second, to produce a deuterium isotopologue of a molecule additional chemical pathways (e.g., isotope exchange processes) are required, increasing the accumulation of rate uncertainties. For many hydrocarbons (C_nH_m, $C_nH_m^+$ with $m, n = 2, 3$) the abundance uncertainties of their deuterated isotopologues are comparable to those of the main isotopologues (with ratios of $\sim 0.7 - 2$). These hydrocarbons form through ions of hydrocarbons reacting with H_2 or smaller neutral hydrocarbons, such as CH_4 and C_2H_3, and their reactions originate purely from the cloning procedure.

For a limited number of species, the abundance uncertainties of their deuterated isotopologues are even smaller than for the main isotopologues (with ratios of $\sim 0.7 - 0.9$; see Figure 3.5), e.g., C_2D^+ and D^-. These are simple radicals and ions produced by a limited set of reactions, with relatively well-known rate coefficients and thus small uncertainties. The relevant deuterium fractionation chemistry is also limited and has comparably low uncertainties ($\sim 0.7 - 1.1$). Note that the spread in abundance uncertainties ratios appears to decrease with increasing number of atoms in species, getting closer to unity. This effect in Fig. 3.5 occurs because we plot only species with relative abundances exceeding 10^{-25} (with respect to hydrogen), whose numbers decrease substantially with size. If we also add species with such low abundances, this feature disappears and the trend in the uncertainties between small and large molecules is similar.

For HD and D_2, we find that the ratio of their abundance uncertainties to that of H_2 can reach very large values, $\sim$ 1 000 and $\sim$ 10 000, respectively. This effect occurs because abundances of H_2 are very well constrained (uncertainties are $\sim 10^{-5}$), while HD and D_2 have typical values of abundance uncertainties up to one order of magnitude.

Finally, in Figure 3.6 we plot the abundance uncertainties of deuterated species as a function of number of D-atoms, once again restricted to species with relative abundances $> 10^{-25}$. We see an increase in uncertainty with number of D-atoms, as expected from the increasing number of reactions involved for subsequently adding more D-atoms. We also notice a wider spread in uncertainties for species with lower levels of deuteration because smaller species, such as OD, HDO, DCO^+, often have lower uncertainties because there are not as many steps involved in their formation compared to larger species. Larger multiply-deuterated species cannot have these low uncertainties as there are too many steps involved in their formation. Once again we also find that

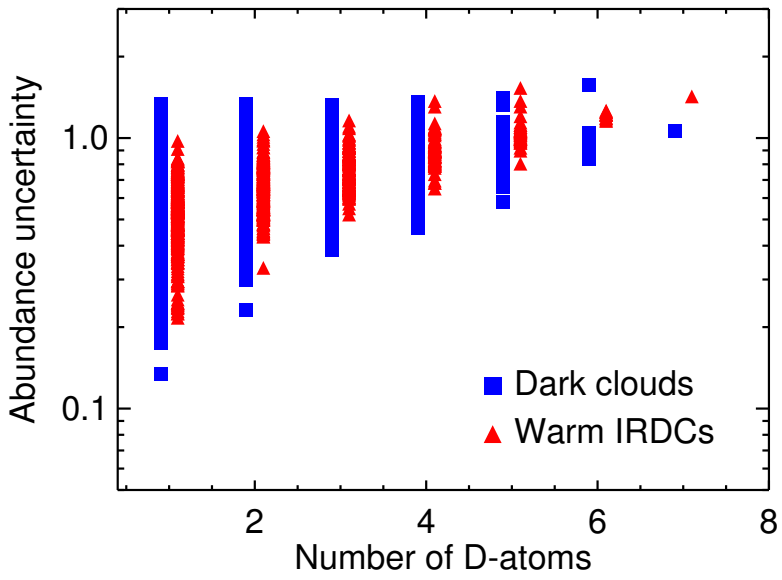

Figure 3.6: Abundance uncertainties in orders of magnitude for deuterated species as a function of number of D-atoms. The dark clouds model results are denoted by squares and the warm infrared dark clouds model results by triangles. A colored version of the plot is available in the online version.

DCs have a larger spread in uncertainties than warm IRDCs. Again we argue that this difference occurs because DC environments overall have higher abundances of deuterated species which are processed through more reactions.

3.4.1 *Problematic reactions*

Table 3.1 lists the subset of reactions with cumulative correlation coefficients $c > 0.05$, which are the most problematic for the chemical evolution of the following species (and their isotopologues and isomers): H_3^+, HCO^+, HCN, H_2O, H_3O^+, CH_3^+, $C_2H_2^+$ and CO.

As can clearly be seen, ion-neutral processes dominate Table 3.1, accompanied by a few dissociative recombination and neutral-neutral reactions as well as cosmic ray ionization of the two critical species: H_2 and He. The last process may require more detailed description in astrochemical models, such as recently presented in Rimmer et al. (2012) and Glassgold et al. (2012), so we assigned a relatively large uncertainty of a factor of 2 for this group of processes. Approximately half of the bimolecular reactions are connected to the chemical evolution of water and light hydrocarbons in the gas. Abundances of species mostly produced on grains, such as methanol, will not be strongly affected by the uncertainties. However, a small fraction of these species is still present in the gas in the center of dense cores, for which uncertainties in the gas-phase chemistry may become important. Many of the deuterated reactions in the table are produced by our cloning procedure, so their error coefficients

are only an approximation, and can, in fact, be larger than estimated. Also, isomerization reactions for HOC^+ and DOC^+ with reaction rate uncertainties of a factor of two possess strong correlation coefficients ($0.3 - 0.4$).

Table 3.1: Problematic reactions that show correlation coefficients > 0.05 and strong chemical ties to any of the following species, including their isotopologues and isomers: water, H_3^+, HCO^+ and HCN. An asterisk alongside the uncertainty signifies a reaction resulting from cloning the network.

Reaction			Uncertainty
H_2 + CRP	$\Rightarrow$	$H_2^+ + e^-$	2.00
He + CRP	$\Rightarrow$	$He^+ + e^-$	2.00
H_3^+ isotopologues			
$H_3^+ + e^-$	$\Rightarrow$	H + H + H	2.00
$H_2D^+ + e^-$	$\Rightarrow$	D + H + H	2.00
$HD_2^+ + e^-$	$\Rightarrow$	D + D + H	2.00
$H_3^+ + HD$	$\Rightarrow$	$H_2D^+ + H_2$	1.25
$H_2D^+ + HD$	$\Rightarrow$	$HD_2^+ + H_2$	1.25
$HD_2^+ + HD$	$\Rightarrow$	$D_3^+ + H_2$	1.25
$H_2D^+ + H_2$	$\Rightarrow$	$H_3^+ + HD$	2.00
$HD_2^+ + H_2$	$\Rightarrow$	$H_2D^+ + HD$	2.00
$D_3^+ + H_2$	$\Rightarrow$	$HD_2^+ + HD$	2.00
$H_3^+ + D_2$	$\Rightarrow$	$HD_2^+ + H_2$	2.00
$H_2D^+ + D_2$	$\Rightarrow$	$D_3^+ + H_2$	2.00
$H_3^+ + D$	$\Rightarrow$	$H_2D^+ + H$	2.00
$H_2D^+ + D$	$\Rightarrow$	$HD_2^+ + H$	2.00
$HD_2^+ + D$	$\Rightarrow$	$D_3^+ + H$	2.00
$H_3^+ + CO$	$\Rightarrow$	$HCO^+ + H_2$	1.25
$H_2D^+ + CO$	$\Rightarrow$	$DCO^+ + H_2$	1.25*
$HD_2^+ + CO$	$\Rightarrow$	$DCO^+ + HD$	1.25*
$D_3^+ + CO$	$\Rightarrow$	$DCO^+ + D_2$	1.25*
$H_3^+ + OH$	$\Rightarrow$	$H_2O^+ + H_2$	2.00
$H_2D^+ + OH$	$\Rightarrow$	$H_2O^+ + HD$	2.00
$H_3^+ + OD$	$\Rightarrow$	$H_2O^+ + HD$	2.00
HCO^+ isotopologues			
$H_3^+ + CO$	$\Rightarrow$	$HCO^+ + H_2$	1.25
$H_3^+ + CO$	$\Rightarrow$	$HOC^+ + H_2$	1.25
$H_2D^+ + CO$	$\Rightarrow$	$DCO^+ + H_2$	1.25

Reaction			Uncertainty
$H_2D^+ + CO$	$\Rightarrow$	$DOC^+ + H_2$	1.25
$HCO^+ + e^-$	$\Rightarrow$	$CO + H$	1.25
$HOC^+ + e^-$	$\Rightarrow$	$CO + H$	1.25
$DCO^+ + e^-$	$\Rightarrow$	$CO + D^*$	1.25
$DOC^+ + e^-$	$\Rightarrow$	$CO + D$	1.25*
$HOC^+ + H_2$	$\Rightarrow$	$HCO^+ + H_2$	2.00
$HCO^+ + D$	$\Rightarrow$	$DCO^+ + H$	2.00
$DOC^+ + H_2$	$\Rightarrow$	$DCO^+ + H_2$	2.00
$DOC^+ + H_2$	$\Rightarrow$	$HCO^+ + HD$	2.00
$HCO^+ + OH$	$\Rightarrow$	$H_2O^+ + CO$	2.00
$H^+ + D$	$\Rightarrow$	$D^+ + H$	2.00
HCN isotopologues			
$H_2CN^+ + e^-$	$\Rightarrow$	$HCN + H$	2.00
$H_2CN^+ + e^-$	$\Rightarrow$	$HNC + H$	2.00
$HDCN^+ + e^-$	$\Rightarrow$	$HCN + D$	2.00*
$HDCN^+ + e^-$	$\Rightarrow$	$DCN + H$	2.00
$HDCN^+ + e^-$	$\Rightarrow$	$HNC + D$	2.00
$HDCN^+ + e^-$	$\Rightarrow$	$DNC + H$	2.00*
$H_2CN^+ + e^-$	$\Rightarrow$	$CN + H + H$	2.00
$HDCN^+ + e^-$	$\Rightarrow$	$CN + H + D$	2.00
$C^+ + HNC$	$\Rightarrow$	$H_2CN^+ + H_2O$	2.00*
$C^+ + HCN$	$\Rightarrow$	$C_2N^+ + H$	2.00
$C^+ + DNC$	$\Rightarrow$	$C_2N^+ + D$	2.00*
$C^+ + DCN$	$\Rightarrow$	$C_2N^+ + D$	2.00*
$C^+ + HCN$	$\Rightarrow$	$CNC^+ + H$	2.00
$C^+ + NH_2$	$\Rightarrow$	$HCN^+ + H$	2.00
$C^+ + NH_3$	$\Rightarrow$	$H_2CN^+ + H$	2.00
$NH_2 + O$	$\Rightarrow$	$HNO + H$	2.00
$N + CN$	$\Rightarrow$	$C + N_2$	2.00
H_2O isotopologues			
$H_3O^+ + e^-$	$\Rightarrow$	$H_2O + H$	1.25*
$H_2DO^+ + e^-$	$\Rightarrow$	$HDO + H$	1.25*
$HD_2O^+ + e^-$	$\Rightarrow$	$D_2O + H$	1.25*
$H_3O^+ + e^-$	$\Rightarrow$	$OH + H + H$	1.25
$H_2DO^+ + e^-$	$\Rightarrow$	$OH + D + H$	1.25*
$HD_2O^+ + e^-$	$\Rightarrow$	$OD + D + H$	1.25*
$H_3^+ + H_2O$	$\Rightarrow$	$H_3O^+ + H_2$	1.25

Reaction			Uncertainty
H_3^+ + HDO	⇒	H_3O^+ + HD	1.25*
H_3^+ + HDO	⇒	H_2DO^+ + H_2	1.25*
H_3^+ + O	⇒	H_2O^+ + H	1.40
HCO^+ + H_2O	⇒	H_3O^+ + CO	1.50
HCO^+ + HDO	⇒	H_2DO^+ + CO	1.50*
DCO^+ + H_2O	⇒	H_2DO^+ + CO	1.50*
DCO^+ + HDO	⇒	HD_2O^+ + CO	1.50*
HCO^+ + D_2O	⇒	HD_2O^+ + CO	1.50*

We find it clear that fractionation channels of the H_3^+ and CH_3^+ isotopologues require further study, as do reactions involving the isotopologues of H_3^+ reacting with CO, water, OH and their isotopologues, forming the initial steps towards more complex molecules. Reactions with H_3^+ and H_2D^+ are both well represented in the list and initiate the ion-molecule chemistry, while HD_2^+ and D_3^+ are often not abundant enough to have a significant effect in our models. H_3^+ and H_2D^+ react with CO to form the isotopologues of HCO^+, with OH and OD to form ionized water (H_2O^+, HDO^+) as well as the water isotopologues, which strongly affect water abundances and D/H ratios. We also see many other interconnecting reactions among our set of key species. Several dissociative recombination reactions, which proceed very rapidly, show strong correlations.

3.5 CONCLUSIONS

In this chapter the limits of accuracy for the deuterium chemistry model presented in Chapter 2 have been investigated with a sensitivity analysis. The most problematic reactions for the chemical evolution of H_3^+, HCO^+, HOC^+, HCN, HNC, H_2O, CH_3OH, H_3O^+, CH_3^+, $C_2H_2^+$ and their isotopologues as well as CO are listed. Ion-neutral and dissociative recombination reactions dominate the list, accompanied by a smaller number of neutral-neutral reactions and the cosmic ray ionization of H_2 and He. It is clear that the reaction systems of HD reacting with H_3^+, CH_3^+, and their isotopologues, are still causing large uncertainties in the deuterium chemistry networks. Other specifically important reactions to study are the isotopologues of H_3^+ reacting with CO and the isotopologues of H_2O and OH. These reactions are responsible for the first steps towards more complex molecules and therefore greatly affect abundances.

In order to quantify uncertainties for comparisons with observations, I have also quantified uncertainties in abundances of deuterated species and their D/H ratios. In general, using the 1σ confidence level, the abundances and column densities of species made of $\lesssim$ 3 atoms (e.g., CO, HCO^+, DCO^+) are

uncertain by factors $1.5 - 5.0$, those for species made of $4 - 7$ atoms are uncertain by a factor of $1.5 - 7$, and those for more complex species made of > 7 atoms are uncertain by a factor of $2 - 10$. For D/H ratios the uncertainties are, for the same different ranges of molecule sizes, a factor of $1.6 - 5$, $1.6 - 10$ and $2.5 - 10$, respectively. Furthermore, uncertainties are larger in DCs than in warm IRDCs, and also increase with the size of the molecule, owing to the propagation of uncertainties through the long chain of reactions involved in their formation.

4

ORTHO-PARA RATIOS OF H_2 AND H_3^+ IN THE DIFFUSE INTERSTELLAR MEDIUM

Adapted from Albertsson, Indriolo, Kreckel, Crabtree, Semenov & Henning (2013), ApJ, submitted [1]

4.1 ABSTRACT

The chemistry in the diffuse ISM initiates the gradual increase of molecular complexity during the life cycle of matter in galaxies. A key molecule that enables build up of new molecular bonds and new molecules via donation of a proton is H_3^+. Its evolution is tightly related to molecular hydrogen and thought to be well-understood both from a theoretical and laboratory perspective. However, recent observations of ortho and para modes of H_2 and H_3^+ in the diffuse ISM showed a puzzling discrepancy in nuclear spin excitation temperatures and population between these two key species toward many lines of sight. H_3^+, unlike H_2, seems to be out of thermal equilibrium, contrary to the predictions of modern astrochemical models. In order to analyze the chemistry of $H_3{}^+$ in detail, we conduct the first time-dependent modeling of the para-fractions of H_2 and $H_3{}^+$ in the diffuse ISM, using a state-of-the-art astrochemistry network. We compare our results to a set of line-of-sight observations, including new measurements presented in this study. We isolate a set of key reactions for the H_3^+ nuclear spin-state chemistry and find that the main mechanism that controls the ortho/para ratio for H_3^+ is the difference between the rates of destruction of of the lowest rotational states of H_3^+, (J=1, K=1) and (J=1, K=0) by DR. A plausible agreement with observations cannot be achieved, unless an equal probability for the destruction of $(1,1)-$ and $(1,0)-$form of H_3^+ is assumed. Thus our study calls for new laboratory measurements of the DR rate and branching of the key astrochemistry ion H_3^+ under the space conditions, as well as better models for time scales of diffuse interstellar clouds. Additionally, variations of individual physical parameters, such as density and chemical age, within a range of values typical of the diffuse ISM, have only a minor effect on the predicted ortho/para ratios, but we find that these small effects cumulatively improve the agreement between our model and the observations. Thus our study calls for new laboratory measurements of the DR rate and branching ratio of the key interstellar ion H_3^+ under interstellar conditions, as well as better model for the time scales of diffuse interstellar cloud evolution.

1 The review on laboratory experiments of H_3^+ DR was written by Dr. H. Kreckel. The proposal, measurements and text about the observations presented in this chapter were done by Dr. N. Indriolo. Reduction of the chemical network was done by Dmitry Semenov. Everything else in this chapter was done by me.

4.2 INTRODUCTION

H_3^+ plays a pivotal role in the gas-phase chemistry of the interstellar medium due to its very low proton affinity. The formation process via the ion-molecule reaction H_2^+ + H_2 -> H_3^+ + H is well-established (e.g. Liszt 2006) and the destruction of H_3^+ can occur via ion-molecule reactions or DR with free electrons. H_3^+ was observed in the interstellar medium by Geballe & Oka (1996) for the first time, followed by other detections (e.g. McCall et al. 1998; Geballe et al. 1999; McCall et al. 2002; Goto et al. 2008; Indriolo et al. 2007; Indriolo & McCall 2012). These observations have also revealed several unexpected results, which are summarized below.

In the simple gas-phase chemistry of H_3^+ only three parameters can strongly affect its abundance: the DR rate coefficients, the electron abundance, and the CRP ionization rate (McCall et al. 2003). The former two parameters are thought to be well constrained in the diffuse interstellar clouds (Cardelli et al. 1996; McCall et al. 2003), which left the CRP ionization rate as the only controlling parameter. McCall et al. (2003), Indriolo et al. (2007) and Indriolo & McCall (2012) observed absorption lines of H_3^+ toward several diffuse cloud sight lines, and inferred CRP ionization ratios on the order of $\sim 10^{-16}$ s^{-1}, about an order of magnitude higher than the value inferred for dark prestellar cores ($\sim 10^{-17}$ s^{-1}, see e.g. Webber 1998; van der Tak & van Dishoeck 2000; Caselli 2003; van der Tak 2006).

Interestingly, the average excitation temperature derived from the two lowest rotational states of H_3^+, $(J,K) = (1,0)$ and $(J,K) = (1,1)$, has been observed at $T(H_3^+) \approx 30$ K (Indriolo et al. 2007; Indriolo & McCall 2012), which differs significantly from that of the two lowest rotational states of H_2, $T_{01} \approx 70$ K (Rachford et al. 2002, 2009). Because the conversion between the two lowest nuclear spin states of H_2 (ortho and para) in collisions with free protons is very efficient, the H_2 ortho−para ratio is expected to be thermalized with the gas kinetic temperature. Hence, the excitation temperature derived from the relative intensities of H_2 ortho and para levels are also expected to be an accurate measure of the gas kinetic temperature in the diffuse ISM ($\approx$ 70 K). Assuming that collisional thermalization between H_3^+ and H_2 is also efficient, in previous studies by McCall et al. (2003) and Gibb et al. (2010) the nuclear spin states of H_3^+ were assumed to be in thermal equilibrium with the kinetic cloud temperature. However, in later studies the excitation temperatures of H_2 and H_3^+directly derived from observations did not agree with each other, indicating that a large population of H_3^+ is not thermalized with the diffuse ISM gas.

Crabtree et al. (2011) have investigated this discrepancy by comparing observations of the nuclear spin temperature of H_3^+ (subsequently refined by Indriolo & McCall 2012) to that of H_2 for a sample of diffuse interstellar clouds. Their results confirmed that the excitation temperature of H_3^+ and H_2 do not agree. Crabtree et al. (2011) concluded that the H_3^+ ortho/para ratio is likely governed by a competition between the collisionally-driven thermalization of H_3^+ and the DR reactions with electrons. The thermalization reaction ortho/para−H_3^+ + H_2 $\rightarrow$ ortho/para H_3^+ + H_2 has been studied experimen-

tally recently by Grussie et al. (2012). It was found that the reaction has indeed the expected thermal outcome.

From a theoretical point of view, there are more unknown factors related to the chemistry of H_3^+. Theoretical calculations have shown that the photodissociation of H_3^+ is not efficient in the diffuse interstellar medium, where H_3^+ is believed to exist in its two lowest rotational states exclusively (see e.g. van Dishoeck 1987). In the absence of other abundant molecules like CO and H_2O, this leaves DR as the only major destruction pathway for H_3^+. Recent theoretical calculations by dos Santos et al. (2007) predict the DR rate coefficient for para$-H_3^+$ at low temperature to be an order of magnitude higher than that for ortho$-H_3^+$. This claim has later been backed up by the plasma experiments of Varju et al. (2011). Meanwhile, other laboratory groups have observed a different dependence, with similar dissociation rates between the two nuclear spin states of H_3^+ (see e.g. Kreckel et al. 2005; Tom et al. 2009; Kreckel et al. 2010).

In this chapter we conduct the first time-dependent study of the ortho$-$para chemistry of H_3^+ in the diffuse interstellar medium. We isolate a set of key processes for the evolution of the ortho- and para-states of H_3^+, and we present new observational measurements to better test our model predictions. The chapter is structured as follows. In Section 4.3 we discuss the new observations. In Section 4.4 we describe the chemical and physical models utilized in the analysis of the observations. Our results and the underlying chemistry is presented and discussed in Section 4.5, followed by conclusions given in Section 4.6.

4.3 OBSERVATIONS

The sight lines toward HD 27778, HD 43384, and HD 41117 were observed on 2011 Nov 6, 2011 Dec 1, and 2012 Apr 1, respectively, using the CRyogenic high-resolution InfraRed Echelle Spectrograph (CRIRES) (Kaeufl et al. 2004) on UT1 at the VLT. Observations were performed in service mode, and CRIRES was used with its 0,¨2 slit to provide a resolving power (resolution) of about 100,000 (3 km s^{-1}), and a reference wavelength of 3715.0 nm to position the H_3^+ $R(1,1)^l$ ($\lambda = 3.715479$ μm) transition on detector 3, and the $R(1,1)^u$ ($\lambda = 3.668083$ μm) and $R(1,0)$ ($\lambda = 3.668516$ μm) transitions on detector 1. The adaptive optics system was utilized in all cases to maximize starlight passing through the narrow slit. Spectra were obtained in an ABBA pattern with 10¨ between the two nod positions and $\pm$3¨ jitter width. Total integration times for the three targets were as follows: HD 27778: 34 min; HD 43384: 12 min; HD 41117: 12 min.

Raw data images were processed using the CRIRES pipeline version 2.2.1. Standard calibration techniques, including subtraction of dark frames, division by flat fields, interpolation over bad pixels, and correction for detector nonlinearity effects, were utilized. Consecutive A and B nod position images were subtracted from each other to remove sky emission features. One-dimensional spectra were extracted from these images using the *apall* routine in IRAF[2], and

2 http://iraf.noao.edu/

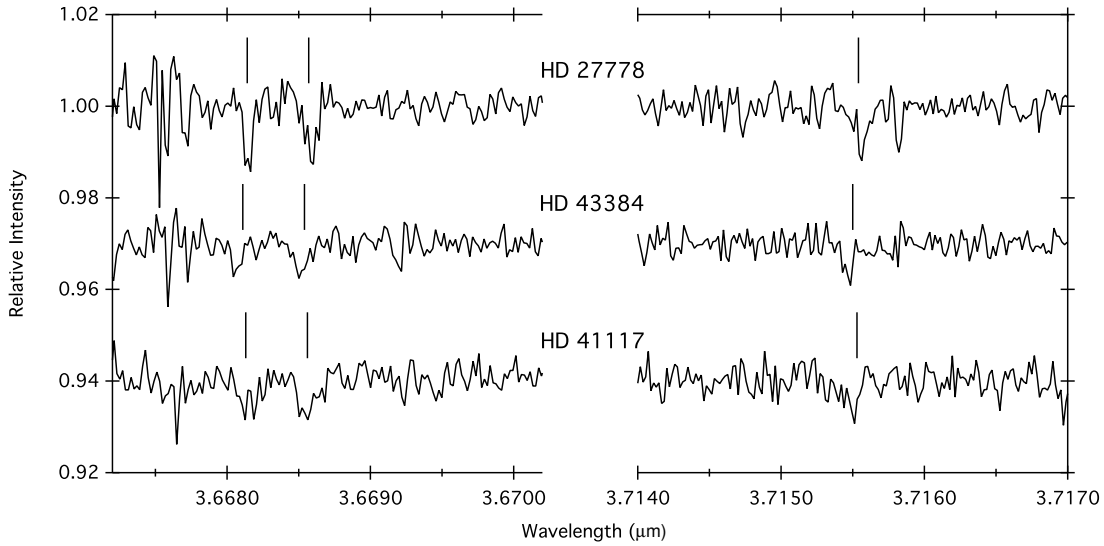

Figure 4.1: Spectra of HD 27778, HD 43384, and HD 41117 showing absorption due to the $R(1,1)^u$ and $R(1,0)$ (bottom) and $R(1,1)^l$ (top) transitions of H_3^+. Vertical lines above spectra mark the expected positions of absorption features given previously determined interstellar gas velocities.

any remaining bad pixels were interpolated over. Spectra were then imported to Igor Pro[3], and all spectra from each nod position were added together. Wavelength calibration of the summed A and summed B spectra was performed using atmospheric absorption lines (accurate to ± 1 km s^{-1}), after which the spectra from the A and B nod positions were averaged onto a common wavelength scale.[4] In order to remove atmospheric absorption features, science target spectra were divided by spectra of telluric standard stars. Resulting spectra are shown in Figure 4.1.

Absorption features due to H_3^+ were fit with Gaussian functions for the purpose of determining equivalent widths (W_λ), velocity FWHM, and interstellar gas velocities in the local standard of rest (LSR). Equivalent widths were used to compute column densities in the lower state, and the para-H_3^+ column density was then determined by taking a variance-weighted average of the values found from the $R(1,1)^u$ and $R(1,1)^l$ transitions. As we in this section will discuss our results in terms of the para−to−total ratio (para fraction), we here define these parameters for H_2 and $H_3{}^+$ as: p_2 = [para-H_2]/[H_2] and p_3 = [para-$H_3{}^+$]/[$H_3{}^+$]. All of the absorption line parameters and derived column densities are presented in Table 4.1, along with the inferred p_3 and excitation temperatures, $T(H_3^+)$. Also shown are H_2 column densities, H_2 para fractions (p_2), and T_{01} presented in Rachford et al. (2002, 2009).

3 http://www.wavemetrics.com/

4 Combination of A and B spectra is done after wavelength calibration due to a slight (about one-half pixel) shift in wavelength along the dispersion direction between the two nod positions.

Table 4.1: Absorption line parameters and derived values.

		HD 27778[a]	HD 41117[b]	HD 43384[b]
$v_{\rm LSR}$ $R(1,1)^u$	(km s^{-1})	5.2	5.7	−1.5
$v_{\rm LSR}$ $R(1,0)$	(km s^{-1})	5.9	2.5	−0.1
$v_{\rm LSR}$ $R(1,1)^l$	(km s^{-1})	6.9	2.2	−0.8
FWHM $R(1,1)^u$	(km s^{-1})	4.7	8.4	5.6
FWHM $R(1,0)$	(km s^{-1})	6.5	7.4	8.5
FWHM $R(1,1)^l$	(km s^{-1})	7.3	4.9	5.4
W_λ $R(1,1)^u$	(10^{-6} μm)	0.93±0.14	1.11±0.23	0.49±0.11
W_λ $R(1,0)$	(10^{-6} μm)	1.00±0.17	0.82±0.20	0.73±0.15
W_λ $R(1,1)^l$	(10^{-6} μm)	0.91±0.21	0.56±0.15	0.55±0.13
$N(J,K)$ $R(1,1)^u$	(10^{13} cm^{-2})	3.87±0.58	4.60±0.97	2.03±0.47
$N(J,K)$ $R(1,0)$	(10^{13} cm^{-2})	2.53±0.42	2.07±0.52	1.85±0.37
$N(J,K)$ $R(1,1)^l$	(10^{13} cm^{-2})	4.18±0.94	2.55±0.68	2.54±0.62
$N(1,1)$	(10^{13} cm^{-2})	3.96±0.22	3.22±1.45	2.22±0.36
$N(1,0)$	(10^{13} cm^{-2})	2.53±0.42	2.07±0.52	1.85±0.37
p_3		0.61±0.04	0.61±0.12	0.55±0.06
$T(H_3^+)$	(K)	29±4	29±13	38±11
$\log[N(0)]$		20.64±0.05	20.51±0.10	20.59±0.10
$\log[N(1)]$		20.27±0.10	20.22±0.10	20.54±0.18
p_2		0.70±0.05	0.66±0.07	0.53±0.12
T_{01}	(K)	56±5	60±7	74±15

H_2 data collected from (a) Rachford et al. (2002) and (b) Rachford et al. (2009).

4.4 MODEL

4.4.1 *Physical model*

We have utilized the gas-grain chemical model "ALCHEMIC" developed by Semenov et al. (2010c), where a detailed description of the code and its performance is presented. The code is optimized for modeling the time-dependent evolution of large chemical networks, including both gas-phase and surface species, and has been modified to handle the ortho−para chemistry. For initial abundances we implement the "low metal" abundances from Graedel et al. (1982) and Lee et al. (1998b).

In this work we are primarily concerned with reproducing observed ortho− and para−abundances of H_3^+ and H_2. We conduct a parametric study using our pseudo-time-dependent chemical model. For this goal, gas density, DR and CRP ionization rates, as well as initial ortho/para ratio of H_2 and chemical age, are varied within the ranges typical of the diffuse ISM, and the modeled p_2 and p_3 values are compared with the observed values.

Diffuse molecular clouds have typical densities of 10 - 100 cm^{-3}, typical extinction of $A_V = 0.5$ mag (Snow & McCall 2006b), and total CRP ionization rates $\zeta_{CRP} \approx 10^{-16}$ s^{-1} (Indriolo et al. 2007; Indriolo & McCall 2012). The lifetime of giant molecular clouds is typically in the range of several 10^7 years (McKee & Ostriker 2007), giving us an upper limit for the time scales of diffuse cloud evolution. Therefore, our cloud models are calculated within a time span of 10^6 years, but we will investigate the time effects on results for longer life times. As a "Standard" model ("S") we consider a hydrogen gas density n_H = 10 cm^{-3}, ζ_{CRP} = 10^{-16} s^{-1}, A_V = 0.5 mag, and temperatures between 10 and 100 K, adopting the H_3^+ DR rates of McCall et al. (2004). The initial ortho:para ratio is set to 1:10.

4.4.2 *Chemical network*

We used a reduced version of the chemical network developed by Albertsson et al. (2013), where only H-bearing reactions with < 4 H atoms, < 4 C atoms and molecules made of < 8 atoms are cloned. In this study we extended it to include the ortho−para states of H_2, H_2^+ and H_3^+, and related nuclear spin-state exchange processes. Reaction rates for a small number of reactions have already been measured or theoretically predicted. For this, we have added rates from several sources (Gerlich 1990; Walmsley et al. 2004b; Flower et al. 2004a; Pagani et al. 2009a; Honvault et al. 2011), including reaction rates for the H_3^+ + H_2 system by Hugo et al. (2009). For any remaining reactions involving H_2, H_2^+, or H_3^+ with unknown rates, we extracted reactions containing these species and employed a separation scheme, similar to that from Sipilä et al.

(2013b), in order to generate ortho− and para−variations of the reactions. We illustrate the process of our separation scheme with the following example:

$$\mathrm{H_3^+ + CO \rightarrow HCO^+ + H_2} \begin{cases} \mathrm{ortho-H_3^+ + CO \rightarrow HCO^+ + ortho-H_2} \\ \mathrm{para-H_3^+ + CO \rightarrow HCO^+ + ortho-H_2} \\ \mathrm{para-H_3^+ + CO \rightarrow HCO^+ + ortho-H_2} \end{cases}$$

where the left side is the original reaction, and the right shows the pathways resulting from the separation scheme. The reaction rate R is the same as the original R_{org} for the first pathway, while the reaction for para-H_3^+ has two possible sets of products, and the reaction rate is divided between the two pathways, $R_{\mathrm{org}}/2$. This branching ratio is due to spin statistics (see e.g. Crabtree & McCall 2013; Okumura et al. 2013). Contrary to Sipilä et al. (2013b), we allow reactions without $H_3{}^+$ or $H_2{}^+$ as reactants to form not only the para-H_2, but also ortho−H_2 with an energy barrier of $\gamma = 170$ K. The final network consists of 1 300 species connected by 40 000 reactions.

4.4.2.1 H_3^+ *Dissociative recombination*

One of the crucial reactions for the hydrogen chemistry in the diffuse interstellar gas is the DR of H_3^+ with free electrons:

$$\mathrm{H_3^+ + e^- \rightarrow} \begin{cases} \mathrm{H + H + H} \\ \mathrm{H_2 + H} \end{cases}$$

The DR process is one of the dominant destruction processes for H_3^+ in the environments considered here, it influences the ionization balance by removing the reactive H_3^+ ion and yielding neutral fragments. Owing to its astrophysical relevance, the DR of H_3^+ is a much-studied process, both experimentally and theoretically. The outcome of H_3^+ DR studies has varied over the years, and to date there are more than 30 published experimental rate coefficients for this reaction. Historically, there were orders of magnitude discrepancies between different experimental approaches at times, with flowing and stationary afterglow experiments resulting in substantially lower rates than storage ring experiments, which have become the prevalent method for DR studies since the early nineties. However, the afterglow experiments have been re-evaluated recently (Glosík et al. 2009), and the inclusion of ternary collisions in the analysis has led to a good overall agreement between different methods concerning the absolute scale of the low-energy rate coefficient for H_3^+. A review on the early measurements and disagreements can be found in Larsson (2000); here we will focus on the current state-of-the-art and the best rate coefficient to use for our purpose.

The commonly accepted experimental value for the absolute DR rate is given as a thermal rate coefficient in McCall et al. (2004), as a function of temperature:

$$r_{\mathrm{DR,McCall}} = -1.3 \times 10^{-8} + 1.27 \times 10^{-6} T^{-0.48} \tag{4.1}$$

The underlying measurements were carried out using a supersonic expansion ion source at the CRYRING storage ring and confirmed over a wide range of relative energies by subsequent measurements at the Test Storage Ring (TSR) in Heidelberg (Kreckel et al. 2005, 2010). However, the latest of these studies (Kreckel et al. 2010; Petrignani et al. 2011) revealed that the expansion ion source delivered much hotter ions than previously assumed, and the best characterized measurements were carried out at ∼370 K (Petrignani et al. 2011). The implications for the rate coefficient at $T < 100$ K are uncertain.

Theoretically, the DR of H_3^+ has proven difficult to describe. The classical picture of direct DR that proceeds through a curve-crossing of a dissociative state does not apply for H_3^+, and thus initial studies predicted a very low rate coefficient. This picture has changed when more modern studies in full-dimensionality became available and identified the Jahn-Teller effect as the driving force behind H_3^+ DR (Kokoouline et al. 2001; Kokoouline & Greene 2003a,b). With these major advances, the more recent calculations of dos Santos et al. (2007) agree quite well with the storage ring measurements for the absolute recombination rate, while discrepancies remain for the detailed energy-dependence (Petrignani et al. 2011). We adopt rate coefficients converted to the Kooji formulation, by adjusting the coefficients for best agreement in our temperature range of 10−100 K:

$$r_{\mathrm{DR,dosSantos}} = -1.1 \times 10^{-7} \times (T/300)^{-0.52} \tag{4.2}$$

Deviations from the original fit in this temperature range are below ∼ 20 %. The situation gets even more complicated when one considers the dependence of the DR rate on the nuclear spin of H_3^+. The calculations of dos Santos et al. (2007) predict that at $T < 100$ K the DR rate is dominated by the para-H_3^+ states and at 10 K the rate for $(1,0)-H_3^+$ is more than an order of magnitude lower than for $(1,1)-H_3^+$. These theoretical values are supported by recent afterglow results that see a similar trend (Varju et al. 2011). It should be kept in mind, though, that the calculated rate coefficient at these temperatures depends on the precise position of Rydberg resonances that are difficult to predict, and the initial calculations actually showed the opposite trend (Kokoouline & Greene 2003b).

The first measurements that showed a nuclear spin dependence of the H_3^+ DR rate were carried out at the TSR (Kreckel et al. 2005), however, only a slight enhancement of the rate for para$-H_3^+$ was seen. The same trend has been observed in more recent studies by Tom et al. (2009) and Kreckel et al. (2010). The caveat of these measurements is again the fact that the ions were probably not in their rotational ground states. More detailed studies with state-selected molecular ions are clearly desirable for this important reaction. For now, we implement both extremes in our model calculations, the almost exclusive dominance of the low-energy DR by para-H_3^+, as predicted by the calculations of dos Santos et al. (2007), and basically equal rate coefficients for $(1,0)-H_3^+$ and $(1,1)-H_3^+$, as seen in the storage ring measurements.

Furthermore, we found inconsistencies in the main public astrochemical networks related to the reaction rates of the photodissociation of $H_3{}^+$. Because $H_3{}^+$ is expected to be in the ground state in the diffuse interstellar medium,

a photon with energy $\gtrsim$ 20 eV is required for it to be photo-dissociated. This essentially means that the H_3^+ photodissociation is inactive under the ISM conditions. Theoretical modeling agrees with this (see e.g. van Dishoeck 1987; van Dishoeck et al. 2006). In the UMIST database (latest version UMIST 2012; McElroy et al. 2013b), the correct photodissociation rates for H_3^+ are incorporated. However, this rate is seven orders of magnitude higher in other databases, such as KIDA[5] and OSU[6]. Because our network is based on the recent osu.2009 network, it had an incorrect rate for the H_3^+ photodissociation on the order of $\sim 10^{-8}$ s^{-1}, which we have corrected in this study by adopting the corrected value of 5×10^{-15} s^{-1} from van Dishoeck (1987).

4.5 RESULTS

4.5.1 *Observations*

The three new detections of H_3^+ presented in this study increase the total number of diffuse cloud sight lines with measurements of column densities of the ortho and para forms of both H_3^+ and H_2 from six to nine. Two of these sight lines—HD 27778 and HD 41117[7]—were observed previously but H_3^+ was not detected (McCall et al. 2002; Indriolo & McCall 2012). Column densities in the (1,0) and (1,1) levels reported in this study are consistent with the previously reported upper limits. The newly reported values of p_3 and p_2 follow the same trend shown by the six older data points in Crabtree et al. (2011) and Crabtree & McCall (2012). This continues to demonstrate that in diffuse clouds the excitation temperatures of H_2 and H_3^+ do not agree with each other, even when both species are observed in the same line of sight. This developing trend, and the lack of an adequate explanation from simple chemical models, is part of the reason for the present study.

4.5.2 *Dominant pathways*

First, to ease our detailed analysis of the chemical processes relevant for the evolution of H_2 and H_3^+ spin states, we identify the dominant pathways in their chemistry. For that we reduce our initially huge gas-grain chemical network with surface reaction to a much smaller set of gas-phase reactions, using our "Automatic Reduction Technique" (ART) tool (see, e.g., Semenov et al. 2006). The reduced network consists of only 19 species and 112 reactions, and is accurate within $< 10\%$ in the studied parameter space for the abundances of H_2 and H_3^+ (see Table 2).

The dominant pathways include ionization by CRP particles and UV photons as well as DR and ion-molecule reactions. In comparison to Crabtree et al. (2011), who considered a much simpler chemistry, we find additional pathways

5 http://kida.obs.u-bordeaux1.fr/

6 http://www.physics.ohio-state.edu/~eric/research.html

7 Note that these sight lines are frequently referred to by the alternate identifiers 62 Tau and χ^2 Ori, respectively.

that, when combined, bear a significant effect on the resulting para-fraction values. Because of the importance that H^+ plays for the H_2 ortho−para ratios, it becomes necessary to consider the photodissocation of $H_2{}^+$, a major formation pathway of H^+. Equally important are the DR of the simple molecular ions made of H, C, O, which affects the rate of the $H_3{}^+$ DR reaction. We also find that elements heavier than oxygen do not have any impact on the hydrogen chemistry.

Much as Crabtree et al. (2011), we find that surface processes do not play a significant role in the chemistry of H_2 and H_3^+. This is because we begin our chemical simulations with hydrogen already being essentially in molecular form. The gas-phase formation of H_2 proceeds via slow neutral-neutral collisions of H atoms or ion-molecule reactions like $H_3{}^+ + O \rightarrow OH^+ + H_2$, and is not efficient.

Aside from DR reactions, there are a small number of ion-molecule reactions that aid in the removal of $H_3{}^+$. The two most notable of the less effective destruction pathways is $H_3{}^+$ reacting with OH or O, forming H_2O^+ or OH^+ respectively and H_2. As we will show below, at gas hydrogen density of ~ 10 cm^{-3} these reactions can slow down the increase in p_3, making the chemistry less steady-state.

4.5.3 *Parameter effects*

Implementation of the chemical processes as well as properties of the environment, including density, temperature, and the choice of the chemical age, are the major actors for chemical kinetics modeling. Among these factors, we find that the adopted values of the DR rates have the greatest effect on modeled abundances of ortho− and para$-H_3^+$, while the chemical age, the density, and the CRP ionization rate are less important. In our models the p_2 value is already at a quasi steady-state after $\sim 10^5$ years, which is shorter than our standard adopted chemical age of $\sim 10^6$ years. Hence, unless otherwise specified, we discuss only the time-dependent evolution of the p_3 values.

In Table 4.2 we summarize the different models used to study the effects of physical and chemical parameters. and in Figure 4.2 we show the resulting p_3 and p_2 values for our different models, varying density (model "N"), CRP ionization rate (model "C"), time (model "T") and reaction rates for the H_3^+ DR reactions (model "D"), compared to the "Standard" model (model "S"). The "S" model does not agree with the trend observed towards diffuse clouds (see Figure 4.2), but is very similar to the distribution calculated by Crabtree et al. (2011) (see their Figure 8), where they considered only the H_3^+ formation and its destruction by DR. Our models are also compared to thermalized distributions, calculated using energy levels from Lindsay & McCall (2001), and the nascent distribution, where $p_3 = 1/3 + 2/3p_2$, assuming the exclusive formation of $H_3{}^+$ from the reaction $H_2{}^+ + H_2$ using the branching ratios adopted from nuclear spin selection rules of Quack (1977) and Oka (2004), and assuming that the CRP ionization of H_2 does not affect the $H_2{}^+$ nuclear spin configuration.

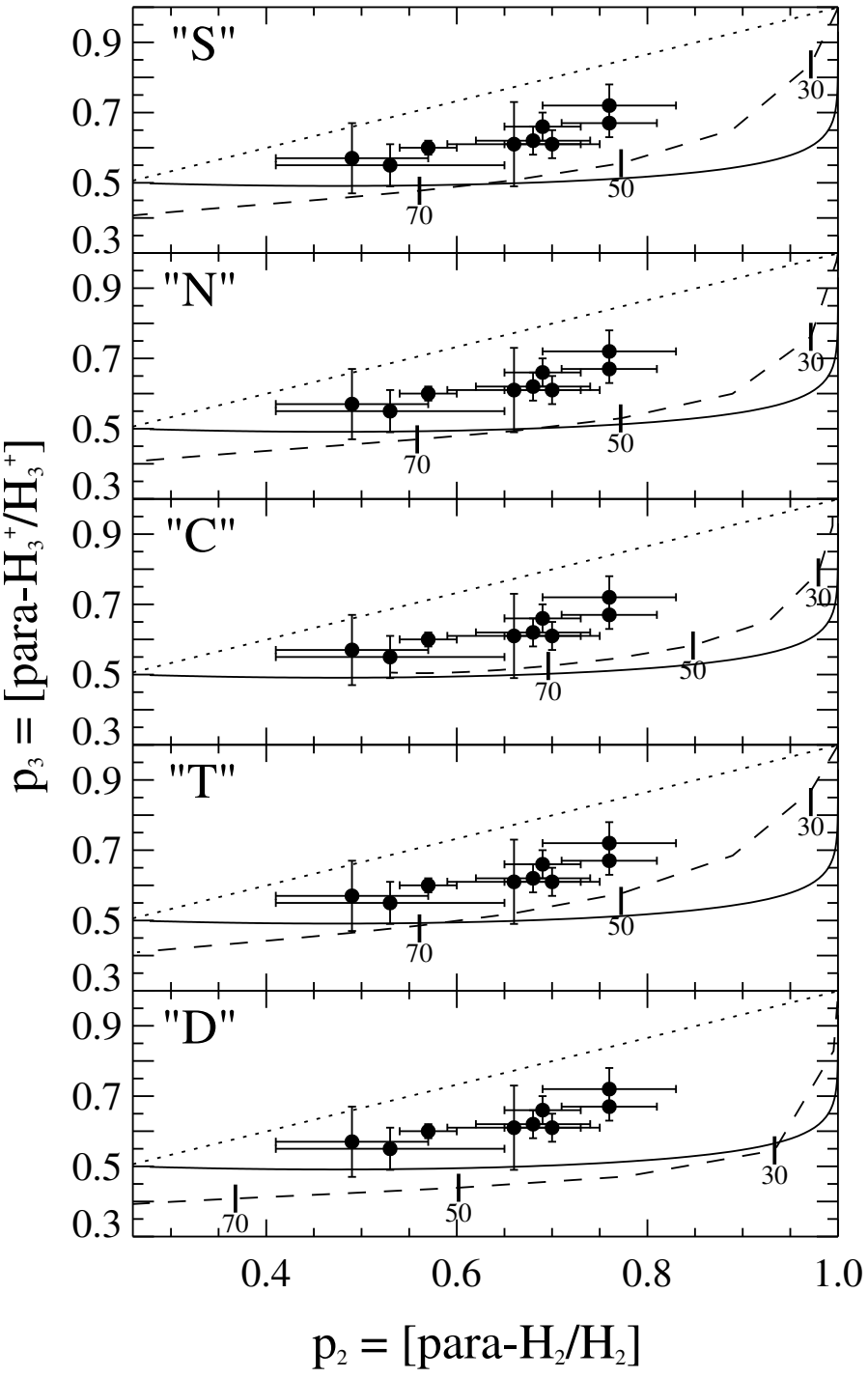

Figure 4.2: Comparison of the effects on p_3 and p_2 values from density, cosmic-ray particles ionization rate, time and Dissociative recombination reaction rates compared between our different models, calculated for kinetic temperatures 10 - 100 K. The dotted line is the nascent distribution and solid line the thermal distribution. The calculated p_2 and p_3 values at temperatures 30, 50, 70 and 90 K are marked specifically in the figures. Observation are shown with 1σ error bars.

Table 4.2: Summary of studied models.

Model	n_H [cm^{-3}]	CRP rate [s^{-1}]	Time [years]	DR rates [references]	Initial ortho:para
S	10	10^{-16}	10^6	McCall et al. (2004)	1:10
N	100	10^{-16}	10^6	McCall et al. (2004)	1:10
C	10	10^{-17}	10^6	McCall et al. (2004)	1:10
T	10	10^{-16}	10^7	McCall et al. (2004)	1:10
D	10	10^{-16}	10^6	dos Santos et al. (2007)	1:10
O	10	10^{-16}	10^6	McCall et al. (2004)	3:1
2X	10	10^{-16}	10^6	2× McCall et al. (2004)	1:10
4X	10	10^{-16}	10^6	4× McCall et al. (2004)	1:10
2X+T	10	10^{-16}	10^7	2× McCall et al. (2004)	1:10

Although the diffuse interstellar clouds are likely clumpy, they are often assumed to be homogeneous in astrochemical models. We consider two gas densities typical of diffuse ISM, 10 and 100 cm^{-3} (see Model "S" and "N"). We find that results for model "S" with a hydrogen density of 10 cm^{-3} are in better agreement with the observed values of p_3. The reason for the higher para-H_3^+ fraction with a lower density is the ionization degree of the medium, which is largely determined by $H^+$and C^+. At lower densities the neutralization of the medium through DR reactions proceeds slower, causing a higher ionization degree due to a higher H^+ abundances, however it is not enough to affect the p_2 value.

While we can not predict column densities as our models have no spatial dimension, we can compare the ratios of calculated H_3^+ / H_2 abundances to the observed column densities, which should agree unless due to extreme clumpiness. Doing this, for the final abundances at 1 Myr in model "S" and "N", our models predicts for temperatures 30 − 70 K abundances ratios H_3^+ / H_2 = $2.13 - 8.70 \times 10^{-7}$ for 10 cm^{-3} and $1.12 - 2.34 \times 10^{-7}$ for 100 cm^{-3}, while observed column density ratios are typically $\sim 10^{-7}$ (Crabtree et al. 2011; Indriolo & McCall 2012, and this study). This means that modeled abundances for the gas density 100 cm^{-3} agree better with the observed H_3^+ / H_2 ratios, but is still not in agreement with predicted p_3 values. The values from 10 cm^{-3} is still within uncertainty limits. It also becomes clear that the temperature has a larger effect on abundances at 10 cm^{-3} than at 100 cm^{-3}, considering the predicted wide range of abundances for the 10 cm^{-3} model.

Decreasing the CRP ionization rate to $\zeta = 10^{-17}$ s^{-1} (model "C") has only a small effect on p_3 values, but significantly increases p_2 values. In Figure 4.3 we show the evolution of p_2 values as a function of time for two separate temperatures, 30 K (grey lines) and 70 K (black lines). At 30 K the p_2 values do not change significantly in either of model "S" and "C", as they are initiated close to the thermalized value at 30 K. However, at 70 K it is evident that the

environment takes longer time to reach its thermalized in the "C" model. is initiated with its thermalized ortho/para value. The lower CRP ionization rate slows down the production of H^+, the essential thermalization coreactant of H_2 and this delays the time the environment reaches the thermalized ortho/-para ratio. However, these results are affected by the initial p_2 value. If we would initiate the environment with statistical ortho/para ratio of 3:1 (p_2 = 0.25), the situation would be the opposite and it would take longer to reach the thermalized value at 30 K, while at 70 K there would be no significant change.

This means that the results are strongly time-dependent, and the steady-state p_2 values have not changed, but merely the process of reaching the steady-state values is slowed down. The calculated *para*−fractions become independent of the modeling assumptions on longer time scales at $\gtrsim 10^7 - 10^8$ years. Typical H_3^+ / H_2 values are in the range $1.31 - 2.30 \times 10^{-7}$, approximately a factor $\sim$ 2-3 lower than the "S" model, because the production of H_3^+ depends on the ionization of H_2.

In the "S" model the p_2 value does not vary significantly after $\sim 10^5$ years. But in order to fully evaluate this statement we also reran our "S" model with the statistical ortho:para ratio of 3:1 ("O" model). . The initial ortho/para H_2 ratio does not affect strongly our modeling results within a time frame of $\sim 10^6$ years, see Figure 4.3. Note however that the diffuse ISM model considered in this study requires approximately 1 Myr in order for the standard ionization degree of 10^{-16} s^{-1} to reset the ortho:para ratios of H_2, while longer time scales were necessary for a lower ionization degree, as discussed above. If the initial fraction of hydrogen in H_2 is lowered, and is instead put in H^+, the diffuse ISM is not initially neutral, and this timescale is shortened. Effects on H_3^+ / H_2 from varying the initial H_2 ortho/para ratio are small, $< 10\%$.

Since the modeled ortho−para H_3^+ abundances have not reached steady-state by the chemical age of 10^6 years, we study how p_3 evolves at later times, up to 10^7 years (model "T"). In general, the p_3 values increase with temperature and the temperature distribution slowly approaches the nascent distribution. However, this process appears to require an unrealistic amount of time exceeding 10^8 years, and even longer for model "N" with a hydrogen density of 100 cm^{-3}. It is clear however that after $\sim 10^7$ years the p_3 distribution is approaching an agreement with the observations. Furthermore, the H_3^+ abundances decrease, and at 10^7 years the H_3^+ / H_2 ratio drops to $2.76 - 7.37 \times 10^{-7}$.

The total rate and branching ratios for the DR of (1,0)− and (1,1)−$H_3{}^+$ greatly affects the modeled p_3 values (see Figure 4.2). In model "D" we compare the p-values of $H_3{}^+$ and H_2 for the chemical models adopting a branching ratios of ∼1:15, as predicted from dos Santos et al. (2007), for the ortho:para H_3^+ DR. There are clear differences between the various models and the observed values, with the largest discrepancy arising at temperatures $\lesssim$ 60 K, which are typical representative temperatures of the diffuse ISM (Snow & McCall 2006b). The H_3^+ DR process with a preferred destruction of $(1,1)-H_3{}^+$ results in p_3 values that are lower than the thermalized distribution at temperatures $>$ 30 K. The p_3 values continues to decrease with time. As we adjust the DR branching ratio for (1,0)− and (1,1)−H_3^+ towards unity, the overall p_3 values increase,

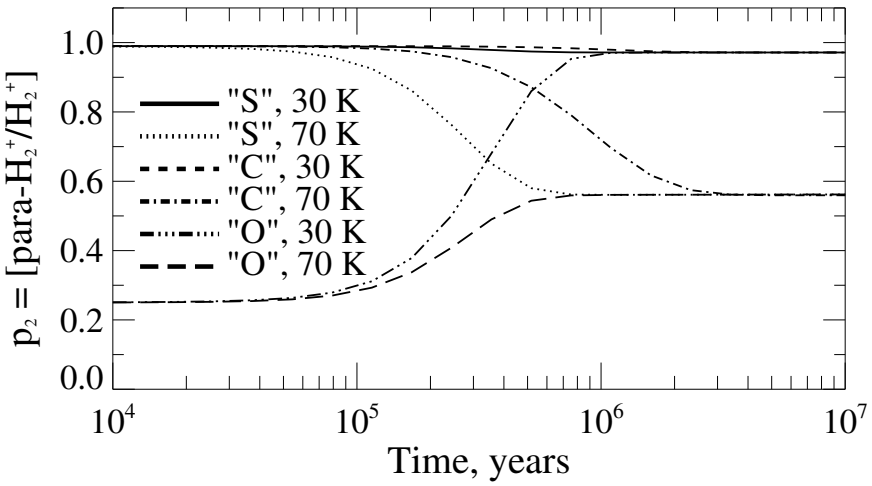

Figure 4.3: Evolution of p_2 with time. Results from the "S" model is shown in the solid line, the "C" model in dotted and the "O" model in dashed. Calculated p_2 values for 30 K are shown in gray and for 70 K in black.

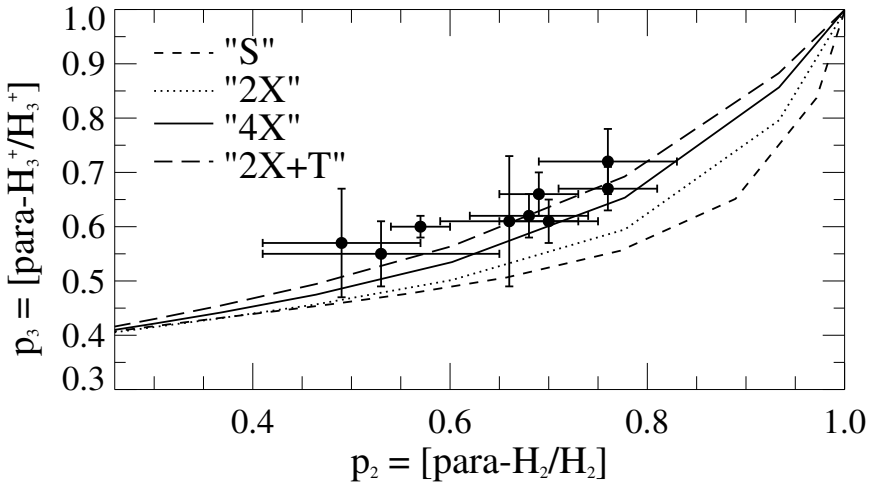

Figure 4.4: The p_3 and p_2 values calculated with the standard chemical model for 1 Myr (dashed line) for temperatures of 10 - 100 K, with variation in the total Dissociative recombination reaction rates increase by a factor 2 (dotted line, model "2X") and factor 4 (solid line, model "4X"), and finally an increase of the total Dissociative recombination rate by a factor 2 at 10^7 years (long dash line, model "2X+T"). The calculated p_2 and p_3 values at temperatures 30, 50, 70 and 90 K are marked specifically in the figures. Observation are shown with error bars.

most notably at low temperatures, and approximately at a ratio of $1:5$ the time dependence is reversed, and the p_3 values begin to slowly increase with time. The key conclusion is that an DR branching ratio of $\sim 1:1$ for $(1,1)-$ and $(1,0)-H_3^+$ is necessary in order to reproduce the observed distributions. We note that the precision in values for the rate coefficient does not play a

significant role as long as the branching ratio is lower than $\sim$ 1:5. Furthermore, the H_3^+ / H_2 ratios in the "D" model are not significantly affected by variations in the DR branching ratio as values are similar to those predicted for the "S" model.

From this, it is clear that the increased DR rate of ortho$-H_3^+$ improves the fit to observations, but the question remains if a higher total DR rate can also affect results, while the relative rate between $(1,1)-$ and $(1,0)-H_3^+$ remains the same. In Figure 4.4 we compare the results of increasing the total DR rate in the "S" model by a factor 2 (dotted line, model "2X") and 4 (solid line, model "4X"). This significantly improves the fit, but an increase by a factor $\sim$ 4 is necessary to bring our predicted p_3 values to agree with observations, which is higher than what laboratory experiments indicates. Because the H_3^+ abundance is strongly affected also by the DR rate, the H_3^+ / H_2 ratio decreases by a similar factor of $\sim$ 2 and $\sim$ 4 for the same increase in the total DR rate, respectively. The H_3^+ / H_2 ratio drops to values similar to the observed values at $\sim 10^{-7}$. It means that an increased total DR rate also has the added benefit of improving the agreement to the calculations of the H_3^+ column densities.

However, a high total DR rate will cause the time effect to be more significant, hence we have also added the distribution for a model with increased total DR rate by a factor 2 at 10^7 years (see Figure 4.4, long dashed line, model "2X+T"). The additional longer time scale of $\sim 10^7$ years improves our fit further as the distribution goes through the observed points. Furthermore, the total H_3^+ abundance decreases further, and at 10^7 years H_3^+ / H_2 = $(1.41 - 2.62) \times 10^{-7}$.

4.6 CONCLUSIONS

We publish the results of three new sight lines towards diffuse clouds, where both H_3^+ and H_2 have been observed in their ortho and para forms. The new observations follow the same trend as found by Crabtree et al. (2011), lying between the nascent and thermalized distribution, from which they concluded that H_3^+ is not fully thermalized as the thermalization by reactions with H_2 is competing with destruction by DR of H_3^+.

To study this in more detail, we conducted the first time-dependent modeling of the nuclear spin-states of H_2 and $H_3{}^+$ in the diffuse interstellar medium, and compared our results to the observed values, including the new measurements. We find that the initial H_2 ortho/para ratio and CRP ionization rate have no substantial effect on our predicted p_3 distributions. However, a decreased CRP ionization rate increases p_2 values too much, such that H_2 excitation temperatures are too high compared to observed values, hence we find that higher CRP ionization rates of $\sim 10^{-16}$ s^{-1} are favored by our models. The gas density also affects the rate at which the modeled p_3 distribution approaches the observed data points, and we conclude that these diffuse clouds likely have densities of $\sim$ 10 cm^{-3}.

We found that the DR of H_3^+ is a key process that governs the p_3 values. Our model indicates that a branching ratio of $\sim$ 1 between the $(1,1)$- and $(1,0)$-H_3^+ dissociation is needed to achieve an agreement with the observations. The

remaining studied parameters, n_H, time and total DR rates will increase the pace at which the p_3 values approach the nascent distribution by a smaller, but significant amount. Our model favors a gas hydrogen density of ~ 10 cm^{-3} as a representative value for the diffuse ISM, in the lower range of diffuse ISM densities (Snow & McCall 2006b). It allows the p_3 distribution to agree with the observed distribution within a reasonable time frame $< 10^8$ years. Finally, we find that an increase of the total DR rate by a factor of 2, along with a time scale of 10^7 years give us an excellent agreement with observations. We find that our predicted H_3^+ / H_2 values match that from the observed column densities well within an order of magnitude, where the largest effect of our predicted values comes from the adopted density and CRP ionization rate.

We conclude that the best fit to observations is achieved for a density of 10 cm^{-3}, CRP ionization rate 10^{-16} s^{-1}, a 1:1 DR branching ratio, a total DR rate similar to that predicted by dos Santos et al. (2007), and finally a time scale of $\sim 10^7$ years (model "2X+T"). However, the models used in this study have no spatial dimension and it is likely that these diffuse clouds are clumpy, which may affect distributions as well as column densities.

It is evident that better estimates of DR processes are vital if we are to better understand the ortho−para hydrogen chemistry in the diffuse ISM. For that, one has to bring in agreement the laboratory results on the DR of H_3^+ obtained with various experimental setups, such as the storage ring experiments (Kreckel et al. 2005; Tom et al. 2009; Kreckel et al. 2010), and the afterglow experiments (e.g. Glosík et al. 2009). Therefore, we highly recommend new accurate studies of the H_3^+ DR reactions, in order to both determine the absolute DR rate as well as the nuclear spin dependence for the lowest rotational states.

Table 4.3: The dominant reactions for the hydrogen chemistry in the diffuse ISM. Values in parenthesis are exponential factors. Errors are defined as values for a log-normal distribution, with standard deviation $k\pm$ error. Errors marked with an asterisk (*) are resulting from our separation scheme to generate ortho-para reactions, and uncertainties are taken from the original reaction, but are likely higher.

Reaction			α	β	γ	Error
H + CRP	$\rightarrow$	$H^+ + e^-$	0.46	0	0	2.00
oH_2 + CRP	$\rightarrow$	$H^+ + H + e^-$	0.02	0	0	2.00*
pH_2 + CRP	$\rightarrow$	$H^+ + H + e^-$	0.02	0	0	2.00*
oH_2 + CRP	$\rightarrow$	$oH_2^+ + e^-$	0.93	0	0	2.00*
pH_2 + CRP	$\rightarrow$	$pH_2^+ + e^-$	0.93	0	0	2.00*
oH_2 + CRP	$\rightarrow$	H + H	0.10	0	0	2.00*
pH_2 + CRP	$\rightarrow$	H + H	0.10	0	0	2.00*
He + CRP	$\rightarrow$	$He^+ + e^-$	0.50	0	0	2.00
C + CRP	$\rightarrow$	$C^+ + e^-$	1.02 (3)	0	0	2.00
O + CRP	$\rightarrow$	$O^+ + e^-$	2.80	0	0	2.00

Reaction			α	β	γ	Error
C + UV	→	$C^+ + e^-$	0.22 (−9)	0	2.61	2.00*
oH_2 + UV	→	H + H	0.34 (−10)	0	2.50	2.00*
pH_2 + UV	→	H + H	0.34 (−10)	0	2.50	2.00*
oH_2^+ + UV	→	H^+ + H	0.26 (−9)	0	1.80	2.00*
pH_2^+ + UV	→	H^+ + H	0.26 (−9)	0	1.80	2.00*
OH + UV	→	O + H	0.17 (−9)	0	1.66	2.00*
OH^+ + UV	→	H^+ + O	0.72 (−11)	0	1.80	2.00*
H^+ + O	→	O^+ + H	0.70 (−9)	0	2.32 (2)	1.50
H^+ + OH	→	OH^+ + H	0.16 (−7)	−0.50	0	2.00
oH_2^+ + H	→	H^+ + oH_2	0.64 (−9)	0	0	1.25*
pH_2^+ + H	→	H^+ + pH_2	0.64 (−9)	0	0	1.25*
oH_2^+ + O	→	OH^+ + H	0.15 (−8)	0	0	2.00*
pH_2^+ + O	→	OH^+ + H	0.15 (−8)	0	0	2.00*
oH_2^+ + OH	→	H_2O^+ + H	0.76 (−9)	0	0	2.00*
pH_2^+ + OH	→	H_2O^+ + H	0.76 (−9)	0	0	2.00*
oH_2^+ + OH	→	OH^+ + oH_2	0.76 (−9)	0	0	2.00*
pH_2^+ + OH	→	OH^+ + pH_2	0.76 (−9)	0	0	2.00*
H_2O^+ + oH_2	→	H_3O^+ + H	0.61 (−9)	0	0	1.25*
H_2O^+ + pH_2	→	H_3O^+ + H	0.61 (−9)	0	0	1.25*
H_2O^+ + OH	→	H_3O^+ + O	0.69 (−9)	0	0	2.00
oH_3^+ + O	→	OH^+ + oH_2	0.80 (−9)	−0.16	1.41	1.41*
pH_3^+ + O	→	OH^+ + oH_2	0.40 (−9)	−0.16	1.41	1.41*
pH_3^+ + O	→	OH^+ + pH_2	0.40 (−9)	−0.16	1.41	1.41*
oH_3^+ + OH	→	H_2O^+ + oH_2	0.95 (−8)	−0.50	0	2.00*
pH_3^+ + OH	→	H_2O^+ + oH_2	0.47 (−8)	−0.50	0	2.00*
pH_3^+ + OH	→	H_2O^+ + pH_2	0.47 (−8)	−0.50	0	2.00*
He^+ + H	→	H^+ + He	0.19 (−14)	0	0	1.25
He^+ + oH_2	→	oH_2^+ + He	0.96 (−14)	0	0	2.00*
He^+ + pH_2	→	oH_2^+ + He	0.64 (−14)	0	0	2.00*
He^+ + pH_2	→	pH_2^+ + He	0.32 (−14)	0	0	2.00*
He^+ + oH_2	→	H^+ + H + He	0.11 (−12)	−0.24	0	2.00*
He^+ + pH_2	→	H^+ + H + He	0.11 (−12)	−0.24	0	2.00*
He^+ + OH	→	O^+ + H + He	0.85 (−8)	−0.50	0	2.00
O^+ + H	→	H^+ + O	0.70 (−9)	0	0	1.50
O^+ + oH_2	→	OH^+ + H	0.16 (−8)	0	0	1.25*
O^+ + pH_2	→	OH^+ + H	0.16 (−8)	0	0	1.25*
O^+ + OH	→	OH^+ + O	0.36 (−9)	0	0	2.00

Reaction			α	β	γ	Error
$OH^+ + oH_2$	$\rightarrow$	$H_2O^+ + H$	0.11 (−8)	0	0	1.25*
$OH^+ + pH_2$	$\rightarrow$	$H_2O^+ + H$	0.11 (−8)	0	0	1.25*
$OH^+ + OH$	$\rightarrow$	$H_2O^+ + O$	0.70 (−9)	0	0	2.00
$H + OH$	$\rightarrow$	$O + oH_2$	0.69 (−13)	2.80	1.70 (2)	2.00*
$H + OH$	$\rightarrow$	$O + pH_2$	0.69 (−13)	2.80	1.95 (3)	2.00*
$oH_2 + O$	$\rightarrow$	$OH + H$	0.34 (−12)	2.67	3.16 (3)	3.16*
$pH_2 + O$	$\rightarrow$	$OH + H$	0.34 (−12)	2.67	3.16 (3)	3.16*
$H + O$	$\rightarrow$	OH	0.99 (−18)	−0.38	0	10.0
$oH_2^+ + e^-$	$\rightarrow$	$H + H$	0.16 (−7)	−0.43	0	2.00*
$pH_2^+ + e^-$	$\rightarrow$	$H + H$	0.16 (−7)	−0.43	0	2.00*
$H_2O^+ + e^-$	$\rightarrow$	$OH + H$	0.86 (−7)	−0.50	0	1.25
$H_2O^+ + e^-$	$\rightarrow$	$O + H + H$	0.30 (−6)	−0.50	0	1.25
$H_2O^+ + e^-$	$\rightarrow$	$O + oH_2$	0.39 (−7)	−0.50	1.70 (2)	1.25*
$H_2O^+ + e^-$	$\rightarrow$	$O + pH_2$	0.39 (−7)	−0.50	0	1.25*
$oH_3^+ + e^-$	$\rightarrow$	$oH_2 + H$	0.12 (−7)	0	0	2.00*
$pH_3^+ + e^-$	$\rightarrow$	$oH_2 + H$	0.94 (−7)	0	0	2.00*
$pH_3^+ + e^-$	$\rightarrow$	$pH_2 + H$	0.94 (−7)	0	0	2.00*
$oH_3^+ + e^-$	$\rightarrow$	$H + H + H$	0.36 (−7)	0	0	2.00*
$pH_3^+ + e^-$	$\rightarrow$	$H + H + H$	0.56 (−6)	0	0	2.00*
$H_3O^+ + e^-$	$\rightarrow$	$OH + oH_2$	0.60 (−7)	−0.50	1.70 (2)	1.25*
$H_3O^+ + e^-$	$\rightarrow$	$OH + pH_2$	0.60 (−7)	−0.50	0	1.25*
$H_3O^+ + e^-$	$\rightarrow$	$oH_2 + H + O$	0.56 (−8)	−0.50	1.70 (2)	1.25*
$H_3O^+ + e^-$	$\rightarrow$	$pH_2 + H + O$	0.56 (−8)	−0.50	0	1.25*
$H_3O^+ + e^-$	$\rightarrow$	$OH + H + H$	0.26 (−6)	−0.50	0	1.25
$OH^+ + e^-$	$\rightarrow$	$O + H$	0.63 (−8)	−0.48	0	1.25
$C^+ + e^-$	$\rightarrow$	C	0.44 (−11)	−0.61	0	1.50
$H^+ + e^-$	$\rightarrow$	H	0.35 (−11)	−0.70	0	2.00
$oH_2^+ + e^-$	$\rightarrow$	oH_2	0.22 (−6)	−0.40	0	2.00*
$pH_2^+ + e^-$	$\rightarrow$	oH_2	0.11 (−6)	−0.40	0	2.00*
$pH_2^+ + e^-$	$\rightarrow$	pH_2	0.11 (−6)	−0.40	0	2.00*
$oH_3^+ + O$	$\rightarrow$	$H_2O^+ + H$	0.34 (−9)	−0.16	1.41	1.41*
$pH_3^+ + O$	$\rightarrow$	$H_2O^+ + H$	0.34 (−9)	−0.16	1.41	1.41*
$H + H$	$\rightarrow$	oH_2	0.50 (−16)	0.50	1.70 (2)	2.00*
$H + H$	$\rightarrow$	pH_2	0.50 (−16)	0.50	0	2.00*
$C + h\nu_{CRP}$	$\rightarrow$	$C^+ + e^-$	1.02 (3)	0	0	2.00
$H + h\nu_{CRP}$	$\rightarrow$	$H^+ + e^-$	0.46	0	0	2.00
$He + h\nu_{CRP}$	$\rightarrow$	$He^+ + e^-$	0.50	0	0	2.00

Reaction			α	β	γ	Error
$O + h\nu_{CRP}$	$\rightarrow$	$O^+ + e^-$	2.80	0	0	2.00
$oH_2 + h\nu_{CRP}$	$\rightarrow$	$H + H$	0.10	0	0	2.00*
$pH_2 + h\nu_{CRP}$	$\rightarrow$	$H + H$	0.10	0	0	2.00*
$oH_2 + h\nu_{CRP}$	$\rightarrow$	$H^+ + H + e^-$	0.02	0	0	2.00*
$pH_2 + h\nu_{CRP}$	$\rightarrow$	$H^+ + H + e^-$	0.02	0	0	2.00*
$oH_2 + h\nu_{CRP}$	$\rightarrow$	$oH_2^+ + e^-$	0.93	0	0	2.00*
$pH_2 + h\nu_{CRP}$	$\rightarrow$	$pH_2^+ + e^-$	0.93	0	0	2.00*
$H_3O^+ + H$	$\rightarrow$	$H_2O^+ + oH_2$	0.61 (−9)	0	1.70 (2)	2.00*
$C + H^+$	$\rightarrow$	$C^+ + H$	1.00 (−14)	0	0	2.00
$He^+ + OH$	$\rightarrow$	$OH^+ + He$	0.20 (−9)	−0.50	0	2.00
$pH_2^+ + oH_2$	$\rightarrow$	$pH_3^+ + H$	0.14 (−8)	0	0	2.00
$pH_2^+ + oH_2$	$\rightarrow$	$oH_3^+ + H$	0.70 (−9)	0	0	2.00
$pH_2^+ + pH_2$	$\rightarrow$	$pH_3^+ + H$	0.21 (−8)	0	0	2.00
$oH_2^+ + pH_2$	$\rightarrow$	$pH_3^+ + H$	0.14 (−8)	0	0	2.00
$oH_2^+ + pH_2$	$\rightarrow$	$oH_3^+ + H$	0.70 (−9)	0	0	2.00
$oH_2^+ + oH_2$	$\rightarrow$	$oH_3^+ + H$	0.14 (−8)	0	0	2.00
$oH_2^+ + oH_2$	$\rightarrow$	$pH_3^+ + H$	0.70 (−9)	0	0	2.00
$H^+ + pH_2$	$\rightarrow$	$H^+ + oH_2$	0.20 (−8)	0	1.67 (2)	2.00
$H^+ + oH_2$	$\rightarrow$	$H^+ + pH_2$	0.11 (−9)	0	0	2.00
$pH_3^+ + pH_2$	$\rightarrow$	$pH_3^+ + oH_2$	0.82 (−9)	0	1.65 (2)	2.00
$pH_3^+ + pH_2$	$\rightarrow$	$oH_3^+ + oH_2$	0.59 (−9)	0	1.98 (2)	2.00
$pH_3^+ + oH_2$	$\rightarrow$	$pH_3^+ + pH_2$	0.30 (−9)	0	0	2.00
$pH_3^+ + oH_2$	$\rightarrow$	$oH_3^+ + pH_2$	0.35 (−9)	0	0	2.00
$pH_3^+ + oH_2$	$\rightarrow$	$oH_3^+ + oH_2$	0.80 (−9)	0	32.60	2.00
$oH_3^+ + pH_2$	$\rightarrow$	$pH_3^+ + oH_2$	0.15 (−8)	0	1.36 (2)	2.00
$oH_3^+ + pH_2$	$\rightarrow$	$oH_3^+ + oH_2$	0.88 (−8)	0	1.70 (2)	2.00
$oH_3^+ + oH_2$	$\rightarrow$	$pH_3^+ + pH_2$	0.10 (−9)	0	0	2.00

5

CHEMO-DYNAMICAL DEUTERIUM FRACTIONATION IN THE EARLY SOLAR NEBULA: THE ORIGIN OF WATER ON EARTH AND IN ASTEROIDS AND COMETS.

Adapted from Albertsson, Semenov & Henning (2013), ApJ, submitted [1]

5.1 ABSTRACT

Formation and evolution of water in the Solar System and the origin of water on Earth constitute one of the most interesting questions in astronomy. The prevailing hypothesis for the origin of water on Earth is by delivery through water-rich small Solar system bodies. In this paper, the isotopic and chemical evolution of water during the early history of the solar nebula, before the onset of planetesimal formation, is studied. A gas-grain chemical model that includes multiply-deuterated species and nuclear spin-states is combined with a steady-state solar nebula model. To calculate initial abundances, we simulated 1 Myr of evolution of a cold and dark TMC1-like prestellar core. Two time-dependent chemical models of the solar nebula are calculated over 1 Myr: (1) a laminar model and (2) a model with 2D turbulent mixing. We find that the radial outward increase of the H_2O D/H ratio is shallower in the chemo-dynamical nebular model compared to the laminar model. This is related to more efficient de-fractionation of HDO via rapid gas-phase processes, as the 2D mixing model allows the water ice to be transported either inward and thermally evaporated or upward and photodesorbed. The laminar model shows the Earth water D/H ratio at $r \lesssim 2.5$ AU, while for the 2D chemo-dynamical model this zone is larger, $r \lesssim 9$ AU. Similarly, the water D/H ratios representative of the Oort-family comets, $\sim 2.5 - 10 \times 10^{-4}$, are achieved within $\sim 2 - 6$ AU and $\sim 2 - 20$ AU in the laminar and the 2D model, respectively. While the H_2 ortho:para ratio in molecular clouds is uncertain we also studied the impact of the initial abundance by adjusting the TMC-1 H_2 ortho:para ratio to the statistical value 3:1. As an extreme case, we found that this can reduce D/H ratios by up to an order of magnitude at radii ~ 10 AU. This does not affect our predictions for carbonaceous chondrites or in the outer regions of the solar nebula $\gtrsim 30$ AU, but allows Jupiter-family comets to have formed in a larger zone of the solar nebula. We find that with regards to the water isotopic composition and the origin of the comets, the mixing model seems to be favored over the laminar model.

1 Reduction of the chemical network as well as all model runs and figures were prepared by Dmitry Semenov. Everything else was done and written by me.

5.2 INTRODUCTION

Water is one of the most abundant molecules detected in interstellar space, found throughout all stages of the stellar evolution, from prestellar cores till PPDs. The ultimate role of liquid water for the origin of life on Earth is well recognized in biochemistry and astronomy (e.g., Kasting et al. 1993; Hoover 2006; Costanzo et al. 2009; Javaux & Dehant 2010; Lis et al. 2013). One of the main difficulties in tracing the origin of the Earth water is strong evidence that it came from exogenous sources, since the solar nebula was too hot in the terrestrial planet-formation zone to form water-rich planetesimals from smaller icy precursors (Boss 1998; Morbidelli et al. 2000; Min et al. 2011; Elser et al. 2012). In addition, no evidence for hydrous silicates in the inner regions of PPDs has been found (Juhász et al. 2010).

The most promising mechanism of water delivery to Earth is bombardment by carbonaceous asteroids and/or comets that have formed in the ice-rich, outer region of the young Solar System (e.g. Oró 1961; Owen et al. 1992; Morbidelli et al. 2000; Robert 2011; Izidoro et al. 2013). This idea is supported by modern sophisticated dynamical models of the early Solar System, which show that complex gravitational interactions between Jupiter and Saturn had likely scattered other small bodies into the inner and far outer regions (see e.g. Morbidelli et al. 2005; Gomes et al. 2005; Tsiganis et al. 2005; Walsh et al. 2012). More evidence of the Solar System's dynamical past comes from the presence of crystalline silicates annealed at temperatures above 800 K in cometary samples collected by the *Stardust* mission (Wozniakiewicz et al. 2012) and revealed by infrared observations of comets (e.g. Crovisier et al. 1997; Kelley et al. 2006) suggests that transport or highly energetic local processes occurred in the solar nebula. The importance of dynamical activity of the young solar nebula and PPDs on its chemical and isotopic evolution was also demonstrated in numerous theoretical studies (e.g. Morfill & Voelk 1984; Cyr et al. 1998; Aikawa & Herbst 1999a; Gail 2001; Ilgner et al. 2004; Boss 2004; Willacy et al. 2006; Tscharnuter & Gail 2007; Willacy 2007; Willacy & Woods 2009; Semenov & Wiebe 2011; Heinzeller et al. 2011a; Wozniakiewicz et al. 2012).

The individual contributions from particular exogenous sources is still heavily debated. Water has likely formed on surfaces of dust grains even before the formation of the solar nebula in the protosolar molecular cloud and inherited specific isotopic composition and ortho/para ratios from that epoch (e.g., Jørgensen & van Dishoeck 2010; Cazaux et al. 2011; Taquet et al. 2013b), which may have been preserved in primitive Solar System bodies such as comets. It is plausible to assume though that the water isotopic composition (and may be even the ortho/para ratio) could have been partly or fully reset during the violent physical conditions in the inner, dynamically active solar nebula (e.g., Robert et al. 2000; Boss 2004). Other processes such as grain growth and sedimentation have shown to bear a profound effect on the water abundance and deuterium fractionation (Fogel et al. 2011; Vasyunin et al. 2011; Akimkin et al. 2013). The importance of the ortho- and para-states of H_2 for deuterium fractionation is well established and also has to be taken into account (e.g., Flower et al. 2006).

The water D/H ratio remains the most essential probe for disentangling the individual contributions from the various exogenous sources. Since comets are reservoirs of pristine material in the solar nebula, a comparison of the water D/H ratios measured in comets and asteroids to that measured in PPDs is vital. These observations are challenging because most of the water is frozen out onto dust grains in disks around cool Sun-like stars (Dominik et al. 2005; Bergin et al. 2010; Hogerheijde et al. 2011). Furthermore, disks have relatively compact sizes ($\lesssim 100 - 1000$ AU) and are not massive ($\lesssim 0.01 M_{\odot}$). Therefore, detailed high-resolution studies remain a challenge. Ground-based observations are further compromised by the absorption and veiling of water vapor lines in the Earth atmosphere. In order to better understand the origin of water on Earth, other Solar System bodies, and possibly in other exoplanetary systems, one has to study the chemical evolution of water prior and during the onset of planet formation.

The water evolution begins in prestellar cores, where the low temperatures cause many molecules to freeze-out onto grains, and the gas remains largely void of molecules (Caselli et al. 2010). This drives a rich surface-chemistry along with an efficient deuterium fractionation, resulting in high water abundances on the grains ($\sim 10^{-4}$ relative to H) and D/H ratios ($\sim 10^{-2}$). As the cores contracts, and begins to heat up, volatiles are released into the gas. Water has been detected towards several class o protostellar objects (e.g. Ceccarelli et al. 1999; Kristensen et al. 2010; Visser et al. 2013; Mottram et al. 2013), but only a few detections of HDO (and D_2O) have allowed determination of D/H ratios, with values$\sim 10^{-4}$ in the hot cores, and retaining $\sim 10^{-2}$ in the cold outer regions (Jørgensen & van Dishoeck 2010; Liu et al. 2011; Coutens et al. 2012; Persson et al. 2013; Taquet et al. 2013a; Coutens et al. 2013).

Several detections of water have been done in PPDs (e.g. Pontoppidan et al. 2005; Meeus et al. 2010; Bergin et al. 2010; Fedele et al. 2012), including also several using *PACS/Herschel* (Hogerheijde et al. 2011; Tilling et al. 2012; Fedele et al. 2012; Herczeg et al. 2012; Riviere-Marichalar et al. 2012) within the WISH program (Water In Star-forming Regions with Herschel van Dishoeck et al. 2011). In particular, hot water vapor ($\gtrsim 500$ K) has been discovered in the inner, planet-forming regions of PPDs around young solar-mass T Tauri stars, mainly, by infrared spectroscopy with the *Spitzer* satellite (Carr & Najita 2008; Pontoppidan et al. 2008, 2010; Najita et al. 2011; Teske et al. 2011; Banzatti et al. 2012).

The first detection of the ground transition of HDO in absorption in the disk around DM Tau was reported by Ceccarelli et al. (2005). Although they have not observed H_2O, Ceccarelli et al. (2005) predicted water D/H ratios of > 0.01, based on H_2O measurements in molecular clouds and protostellar envelopes. This discovery was later disputed by Guilloteau et al. (2006). Qi et al. (2008) have derived upper limits for the water column densities in the disk around TW Hya, $\lesssim 9.0 \times 10^{14}$ cm^{-2}, but were not able to determine its D/H ratio.

The discovery of the ground-state rotational emission of both spin isomers of H_2O from the outer, $\gtrsim 50 - 100$ AU disk around TW Hya with *Herschel* allowed to derive a water abundance of $\approx 10^{-7}$ relative to H_2 (Hogerheijde et al. 2011). The authors also derived a water ortho/para ratio of 0.77 ± 0.07,

which indicates that the water formation took place on cold dust grains with temperatures $\sim 10-20$ K. In contrast, the water ortho/para ratios measured in comets are indicative of higher temperatures of $\sim 25-50$ K, more typical for the inner solar nebula at $\lesssim 20-30$ AU (Mumma et al. 1987; Woodward et al. 2007; Bockelée-Morvan et al. 2009; Shinnaka et al. 2012; Bonev et al. 2013).

Studies of carbonaceous chondrites have revealed that their phyllosilicates have D/H ratios that are very similar to that in the Earth's ocean water, $\sim 1.56\times 10^{-4}$, with as large overall water content as $\lesssim 20\%$, thus favoring asteroids as the main water source (e.g., Owen et al. 1992; Hoover 2006; Marty 2012; Alexander et al. 2012). Since observations of Oort-family comets have yielded water D/H ratios in their comae of about 2-3 times higher that in the Earth' oceans (Robert et al. 2000, and references therein), and because of the low amount of volatile noble gases on Earth (e.g., Marty et al. 2012), it was concluded that comets contributed at most up to $\sim 10\%$ to the water delivery on Earth. However, recent HDO observation of the short-period, Jupiter-family comet Hartley-2 with *Herschel* by Hartogh et al. (2011) revealed a water D/H ratio of 1.6×10^{-4}, which is very close to the Earth value. Additionally, Lis et al. (2013) studied the Jupiter-family comet 45P/Honda-Mrkos-Pajdusakova but could not detect HDO with an upper water D/H ratio 2×10^{-4}. Their upper limit is still consistent with the value found by Hartogh et al. (2011) and aids in confirming the diversity of D/H ratios between different comet populations. These observations have reignited again debates about the relative role of asteroids and comets in the origin of the Earth water. One has to bear in mind, however, that a major problem could be that the gases in cometary comae may have lower D/H ratios compared to the D/H ratios of the nucleus, as indicated by experiments of Brown et al. (2012).

While we have made many advances in our understanding in regards of the origin of Earth's oceans, we still do not fully understand the reprocessing of water during the PPD stage, nor is there any consensus for contribution from the various exogenous sources. In this paper, we focus on the history and evolution of the early solar nebula and investigate the chemistry of frozen and gaseous water at the stage when planetesimals have not yet formed, and the micron-sizes dust grains were the dominant population of solids. We use an extended gas-grain chemical model that includes multiply-deuterated species, high-temperature reactions, surface reactions, and nuclear spin-states processes. This network is combined with a 1+1D steady-state α-viscosity nebula model to calculate molecular abundances and D/H ratios within the first 1 Myr of its lifetime. We consider both the laminar case with chemistry not affected by dynamics and a model with 2D turbulent mixing transport. The organization of the paper is the following. In Section 5.3 we describe our physical and chemical model of the solar nebula and introduce the considered deuterium processes. The results are presented in Sect. 5.4, followed by Discussion and Conclusions.

5.3 MODEL

5.3.1 *Physical model*

We used a similar disk structure as in Semenov & Wiebe (2011), but adopted parameters characteristic of the young Sun and early solar nebula. The physical model is based on a 1+1D steady-state α-model of a flaring PPD described by D'Alessio et al. (1999), see Fig. 5.1. We used the parametrization of Shakura & Sunyaev (1973) of the turbulent viscosity ν in terms of the characteristic scale height $H(r)$, the sound speed $c_s(r,z)$, and the dimensionless parameter α:

$$\nu(r,z) = \alpha\, c_s(r,z)\, H(r). \tag{5.1}$$

From observations and detailed MHD modeling the α parameter has values $\sim 0.001 - 0.1$ (Andrews & Williams 2007; Guilloteau et al. 2011; Flock et al. 2011). A constant value of $\alpha = 0.01$ was used in our simulations. Equal gas and dust temperatures were assumed.

The central star has a mass of $1 M_\odot$, a radius of $1.2 R_\odot$, and an effective temperature of 6 000 K. The non-thermal FUV radiation from the young Sun is represented by the interstellar radiation field of Draine (1978), with the un-attenuated intensity at 100 AU of $\chi_*(100) = 10\,000\ \chi_{\rm draine}$. For the X-ray luminosity of the young Sun we adopted a typical value for T Tauri stars, 10^{30} erg s^{-1}. The model disk has an inner radius of 0.03 AU (dust sublimation front, $T \approx 1\,600$ K), an outer radius of 800 AU, and an accretion rate of $\dot{M} = 10^{-8}\, M_\odot\, {\rm yr}^{-1}$. The mass of the solar nebula disk is not well-known but studies suggest it to be $\gtrsim 0.1$ M$_\odot$ (see e.g. Ruzmaikina et al. 1993; Desch 2007), and hence we adopt a disk model with a total mass of $M = 0.11\, M_\odot$.

We assume that the dust grains are uniform spherical particles, with a radius of $a_{\rm d} = 0.1\,\mu$m, made of amorphous silicates with olivine stoichiometry, with a density $\rho_d = 3$ g cm^{-3} and a dust-to-gas mass ratio $m_{d/g} = 0.01$. The surface density of sites is $N_s = 1.5 \times 10^{15}$ sites cm^{-2}, and the total number of sites per each grain is $S = 1.885 \times 10^6$. No substantial grain growth is assumed in this early disk phase, an assumption which may be challenged in other studies.

In our simulations we assume that gas-phase species and dust grains are well mixed and coupled, and transported with the same diffusion coefficient

$$D_{\rm turb}(r,z) = \nu(r,z)/Sc, \tag{5.2}$$

where $Sc = 1$ is the Schmidt number that describes the efficiency of turbulent diffusivity (see e.g. Shakura & Sunyaev 1973; Schräpler & Henning 2004). We treat diffusion of mantle materials similarly to gas-phase molecules, without relating it to individual grain dynamics.

As boundary conditions for mixing, we assume that there is no inward and outward diffusion across boundaries of the solar nebula, and that there is no flux through its central plane. All the equations are solved on a non-uniform staggered grid consisting of 65 radial points (from 0.5 to 800 AU) and 91 vertical points.

The physical structure of the solar nebula and the chemical model with and without turbulent mixing are used to solve chemical kinetics equations (see

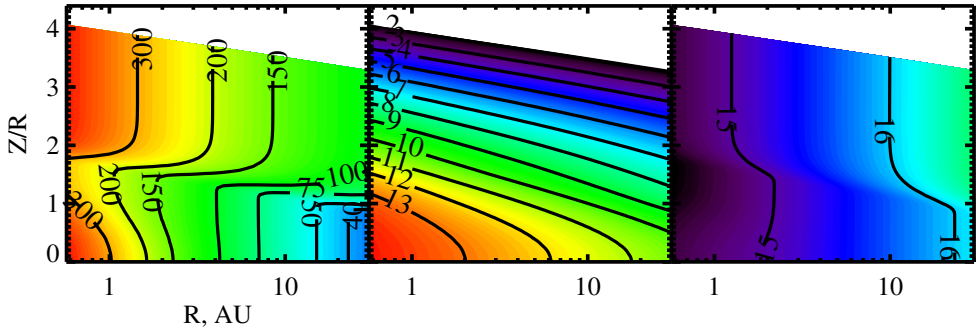

Figure 5.1: (Left to right) Distributions of temperature in K, density in cm^{-3} (log_{10} scale), and diffusion coefficient in $cm^2\,s^{-1}$ (log_{10} scale) in the solar nebula model.

Eq. 3 in Semenov & Wiebe 2011). The equations of chemical kinetics are integrated together with the diffusion terms in the Eulerian description, using a fully implicit 2D integration scheme, and a sparse matrix formalism for inversion of the Jacobi matrices (Semenov et al. 2010a).

5.3.2 *Chemical network and model*

To calculate photoreaction rates through the various disk environments, we adopt precomputed fits of van Dishoeck et al. (2006) for a 1D plane-parallel slab, using the Draine far-UV interstellar radiation field. The self-shielding of H_2 from photodissociation is calculated by Equation (37) from Draine & Bertoldi (1996) and the shielding of CO by dust grains, H_2, and its self-shielding are calculated using the precomputed table of Lee et al. (1996). We do not take the Ly_α radiation into account.

We used the gas-grain chemical network developed by Albertsson et al. (2013), which includes an extended list of fractionation reactions for up to triply-deuterated species. In addition, the high-temperature reaction network from Harada et al. (2010, 2012) has been added. Recently, it was realized that the ortho/para ratio of H_2 and other species can lower the pace of deuterium fractionation (Flower et al. 2006; Pagani et al. 2009b). The internal energy of ortho-H_2 is higher than that of para-H_2, which helps to overcome the barrier of the backward reaction of deuterium enrichment. Consequently, it results in a lower degree of deuterium fractionation in a medium having a sufficient amount of ortho-H_2 (Flower et al. 2006). Given the importance of the ortho/-para ratios of H_2 and H_3^+ for efficiency of deuterium fractionation, particularly, in the solar nebula regions with $T \gtrsim 15 - 30$ K, the nuclear spin-state processes and ortho-para states of H_2, H_2^+ and H_3^+ were added to our chemical network.

Reaction rates for a small number of reactions have already been measured or theoretically predicted. For this, we have added rates from several sources (Gerlich 1990; Walmsley et al. 2004a; Flower et al. 2004b; Pagani et al. 2009b; Honvault et al. 2011), including reaction rates for the $H_3^+ + H_2$ system by Hugo et al. (2009). In order to include the nuclear spin states of any reactions including H_2, H_2^+, H_3^+, or any of their isotopologues, we employed a separation

Table 5.1: Initial abundances for the models (fractional abundances).

Species	Abundances	Species	Abundances
p-H_2	4.783×10^{-1}	CH_4 (ice)	5.832×10^{-6}
He	9.750×10^{-2}	N_2	5.135×10^{-6}
o-H_2	2.146×10^{-2}	O_2 (ice)	4.619×10^{-6}
H	2.681×10^{-4}	O	2.661×10^{-6}
H_2O (ice)	7.658×10^{-5}	N_2 (ice)	2.464×10^{-6}
CO (ice)	5.219×10^{-5}	C_3H_2 (ice)	6.493×10^{-6}
CO	1.816×10^{-5}	HD	1.479×10^{-5}
HNO (ice)	3.541×10^{-6}	O_2	9.645×10^{-6}
HDO (ice)	2.887×10^{-6}	NH_3 (ice)	8.663×10^{-6}
D	2.731×10^{-6}	OH	2.295×10^{-6}

scheme similar to that described in Sipilä et al. (2013c). This routine will be adopted and evaluated in Albertsson et al. 2013, in prep. Contrary to Sipilä et al. (2013c), we allow reactions without H_3^+ or H_2^+ as reactants to form both ortho- and para-H_2, since we are interested in modeling chemistry in the inner warm nebula region. The size of the original network was reduced to facilitate the performance of our 2D chemo-dynamical model by allowing fractionation only for species with < 4 hydrogen atoms, < 4 carbon atoms, and species not larger than 7 atoms.

We find that the inclusion of the high-temperature reactions can increase the abundance of HDO and H_2O by up to a factor of 2 inside the snow line ($\lesssim 2-3$ AU). In contrast, the reduction of the original network to $\sim$ 39 000 reactions and $\sim$ 1 300 species bears only insignificant effect on the calculated time-dependent abundances of the H_2O isotopologues.

We also added neutral-neutral reactions. The pre-exponential rate factors were calculated using a simple collisional theory and the reactions barriers are adopted from Lécluse & Robert (1994). The added neutral-neutral reactions are listed below:

$$\begin{aligned}
\text{HDO} + p\text{-}H_2 &\Rightarrow \text{H}_2\text{O} + \text{HD}; && 2.0\times10^{-10}\ \text{cm}^{-3}\ \text{s}^{-1},\ 5170\ \text{K}\\
\text{HDO} + o\text{-}H_2 &\Rightarrow \text{H}_2\text{O} + \text{HD}; && 2.0\times10^{-10}\ \text{cm}^{-3}\ \text{s}^{-1},\ 5000\ \text{K}\\
\text{H}_2\text{O} + \text{HD} &\Rightarrow \text{HDO} + p\text{-}H_2; && 5.0\times10^{-11}\ \text{cm}^{-3}\ \text{s}^{-1},\ 4840\ \text{K}\\
\text{H}_2\text{O} + \text{HD} &\Rightarrow \text{HDO} + o\text{-}H_2; && 1.5\times10^{-10}\ \text{cm}^{-3}\ \text{s}^{-1},\ 4840\ \text{K}
\end{aligned}$$

We find however that the addition of these reactions has no significant effect on our results. For initial abundances we model the chemical evolution of a cold and dark TMC 1-like prestellar core for 1 Myr using the "low metals" initial abundance set from Lee et al. (1996, Table 11), with an initial H_2 ortho:para ratio 1:100, as most H_2 exist in para-form in cold environments, temperature 10 K, density 10^4 cm^{-3} and extinction $A_V = 10$ mag. We note that the initial H_2 ortho:para plays an essential role here, as it affects the deuterium chemistry,

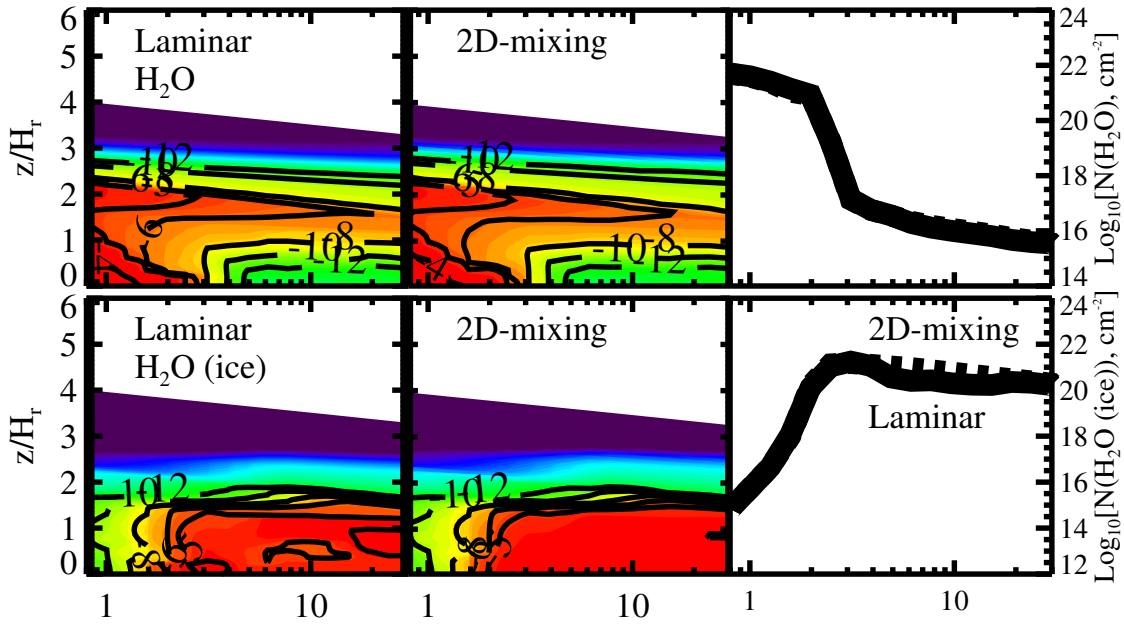

Figure 5.2: The distributions of gaseous (upper row) and solid (bottom row) water abundances (wrt total H) in the solar nebula between 0.8 and 30 AU at 1 Myr. The laminar model is shown on the left panel, the 2D-mixing model is shown in the middle panel. The vertically integrated column densities are compared in the right panel, with the laminar model depicted by solid line and the 2D-mixing model depicted by dashed lines. The thickness of these lines correspond to intrinsic uncertainties in the calculated abundances and thus column densities.

and adopting the statistical 3:1 ortho:para for H_2 as initial abundance for our TMC 1 model, ice HDO abundances drop by a factor of 10, and gas HDO abundances by a factor 20. Gas and ice H_2O are not significantly affected. The most abundant species in the initial abundances are listed in Table 5.1.

5.4 RESULTS

Our main set of chemical simulations consists of the two runs: (1) the laminar nebular model without transport processes, and (2) the 2D-mixing model with $Sc = 1$. The water abundance is limited by the initial oxygen abundance in the models and change throughout the disk. Given the rapid, $\sim 2-3$ Myr, dynamical evolution of solids in the nebula, we modeled chemistry only within 1 Myr.

In Figure 5.2 we show the gas- and solid-phase water abundances between 0.8 and 30 AU for the laminar (left panel) and the 2D-mixing model (middle panel). D/H ratios from column densities are shown in the right panel. Column densities vary strongly with scale height. Both the laminar and 2D-mixing show similar relative abundances of water (with respect to H) vapor going from 10^{-5} close to the midplane and quickly dropping to $< 10^{-12}$ at

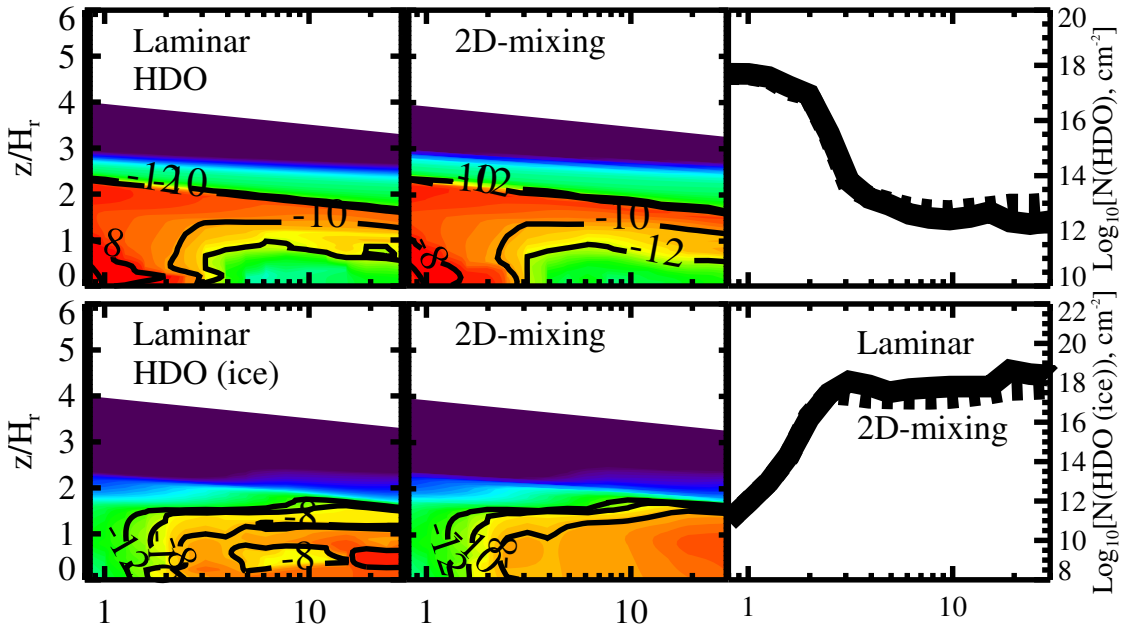

Figure 5.3: The same as Fig. 5.2 but for HDO.

around 0.15 scale heights in the inner regions, while in the outer regions relative abundances in the cold midplane are $\sim 10^{-12}$, increasing to $\sim 10^{-6}$ at 0.15 scale heights and then dropping again to $< 10^{-12}$ at ~ 0.4 scale heights. Also for water ice the two models show similar the relative abundances, with only smaller differences arising in the outer region ~ 10 AU. In the warm inner regions relative abundances are $\sim 10^{-8} - 10^{-6}$ in the midplane, dropping $< 10^{-12}$ at ~ 0.15 scale heights. Further out in the disk, beyond the snow line at $\sim 2-3$ AU, a thick layer of abundant ices with relative abundances $\sim 10^{-4}$ stretches between 0.15 up to 0.3 scale heights, after which we see again a quick drop with relative abundances going below 10^{-12}. The calculated vertical column densities for both models are compared in the right panel.

The same panels are shown in Figure 5.3 for HDO. Here layers of different relative abundances are more clear, with relative abundances of HDO vapor in the inner disk of $\sim 10^{-10}$, dropping quickly $< 10^{-12}$ at 0.15 scale heights. In the outer regions we have a low vapor abundance in the midplane of $\sim 10^{-14} - 10^{-12}$, increasing up to 10^{-10} in the molecular layer and then at around 0.2 scale heights dropping $< 10^{-12}$. For HDO ice both models show relative abundances $\sim 10^{-12}$ in the inner region and a thick layer of abundances $\sim 10^{-8}$ between 0.15 - 0.3 scale heights in the outer regions. While the 2D-mixing model show a smooth decline in abundances towards the inner disk, the laminar model show larger variations, especially evident at $5-30$ AU. As can be clearly seen, the snow line is not affected by slow diffusive transport and is located at $\sim 2-3$ AU in both models, thus leaving dust grains in the Earth-formation zone barren of ices. Hence, the water delivery to Earth could occur only at a later stage, when dust grains were assembled to larger planetesimals that were able to reach 1 AU without complete loss of volatile materials.

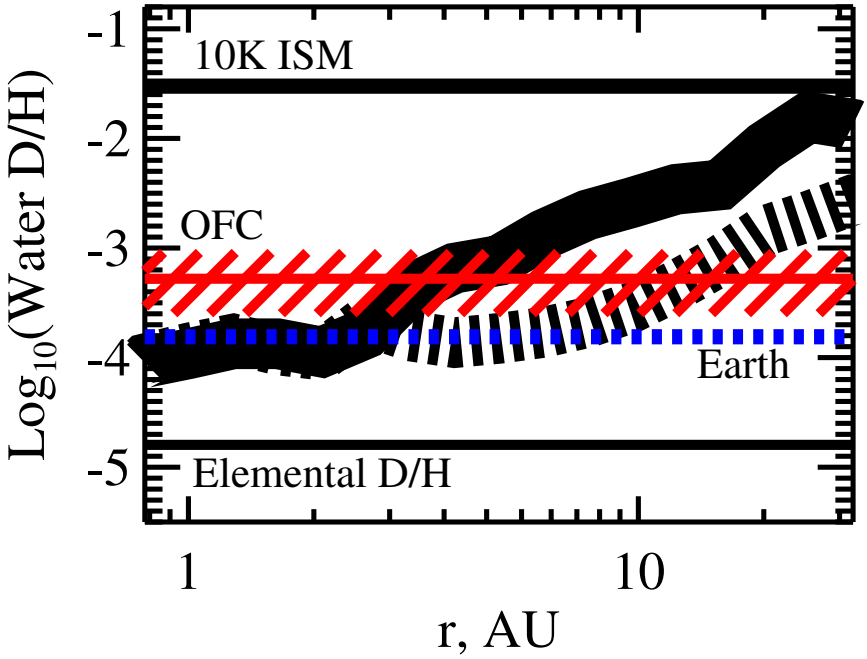

Figure 5.4: The radial distributions of the D/H ratios of the total water budget in the solar nebula between $1-30$ AU at 1 Myr are shown, both for the the laminar (solid line) and the 2D-mixing model (thick dashed line). The thickness of these lines reflects the uncertainties in the calculated water abundances, a factor of ~ 2 (Vasyunin et al. 2008a). The elemental D/H ratio of 1.5×10^{-5} is indicated by the thin straight solid line in the bottom (Stancil et al. 1998; Linsky 2003). The D/H ratio for water in the cold interstellar medium, 3×10^{-2}, is depicted by the thick solid line on the top (our model). The Earth ocean's water D/H ratio, 1.59×10^{-4} (Lecuyer et al. 1998), is marked by the straight blue dashed line. The water D/H ratios in the Oort-family comets, which are a few times higher than the Earth value, are shown with the red rectangle filled with lines and denoted by "OFC" on the plot (see Table 5.2).

The resulting distribution of the D/H ratio for the total water budget (ice + vapor) is shown in Figure 5.4. The water D/H ratio of the Earth' oceans and the measured value in carbonaceous meteorites ("Earth") are shown for comparison, also similar to what observed in Jupiter-family comets. The D/H ratios for the Oort-family comets ("OFC") are also indicated.

As can be clearly seen, the laminar model shows the Earth water D/H ratio at $0.8-2.5$ AU, while for the 2D chemo-dynamical model such a low D/H value extends towards larger radii, $\lesssim 9$ AU. Similarly, the elevated water D/H ratios representative of the Oort-family comets, $\sim 2.5-10 \times 10^{-4}$, are achieved within $\sim 2-6$ AU and $\sim 2-20$ AU in the laminar and the 2D model, respectively. The reason for this behavior is a shallower radial gradient of the water D/H ratio in the 2D mixing model. Turbulent mixing slowly transports some of the water ice into warmer or irradiated regions where it desorbs and is

quickly de-fractionated by ion-molecule and dissociative recombination processes in the gas phase. As a consequence, lower water D/H ratios can be retained further out in the nebula, which seems to be more consistent with the delivery of water on Earth by comets. Both the laminar and the mixing nebular models have the Earth' oceans and the Jupiter-family comets' water D/H ratios at radii $\sim 2-3$ AU, where carbonaceous chondrites are believed to have formed. Thus both the laminar and dynamical nebular model can reproduce the water D/H ratios observed in carbonaceous asteroids. With regard to the water isotopic composition and the origin of the Jupiter-family and Oort-family comets, the mixing model seems to be favored over the laminar model. It allows for a larger region for their formation with the appropriate water D/H ratios, extending to the distance of $\sim 10-30$ AU.

We have also studied how other processes may affect the results of our chemical modeling. First, given observational evidence for the presence of bigger grains in PPDs (e.g. Testi et al. 2003; van Boekel et al. 2005; Rodmann et al. 2006; Bouwman et al. 2008; Pérez et al. 2012), for reviews see Natta (2008); Henning & Meeus (2011), we have increased the uniform grain sizes to 1 and 10μm and calculated the nebular water D/H ratios. The average 1μm and 10μm grain sizes imply 10 and 100 times smaller surface area (per unit volume of gas), respectively, making gas-grain interactions less prominent, and allowing the high-energy radiation to penetrate deeper into the disk. The thermal desorption rates are independent of the grain size, while the cosmic-ray particle (CRP)-desorption rate depends on the grain size only weakly (Leger et al. 1985). The overall photodesorption rate increases because the nebula becomes more UV-transparent.

In contrast, the accretion rate on to the grains decreases when the total grain surface area per unit gas volume decreases. Consequently, in the inner warm nebular region at $r \lesssim 10-20$ AU the amount of gaseous water increases by a factor of ~ 10 for $a_{\rm dust} = 1\mu$m and ~ 100 for $a_{\rm dust} = 10\mu$m, respectively, but it still constitutes only a tiny fraction of the total water budget. As a result, the water D/H ratio is not significantly affected and the three modeled D/H radial distributions are within the uncertainties of the calculated D/H values (see Vasyunin et al. 2008a; Albertsson et al. 2013). The same is found for the nebular model with the standard grains but 100 times lower UV-desorption yield of 10^{-5}.

Next, we studied how the calculated water D/H ratios are affected if only a limited set of the nuclear spin-state processes is included in our chemical network. For that test we calculated a model in which only the para states of H_2, H_2^+, and H_3^+ isotopologues were considered, implying more efficient deuterium isotope exchange. The water D/H ratios calculated with this model coincide with the ratios calculated with our standard model with ortho/para-species (within the factor of ~ 3 in intrinsic chemical uncertainties).

This result is a combination of two extreme situations. First, the initial abundances are calculated using the physical conditions of a dark, dense, 10 K cloud core. At such conditions almost the entire H_2 population exists in the lowest energy para-state, and the isotope exchange reactions involving ortho-species are still out of equilibrium. This leads to similar values of the initial

water D/H ratio. Second, in the water de-fractionation zone in the nebula, at $r \lesssim 10 - 30$ AU, temperatures are higher than 30 K. These temperatures are high enough to enable rapid gas-phase de-fractionation regardless of the dominant nuclear spin-state form of H_2, H_2^+, and H_3^+, mainly due to X-ray- and CRP-driven reprocessing of CO by He^+, followed by rapid gas-phase production of H_2O. This combination of effects leads to the somewhat surprising result that a reduced network produce roughly the same abundances as the complete network.

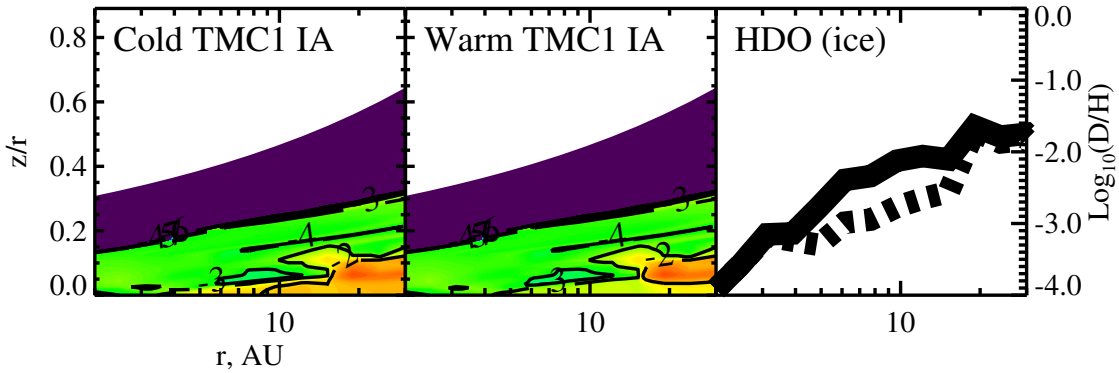

Figure 5.5: The distributions of solid HDO D/H ratios in the solar nebula between 0.8 and 30 AU at 1 Myr. The 'cold" TMC-1 initial abundance model is shown on the left panel and the "warm" model is shown in the middle panel. The vertically integrated column densities are compared in the right panel, with the "cold" TMC-1 initial abundance model depicted by solid line and "cold" model depicted by dashed lines. The thickness of these lines correspond to intrinsic uncertainties in the calculated abundances and thus column densities.

The initial H_2 ortho:para ratio in cold dark clouds is unknown, and the warmer protostellar phase has processed it above the typical cold value where H_2 only exists in its para state. As such the ortho:para ratio can be closer to the statistical ortho:para ratio of 3:1 in the initial phase of the PPD. We take the statistical value 3:1 as the upper extreme of the H_2 ortho:para ratio and initiate another run of the static model with initial abundances resulting from a TMC-1 model with an initial 3:1 ortho:para ratio for H_2. This is not a likely case, but will give us estimates on the upper limits that the ortho-para chemistry from the previous stages might have on the water ice abundances and D/H ratios.

In Figure 5.5 we show the D/H ratios of solid-phase HDO between 0.8 and 30 AU for the laminar using our previous "cold" TMC-1 initial abundance (left panel) and "warm" TMC-1 initial abundance (middle panel), and in the right panel the D/H ratio determined from column densities is shown. In the disk midplane there are small but significant differences where D/H ratios have droops from $\sim 10^{-2}$ down to $\sim 10^{-4} - 10^{-3}$ around 10 AU. This cause the column density D/H ratios in the right panel to drop approximately an order of magnitude while the minimum and maximum D/H ratios remain unchanged at ~ 1 AU and $\gtrsim 30$ AU, respectively. Thus our conclusion that carbonaceous

asteroids formed at 2-3 AU will inherit Earth water-like D/H ratios remains valid. The fact that the H_2O D/H ratio gets lower at intermediate radii ($\sim$ 10 AU) will only help us to achieve a larger zone where Hartley-2-like comets with the Earth water D/H ratio could form, while still leaving a zone for the Oort comets to form at $\sim$ 10 AU.

Finally, we discuss the effects of the underlying chemistry on the D/H ratios throughout the disk. In the midplane, temperatures are low enough to drive a rich surface chemistry, where O atoms are adsorbed on the grain surfaces and become hydrogenated, forming H_2O, and/or reacting with deuterium atoms to form HDO or D_2O. There is a small chance for the water molecules to be released into the gas-phase directly through chemisorption, but more likely they remain on the grains and desorb as material is transported into warmer regions, i.e. the inner regions or the atmosphere, where water, and its D/H ratio, will be reprocessed.

The reprocessing of water occurs in the gas phase, so the relative adsorption and desorption plays an important role. These processes are heavily effected by temperature and density. In the warmer regions, the water abundances steadily increase by $\lesssim$ 30% during the first 10 000 - 100 000 years. As soon as the water reaches the gas-phase, it is reprocessed. After that, the abundances of water ice and water vapor are at quasi steady-state. However, constant evaporation and re-accretion result in cycling of water between solid and gaseous phases. One important fact is that the D/H ratio never drops to the cosmic ratio, even in the warm, inner regions within a few AU of the Sun. In the inner solar nebula there are several important processes at work that sets the D/H ratio. First of all these regions experience strong X-ray or CRP-ionization and water is either ionized or protonated by reacting with various abundant ions, such as H_3^+, HCO^+, and their isotopologues:

$$
\begin{aligned}
&H_2O + o\text{–}H_3^+ \Rightarrow H_3O^+ + o\text{–}H_2; && 4.5 \times 10^{-9}\ \mathrm{cm^{-3}\ s^{-1}} && \beta = -0.5\\
&H_2O + p\text{–}H_3^+ \Rightarrow H_3O^+ + o\text{–}H_2; && 2.3 \times 10^{-9}\ \mathrm{cm^{-3}\ s^{-1}} && \beta = -0.5\\
&H_2O + p\text{–}H_3^+ \Rightarrow H_3O^+ + p\text{–}H_2; && 2.3 \times 10^{-9}\ \mathrm{cm^{-3}\ s^{-1}} && \beta = -0.5\\
&H_2O + HCO^+ \Rightarrow H_3O^+ + CO; && 2.1 \times 10^{-9}\ \mathrm{cm^{-3}\ s^{-1}} && \beta = -0.5
\end{aligned}
$$

And equivalent for HDO protonated into H_2DO^+. The H_3O^+ isotopologues can then reform water through dissociative recombination, but the D/H ratios will be reset, characteristic of the temperature in the environment at which they are reforming:

$$
\begin{aligned}
&H_3O + e^- \Rightarrow H_2O + H; && 1.1 \times 10^{-7}\ \mathrm{cm^{-3}\ s^{-1}} && \beta = -0.5\\
&H_2DO + e^- \Rightarrow H_2O + D; && 7.3 \times 10^{-8}\ \mathrm{cm^{-3}\ s^{-1}} && \beta = -0.5\\
&H_2DO + e^- \Rightarrow HDO + H; && 7.3 \times 10^{-8}\ \mathrm{cm^{-3}\ s^{-1}} && \beta = -0.5
\end{aligned}
$$

The reprocessing of water involves several additional reactions that compete in both lowering and increasing the D/H ratio. In the warm inner nebular region the normal H_3^+ fractionation pathway is not active and instead fractionation is driven mostly via the "warm" fractionation route that includes light hydrocarbons such as CH_2D^+ and C_2HD^+ and is active at $T \lesssim 80$ K (e.g., Millar et al.

1989; Roueff et al. 2005; Parise et al. 2009). Consequently, the initially high D/H ratios of light hydrocarbons, $\sim 10^{-3}$, is not fully equilibrated with the cosmic D/H ratio of $\sim 10^{-5}$. Neutral-neutral reactions of these hydrocarbons with atomic or molecular oxygen are able to produce normal or heavy water, e.g.:

$$CH_3 + O_2 \Rightarrow HCO + H_2O; \quad 1.66 \times 10^{-12}\ cm^{-3}\ s^{-1} \tag{5.3}$$

Another important channel of the water formation in the gas-phase is through the neutral-neutral reaction with OH or OD of H/D or *ortho*/*para*$-H_2$/HD:

$OH + H \Rightarrow H_2O;$	$4.0 \times 10^{-18}\ cm^{-3}\ s^{-1}$	
$OH + D \Rightarrow HDO;$	$4.0 \times 10^{-18}\ cm^{-3}\ s^{-1}$	
$OD + H \Rightarrow HDO;$	$4.0 \times 10^{-18}\ cm^{-3}\ s^{-1}$	
$OH + o/p{-}H_2 \Rightarrow H_2O + H;$	$8.4 \times 10^{-13}\ cm^{-3}\ s^{-1}$	1040 K
$OH + HD \Rightarrow HDO + H;$	$4.2 \times 10^{-13}\ cm^{-3}\ s^{-1}$	1040 K
$OH + HD \Rightarrow H_2O + D;$	$4.2 \times 10^{-13}\ cm^{-3}\ s^{-1}$	1040 K

While OH/OD, *ortho*/*para*$-H_2$/HD and H/D are formed through various processes, including the dissociation of water, the D/H ratio of OH is dominantly controlled by the equilibrium of the following forward and backward processes:

$$\begin{aligned} OH + D &\Rightarrow OD + H; \quad 1.3 \times 10^{-10}\ cm^{-3}\ s^{-1} \\ OD + H &\Rightarrow OH + H; \quad 1.3 \times 10^{-10}\ cm^{-3}\ s^{-1} \quad 810\ K \end{aligned} \tag{5.4}$$

At around 100 K, the equilibrium state of this reaction will lead to an enhancement by a factor of approximately 100 in OD, which will transfer into the water D/H ratio, and competes with other de-fractionation processes, eventually leading to the enhanced D/H ratios of $\sim 10^{-4}$. As we move further our in the disk the efficiency of reaction 5.4 gradually decreases, whereas the pace of water ice de-fractionation decreases due to slower cycling of water through gas and solid phases, and the water D/H ratio increases gradually until we reach the colder outer regions of the solar nebula.

Compare to Thi et al. (2010), we do not find that reactions formation of water through reactions between OH/OD and H_2/HD are the dominant neutral-neutral reactions, instead we find that OH/OD and H/D reacting is more dominant. This discrepancy is likely arising due to the energy barrier of reactions with H_2 or HD, while reactions with H or D are exothermic. Other differences between our models may also contribute to the discrepancies. Thi et al. (2010) used a steady-state model to determine their principal reactions, which may point to that these reactions are important, but at later times beyond our modeled $\sim 10^6$ years. The adoption of different reaction rates, where our values come from the osu.2009 database, Thi et al. (2010) adopt reaction rates from Woodall et al. (2007) (H_2O) and Talukdar & Ravishankara (1996) (HDO), may also account for some of the discrepancy. This also result in different OH and OD column densities, where OH is approximately an order of

magnitude more abundant in our model, decreasing by two order of magnitudes at $\sim$ 30 AU, while OD is approximately an order of magnitude more abundant for Thi et al. (2010). Finally, the inclusion of ortho-para chemistry in our network, and differences in physical structures may contribute further to these differences.

5.5 DISCUSSION

We have shown the importance of 2D-mixing on the water D/H gradient in the young solar nebula, which pushes the (lower) water D/H ratios from the inner disk regions toward larger heliocentric distances as water is defractionated after being transported into the inner regions. Before discussing the implications of our results, it is important to discuss the limitations of our model.

Foremost, PPDs are not static environments, but are ever dynamically evolving systems. Dust grains grow into planetesimals and eventually planets, with an associated evolution of physical conditions affecting the chemistry. As we previously discussed, a moderate increase of grain sizes had no significant effect on our results (see Section 5.4), but this might change with even larger particles. Variations in temperature and density will likely play a significant role. Cazaux et al. (2011) predicted that significant variations in HDO/H_2O ratios can come from even small variations in dust temperatures at the time of ice formation. This would also affect initial abundances of our model, as the warm-up phase following the collapse of a dark pre-stellar core will experience a gradual increase in both temperature and density. In addition, exact masses and structural parameters of the solar nebula remain highly uncertain.

Another large uncertainty is the post-processing of Earth's ocean water. Such processes include biological (life and its evolution) as well as chemical processes. Atmospheric processes can affect the fractionation if the young Earth had a massive hydrogen atmosphere, which would experience a slow hydrodynamic escape, which will be slower for deuterium compared to the lighter hydrogen isotope (Genda & Ikoma 2008). Furthermore, as was first proposed by Campins et al. (2005), processes involved in planetary accretion, such as outgassing and the evolution of hydrosphere and atmosphere, are complex and may have affected the fractionation.

Finally, the giant impact theory which explains the formation of the moon and the similarities of its bulk composition to Earth (see e.g. Canup 2012), requires a collision between early Earth and a large impactor. This scenario implies a heavy loss of the primordial Earth atmosphere and would have likely greatly affected the chemical composition, more specifically the D/H ratio. However, results by Saal et al. (2013) revealed a similar isotopic composition of the water in the interiors of Earth and the Moon, as well as the bulk water in carbonaceous chondrites, suggesting that this reprocessing is of minor importance.

Table 5.2: Compilation of observed deuterated water in disks and comets.

Source	D/H ratio $[\times 10^{-4}]$	Reference
Solar nebula	$1.7 - 2.5$	1
Standard Mean Ocean Water	$1.46 - 1.52$	2
Carbonaceous chondrites	$1.30 - 1.50$	3
Protoplanetary disks		
LkCa 15	640	4
DM Tau	$\gtrsim 100$	5
Oort-family comets		
Halley	$2.55-3.46$	6
Halley	$2.72-3.40$	7
Hyakutake	$1.90-3.90$	8
Hale-Bopp	$2.50-4.10$	9
Ikeya-Zhang	< 3.1	10
C/2002 T7	$1.80-3.20$	11
C/2001 Q4	$3.2-6.0$	12
8p/Tuttle	$2.64-5.54$	13
Machholz	$2.71-3.69$	14
C/2007 W1 (Boattini)	< 12.9	15
C/2007 N3 (Lulin)	< 5.6	16
C/2009 P1 (Garradd)	$1.84-2.28$	17
Jupiter-family comets		
103P/Hartley 2	$1.37-1.85$	18
45P/Honda-Mrkos-Pajdusakova	< 2	19

(1) Lellouch et al. (2001); (2) Lecuyer et al. (1998);
(3) From Boato (1954); Robert & Epstein (1982); Kerridge (1985);
(4) Kessler et al. (2003); (5) Ceccarelli et al. (2005);
(6) Balsiger et al. (1995); (7) Eberhardt et al. (1995);
(8) Bockelee-Morvan et al. (1998); (9) Meier et al. (1998);
(10) Biver et al. (2006); (11) Hutsemékers et al. (2008);
(12) Weaver et al. (2008); (13) Villanueva et al. (2009);
(14) Kawakita & Kobayashi (2009); (15) Villanueva et al. (2011);
(16) Gibb et al. (2012); (17) Bockelée-Morvan et al. (2012);
(18) Hartogh et al. (2011); (19) Lis et al. (2013)

5.5.1 *Observations in other protoplanetary disks*

TW Hydrae has been observed on multiple occasions, and its expected disk mass is comparable to the solar nebula and believed to be able to form a planetary system like our own (Bergin et al. 2013), hence one may expect a similar chemistry. Qi et al. (2008) estimated water column densities of $< 9.0 \times 10^{14}$ cm^{-2} in the outer region of TW Hydrae, which is lower compared to our models ($\sim 10^{15}$ cm^{-2}). A small difference in disk mass may, partly, explain the discrepancy, as has been suggested by Najita et al. (2013) from studies of HCN/H_2O flux ratios, where more massive disks have a more efficient formation of large non-migrating bodies, which more efficiently locks up oxygen and water beyond the water line. Hogerheijde et al. (2011) observed a cold water vapor reservoir in the disk of TW Hydrae, predicting instead a relative abundance $\sim 10^{-7}$ at intermediate heights, slightly higher than we predict in the upper layers of the solar nebula ($\sim 10^{-8}$). It is possible that they probe regions further in than Qi et al. (2008), due to the optical depth-effect, corresponding to "warmer" water at ~ 50 AU.

Pontoppidan et al. (2005) observed water ice features in an edge-on circumstellar disk using the *Spitzer* telescope. The orientation means that their observations probe the outermost regions. The high inclination complicates comparisons and the cutoff radius of the disk will affect results. Using models and adopting the best-fitting parameters to their observations, Pontoppidan et al. (2005) estimated an abundance of $\sim 10^{-4}$ with respect to H_2, which is in agreement with our modeled relative abundances in the outer disk, $10^{-5} - 10^{-4}$. Aikawa et al. (2012a) measured with the AKARI satellite several ice features in five edge-on Class II disks with column densities on the order of 10^{17} cm^{-2} as well as a faint HDO feature in one of the disks (HV Tau, D/H $\sim$ 19%). The observed disk has a high inclination ($i \sim 84^\circ$) and probe the outermost regions where our models estimate a water D/H ratio of $\sim 0.03 - 0.05$, a D/H ratio lower by a factor ~ 5 compared to the observed ice features. Our column densities are vertically integrated, and due to the higher density in the disk midplane compared to the surface, horizontally integrated column densities would be expected to be larger by approximately one order of magnitude.

5.5.2 *Previous theoretical studies*

There has been a vast number of studies on the chemistry in PPDs, many of these are not targeting the problem in a similar fashion as us, making any comparison complicated. Therefore, we concentrate on studies with similar approaches to model chemistry and physics in a PPD or solar nebula.

Aikawa & Herbst (1999a) studied the deuterium chemistry in the outer regions of PPDs with an 1D accretion flow, using a collapse model to set up the initial molecular concentrations. They have found that the molecular D/H ratios are enhanced with respect to the protosolar values, and that the ratios at $\sim$ 30 AU agree reasonably well with the D/H ratios observed in comets, meaning that comets may not necessarily be composed of primordial, unpro-

cessed interstellar matter, as we also find in our models. While our two models predict similar abundances, within an order of magnitude, we find different behavior of D/H ratios with radii, such that our models attain higher D/H ratios in the outer regions.

Willacy (2007) have investigated deuterium chemistry in outer disk regions using the UMIST RATE'95 database, which was extended with a set of reactions for multiply-deuterated species, a 1+1D disk model of D'Alessio et al. (2001), and initial molecular abundances obtained by the chemical modeling of a cold prestellar core. Furthermore, they implement a lower stellar and disk mass compared to our model. Similarly to Aikawa & Herbst (1999a), they found that the D/H ratios observed in comets may partly originate from the parental molecular cloud and partly be produced in the disk. They concluded that the D/H ratios of gaseous species are more sensitive to deuterium fractionation processes in disks due to rapid ion-molecule chemistry compared to the deuterated ices, whose D/H values are regulated by slow surface chemistry and are imprints of the cold conditions of the prestellar cloud. We find signs of the same sensitivities to ion-molecule chemistry, which is, in our models, also further aided by high-temperature reactions.

In their later study, Willacy & Woods (2009) investigated deuterium chemistry in the inner 30 AU, accounting for gas and dust thermal balance. While a good agreement between the model predictions and observations of several non-deuterated gaseous species in a number of PPDs was obtained, the calculated D/H ratios for ices were higher than measured in the Solar System Oort-family comets, while our models are in better agreement to observations of Solar System bodies (see Section 5.5.3). Furthermore, we note that their D/H distributions do not show a smooth increase with radii, as our models predict, but which show a spike and swinging variations at radii $\gtrsim$ 10 AU. Willacy & Woods (2009), however, consider a small stellar mass and less turbulent mixing ($\alpha = 0.025$). Their results point to the importance of dynamical processes (shocks, turbulent or advective mixing, non-steady accretion) for deuterium chemistry in the inner regions of disks.

Thi et al. (2010) focused on understanding deuterium fractionation in the inner warm disk regions and investigated the origin of the high H_2O D/H ratios in dense ($\gtrsim 10^6$ cm^{-3}) and warm gas ($\sim 100 - 1000$ K) by gas-phase photochemistry (dominated by photoprocesses and neutral-neutral reactions). Using the time-dependent chemical model based the UMIST RATE'06 database (Woodall et al. 2007) and the T Tau disk structure calculated with "ProDiMo" (Woitke et al. 2009), they predicted that in the terrestrial planet-forming region at $\lesssim$ 3 AU the water D/H ratios may remain high, $\gtrsim$ 1%, which is significantly higher than the value of $\approx 1.5 \times 10^{-4}$ measured in the Earth ocean water as well as predictions from our models. While Thi et al. (2010) a dynamical code, they only included a simple chemical network and did not account for the grain chemistry, which is essential for the calculation of water chemistry.

Yang et al. (2013) coupled a classical dynamic α-viscosity model of material transport, which calculates the evolution of the disk's surface density profile, and mixing with a kinetic study of D-H isotopic exchange amongst gas-phase molecules. They found that the water D/H ratio is low in the hot inner disk

due to rapid exchange reactions with molecular hydrogen and increases outwards where the exchange becomes less efficient. Contrary to previous studies, they found that further out in the disk, the water D/H ratio decreases again as water exchanged at high temperatures near the young star is transported outwards in the early evolutionary stages of the disk. However, their chemical approach is simplistic and only includes neutral-neutral reactions as these would be dominant in the early stages of disk evolution because effects of ion-molecule reactions and photochemistry are significantly diluted. With the two-dimensional mixing in effect, we however find that these processes play a role in the chemistry and deuterium fractionation.

Recently, Furuya et al. (2013) investigated the water chemistry in turbulent PPDs. They found that transportation by turbulence in to the atmosphere allows a reprocessing of water, which is destroyed by photoreactions and then transported back to the midplane where water is (re)formed, and this cycle is most effective at radii $\lesssim$ 30 AU. While Furuya et al. (2013) also discuss the effects of radial transportation, without including them in their models, we have done so, and found that radial transport can further decrease both water abundances and D/H ratios through reprocessing in the warmer, inner regions. They also studied the effects from different desorption energies for atomic hydrogen and deuterium, comparing $E_{des,H/D} = 400$ K and $E_{des,H/D} = 600$ K peak energies as found from molecular dynamics simulations for crystalline and amorphous water ice, respectively (Al-Halabi & van Dishoeck 2007). The higher energy increases the residence time on grains for H and D, and result in a higher reformation rate in the midplane, and as such, the water abundances are slightly higher. The most significant difference to our model is in the calculated D/H ratios throughout the disk. For Furuya et al. (2013), in the inner region, D/H drops to the cosmic ratio $\sim 1.5 \times 10^{-5}$ at radii $\lesssim$ 10 AU, and even lower at radii $\lesssim$ 2 AU, while our 2D-mixing model retain an enhanced D/H ratio of $\sim 10^{-4}$ between $\sim 1 - 7$ AU. We find that the enhanced ratio at radii $\lesssim$ 7 AU is largely because of "warm" fractionation pathways (see Section 5.4), which is included in both models. It is therefore likely that this discrepancy is a result of different physical parameters, such as stellar parameters, where Furuya et al. (2013) implemented values for a larger, but less massive and cooler star compared to our study.

5.5.3 *Solar System bodies*

There is a great variation in chemical composition in the different bodies of the Solar System. Due to the temperature gradient throughout the solar nebula, (see figures in Hartogh et al. 2011; Lis et al. 2013), the D/H ratio varies radially through the disk, as we have also seen in our results (see Figure 5.4). The same behavior has been observed in the solar nebula from observations of small Solar System bodies (Robert et al. 2000): the D/H ratios increasing with radial distance from the Sun. Due to sedimentation in the planetary cores and reprocessing in their atmospheres, the D/H ratios in planetary bodies of the Solar System are no direct measure of the pristine D/H ratio.

While we can understand the rough composition of most of the planets in the Solar System, the more important discussion is the composition of small Solar-System bodies, i.e. asteroids and comets. Their origin is less constrained, but we can derive boundary conditions from the Grand Tack scenario (Morbidelli et al. 2012), the most successful theory of the formation and evolution of the Solar System. In this scenario, Jupiter migrated inwards after its formation, only to be stopped at $\sim$ 1.5 AU by a mean motion resonance with Saturn after which both giant planets move back outwards to their present positions, and before Jupiter had managed to diminish the available material in the inner disk for build-up of the terrestrial planets. In this theory, many of the observed features of the Solar System today can be reproduced, such as the smaller mass of Mars (Walsh et al. 2011). As Jupiter moved through the asteroid belt at $\sim$2-3 AU twice, it scattered much of the belt material. This might explain the mix of C- and S-type asteroids in the inner and outer asteroid belts (Walsh et al. 2012).

Carbonaceous chondrites have measured water D/H ratios very similar to that of Earth's oceans (Robert 2003). Comets, or more specifically Oort-family comets, on the other hand, have been observed with enhanced D/H ratios relative to the Earth's oceans. Observations reveal values $\sim$1.8-6.0 $\times$ 10^{-4} (see Table 5.2), an enhancement to the Earth ocean value by a factor of few. These values would put their formation origin in our models around $10 - 20$ AU. However, new experimental studies of ice sublimation suggest that the D/H measured in the evaporated vapor of comets might be depleted by 70% or more with respect to the bulk D/H ratio in the nucleus (Brown et al. 2012). With this in mind, the measurements of D/H ratios in Oort-family comets would be even more enhanced relative to Earth's oceans, by more than an order of magnitude. Regarding the origin of these comets, it means that they would be expected to have originated further out in the disk, $\sim$ $30 - 40$ AU, and is in agreement that these long-period comets are believed to have formed much further in compared to where they are found today in the Oort cloud (see e.g. Oort 1950; Duncan et al. 1987).

While Oort-family comets have too high D/H ratios to be considered as a major source in the delivery of Earth's ocean, the observation by Hartogh et al. (2011) has revealed D/H ratios similar to Earth's ocean water in the Jupiter-family comet 103P/Hartley-2. The existence of diversity in D/H ratios between the Jupiter- and Oort-family comets has been further confirmed by the observations of Lis et al. (2013) who observed a D/H ratio $< 2 \times 10^{-4}$ in the Jupiter-family comet 45P/Honda-Mrkos-Pajdusakova. Therefore, we may consider the D/H ratio of Hartley-2 as representative of Jupiter-family comets, which puts their possible formation location between $\sim$ 1-10 AU. Most likely they originate in the region between Jupiter and Saturn where the gravitational pull of Jupiter and Saturn have scattered them, giving them their current high-eccentricity orbits past the snow line $\sim$ 3 AU. If they would have formed in the Kuiper belt located beyond the orbit of Neptune, which is the current theory (see e.g. Weissman 1999; Emel'Yanenko et al. 2007; Volk & Malhotra 2008), their D/H ratios would have been much higher in our model as the chemical timescale for de-fractionation of HDO ice is too long. It still means that the

origins of the Jupiter- and Oort-family comets are not as distinct as previously thought.

5.6 CONCLUSIONS

In this paper the isotopic and chemical evolution of water in the early history of the solar nebula before the onset of planetesimal formation is studied. An extended gas-grain chemical model that includes multiply-deuterated species, high-temperature reactions, and nuclear spin-state processes is combined with a 1+1D steady-state α-viscosity nebula model. To calculate initial abundances, we simulated the 1 Myr of the evolution of a cold and dark TMC1-like prestellar core, resulting in initially high D/H ratios for water and other molecules of $\sim 1\%$. Two time-dependent chemical models of the solar nebula are calculated over 1 Myr and for radii $0.8 - 800$ AU: (1) a laminar model and (2) a model with 2D-turbulent mixing transport. We find that both models are able to reproduce the Earth ocean's water D/H ratio of $\approx 1.5 \times 10^{-4}$ at the location of the asteroid belt, $\lesssim 2.5 - 3$ AU, where a transition from predominantly solid to gaseous water occurs.

The water ices there can be incorporated in growing solids, melt, and eventually produce phyllosilicates. At $\lesssim 2$ AU, nebular temperatures are too high for the water ice to exist and the dust grains are water ice-free. Thus the planetesimals, from which Earth would later form, remain water-poor. We find that the radial increase of the D/H ratio in water outward is shallower in the chemo-dynamical nebular model. This is related to more efficient de-fractionation of HDO via rapid gas-phase processes, as the 2D mixing model allows the water ice to be transported either inward and thermally evaporated or upward and photodesorbed. Taking the water D/H abundance uncertainties of the factor of 2 into account, the laminar model shows the Earth water D/H ratio at $r \lesssim 2.5$ AU, while for the 2D chemo-dynamical model this zone is larger, $r \lesssim 9$ AU. Similarly, the enhanced water D/H ratios representative of the Oort-family comets, $\sim 2.5 - 10 \times 10^{-4}$, are achieved within $\sim 2 - 6$ AU and $\sim 6 - 30$ AU in the laminar and the 2D model, respectively. The characteristically, slightly lower, water D/H ratio that has been found for Jupiter-family comets are found further in and we find their possible formation location $\sim 1 - 10$ AU in both models. This means that, in our models, we find an overlap in the possible formation location for Oort- and Jupiter-family comets. However, with regard to the water isotopic composition and the origin of the comets, the mixing model seems to be favored over the laminar model as the former allows Oort-family comets to have formed in the region of Jupiter's and Saturn's present location.

SUMMARY AND OUTLOOK

We are entering a new era of astrochemistry, where the generation of powerful, sensitivity observational facilities such as Herschel, ALMA, VLA, SKA, JWST, etc. have, or will, provide us with new accurate measurements of the molecules in space. Amongst the observed molecules, deuterated species have since long been used as powerful probes of physical and chemical processes, and observations in the various stages of the ISM show a significant enhancement in D/H ratios compared to the cosmic elemental ratio of 1.5×10^{-5}. If we are to make full use of deuterated species as tracers, we need to develop new chemical models in order to study the deuterium fractionation throughout the star formation process. The aim of this thesis is to present and evaluate a new extensive model for studies of deuterium chemistry, with which the tools necessary to explore the treasury of interesting questions that still remain unanswered in astrochemistry is provided.

In Chapter 2 we discuss how the deuterium chemistry model is created, and evaluate its robustness. Cold, dark clouds are simple environments in comparison to later stages of the star formation, with a wealth of observational studies and detected molecules, they make for excellent test beds for evaluating the deuterium chemistry model. We find that the calculated D/H ratios agree within an order of magnitude for observations of deuterated species in various pre- and proto-stellar environments and dominant pathways for a small subset of essential species confirm what has been found in previous studies. Finally, we also discuss the long-term evolution of a few representative, essential species, and find that many of the molecules that are dominantly formed on grains have not reached steady-state abundances within 1 Myr, proving that steady-state models are not a good proxy for the chemical studies of molecular clouds.

A sensitivity analysis of the deuterium model, concentrating on DC and lukewarm IRDC environments, is presented in Chapter 3. Due to the complexity of evaluating uncertainties in the surface chemistry, it only focuses on the gas-phase chemistry. Uncertainties are similar between D- and H-bearing species in DC environments, while in warm IRDCs large ($>$ 4 atoms) D-bearing species typically have uncertainties a factor of two larger than H-bearing species.

Abundance uncertainties increase with the size of the molecule and abundance uncertainties are comparable to that determined for un-deuterated species in diffuse and dark clouds (Vasyunin et al. 2004; Wakelam et al. 2006a), as well as PPDs (Vasyunin et al. 2008b). Small species ($\leq$ 3 atoms) have uncertainties of a factor 1.5 - 5.0, medium-sized molecules (4 - 7 atoms) have higher uncertainties of a factor 1.5 - 7.0, and large molecules, such as complex organics with $>$ 7 atoms typically have uncertainties of factors of $\sim$2.0 - 10.0. The uncertainties in calculated D/H ratios do not show a clear increase with the size of molecules, with values between factors of 2 and $\sim$10.

The biggest contributors to uncertainties in the chemistry are identified for several key species such as CO, H_3^+ and H_2O. CRP ionization rates for H_2 and He largely contribute to uncertainties of all species, however in general ion-neutral reactions dominate the list. A majority of reactions listed as problematic are produced by our cloning procedure, and show the need for more accurate estimates of the reaction rates for these reactions.

An important succession of this sensitivity analysis would be the extension to include also surface reactions and gas-grain interactions in order to study in full extent the uncertainties in deuterium chemistry. This would allow for better constraints on uncertainties for complex organics and other species which are predominantly formed on grains. It would however also increase the complexity of the study and the computational costs, therefore calculations need to be made more effective. A lot of computational effort is spent on "chemical loops", where material is reprocessed and reformed over and over again. The adsorption and desorption of species is a good example of such demanding loops.

In recent years, it has been realized that the ortho−para chemistry has a profound effect on deuterium fractionation. The fraction of H_2 in its ortho levels in the cold ISM is small but not well known. Furthermore, the interaction between H_3^+ and H_2 were long predicted to be thermalized so that the excitation temperatures of H_3^+, just as H_2, would be good probes of the kinetic temperatures. However, observations have revealed discrepancies, suggesting that the thermalization of H_3^+ is competing with other processes, such as DR.

In Chapter 4 the steps for including ortho−para chemistry into the deuterium chemistry models are discussed. It is then utilized in the first time-dependent study of the ortho−para chemistry in the diffuse ISM. Comparing the observed para-fraction of H_3^+ and H_2 to the calculated values, it is evident that DR of H_3^+ has a large effect on the H_3^+ para-fraction, and new laboratory experiments are vital in order to improve our understanding. Additionally, variations of physical parameters such as density, CRP ionization rate and chemical age have a minor effect on the predicted para-fractions.

Finally, in Chapter 5 the deuterium chemistry model is used to study the formation and evolution of water in the early Solar System. The origin of water on Earth constitute one of the most interesting questions in astronomy. By studying the distribution of the D/H ratio of water through the solar nebula, the origin of water can be identified by comparing to values of Earth's ocean water, $\sim 1.6 \times 10^{-4}$. High-temperature reactions, which will be active in the warm inner regions of the solar nebula, are included into the deuterium chemistry model. Results show that turbulent mixing is important, as it transports material from the colder outer regions into the warmer inner regions, where it is reprocessed and high pristine D/H ratios are reset. The resulting distribution of D/H ratios are in much better agreement with the observed D/H ratios of the minor Solar System bodies. Also the importance of the ortho−para chemistry on the deuterium fractionation is evident as the D/H gradient can decrease by as much as an order of magnitude in the comet-forming zone if the H_2 ortho:para ratio in the pre-stellar phase is increased to the upper extreme value, the statistical ratio of 3:1.

Better collaborative efforts to combine the dynamical studies of the planet-forming phases of the solar nebula, and PPDs in general, with the chemical evolution is an important step. Today we know that comets and asteroids are rich in material such as water and complex organics, and by studying the transport of these species through the disks we may learn important details on the habitability and evolution of life on our and other planets. Furthermore, the use of more advanced models is an obvious next step. The effects of grain growth has previously been studied for PPDs but never in the context of deuterium chemistry and D/H ratios.

The next step for the deuterium chemistry model is to conduct a complete and more detailed study of the deuterium chemistry throughout the phases of the star formation, as well as how the D/H ratios propagate through the various phases. This would required sophisticated models taking into account the warm-up phase of contracting prestellar cores, multilayered nature of grains and grain growth in PPDs. Furthermore, this thesis has mainly aimed at simpler molecules, and with the unprecedented accuracy of modern and future observing facilities, detailed studies of more complex organics are of great interest. Laboratory studies of meteoric samples have revealed that many identified amino acids are enriched in D/H ratios and therefore likely have their origins in the cold early phases, thus contain some information on their interstellar heritage.

In conclusions, astrochemistry is a scientific field rich in unsolved interesting questions, and it is reaching a new milestone where highly sensitive observing facilities produce a wealth of high-resolution, high-sensitivity observational data. There is a growing interest for the chemical brewery of interstellar space as we are exploring the chemical inventories of distant worlds and searching for signs of habitability and life on these alien worlds. The key to understanding the complexity of the chemical cosmos lies now in the further development and utilization of sophisticated models to give us an equally theoretical resolution on the chemical processes producing the zoo of molecules that we observe in space.

A

APPENDICES

In the Appendix we list added and updated non-deuterated (Table A.1) and deuterated (Table A.2) reactions to our network. The added and updated reactions have been collected from several literature references as well as newly announced values (as of 2013-4-13) reported in the Kinetic Database for Astronomy (KIDA; http://kida.obs.u-bordeaux1.fr/). In Tables A.3 – A.7 we list dominant pathways identified for isotopologues and isomers of the selected species H_3^+, HCO^+, HCN, H_2O as well as species involved in the formation of these essential species. The intention is to help with future comparisons with our model. Finally, in Table A.8 we have collected and generated an updated listing of observed deuterated species and D/H ratios in the ISM.

A.1 ADDED AND UPDATED NON-DEUTERIUM REACTIONS.

Table A.1: Added and updated non-deuterium reactions.

Reaction			α	β	γ	Ref
$C^+ + H_2$	⇒	CH_2^+	2.00×10^{-16}	-1.30	-23	1
$C^+ + HCOOH$	⇒	$HCO^+ + OH + C$	8.00×10^{-10}	-0.50	0	5
$C_2H_2^+ + H_2$	⇒	$C_2H_4^+$	2.90×10^{-14}	-1.50	0	1
$CH_3^+ + H_2O$	⇒	$CH_3OH_2^+$	5.50×10^{-12}	-1.70	0	3
$CH_3^+ + H_2$	⇒	CH_5^+	3.78×10^{-16}	-2.30	22	4
$CH_3O_2^+ + CH_3OH$	⇒	$H_5C_2O_2^+ + H_2O$	2.00×10^{-9}	-0.50	2810	5
$CH_3OH_2^+ + HCOOH$	⇒	$HCOOH_2^+ + CH_3OH$	3.63×10^{-9}	-0.50	685	5
$CH_5^+ + HCOOH$	⇒	$HCOOH_2^+ + CH_4$	3.00×10^{-9}	-0.50	0	5
$H_2CN^+ + C_2H_2$	⇒	$C_3H_4N^+$	3.30×10^{-16}	-2.00	0	4
$H_2CN^+ + HCOOH$	⇒	$HCOOH_2^+ + HCN$	1.40×10^{-9}	-0.50	0	5
$H_3^+ + HCOOH$	⇒	$HCO^+ + H_2O + H_2$	3.90×10^{-9}	-0.50	0	5
$H_3^+ + O$	⇒	$OH^+ + H_2$	7.98×10^{-10}	-0.156	-1.41	1
$H_3^+ + O$	⇒	$H_2O^+ + H$	3.42×10^{-10}	-0.156	-1.41	1
$H_3CO^+ + HCOOH$	⇒	$HCOOH_2^+ + H_2CO$	2.00×10^{-9}	-0.50	0	5
$H_3O^+ + C_2H_4$	⇒	$C_2H_5OH_2^+$	1.90×10^{-14}	-2.80	0.25	4
$H_3CO^+ + H_2CO$	⇒	$H_5C_2O_2^+$	8.15×10^{-15}	-3.00	0	6
$H_3S^+ + HCOOH$	⇒	$HCOOH_2^+ + H_2S$	2.00×10^{-9}	-0.50	0	5
$HCOOH_2^+ + CH_3OH$	⇒	$CH_3OH_2^+ + HCOOH$	2.29×10^{-9}	-0.50	0	5
$He^+ + HCOOH$	⇒	$HCO^+ + OH + He$	9.00×10^{-10}	-0.50	0	5
$N_2H^+ + HCOOH$	⇒	$HCOOH_2^+ + N_2$	1.70×10^{-9}	-0.50	0	5
$C + O_2$	⇒	$CO + O$	1.28×10^{-9}	-0.32	0	4
$C + OH$	⇒	$CO + H$	1.15×10^{-10}	-0.34	0	4
$C_2 + O$	⇒	$CO + C$	2.00×10^{-10}	-0.12	0	1
$C_2 + OCS$	⇒	$CO + C_2S$	1.00×10^{-10}	0.00	0	4
$C_2H + N$	⇒	$C_2N + H$	1.00×10^{-10}	0.18	0	1
$C_2H + O$	⇒	$CO + CH$	1.00×10^{-10}	0.00	0	1

Reaction			α	β	γ	Ref
$C_3H + O$	$\Rightarrow$	$C_2H + CO$	1.00×10^{-10}	0.00	0	1
$C_3O + O$	$\Rightarrow$	$C_3 + O_2$	1.00×10^{-10}	0.00	0	1
$CH + OCS$	$\Rightarrow$	$H + CO + CS$	4.00×10^{-10}	0.00	0	4
$CH + SO$	$\Rightarrow$	$H + OCS$	1.10×10^{-10}	0.00	0	4
$CH + SO$	$\Rightarrow$	$CO + HS$	9.00×10^{-11}	0.00	0	4
$CH_2 + H$	$\Rightarrow$	$CH + H_2$	2.20×10^{-10}	0.00	0	1
$CH_4 + CH$	$\Rightarrow$	$C_2H_4 + H$	1.06×10^{-10}	-1.04	0	4
$CN + N$	$\Rightarrow$	$C + N_2$	1.00×10^{-10}	0.00	0	1
$CN + O$	$\Rightarrow$	$CO + N$	2.60×10^{-11}	-0.12	0	1
$CN + O_2$	$\Rightarrow$	$OCN + O$	1.99×10^{-11}	-0.63	0	4
$H_2 + CH$	$\Rightarrow$	$CH_2 + H$	1.20×10^{-9}	0.00	0	4
$HNO + O$	$\Rightarrow$	$NO + OH$	3.77×10^{-11}	-0.08	0	1
$NH + O$	$\Rightarrow$	$NO + H$	6.60×10^{-11}	0.00	0	1
$NH_2 + O$	$\Rightarrow$	$HNO + H$	6.39×10^{-11}	-0.10	0	1
$NH_2 + O$	$\Rightarrow$	$NH + OH$	7.10×10^{-12}	-0.10	0	1
$NH_3 + CN$	$\Rightarrow$	$HCN + NH_2$	2.77×10^{-11}	-0.85	0	1
$O + C_2S$	$\Rightarrow$	$CO + CS$	1.00×10^{-10}	0.00	0	4
$O + OCS$	$\Rightarrow$	$CO + CS$	1.00×10^{-10}	0.00	0	4
$O + OH$	$\Rightarrow$	$O_2 + H$	4.00×10^{-11}	0.00	0	4
$S + C_2O$	$\Rightarrow$	$CO + CS$	1.00×10^{-10}	0.00	0	4
$S + HCO$	$\Rightarrow$	$H + OCS$	8.00×10^{-11}	0.00	0	4
$S + HCO$	$\Rightarrow$	$CO + HS$	4.00×10^{-11}	0.00	0	4
$C_3H^+ + e^-$	$\Rightarrow$	$C_2 + CH$	6.00×10^{-9}	-0.50	0	2
$C_3H^+ + e^-$	$\Rightarrow$	$C_2H + C$	9.90×10^{-8}	-0.50	0	2
$C_3H^+ + e^-$	$\Rightarrow$	$C_3 + H$	1.95×10^{-7}	-0.50	0	2
$C_3H_2^+ + e^-$	$\Rightarrow$	$C_2 + CH_2$	1.44×10^{-8}	-0.50	0	2
$C_3H_2^+ + e^-$	$\Rightarrow$	$C_2H + CH$	1.44×10^{-8}	-0.50	0	2
$C_3H_2^+ + e^-$	$\Rightarrow$	$C_2H_2 + C$	8.64×10^{-8}	-0.50	0	2
$C_3H_2^+ + e^-$	$\Rightarrow$	$C_3H + H$	1.66×10^{-7}	-0.50	0	2
$C_3H_2^+ + e^-$	$\Rightarrow$	$C_3 + H_2$	8.28×10^{-8}	-0.50	0	2
$C_4H^+ + e^-$	$\Rightarrow$	$C_4 + H$	1.74×10^{-7}	-0.50	0	2
$C_4H^+ + e^-$	$\Rightarrow$	$C_3H + C$	7.80×10^{-8}	-0.50	0	2
$C_4H^+ + e^-$	$\Rightarrow$	$C_2H + C_2$	4.80×10^{-8}	-0.50	0	2
$C_5^+ + e^-$	$\Rightarrow$	$C_4 + C$	3.90×10^{-8}	-0.50	0	2
$C_5^+ + e^-$	$\Rightarrow$	$C_3 + C_2$	2.61×10^{-7}	-0.50	0	2
$C_6^+ + e^-$	$\Rightarrow$	$C_5 + C$	1.80×10^{-7}	-0.30	0	2
$C_6^+ + e^-$	$\Rightarrow$	$C_4 + C_2$	2.20×10^{-7}	-0.30	0	2
$C_6^+ + e^-$	$\Rightarrow$	$C_3 + C_3$	1.60×10^{-6}	-0.30	0	2
$C_7^+ + e^-$	$\Rightarrow$	$C_6 + C$	2.30×10^{-8}	-0.30	0	2
$C_7^+ + e^-$	$\Rightarrow$	$C_5 + C_2$	4.37×10^{-7}	-0.30	0	2
$C_7^+ + e^-$	$\Rightarrow$	$C_4 + C_3$	1.84×10^{-6}	-0.50	0	2
$C_8^+ + e^-$	$\Rightarrow$	$C_7 + C$	6.00×10^{-8}	-0.30	0	2
$C_8^+ + e^-$	$\Rightarrow$	$C_6 + C_2$	2.00×10^{-8}	-0.30	0	2
$C_8^+ + e^-$	$\Rightarrow$	$C_5 + C_3$	1.80×10^{-6}	-0.30	0	2
$C_8^+ + e^-$	$\Rightarrow$	$C_4 + C_4$	1.20×10^{-7}	-0.30	0	2
$C_9^+ + e^-$	$\Rightarrow$	$C_7 + C_2$	1.20×10^{-7}	-0.30	0	2
$C_9^+ + e^-$	$\Rightarrow$	$C_6 + C_3$	1.32×10^{6}	-0.30	0	2
$C_9^+ + e^-$	$\Rightarrow$	$C_5 + C_4$	5.60×10^{-7}	-0.30	0	2
$C_{10}^+ + e^-$	$\Rightarrow$	$C_9 + C$	2.00×10^{-8}	-0.30	0	2
$C_{10}^+ + e^-$	$\Rightarrow$	$C_8 + C_2$	2.00×10^{-8}	-0.30	0	2

Reaction			α	β	γ	Ref
$C_{10}^+ + e^-$	⇒	$C_7 + C_3$	1.40×10^{-6}	-0.30	0	2
$C_{10}^+ + e^-$	⇒	$C_6 + C_4$	6.00×10^{-8}	-0.30	0	2
$C_{10}^+ + e^-$	⇒	$C_5 + C_5$	5.00×10^{-7}	-0.30	0	2
$CNC^+ + e^-$	⇒	$C_2 + N$	2.00×10^{-8}	-0.60	0	1
$CNC^+ + e^-$	⇒	CN + C	3.80×10^{-7}	-0.60	0	1
$H_3^+ + e^-$	⇒	H + H + H	5.44×10^{-8}	-0.50	0	3
$H_3^+ + e^-$	⇒	$H_2 + H$	1.36×10^{-8}	-0.50	0	3
$H_2CO^+ + e^-$	⇒	$CH_2 + O$	2.50×10^{-8}	-0.70	0	1
$H_2CO^+ + e^-$	⇒	CO + H + H	2.50×10^{-7}	-0.70	0	1
$H_2CO^+ + e^-$	⇒	$CO + H_2$	7.50×10^{-8}	-0.70	0	1
$H_2CO^+ + e^-$	⇒	HCO + H	1.50×10^{-7}	-0.70	0	1
$HC_5NH^+ + e^-$	⇒	$C_5N + H_2$	8.00×10^{-8}	-0.70	0	1
$HC_5NH^+ + e^-$	⇒	$HC_3N + C_2H$	1.20×10^{-7}	-0.70	0	1
$HC_5NH^+ + e^-$	⇒	$HC_5N + H$	9.20×10^{-7}	-0.70	0	1
$HC_5NH^+ + e^-$	⇒	$HCN + C_4H$	4.40×10^{-7}	-0.70	0	1
$HC_5NH^+ + e^-$	⇒	$HNC + C_4H$	4.40×10^{-7}	-0.70	0	1
$HCNH^+ + e^-$	⇒	CN + H + H	9.06×10^{-8}	-0.65	0	1
$HCNH^+ + e^-$	⇒	HCN + H	9.62×10^{-8}	-0.65	0	1
$HCNH^+ + e^-$	⇒	HNC + H	9.62×10^{-8}	-0.65	0	1
C_2H + CRPHOT	⇒	$C_2 + H$	5.27×10^{-14}	0.00	0	2
C_2H + CRPHOT	⇒	C + CH	1.24×10^{-14}	0.00	0	2
C_3H + CRPHOT	⇒	$C_2H + C$	2.15×10^{-14}	0.00	0	2
C_3H + CRPHOT	⇒	$C_2 + CH$	1.30×10^{-15}	0.00	0	2
C_3H + CRPHOT	⇒	$C_3 + H$	4.23×10^{-14}	0.00	0	2
C_3H_2 + CRPHOT	⇒	$C_3H + H$	2.99×10^{-14}	0.00	0	2
C_3H_2 + CRPHOT	⇒	$C_3 + H_2$	1.56×10^{-14}	0.00	0	2
C_3H_2 + CRPHOT	⇒	$C_2H_2 + C$	1.50×10^{-14}	0.00	0	2
C_3H_2 + CRPHOT	⇒	$C_2H + CH$	2.60×10^{-15}	0.00	0	2
C_3H_2 + CRPHOT	⇒	$C_2 + CH_2$	1.95×10^{-15}	0.00	0	2
C_4 + CRPHOT	⇒	$C_3 + C$	1.00×10^{-14}	0.00	0	2
C_4 + CRPHOT	⇒	$C_2 + C_2$	2.99×10^{-15}	0.00	0	2
C_4H + CRPHOT	⇒	$C_4 + H$	3.77×10^{-14}	0.00	0	2
C_4H + CRPHOT	⇒	$C_3H + C$	1.69×10^{-14}	0.00	0	2
C_4H + CRPHOT	⇒	$C_2H + C_2$	1.04×10^{-14}	0.00	0	2
C_5 + CRPHOT	⇒	$C_4 + C$	1.69×10^{-15}	0.00	0	2
C_5 + CRPHOT	⇒	$C_3 + C_2$	1.13×10^{-14}	0.00	0	2
C_6 + CRPHOT	⇒	$C_5 + C$	1.17×10^{-15}	0.00	0	2
C_6 + CRPHOT	⇒	$C_4 + C_2$	1.43×10^{-15}	0.00	0	2
C_6 + CRPHOT	⇒	$C_3 + C_3$	1.04×10^{-14}	0.00	0	2
C_7 + CRPHOT	⇒	$C_6 + C$	1.30×10^{-16}	0.00	0	2
C_7 + CRPHOT	⇒	$C_5 + C_2$	2.47×10^{-15}	0.00	0	2
C_7 + CRPHOT	⇒	$C_4 + C_3$	1.04×10^{-14}	0.00	0	2
C_8 + CRPHOT	⇒	$C_7 + C$	3.90×10^{-16}	0.00	0	2
C_8 + CRPHOT	⇒	$C_6 + C_2$	1.30×10^{-16}	0.00	0	2
C_8 + CRPHOT	⇒	$C_5 + C_3$	1.17×10^{-15}	0.00	0	2
C_8 + CRPHOT	⇒	$C_4 + C_4$	7.80×10^{-16}	0.00	0	2
C_9 + CRPHOT	⇒	$C_7 + C_2$	7.80×10^{-16}	0.00	0	2
C_9 + CRPHOT	⇒	$C_6 + C_3$	8.58×10^{-15}	0.00	0	2
C_9 + CRPHOT	⇒	$C_5 + C_4$	3.64×10^{-15}	0.00	0	2
CH + PHOTON	⇒	$CH^+ + e^-$	7.60×10^{-10}	0.00	3.80	4

Reaction			α	β	γ	Ref
CH + PHOTON	⇒	C + H	9.20×10^{-10}	0.00	1.72	4
C_2H + PHOTON	⇒	C_2 + H	8.10×10^{-10}	0.00	1.7	2
C_2H + PHOTON	⇒	CH + C	1.90×10^{-10}	0.00	1.7	2
C_3H + PHOTON	⇒	C_3 + H	6.50×10^{-10}	0.00	1.7	2
C_3H + PHOTON	⇒	C_2H + C	3.30×10^{-10}	0.00	1.7	2
C_3H + PHOTON	⇒	C_2 + CH	2.00×10^{-11}	0.00	1.7	2
C_3H_2 + PHOTON	⇒	C_2H_2+ C	1.33×10^{-9}	0.00	1.7	2
C_3H_2 + PHOTON	⇒	C_2H + CH	1.16×10^{-10}	0.00	1.7	2
C_3H_2 + PHOTON	⇒	CH_2 + C_2	1.16×10^{-10}	0.00	1.7	2
C_3H_2 + PHOTON	⇒	C_3H + H	1.33×10^{-9}	0.00	1.7	2
C_3H_2 + PHOTON	⇒	C_3 + H_2	6.67×10^{-10}	0.00	1.7	2
C_4 + PHOTON	⇒	C_3 + C	3.08×10^{-10}	0.00	1.7	2
C_4 + PHOTON	⇒	C_2 + C_2	9.02×10^{-11}	0.00	1.7	2
C_4H + PHOTON	⇒	C_3H + C	5.20×10^{-10}	0.00	1.7	2
C_4H + PHOTON	⇒	C_4 + H	1.16×10^{-9}	0.00	1.7	2
C_4H + PHOTON	⇒	C_2H + C_2	3.20×10^{-9}	0.00	1.7	2
C_5 + PHOTON	⇒	C_3 + C_2	8.70×10^{-12}	0.00	1.7	2
C_5 + PHOTON	⇒	C_4 + C	1.30×10^{-12}	0.00	1.7	2
C_6 + PHOTON	⇒	C_5 + C	9.00×10^{-11}	0.00	1.7	2
C_6 + PHOTON	⇒	C_4 + C_2	1.10×10^{-10}	0.00	1.7	2
C_6 + PHOTON	⇒	C_3 + C_3	8.00×10^{-10}	0.00	1.7	2
C_7 + PHOTON	⇒	C_6 + C	1.00×10^{-11}	0.00	1.7	2
C_7 + PHOTON	⇒	C_5 + C_2	1.90×10^{-10}	0.00	1.7	2
C_7 + PHOTON	⇒	C_4 + C_3	8.00×10^{-10}	0.00	1.7	2
C_8 + PHOTON	⇒	C_7 + C	3.00×10^{-11}	0.00	1.7	2
C_8 + PHOTON	⇒	C_6 + C_2	1.00×10^{-11}	0.00	1.7	2
C_8 + PHOTON	⇒	C_5 + C_3	9.00×10^{-10}	0.00	1.7	2
C_8 + PHOTON	⇒	C_4 + C_4	6.00×10^{-11}	0.00	1.7	2
C_9 + PHOTON	⇒	C_7 + C_2	6.00×10^{-11}	0.00	1.7	2
C_9 + PHOTON	⇒	C_6 + C_3	6.60×10^{-10}	0.00	1.7	2
C_9 + PHOTON	⇒	C_5 + C_4	2.80×10^{-10}	0.00	1.7	2
C_{10} + PHOTON	⇒	C_9 + C	1.14×10^{-11}	0.00	1.7	2
C_{10} + PHOTON	⇒	C_8 + C_2	1.14×10^{-11}	0.00	1.7	2
C_{10} + PHOTON	⇒	C_7 + C_3	7.98×10^{-10}	0.00	1.7	2
C_{10} + PHOTON	⇒	C_6 + C_4	3.42×10^{-11}	0.00	1.7	2
C_{10} + PHOTON	⇒	C_5 + C_5	2.50×10^{-10}	0.00	1.7	2
		Removed reactions				
$CH_3OH_2^+$ + H_2CO	⇒	$H_7C_2O_2^+$	−−	−−	−−	7
H_3CO^+ + CH_4	⇒	$CH_3OCH_4^+$	−−	−−	−−	4
HCO^+ + CH_4	⇒	$CH_3CH_2O^+$	−−	−−	−−	4
C_4H^+ + e^-	⇒	C_3 + CH	−−	−−	−−	2
C_9^+ + e^-	⇒	C_8 + C	−−	−−	−−	2
C_9 + PHOTON	⇒	C_8 + C	−−	−−	−−	2
C_9 + CRPHOT	⇒	C_8 + C	−−	−−	−−	2
HNO + O	⇒	NO_2 + H	−−	−−	−−	1
O + NH	⇒	OH + N	−−	−−	−−	1
NH_2 + O	⇒	NO + H_2	−−	−−	−−	1
NH_3 + CN	⇒	NH_2CN + H	−−	−−	−−	1

(1) Wakelam et al. (2010b); (2) Chabot et al. (2010); (3) Roberts et al. (2004); (4) KIDA database; (5) Laas et al. (2011); (6) Garrod & Herbst (2006); (7) Horn et al. (2004)

Table A.2: Added and updated deuterium reactions.

Reaction			α	β	γ	Ref
$C_2D + H$	$\Rightarrow$	$C_2H + D$	5.00×10^{-11}	0.50	832	9
$C_2H + D$	$\Rightarrow$	$C_2D + H$	5.00×10^{-11}	0.50	250	9
$C_2H_2^+ + HD$	$\Rightarrow$	$C_2HD^+ + H_2$	1.00×10^{-9}	0.00	0	5
$C_2HD^+ + H_2$	$\Rightarrow$	$C_2H_2^+ + HD$	2.50×10^{-9}	0.00	550	5
$CH_3^+ + D_2$	$\Rightarrow$	$CH_2D^+ + HD$	4.40×10^{-10}	0.00	0	3
$CH_3^+ + D_2$	$\Rightarrow$	$CHD_2^+ + H_2$	6.60×10^{-10}	0.00	0	3
$CH_3^+ + HD$	$\Rightarrow$	$CH_2D^+ + H_2$	1.30×10^{-9}	0.00	0	3
$CH_2D^+ + H_2$	$\Rightarrow$	$CH_3^+ + HD$	8.70×10^{-10}	0.00	370	3
$CH_2D^+ + HD$	$\Rightarrow$	$CHD_2^+ + H_2$	1.60×10^{-9}	0.00	0	3
$CH_2D^+ + HD$	$\Rightarrow$	$CH_3^+ + D_2$	4.40×10^{-10}	0.00	400	3
$CH_2D^+ + D_2$	$\Rightarrow$	$CHD_2^+ + HD$	1.20×10^{-9}	0.00	0	3
$CHD_2^+ + H_2$	$\Rightarrow$	$CH_2D^+ + HD$	1.60×10^{-9}	0.00	370	3
$CHD_2^+ + H_2$	$\Rightarrow$	$CH_3^+ + D_2$	6.60×10^{-10}	0.00	400	3
$CHD_2^+ + HD$	$\Rightarrow$	$CD_3^+ + H_2$	1.50×10^{-9}	0.00	0	3
$CHD_2^+ + HD$	$\Rightarrow$	$CH_2D^+ + D_2$	1.20×10^{-9}	0.00	400	3
$CD_3^+ + H_2$	$\Rightarrow$	$CHD_2^+ + HD$	1.50×10^{-9}	0.00	370	3
$D^+ + H$	$\Rightarrow$	$H^+ + D$	1.00×10^{-9}	0.00	0	6
$D^+ + H_2$	$\Rightarrow$	$H^+ + HD$	2.10×10^{-9}	0.00	0	3
$D_3^+ + H$	$\Rightarrow$	$HD_2^+ + D$	2.00×10^{-9}	0.00	655	4
$D_3^+ + H_2$	$\Rightarrow$	$H_2D^+ + D_2$	7.00×10^{-10}	0.00	341	2
$D_3^+ + H_2$	$\Rightarrow$	$HD_2^+ + HD$	2.00×10^{-10}	0.00	234	15
$D_3^+ + HD$	$\Rightarrow$	$HD_2^+ + D_2$	8.70×10^{-10}	0.00	159	2
$DCN + H$	$\Rightarrow$	$HCN + D$	1.00×10^{-10}	0.50	500	9*
$DCO^+ + H$	$\Rightarrow$	$HCO^+ + D$	2.20×10^{-9}	0.00	796	7
$H^+ + D$	$\Rightarrow$	$D^+ + H$	1.00×10^{-9}	0.00	41	6
$H^+ + HD$	$\Rightarrow$	$D^+ + H_2$	1.00×10^{-9}	0.00	464	3
$H_2D^+ + H$	$\Rightarrow$	$H_3^+ + D$	1.00×10^{-9}	0.00	632	7
$H_2D^+ + H_2$	$\Rightarrow$	$H_3^+ + HD$	3.50×10^{-9}	0.00	220	15
$H_3^+ + D$	$\Rightarrow$	$H_2D^+ + H$	1.00×10^{-9}	0.00	0	7*
$H_3^+ + D_2$	$\Rightarrow$	$H_2D^+ + HD$	3.50×10^{-10}	0.00	0	2
$H_3^+ + D_2$	$\Rightarrow$	$HD_2^+ + H_2$	1.10×10^{-9}	0.00	0	2
$H_3^+ + HD$	$\Rightarrow$	$H_2D^+ + H_2$	3.50×10^{-10}	0.00	0	15
$H_2D^+ + D$	$\Rightarrow$	$HD_2^+ + H$	2.00×10^{-9}	0.00	0	4
$H_2D^+ + HD$	$\Rightarrow$	$H_3^+ + D_2$	3.50×10^{-10}	0.00	63	2
$H_2D^+ + HD$	$\Rightarrow$	$HD_2^+ + H_2$	2.60×10^{-10}	0.00	0	15
$H_2D^+ + D_2$	$\Rightarrow$	$HD_2^+ + HD$	7.00×10^{-10}	0.00	0	2
$H_2D^+ + D_2$	$\Rightarrow$	$D_3^+ + H_2$	7.00×10^{-10}	0.00	0	2
$HCN + D$	$\Rightarrow$	$DCN + H$	1.00×10^{-10}	0.50	500	9*
$HCO^+ + D$	$\Rightarrow$	$DCO^+ + H$	1.00×10^{-9}	0.00	0	7
$HD_2^+ + D$	$\Rightarrow$	$D_3^+ + H$	2.00×10^{-9}	0.00	0	4
$HD_2^+ + H$	$\Rightarrow$	$H_2D^+ + D$	2.00×10^{-9}	0.00	550	4
$HD_2^+ + D_2$	$\Rightarrow$	$D_3^+ + HD$	8.70×10^{-10}	0.00	0	2
$HD_2^+ + H_2$	$\Rightarrow$	$H_3^+ + D_2$	1.10×10^{-9}	0.00	251	2
$HD_2^+ + H_2$	$\Rightarrow$	$H_2D^+ + HD$	2.60×10^{-10}	0.00	187	15
$HD_2^+ + HD$	$\Rightarrow$	$H_2D^+ + D_2$	7.00×10^{-10}	0.00	107	2
$HD_2^+ + HD$	$\Rightarrow$	$D_3^+ + H_2$	2.00×10^{-10}	0.00	0	15

Reaction			α	β	γ	Ref
$N_2H^+ + D$	$\Rightarrow$	$N_2D^+ + H$	1.00×10^{-9}	0.00	0	7
$N_2D^+ + H$	$\Rightarrow$	$N_2H^+ + D$	2.20×10^{-9}	0.00	550	7
OH + D	$\Rightarrow$	OD + H	1.30×10^{-10}	0.50	0	8
OD + H	$\Rightarrow$	OH + D	1.30×10^{-10}	0.50	810	8
$C_2HD^+ + H_2$	$\Rightarrow$	$C_2H_3D^+$	3.39×10^{-14}	-1.50	0	12
$CH_3^+ + D_2$	$\Rightarrow$	$CH_3D_2^+$	3.50×10^{-14}	-1.00	0	12
$CH_3^+ + D_2O$	$\Rightarrow$	$CH_3OD_2^+$	1.65×10^{-11}	-1.70	0	12
$CH_3^+ + HDO$	$\Rightarrow$	CH_3OHD^+	1.10×10^{-11}	-1.70	0	12
$CH_2D^+ + D_2O$	$\Rightarrow$	$CH_2DOD_2^+$	2.20×10^{-11}	-1.70	0	12
$CH_2D^+ + H_2$	$\Rightarrow$	CH_4D^+	2.00×10^{-14}	-1.00	0	12
$CH_2D^+ + H_2O$	$\Rightarrow$	$CH_2DOH_2^+$	1.10×10^{-11}	-1.70	0	12
$CH_2D^+ + HDO$	$\Rightarrow$	CH_2DOHD^+	1.65×10^{-11}	-1.70	0	12
$CH_2D^+ + HD$	$\Rightarrow$	$CH_3D_2^+$	3.50×10^{-14}	-1.00	0	12
$CHD_2^+ + D_2O$	$\Rightarrow$	$CHD_2OD_2^+$	2.75×10^{-11}	-1.70	0	12
$CHD_2^+ + H_2$	$\Rightarrow$	$CH_3D_2^+$	3.50×10^{-14}	-1.00	0	12
$CHD_2^+ + H_2O$	$\Rightarrow$	$CHD_2OH_2^+$	1.65×10^{-11}	-1.70	0	12
$CHD_2^+ + HDO$	$\Rightarrow$	CHD_2OHD^+	2.20×10^{-11}	-1.70	0	12
$CD_3^+ + D_2$	$\Rightarrow$	$CD_3OD_2^+$	2.75×10^{-11}	-1.70	0	12
$CD_3^+ + H_2$	$\Rightarrow$	$CH_2D_3^+$	6.30×10^{-14}	-1.00	0	12
$CD_3^+ + H_2O$	$\Rightarrow$	$CD_3OH_2^+$	2.20×10^{-11}	-1.70	0	12
$CD_3^+ + HDO$	$\Rightarrow$	CD_3OHD^+	2.75×10^{-11}	-1.70	0	12
$CD_3OCD_4^+ + e^-$	$\Rightarrow$	$CD_3OCD_3 + D$	8.50×10^{-8}	-0.70	0	14
$CD_3OCD_4^+ + e^-$	$\Rightarrow$	$CD_3OD + CD_3$	9.18×10^{-7}	-0.70	0	14
$CD_3OCD_4^+ + e^-$	$\Rightarrow$	$CD_3 + CD_4 + O$	6.97×10^{-7}	-0.70	0	14
$D_3^+ + e^-$	$\Rightarrow$	$D_2 + D$	5.40×10^{-9}	-0.50	0	12
$D_3^+ + e^-$	$\Rightarrow$	D + D + D	2.16×10^{-8}	-0.50	0	12
$H_2D^+ + e^-$	$\Rightarrow$	D + H + H	4.38×10^{-8}	-0.50	0	10
$H_2D^+ + e^-$	$\Rightarrow$	$H_2 + D$	4.20×10^{-9}	-0.50	0	10
$H_2D^+ + e^-$	$\Rightarrow$	HD + H	1.20×10^{-8}	-0.50	0	10
$HD_2^+ + e^-$	$\Rightarrow$	D + D + H	4.38×10^{-8}	-0.50	0	11
$HD_2^+ + e^-$	$\Rightarrow$	$D_2 + H$	1.20×10^{-8}	-0.50	0	11
$HD_2^+ + e^-$	$\Rightarrow$	HD + D	4.20×10^{-9}	-0.50	0	11
$DCNH^+ + e^-$	$\Rightarrow$	DCN + H	2.33×10^{-7}	-0.50	0	13
$DCNH^+ + e^-$	$\Rightarrow$	HNC + D	1.16×10^{-7}	-0.50	0	13
$HCND^+ + e^-$	$\Rightarrow$	DNC + H	2.33×10^{-7}	-0.50	0	13
$HCND^+ + e^-$	$\Rightarrow$	HCN + D	1.16×10^{-7}	-0.50	0	13
$HDCN^+ + e^-$	$\Rightarrow$	NHD + C	1.75×10^{-7}	-0.50	0	13
$HDNC^+ + e^-$	$\Rightarrow$	HNC + D	0.58×10^{-7}	-0.50	0	13
$HDNC^+ + e^-$	$\Rightarrow$	DNC + H	1.16×10^{-7}	-0.50	0	13
Removed reactions						
$C_2H_2^+ + HD$	$\Rightarrow$	$C_2H_3D^+$	$--$	$--$	$--$	11
$CH_3^+ + HD$	$\Rightarrow$	CH_4D^+	$--$	$--$	$--$	11
$CH_2D^+ + D_2$	$\Rightarrow$	$CH_2D_3^+$	$--$	$--$	$--$	11
$CHD_2^+ + HD$	$\Rightarrow$	$CH_2D_3^+$	$--$	$--$	$--$	11

* Estimate

(1) Ceccarelli & Dominik (2005); (2) Giles et al. (1992); (3) Smith et al. (1982a), Smith et al. (1982b); (4) Walmsley et al. (2004a); (5) Herbst et al. (1987); (6) Watson (1976); (7) Adams & Smith (1985); (8) Croswell & Dalgarno (1985); (9) Schilke et al. (1992); (10) Sundstrom et al. (1994); (11) Roberts et al. (2004); (12) Larsson et al. (1997); (13) Roueff et al. (2005); (14) Hamberg et al. (2010a); (15) Gerlich et al. (2002)

Table A.3: Most essential formation and destruction pathways for H_3^+, H_2D^+, HD_2^+ and D_3^+.

Reaction			α	β	γ	Accuracy	Ref	Note
$H_3^+ + HD$	$\Rightarrow$	$H_2D^+ + H_2$	1.70E-09	0.00E+00	0.00E+00	*factor 2*	(1)	T
$H_3^+ + D$	$\Rightarrow$	$H_2D^+ + H$	1.00E-09	0.00E+00	0.00E+00	*factor 2*	(2)	T
$H_2D^+ + HD$	$\Rightarrow$	$HD_2^+ + H_2$	8.10E-10	0.00E+00	0.00E+00	$\pm$15%	(3)	M
$H_2D^+ + D$	$\Rightarrow$	$HD_2^+ + H$	2.00E-09	0.00E+00	0.00E+00	*factor 2*	(4)	T
$H_3^+ + D_2$	$\Rightarrow$	$HD_2^+ + H_2$	1.10E-09	0.00E+00	0.00E+00	$\pm$15%	(3)	M
$HD_2^+ + HD$	$\Rightarrow$	$D_3^+ + H_2$	6.40E-10	0.00E+00	0.00E+00	$\pm$15%	(3)	M
$HD_2^+ + D$	$\Rightarrow$	$D_3^+ + H$	2.00E-09	0.00E+00	0.00E+00	*factor 2*	(4)	T
$H_2D^+ + D_2$	$\Rightarrow$	$D_3^+ + H_2$	7.00E-10	0.00E+00	0.00E+00	$\pm$15%	(3)	M
$H_2D^+ + CO$	$\Rightarrow$	$DCO^+ + H_2$	5.37E-10	0.00E+00	0.00E+00	$<$ 25%	(5)	C
$H_2D^+ + CO$	$\Rightarrow$	$HCO^+ + HD$	1.07E-09	0.00E+00	0.00E+00	$<$ 25%	(5)	C
$HD_2^+ + CO$	$\Rightarrow$	$DCO^+ + HD$	1.07E-09	0.00E+00	0.00E+00	$<$ 25%	(5)	C
$HD_2^+ + CO$	$\Rightarrow$	$HCO^+ + D_2$	5.37E-10	0.00E+00	0.00E+00	$<$ 25%	(5)	C
$D_3^+ + CO$	$\Rightarrow$	$DCO^+ + D_2$	1.61E-09	0.00E+00	0.00E+00	$<$ 25%	(5)	C
$D_3^+ + e^-$	$\Rightarrow$	D + D + D	2.16E-08	-0.50E+00	0.00E+00	$<$ 25%	(5)	C

T, Theoretical/Calculated

M, Laboratory measurements

C, Cloned

Pathways extracted at 1 Myr from four points with T = 10 or 100 K and densities = 10^4 and 10^8 cm^{-3} in the "Primordial" model

(1) Sidhu et al. (1992); (2) Adams & Smith (1985); (3) Giles et al. (1992); (4) Walmsley et al. (2004a);

(5) OSU www.physics.ohio-state.edu/~eric/

Table A.4: Most essential formation and destruction pathways for HCO^+, HOC^+, DCO^+ and DOC^+.

Reaction			α	β	γ	Accuracy	Ref	Note
H_3^+ + CO	⇒	HCO^+ + H_2	1.61E-09	0.00E+00	0.00E+00	< 25%	(1)	M
H_3^+ + CO	⇒	HOC^+ + H_2	9.44E-11	0.00E+00	0.00E+00	< 25%	(1)	M
HOC^+ + H_2	⇒	HCO^+ + H_2	1.00E-11	0.00E+00	0.00E+00	factor 2	(1)	?
CH_3^+ + O	⇒	HCO^+/HOC^+ + H_2	2.05E-10	0.00E+00	0.00E+00	factor 2	(1)	?
HCO^+ + SO	⇒	HSO^+ + CO	3.30E-09	-0.50E+00	0.00E+00	factor 2	(1)	?
HCO^+ + e^-	⇒	CO + H	2.80E-07	-0.69E+00	0.00E+00	< 25%	(1)	?
HCO^+ + C	⇒	CH^+ + CO	1.10E-09	0.00E+00	0.00E+00	factor 2	(1)	?
H_2D^+ + CO	⇒	DCO^+ + H_2	5.37E-10	0.00E+00	0.00E+00	< 25%	(1)	M
HCO^+ + D	⇒	DCO^+ + H	1.00E-09	0.00E+00	0.00E+00	*factor 2*	(2)	M
D_3^+ + CO	⇒	DCO^+ + D_2	1.61E-09	0.00E+00	0.00E+00	< 25%	(1)	C
DOC^+ + H_2	⇒	DCO^+ + H_2	3.33E-12	0.00E+00	0.00E+00	< 50%	(1)	C
CH_2D^+ + O	⇒	DCO^+ + H_2	6.83E-11	0.00E+00	0.00E+00	< 25%	(1)	C
DCO^+ + e^-	⇒	CO + D	2.40E-07	-0.69E+00	0.00E+00	< 25%	(1)	C
DCO^+ + SO	⇒	DSO^+ + CO	3.30E-09	-0.50E+00	0.00E+00	factor 2	(1)	C
DCO^+ + H	⇒	HCO^+ + D	2.20E-09	0.00E+00	7.69E+02	*factor 2*	(2)	M
DCO^+ + C	⇒	CD^+ + CO	1.10E-09	0.00E+00	0.00E+00	factor 2	(1)	C
DCO^+ + HCN	⇒	$HDCN^+$ + CO	7.30E-09	-0.50E+00	0.00E+00	factor 2	(1)	C
DCO^+ + HNC	⇒	$HDCN^+$ + CO	6.63E-09	-0.50E+00	0.00E+00	factor 2	(1)	C

M, Laboratory measurements

C, Cloned

?, No listing for estimation method, most likely theoretical

Pathways extracted at 1 Myr from four points with T = 10 or 100 K and densities = 10^4 and 10^8 cm^{-3} in the "Primordial" model

(1) OSU www.physics.ohio-state.edu/~eric/; (2) KIDA: http://kida.obs.u-bordeaux1.fr/

Table A.5: Most essential formation and destruction pathways for HCN, HNC, DCN and DNC.

Reaction			α	β	γ	Accuracy	Ref	Note
$H_2CN^+ + e^-$	⇒	HCN + H	9.62E-08	-0.65E+00	0.00E+00	factor 2	(1)	M
$H_2CN^+ + e^-$	⇒	HNC + H	1.85E-07	-0.65E+00	0.00E+00	$< 25\%$	(2)	?
$H_2NC^+ + e^-$	⇒	HNC + H	1.80E-07	-0.50E+00	0.00E+00	$< 25\%$	(2)	?
CH_2 + N	⇒	HCN /HNC + H	3.95E-11	-0.17E+00	0.00E+00	$< 25\%$	(2)	T
HNC + H^+	⇒	HCN + H^+	2.78E-08	-0.50E+00	0.00E+00	factor 2	(2)	?
NH (ice) + C (ice)	⇒	HCN (ice)	1.00	0.00	0.00	–	(3)	-
CN (ice) + H (ice)	⇒	HCN (ice)	1.00	0.00	0.00	–	(3)	-
ND (ice) + C (ice)	⇒	DCN (ice)	1.00	0.00	0.00	–	(3)	-
CN (ice) + D (ice)	⇒	DCN (ice)	1.00	0.00	0.00	–	(3)	-
$HDCN^+ + e^-$	⇒	DCN + H	2.33E-07	-0.50E+00	0.00E+00	*factor 2*	(4)	T
$D_2CN^+ + e^-$	⇒	DCN/DNC + D	1.85E-07	-0.65E+00	0.00E+00	*factor 2*	(2)	C
$HDNC^+ + e^-$	⇒	DNC + H	1.66E-07	-0.50E+00	0.00E+00	*factor 2*	(4)	T
HCN + D	⇒	DCN + H	1.00E-10	0.50E+00	5.00E+02	*factor 2*	(5)	T
CHD + N	⇒	DCN + H	1.98E-11	1.67E-01	0.00E+00	$< 50\%$	(5)	T
DCN + H_3^+	⇒	$HDCN^+ + H_2$	8.50E-09	-0.50E+00	0.00E+00	$< 25\%$	(2)	C
DCN + H_3^+	⇒	H_2CN^+ + HD	8.50E-09	-0.50E+00	0.00E+00	$< 25\%$	(2)	C
DCN + HCO^+	⇒	$HDCN^+$ + CO	7.30E-09	-0.50E+00	0.00E+00	factor 2	(2)	C
DCN + H^+	⇒	$DCN^+ + H$	1.39E-08	-0.50E+00	0.00E+00	factor 2	(2)	C
DCN + H	⇒	HCN + D	1.00E-10	0.50E+00	5.00E+02	*factor 2*	(5)	C
DCN + H_3O^+	⇒	$HDCN^+ + H_2O$	4.10E-09	-0.50E+00	0.00E+00	$< 25\%$	(2)	C
DCN + H_3O^+	⇒	H_2CN^+ + HDO	4.10E-09	-0.50E+00	0.00E+00	$< 25\%$	(2)	C
DCN + D_3O^+	⇒	$D_2CN^+ + D_2$	8.20E-09	-0.50E+00	0.00E+00	$< 25\%$	(2)	C

T, Theoretical/Calculated

M, Laboratory measurements

C, Cloned

?, No listing for estimation method, most likely theoretical

Pathways extracted at 1 Myr from four points with T = 10 or 100 K and densities = 10^4 and 10^8 cm^{-3} in the "Primordial" model

(1) Wakelam et al. (2010b); (2) OSU www.physics.ohio-state.edu/~eric/; (3) Garrod & Herbst (2006); (4) Roueff et al. (2005); (5) Schilke et al. (1992)

Table A.6: Most essential formation and destruction pathways for H_2O, HDO and D_2O.

Reaction			α	β	γ	Accuracy	Ref	Note
$H_3O^+ + e^-$	⇒	$H_2O + H$	1.10E-07	-0.50E+00	0.00E+00	< 25%	(1)	M
$H_3O^+ + HCN$	⇒	$H_2O + H_2CN^+$	8.20E-09	-0.50E+00	0.00E+00	< 25%	(2)	?
$H_3O^+ + HNC$	⇒	$H_2O + H_2NC^+$	7.42E-09	-0.50E+00	0.00E+00	factor 2	(2)	?
OH (ice) + H (ice)	⇒	H_2O (ice)	1.00	0.00	0.00	- -	(3)	-
OD (ice) + H (ice)	⇒	HDO (ice)	1.00	0.00	0.00	- -	(3)	-
OH (ice) + D (ice)	⇒	HDO (ice)	1.00	0.00	0.00	- -	(3)	-
$H_2O + H^+$	⇒	$H_2O^+ + H$	7.30E-09	-0.50E+00	0.00E+00	< 25%	(2)	?
$H_2O + H_3^+$	⇒	$H_3O^+ + H_2$	4.50E-09	-0.50E+00	0.00E+00	< 25%	(2)	?
$H_2DO^+ + e^-$	⇒	HDO + H	7.33E-08	-0.50E+00	0.00E+00	< 25%	(2)	C
$HD_2O^+ + e^-$	⇒	HDO + D	7.33E-08	-0.50E+00	0.00E+00	< 25%	(2)	C
$H_2DO^+ + HCN$	⇒	$HDO + H_2CN^+$	4.10E-09	-0.50E+00	0.00E+00	< 25%	(2)	C
$H_2DO^+ + HNC$	⇒	$HDO + H_2CN^+$	3.71E-09	-0.50E+00	0.00E+00	factor 2	(2)	C
$H_2 + OD$	⇒	HDO + H	5.60E-13	0.00E+00	1.04E+03	factor 2	(2)	C
$HDO + HCO^+$	⇒	$H_2DO^+ + CO$	2.10E-09	-0.50E+00	0.00E+00	< 50%	(2)	C
$HDO + H_3^+$	⇒	$H_2DO^+ + H_2$	2.70E-09	-0.50E+00	0.00E+00	< 25%	(2)	C
$HDO + H_3^+$	⇒	$H_3O^+ + HD$	1.80E-09	-0.50E+00	0.00E+00	< 25%	(2)	C
$HDO + C^+$	⇒	$HOC^+/DOC^+ + H$	9.00E-10	-0.50E+00	0.00E+00	< 25%	(2)	C
$HDO + C^+$	⇒	$HCO^+/DCO^+ + H$	4.45E-10	-0.50E+00	0.00E+00	< 25%	(2)	C
$HD_2O^+ + e^-$	⇒	$D_2O + H$	3.67E-08	-0.50E+00	0.00E+00	< 25%	(2)	C
$D_3O^+ + e^-$	⇒	$D_2O + D$	1.10E-07	-0.50E+00	0.00E+00	< 25%	(2)	C
$HD_2O^+ + HCN$	⇒	$D_2O + H_2CN^+$	1.37E-09	-0.50E+00	0.00E+00	< 25%	(2)	C
$HD_2O^+ + HNC$	⇒	$D_2O + H_2CN^+$	1.24E-09	-0.50E+00	0.00E+00	factor 2	(2)	C
HD + OD	⇒	$D_2O + H$	2.80E-13	1.00E+00	1.04E+03	factor 2	(2)	C
OD (ice) + D (ice)	⇒	D_2O (ice)	1.00	0.00	0.00	- -	(3)	C
$D_2O + C^+$	⇒	$DOC^+ + D$	1.80E-09	-0.50E+00	0.00E+00	< 25%	(2)	C
$D_2O + C^+$	⇒	$DCO^+ + D$	8.90E-10	-0.50E+00	0.00E+00	< 25%	(2)	C
$D_2O + H_3^+$	⇒	$HD_2O^+ + H_2$	1.35E-09	-0.50E+00	0.00E+00	< 25%	(2)	C
$D_2O + H_3^+$	⇒	$H_2DO^+ + HD$	2.70E-09	-0.50E+00	0.00E+00	< 25%	(2)	C
$D_2O + H_3^+$	⇒	$H_3O^+ + D_2$	4.50E-10	-0.50E+00	0.00E+00	< 25%	(2)	C
$D_2O + H^+$	⇒	$D_2O^+ + H$	2.43E-09	-0.50E+00	0.00E+00	< 25%	(2)	C
$D_2O + H^+$	⇒	$HDO^+ + D$	4.87E-09	-0.50E+00	0.00E+00	< 25%	(2)	C

M, Laboratory measurement

C, Cloned

?, No listing for estimation method, but most likely theoretical

Pathways extracted at 1 Myr from four points with T = 10 or 100 K and densities = 10^4 and 10^8 cm^{-3} in the "Primordial" model

(1) Jensen et al. (2000); (2) OSU www.physics.ohio-state.edu/~eric/; (3) Garrod & Herbst (2006)

Table A.7: Important reactions for species involved in the main pathways of the assorted deuterated species; H_2D^+, $HD_2{}^+$, $D_3{}^+$, HDO, D_2O, DCO^+ and DCN.

Formation of:	Reaction			α	β	γ	Accuracy	Ref	Note
$H_2{}^+$	$H_2 + h\nu_{CR}$	$\Rightarrow$	$H_2{}^+ + e^-$	9.30E-01	0.00E+00	0.00E+00	factor 2	(1)	T
$CH_3{}^+$	$H_3{}^+ + C$	$\Rightarrow$	$CH^+ + H_2$	2.00E-09	0.00E+00	0.00E+00	factor 2	(1)	?
	$CH^+ + H_2$	$\Rightarrow$	$CH_2{}^+ + H$	1.20E-09	0.00E+00	0.00E+00	$< 25\%$	(1)	?
	$CH_2{}^+ + H_2$	$\Rightarrow$	$CH_3{}^+ + H$	1.20E-09	0.00E+00	0.00E+00	$< 25\%$	(1)	?
	$CH_3{}^+ + HD$	$\Rightarrow$	$CH_2D^+ + H_2$	1.30E-09	0.00E+00	0.00E+00	*factor 2*	(2)	M
	$CH_2D^+ + HD$	$\Rightarrow$	$CHD_2{}^+ + H_2$	6.60E-10	0.00E+00	0.00E+00	*factor 2*	(2)	M
	$CHD_2{}^+ + HD$	$\Rightarrow$	$CD_3{}^+ + H_2$	6.60E-10	0.00E+00	0.00E+00	*factor 2*	(2)	M
	$D_3{}^+ + CH_2$	$\Rightarrow$	$CD_3{}^+ + H_2$	5.19E-11	-0.50E+00	0.00E+00	factor 2	(1)	C
H_2CN^+	$H_3{}^+ + HCN$	$\Rightarrow$	$H_2CN^+ + H_2$	1.70E-08	-0.50E+00	0.00E+00	$< 25\%$	(1)	?
$HDCN^+$	$DCO^+ + HCN$	$\Rightarrow$	$HDCN^+ + CO$	7.30E-09	-0.50E+00	0.00E+00	factor 2	(1)	C
	$DCO^+ + HNC$	$\Rightarrow$	$HDCN^+ + CO$	6.63E-09	-0.50E+00	0.00E+00	factor 2	(1)	C
$HDNC^+$	$CH_2D^+ + N$	$\Rightarrow$	$HDNC^+ + H$	4.47E-11	0.00E+00	0.00E+00	$< 25\%$	(1)	C
D_2CN^+	$HD_2{}^+ + HCN$	$\Rightarrow$	$D_2CN^+ + H_2$	2.83E-09	-0.50E+00	0.00E+00	factor 2	(1)	C
	$HD_2{}^+ + HNC$	$\Rightarrow$	$D_2CN^+ + H_2$	2.50E-09	-0.50E+00	0.00E+00	factor 2	(1)	C
CH_2	$C + H_2$	$\Rightarrow$	CH_2	1.00E-17	0.00E+00	0.00E+00	factor 10	(1)	?
	$CH + H_2$	$\Rightarrow$	$CH_2 + H$	1.20E-09	0.00E+00	0.00E+00	factor 10	(1)	?
CHD	$HD + C$	$\Rightarrow$	CHD	1.20E-17	0.00E+00	0.00E+00	factor 10	(1)	C
OH	$H_2DO^+ + e^-$	$\Rightarrow$	$OD + H + H$	2.60E-10	-5.00E-01	0.00E+00	factor 2	(1)	C
OD^+	$H_2D^+ + O$	$\Rightarrow$	$OD^+ + H_2$	2.67E-10	0.00E+00	0.00E+00	*factor 2*	(3)	C
	$H^+ + OD$	$\Rightarrow$	$OD^+ + H$	8.00E-09	-0.50E+00	0.00E+00	factor 2	(1)	C
HDO^+	$OD^+ + H_2$	$\Rightarrow$	$HDO^+ + H$	7.33E-10	0.00E+00	0.00E+00	$< 25\%$	(1)	C
	$H_3{}^+ + OD$	$\Rightarrow$	$HDO^+ + H_2$	4.75E-09	-0.50E+00	0.00E+00	factor 2	(1)	C
	$H_2D^+ + O$	$\Rightarrow$	$HDO^+ + H$	2.28E-10	-1.56E-01	-1.41E+00	*factor 2*	(3)	C
H_2DO^+	$HDO^+ + H_2$	$\Rightarrow$	$H_2DO^+ + H$	4.57E-10	0.00E+00	0.00E+00	$< 25\%$	(1)	C
	$HD_2{}^+ + O$	$\Rightarrow$	$D_2O^+ + H$	1.14E-10	-1.56E+00	-1.41E+00	*factor 2*	(3)	C
	$D_2O^+ + H_2$	$\Rightarrow$	$HD_2O^+ + H$	3.05E-10	0.00E+00	0.00E+00	$< 25\%$	(1)	C

M, Laboratory measurement

T, Theoretical/Calculated

C, Cloned

?, No listing for estimation method, but most likely theoretical

Pathways extracted at 1 Myr from four points with T = 10 or 100 K and densities = 10^4 and 10^8 cm^{-3} in the "Primordial" model

(1) OSU www.physics.ohio-state.edu/~eric/; (2) Smith et al. (1982a), Smith et al. (1982b); (3) Wakelam et al. (2010b)

Table A.8: Listings of observed interstellar deuterated species.

Species	Sources		Spatial scale	Refs	Model
	Class -I	Class O/I	Beam size [″]		
D / H	$< 4 \times 10^{-4}$		1.8°	1	$10^{-3} - 10^{-2}$
- -	$\leq 2.7 \times 10^{-5}$			2	- -
- -	2.2×10^{-5}		14°	3	- -
- -	≤ 0.14			4	
ND / NH		0.3 - 1.0	41(ND), 22(NH)	7	$10^{-4} - 10^{0}$
OD / OH	$\leq 2.5 \times 10^{-3}$		1.8°	8	$10^{-2} - 10^{0}$
C_2D / C_2H	0.01		33	9	$10^{-3} - 10^{-2}$
- -	0.01	0.18	20	10	- -
D_2O / H_2O		5×10^{-5}	1.5x1.5	11	$< 10^{-5} - 10^{-3}$
DCN / HCN	0.008-0.015			12	$10^{-3} - 10^{-1}$
- -	0.012 - 0.11			13	- -
- -	0.013		20	10	- -
- -	0.023			14	- -
- -		0.005 - 0.02		15	$< 10^{-5} - 10^{-3}$
DCO^+ / HCO^+	0.007 - 0.081			13	$10^{-2} - 10^{0}$
- -	0.02 - 0.18		20	16	- -
- -	0.006 - 0.04		25-57	17	- -
- -	0.0086 - 0.015		20	10	- -
- -	0.031 - 0.059		30-96	18	- -
- -	≤ 0.03			4	- -
- -		0.04[b]	19	$10^{-4} - 10^{-2}$	
DNC / HNC	< 0.014		10 - 30	20	$10^{-3} - 10^{-1}$
- -	0.02 - 0.09		~ 20	21	- -
- -	0.008 - 0.122		17-20[a]	22	- -
- -	0.015 - 0.03		20	10	- -
H_2D^+ / H_3^+		$< 3 \times 10^{-3}$	13[b]	19	$10^{-4} - 10^{-2}$
HDO / H_2O		0.014 - 0.058		23	$10^{-3} - 10^{-2}$
- -		≥ 0.01	10-30	24	- -
- -		$\geq 6 \times 10^{-4}$	3.1×2.5	25	- -
- -		2.94×10^{-5}	1.5x1.5	11	- -
- -		0.03	10-33	26	- -
- -		$0.6 - 5 \times 10^{-4}$		27	- -
- -		$\gtrsim 0.01$	20	28	- -
HDO / H_2O (ice)		0.005 - 0.02		29	$10^{-3} - 10^{-1}$
- -		$8 \times 10^{-4} - 10^{-2}$		30	- -
HDS / H_2S	0.05 - 0.15		20	10	$10^{-2} - 10^{-1}$
N_2D^+ / N_2H^+	0.016 - 0.051		$\sim$30	31	$10^{-2} - 10^{0}$
- -	0.01 - 0.16		10-20	32	- -
- -	0.03 - 0.04		26.4 [a]	33	- -
- -	0.11		44	34	- -
- -	0.08 - 0.14		18 [a]	35	- -
- -	0.02 - 0.52		11 [a]	36	- -
- -	~ 0.1		9-26[a]	37	- -
- -	0.08 - 0.35		20	16	- -
- -		0.005 - 0.014	11-26 [a]	38	$10^{-4} - 10^{-2}$
- -		0.033 - 0.271	11-16	39	- -
- -		0.003 - 0.027	9-26[a]	40	- -

D_2CO / H_2CO	0.11 - 0.19		27 [a]	41	$10^{-3} - 10^{-2}$
- -	0.40			42	- -
- -	0.01 - 0.1		17	43	- -
- -	$\leq$ 0.07		22	44	- -
- -	2.05 - 3.3 $\times 10^{-2}$		20-60	45	- -
- -		0.01 - 0.04	20-60	46	- -
- -		0.022 - 1.04	10-30	47	$10^{-5} - 10^{-3}$
- -		0.02 - 0.4		48	- -
- -		0.03 - 0.16		49	- -
D_2CS / H_2CS	0.333			50	$10^{-3} - 10^{-1}$
HDCO / H_2CO	0.092 - 0.122		27 [a]	41	$10^{-3} - 10^{-1}$
- -	0.015		20	10	- -
- -		0.07 - 4.3	10-30	47	$10^{-4} - 10^{-2}$
- -		0.09 - 2.6	20-60	45	- -
HDCS / H_2CS	0.333			42	$10^{-2} - 10^{-1}$
- -	0.015 - 0.025		>60	51	$10^{-2} - 10^{-1}$
ND_3 / NH_3	1.1 - 65 $\times 10^{-4}$		22 [b]	52	$< 10^{-5} - 10^{-3}$
- -	8 $\times 10^{-4}$		25	53	- -
- -		9.35 $\times 10^{-4}$	25	54	$< 10^{-5} - 10^{-4}$
NH_2D / NH_3	0.1 - 0.8		7	55	$10^{-3} - 10^{-1}$
- -	0.07 - 0.42		22 [b]	52	- -
- -	0.02 - 0.1		20	16	- -
- -	0.025 - 0.18		18	56	- -
- -	< 0.02		20	10	- -
- -		< 0.1	7	55	$10^{-4} - 10^{-2}$
- -		0.071	$\sim$ 20	57	- -
- -		0.06 - 0.1	22	44	- -
- -		0.04 - 0.33	37	58	- -
- -		0.06- 0.1	20	10	- -
- -		0.06	20	28	- -
- -		2.6 - 17.3 $\times 10^{-2}$	20-60	45	- -
NHD_2 / NH_3	0.03 - 0.27		22 [b]	52	$10^{-4} - 10^{-1}$
- -	$\sim$5 $\times 10^{-3}$		22	44	- -
- -		0.02 - 0.4		59	$< 10^{-5} - 10^{-3}$
C_3HD / C_3H_2	0.05 - 0.15		1.7′ [b]	60	$10^{-3} - 10^{-1}$
C_4D / C_4H	4.30 $\times 10^{-3}$		1.7′ [b]	61	$10^{-3} - 10^{-2}$
- -		0.0043-0.023	17-28	62	- -
C_4HD / C_4H_2		0.013 - 0.051	17-28	62	$10^{-3} - 10^{-1}$
CD_3OH/ CH_3OH		0.001 - 0.028	15	63	$< 10^{-5} - 10^{-2}$
C_3H_3D/ C_3H_4	0.04 - 0.18		40-60	64	$10^{-3} - 10^{-1}$
- -	0.1 - 0.22		40	65	- -
- -	0.05 - 0.06		27[a]	66	- -
CH_2DCN/ CH_3CN		$\gtrsim$ 0.01	27 [a]	67	$10^{-2} - 10^{-1}$
CH_2DOH / CH_3OH		0.01$\pm$ 0.73	17-28	62	$10^{-3} - 10^{-2}$
- -		0.05 - 0.30		68	- -
- -		0.05 - 0.95	10-30	47	- -
- -		0.60 - 1.2	11-30	69	- -
CH_3OD/ CH_3OH		0.008 - 0.076	10-30	44	$10^{-4} - 10^{-2}$
- -		0.02 - 0.06	11-30	69	- -
- -		$\leq$ 0.1	20	10	- -

CHD_2OH/ CH_3OH		0.06 - 0.0.51	10-30	47	$10^{-3} - 10^{0}$
- -		0.1 - 0.3	11-30	69	- -
DC_3N /HC_3N	0.010 - 0.020			70	$10^{-3} - 10^{-2}$
DC_3N /HC_3N		0.02 - 0.045	17-28	62	$10^{-4} - 10^{-3}$
DC_5N/HC_5N	0.006 - 0.016			71	$10^{-3} - 10^{-2}$
DC_5N/HC_5N		0.018 - 0.036	17-28	62	$10^{-5} - 10^{-3}$
- -	0.013 - 0.019			72	- -
$DCOOCH_3$ / $HCOOCH_3$	0.02 - 0.06			73	$10^{-3} - 10^{-1}$
- -	$\sim$ 0.15		9-33	71	- -

Young stellar object IR classification -I: Prestellar objects, O/I: Embedded/revealed protostellar sources

(a) Half-power beam width (HPBW)

(b) Full-width half-maximum (FWHM)

(c) LWRS

(1) Cesarsky et al. (1973); (2) Hébrard (2006); (3) Rogers et al. (2007); (4) Heiles et al. (1993);
(5) Lacour et al. (2005); (6) Snow et al. (2008); (7) Bacmann et al. (2010); (8) Allen et al. (1974);
(9) Friberg & Hjalmarson (1986); (10) van Dishoeck et al. (1995); (11) Butner et al. (2007);
(12) Parise et al. (2007); (13) Lis et al. (2002a); (14) Wootten (1987); (15) (Mangum et al. 1991);
(16) Tiné et al. (2000); (17) Anderson et al. (1999); (18) Butner et al. (1995); (19) Stark et al. (1999);
(20) Goicoechea et al. (2009); (21) Hirota et al. (2003); (22) Hirota et al. (2001);
(23) Coutens et al. (2012); (24) Liu et al. (2011); (25) Jørgensen & van Dishoeck (2010);
(26) Parise et al. (2005); (27) Gensheimer et al. (1996); (28) Jacq et al. (1990); (29) Parise et al. (2003);
(30) Teixeira et al. (1999); (31) Chen et al. (2010); (32) Friesen et al. (2010);
(33) Miettinen et al. (2009); (34) Fontani et al. (2008); (35) Belloche et al. (2006); (36) Crapsi et al. (2005);
(37) Crapsi et al. (2004); (38) Alonso-Albi et al. (2010); (39) Emprechtinger et al. (2009);
(40) Fontani et al. (2006); (41) Bergman et al. (2011); (42) Marcelino et al. (2005); (43) Bacmann et al. (2003);
(44) Roueff et al. (2000); (45) Turner (1990); (46) Roberts & Millar (2007); (47) Parise et al. (2006);
(48) Loinard et al. (2002); (49) Ceccarelli et al. (2001); (50) Marcelino et al. (2005); (51) Minowa et al. (1997);
(52) Roueff et al. (2005); (53) Lis et al. (2002b); (54) van der Tak et al. (2002); (55) Busquet et al. (2010);
(56) Saito et al. (2000); (57) Shah & Wootten (2001); (58) Hatchell (2003); (59) Loinard et al. (2003);
(60) Bell et al. (1988); (61) Sakai et al. (2009); (62) Suzuki (1987); (63) Parise et al. (2004);
(64) Markwick et al. (2005); (65) Markwick et al. (2002); (66) Gerin et al. (1992a); (67) Gerin et al. (1992b);
(68) Bacmann et al. (2007); (69) Parise et al. (2002); (70) Suzuki (1987); (71) MacLeod et al. (1981);
(72) Schloerb et al. (1981); (73) Margulès et al. (2010)

BIBLIOGRAPHY

Adams, N. G. & Smith, D. 1985, ApJ Lett., 294, L63

Adams, W. S. 1941, ApJ, 93, 11

Agundez, M. & Wakelam, V. 2013, ArXiv e-prints

Aikawa, Y. 2007, ApJ Lett., 656, L93

Aikawa, Y. & Herbst, E. 1999a, ApJ, 526, 314

Aikawa, Y. & Herbst, E. 1999b, A&A., 351, 233

Aikawa, Y. & Herbst, E. 2001, A&A., 371, 1107

Aikawa, Y., Kamuro, D., Sakon, I., et al. 2012a, A&A., 538, A57

Aikawa, Y., Ohashi, N., & Herbst, E. 2003, ApJ, 593, 906

Aikawa, Y., Wakelam, V., Garrod, R. T., & Herbst, E. 2008, ApJ, 674, 984

Aikawa, Y., Wakelam, V., Hersant, F., Garrod, R. T., & Herbst, E. 2012b, ApJ, 760, 40

Akimkin, V., Zhukovska, S., Wiebe, D., et al. 2013, Astrophys. J, 766, 8

Al-Halabi, A. & van Dishoeck, E. F. 2007, MNRAS, 382, 1648

Albertsson, T., Semenov, D. A., Vasyunin, A. I., Henning, T., & Herbst, E. 2013, ApJS, 207, 27

Alexander, C. M. O. ., Bowden, R., Fogel, M. L., et al. 2012, Science, 337, 721

Allen, M., Cesarsky, D. A., & Crutcher, R. M. 1974, ApJ, 188, 33

Alonso-Albi, T., Fuente, A., Crimier, N., et al. 2010, A&A., 518, A52

Anders, E. 1989, Nature, 342, 255

Anderson, I. M., Caselli, P., Haikala, L. K., & Harju, J. 1999, A&A., 347, 983

André, P., Basu, S., & Inutsuka, S. 2009, The formation and evolution of prestellar cores, ed. Chabrier, G. (Cambridge University Press), 254

Andrews, S. M. & Williams, J. P. 2007, Astrophys. J, 659, 705

Anicich, V. G. 1993, Journal of Physical and Chemical Reference Data, 22, 1469

Bacmann, A. 2004, Baltic Astronomy, 13, 402

Bacmann, A., Caux, E., Hily-Blant, P., et al. 2010, A&A., 521, L42

Bacmann, A., Lefloch, B., Ceccarelli, C., et al. 2002, A&A., 389, L6

Bacmann, A., Lefloch, B., Ceccarelli, C., et al. 2003, ApJ Lett., 585, L55

Bacmann, A., Lefloch, B., Parise, B., Ceccarelli, C., & Steinacker, J. 2007, in Molecules in Space and Laboratory, ed. J. L. Lemaire & F. Combes

Bacmann, A., Taquet, V., Faure, A., Kahane, C., & Ceccarelli, C. 2012, A&A., 541, L12

Baglin, A. 2003, Advances in Space Research, 31, 345

Balsiger, H., Altwegg, K., & Geiss, J. 1995, J. Geophys. Res., 100, 5827

Banzatti, A., Meyer, M. R., Bruderer, S., et al. 2012, Astrophys. J, 745, 90

Barzel, B. & Biham, O. 2007, ApJ Lett., 658, L37

Bayet, E., Awad, Z., & Viti, S. 2010, ApJ, 725, 214

Bell, M. B., Avery, L. W., Matthews, H. E., et al. 1988, ApJ, 326, 924

Bell, M. B., Feldman, P. A., Travers, M. J., et al. 1997, ApJ Lett., 483, L61

Belloche, A., Parise, B., van der Tak, F. F. S., et al. 2006, A&A., 454, L51

Bergin, E. A., Aikawa, Y., Blake, G. A., & van Dishoeck, E. F. 2007, Protostars and Planets V, 751

Bergin, E. A., Cleeves, L. I., Gorti, U., et al. 2013, Nature, 493, 644

Bergin, E. A., Hogerheijde, M. R., Brinch, C., et al. 2010, A&A., 521, L33

Bergin, E. A. & Tafalla, M. 2007, Ann. Rev. Astron. Astrophys., 45, 339

Bergman, P., Parise, B., Liseau, R., & Larsson, B. 2011, A&A., 527, A39

Beuther, H., Leurini, S., Schilke, P., et al. 2007, A&A., 466, 1065

Biham, O., Furman, I., Pirronello, V., & Vidali, G. 2001, ApJ, 553, 595

Birnstiel, T., Dullemond, C. P., & Brauer, F. 2010a, A&A., 513, A79

Birnstiel, T., Ricci, L., Trotta, F., et al. 2010b, A&A., 516, L14

Biver, N., Bockelée-Morvan, D., Crovisier, J., et al. 2006, A&A., 449, 1255

Boato, G. 1954, Geochimica et Cosmochimica Acta, 6, 209

Bockelée-Morvan, D., Biver, N., Swinyard, B., et al. 2012, A&A., 544, L15

Bockelee-Morvan, D., Gautier, D., Lis, D. C., et al. 1998, Icarus, 133, 147

Bockelée-Morvan, D., Woodward, C. E., Kelley, M. S., & Wooden, D. H. 2009, Astrophys. J, 696, 1075

Boger, G. I. & Sternberg, A. 2005, ApJ, 632, 302

Bonev, B. P., Mumma, M. J., Gibb, E. L., et al. 2009, ApJ, 699, 1563

Bonev, B. P., Villanueva, G. L., Paganini, L., et al. 2013, Icarus, 222, 740

Boogert, A. C. A. & Ehrenfreund, P. 2004, in Astronomical Society of the Pacific Conference Series, Vol. 309, Astrophysics of Dust, ed. A. N. Witt, G. C. Clayton, & B. T. Draine, 547

Borucki, W. J., Koch, D., Basri, G., et al. 2010, Science, 327, 977

Boss, A. P. 1998, Annual Review of Earth and Planetary Sciences, 26, 53

Boss, A. P. 2004, ApJ, 616, 1265

Bottke, W. F., Vokrouhlický, D., Minton, D., et al. 2012, Nature, 485, 78

Bouwman, J., Henning, T., Hillenbrand, L. A., et al. 2008, Astrophys. J, 683, 479

Brauer, F., Dullemond, C. P., & Henning, T. 2008, A&A., 480, 859

Brauer, F., Dullemond, C. P., Johansen, A., et al. 2007, A&A., 469, 1169

Brown, P. D., Charnley, S. B., & Millar, T. J. 1988, MNRAS, 231, 409

Brown, P. N., Byrne, G. D., & Hindmarsh, A. C. 1989, SIAM J. Sci. Stat. Comput., 10, 1038

Brown, R. H., Lauretta, D. S., Schmidt, B., & Moores, J. 2012, Planet. Space Sci., 60, 166

Busquet, G., Palau, A., Estalella, R., et al. 2010, A&A., 517, L6

Butner, H. M., Charnley, S. B., Ceccarelli, C., et al. 2007, ApJ Lett., 659, L137

Butner, H. M., Lada, E. A., & Loren, R. B. 1995, ApJ, 448, 207

Cami, J., Bernard-Salas, J., Peeters, E., & Malek, S. E. 2010, Science, 329, 1180

Campins, H., Swindle, T., & Kring, D. 2005, in Cellular Origin, Life in Extreme Habitats and Astrobiology, Vol. 6, Origins, ed. J. Seckbach (Springer Netherlands), 571–591

Canup, R. M. 2012, Science, 338, 1052

Cardelli, J. A., Meyer, D. M., Jura, M., & Savage, B. D. 1996, ApJ, 467, 334

Carr, J. S. & Najita, J. R. 2008, Science, 319, 1504

Carruthers, G. R. 1970, ApJ Lett., 161, L81

Caselli, P. 2003, Ap&SS, 285, 619

Caselli, P., Hasegawa, T. I., & Herbst, E. 1998, ApJ, 495, 309

Caselli, P., Keto, E., Pagani, L., et al. 2010, A&A., 521, L29

Caselli, P., van der Tak, F. F. S., Ceccarelli, C., & Bacmann, A. 2003, A&A., 403, L37

Caselli, P., Vastel, C., Ceccarelli, C., et al. 2008, A&A., 492, 703

Cazaux, S., Caselli, P., Cobut, V., & Le Bourlot, J. 2008, A&A., 483, 495

Cazaux, S., Caselli, P., & Spaans, M. 2011, ApJ Lett., 741, L34

Ceccarelli, C. 2002, Planet. Space Sci., 50, 1267

Ceccarelli, C., Caux, E., Loinard, L., et al. 1999, A&A., 342, L21

Ceccarelli, C. & Dominik, C. 2005, A&A., 440, 583

Ceccarelli, C., Dominik, C., Caux, E., Lefloch, B., & Caselli, P. 2005, ApJ Lett., 631, L81

Ceccarelli, C., Dominik, C., Lefloch, B., Caselli, P., & Caux, E. 2004, ApJ Lett., 607, L51

Ceccarelli, C., Loinard, L., Castets, A., et al. 2001, A&A., 372, 998

Cernicharo, J., Polehampton, E., & Goicoechea, J. R. 2007, ApJ Lett., 657, L21

Cernicharo, J., Tercero, B., Fuente, A., et al. 2013, ApJ Lett., 771, L10

Cesarsky, D. A., Moffet, A. T., & Pasachoff, J. M. 1973, ApJ Lett., 180, L1

Chabot, M., Tuna, T., Béroff, K., et al. 2010, A&A., 524, A39

Chambers, J. E. 2004, Earth and Planetary Science Letters, 223, 241

Chang, Q. & Herbst, E. 2012, ApJ, 759, 147

Chapillon, E., Parise, B., Guilloteau, S., & Du, F. 2011, A&A., 533, A143

Charnley, S. B. 1998, ApJ Lett., 509, L121

Charnley, S. B. 2001, ApJ Lett., 562, L99

Charnley, S. B., Tielens, A. G. G. M., & Rodgers, S. D. 1997, ApJ Lett., 482, L203

Chen, H., Liu, S., Su, Y., & Zhang, Q. 2010, ApJ Lett., 713, L50

Chen, H.-R., Liu, S.-Y., Su, Y.-N., & Wang, M.-Y. 2011, ApJ, 743, 196

Cheung, A. C., Rank, D. M., Townes, C. H., Thornton, D. D., & Welch, W. J. 1968, Physical Review Letters, 21, 1701

Cheung, A. C., Rank, D. M., Townes, C. H., Thornton, D. D., & Welch, W. J. 1969, Nature, 221, 626

Cortes, S. R., Meyer, M. R., Carpenter, J. M., et al. 2009, ApJ, 697, 1305

Costanzo, G., Pino, S., Ciciriello, F., & Di Mauro, E. 2009, Journal of Biological Chemistry, 284, 33206

Coutens, A., Vastel, C., Caux, E., et al. 2012, A&A., 539, A132

Coutens, A., Vastel, C., Cazaux, S., et al. 2013, A&A., 553, A75

Crabtree, K. N., Indriolo, N., Kreckel, H., Tom, B. A., & McCall, B. J. 2011, ApJ, 729, 15

Crabtree, K. N. & McCall, B. J. 2012, Philosophical Transactions of the Royal Society A: Mathematical, Physical and Engineering Sciences, 370, 5055

Crabtree, K. N. & McCall, B. J. 2013, The Journal of Physical Chemistry A, 117, 9950

Crapsi, A., Caselli, P., Walmsley, C. M., et al. 2005, ApJ, 619, 379

Crapsi, A., Caselli, P., Walmsley, C. M., et al. 2004, A&A., 420, 957

Croswell, K. & Dalgarno, A. 1985, ApJ, 289, 618

Crovisier, J., Leech, K., Bockelée-Morvan, D., et al. 1997, Science, 275, 1904

Cuppen, H. M., van Dishoeck, E. F., Herbst, E., & Tielens, A. G. G. M. 2009, A&A., 508, 275

Cyr, K. E., Sears, W. D., & Lunine, J. I. 1998, Icarus, 135, 537

D'Alessio, P., Calvet, N., & Hartmann, L. 2001, ApJ, 553, 321

D'Alessio, P., Calvet, N., Hartmann, L., Lizano, S., & Cantó, J. 1999, ApJ, 527, 893

Dalgarno, A. & Black, J. H. 1976, Reports on Progress in Physics, 39, 573

Demyk, K., Bottinelli, S., Caux, E., et al. 2010, A&A., 517, A17

Desch, S. J. 2007, ApJ, 671, 878

D'Hendecourt, L. B. & Jourdain de Muizon, M. 1989, A&A., 223, L5

Dobrijevic, M. & Parisot, J. P. 1998, Planet. Space Sci., 46, 491

Dominik, C., Ceccarelli, C., Hollenbach, D., & Kaufman, M. 2005, Astrophys. J, 635, L85

dos Santos, S. F., Kokoouline, V., & Greene, C. H. 2007, The Journal of Chemical Physics, 127, 124309

Douglas, A. E. & Herzberg, G. 1941, ApJ, 94, 381

Draine, B. T. 1978, Astrophys. J, 36, 595

Draine, B. T. & Bertoldi, F. 1996, ApJ, 468, 269

Druard, C. & Wakelam, V. 2012, MNRAS, 426, 354

Du, F. & Parise, B. 2011, A&A., 530, A131

Dulieu, F., Amiaud, L., Congiu, E., et al. 2010, A&A., 512, A30

Dullemond, C. P. & Dominik, C. 2004, A&A., 421, 1075

Dullemond, C. P. & Dominik, C. 2005, A&A., 434, 971

Dullemond, C. P., Dominik, C., & Natta, A. 2001, ApJ, 560, 957

Dumouchel, F., Faure, A., & Lique, F. 2010, MNRAS, 406, 2488

Duncan, M., Quinn, T., & Tremaine, S. 1987, AJ, 94, 1330

Eberhardt, P., Reber, M., Krankowsky, D., & Hodges, R. R. 1995, A&A., 302, 301

Elser, S., Meyer, M. R., & Moore, B. 2012, Icarus, 221, 859

Emel'Yanenko, V. V., Asher, D. J., & Bailey, M. E. 2007, MNRAS, 381, 779

Emprechtinger, M., Caselli, P., Volgenau, N. H., Stutzki, J., & Wiedner, M. C. 2009, A&A., 493, 89

Fayolle, E. C., Öberg, K. I., Cuppen, H. M., Visser, R., & Linnartz, H. 2011, A&A., 529, A74

Fedele, D., Bruderer, S., van Dishoeck, E. F., et al. 2012, A&A., 544, L9

Flock, M., Dzyurkevich, N., Klahr, H., Turner, N. J., & Henning, T. 2011, Astrophys. J, 735, 122

Florescu-Mitchell, A. I. & Mitchell, J. B. A. 2006, Phys. Rep., 430, 277

Flower, D. R., Pineau des Forêts, G., & Walmsley, C. M. 2004a, A&A., 427, 887

Flower, D. R., Pineau des Forêts, G., & Walmsley, C. M. 2004b, A&A., 427, 887

Flower, D. R., Pineau Des Forêts, G., & Walmsley, C. M. 2006, A&A., 449, 621

Fogel, J. K. J., Bethell, T. J., Bergin, E. A., Calvet, N., & Semenov, D. 2011, ApJ, 726, 29

Fontani, F., Caselli, P., Bourke, T. L., Cesaroni, R., & Brand, J. 2008, A&A., 477, L45

Fontani, F., Caselli, P., Crapsi, A., et al. 2006, A&A., 460, 709

Friberg, P. & Hjalmarson, A. 1986, Highlights of Astronomy, 7, 513

Friesen, R. K., Di Francesco, J., Myers, P. C., et al. 2010, ApJ, 718, 666

Furuya, K., Aikawa, Y., Nomura, H., Hersant, F., & Wakelam, V. 2013, ArXiv e-prints

Gail, H.-P. 2001, Astron. Astrophys, 378, 192

Gail, H.-P. 2002, A&A., 390, 253

Gardner, J. P., Mather, J. C., Clampin, M., et al. 2006, Space Sci. Rev., 123, 485

Garrod, R. T. 2008, A&A., 491, 239

Garrod, R. T. 2013, ApJ, 765, 60

Garrod, R. T. & Herbst, E. 2006, A&A., 457, 927

Garrod, R. T. & Pauly, T. 2011, ApJ, 735, 15

Garrod, R. T., Vasyunin, A. I., Semenov, D. A., Wiebe, D. S., & Henning, T. 2009, ApJ Lett., 700, L43

Garrod, R. T., Wakelam, V., & Herbst, E. 2007, A&A., 467, 1103

Garrod, R. T., Weaver, S. L. W., & Herbst, E. 2008, ApJ, 682, 283

Geballe, T. R., McCall, B. J., Hinkle, K. H., & Oka, T. 1999, ApJ, 510, 251

Geballe, T. R. & Oka, T. 1996, Nature, 384, 334

Geiss, J. & Reeves, H. 1981, A&A., 93, 189

Genda, H. & Ikoma, M. 2008, Icarus, 194, 42

Gensheimer, P. D., Mauersberger, R., & Wilson, T. L. 1996, A&A., 314, 281

Geppert, W. D., Hamberg, M., Thomas, R. D., et al. 2006, Faraday Discussions, 133, 177

Geppert, W. D. & Larsson, M. 2008, Molecular Physics, 106, 2199

Geppert, W. D., Thomas, R. D., Ehlerding, A., et al. 2005, Journal of Physics Conference Series, 4, 26

Gerin, M., Combes, F., Wlodarczak, G., Encrenaz, P., & Laurent, C. 1992a, A&A., 253, L29

Gerin, M., Combes, F., Wlodarczak, G., et al. 1992b, A&A., 259, L35

Gerlich, D. 1990, J. Chem. Phys., 92, 2377

Gerlich, D., Herbst, E., & Roueff, E. 2002, Planet. Space Sci., 50, 1275

Gerlich, D. & Horning, S. 1992, Chem. Rev., 92, 1509

Gibb, E. L., Bonev, B. P., Villanueva, G., et al. 2012, ApJ, 750, 102

Gibb, E. L., Brittain, S. D., Rettig, T. W., et al. 2010, ApJ, 715, 757

Giles, K., Adams, N. G., & Smith, D. 1992, The Journal of Physical Chemistry, 96, 7645

Glassgold, A. E., Galli, D., & Padovani, M. 2012, ApJ, 756, 157

Glosík, J., Plašil, R., Korolov, I., et al. 2009, Phys. Rev. A, 79, 052707

Goicoechea, J. R., Pety, J., Gerin, M., Hily-Blant, P., & Le Bourlot, J. 2009, A&A., 498, 771

Gomes, R., Levison, H. F., Tsiganis, K., & Morbidelli, A. 2005, Nature, 435, 466

Goto, M., Usuda, T., Nagata, T., et al. 2008, ApJ, 688, 306

Graedel, T. E., Langer, W. D., & Frerking, M. A. 1982, ApJS, 48, 321

Grussie, F., Berg, M. H., Crabtree, K. N., et al. 2012, ApJ, 759, 21

Guelin, M., Langer, W. D., Snell, R. L., & Wootten, H. A. 1977, ApJ Lett., 217, L165

Guilloteau, S., Dutrey, A., Piétu, V., & Boehler, Y. 2011, Astron. Astrophys, 529, A105

Guilloteau, S., Piétu, V., Dutrey, A., & Guélin, M. 2006, A&A., 448, L5

Hama, T., Kuwahata, K., Watanabe, N., et al. 2012, ApJ, 757, 185

Hamberg, M., Österdahl, F., Thomas, R. D., et al. 2010a, A&A., 514, A83

Hamberg, M., Zhaunerchyk, V., Vigren, E., et al. 2010b, A&A., 522, A90

Hansen, B. M. S. 2009, ApJ, 703, 1131

Harada, N., Herbst, E., & Wakelam, V. 2010, ApJ, 721, 1570

Harada, N., Herbst, E., & Wakelam, V. 2012, ApJ, 756, 104

Harju, J., Haikala, L. K., Lehtinen, K., et al. 2006, A&A., 454, L55

Hartmann, W. K., Ryder, G., Dones, L., & Grinspoon, D. 2000, The Time-Dependent Intense Bombardment of the Primordial Earth/Moon System, ed. R. M. Canup, K. Righter, & et al., 493–512

Hartogh, P., Lis, D. C., Bockelée-Morvan, D., et al. 2011, Nature, 478, 218

Hasegawa, T. I. & Herbst, E. 1993, MNRAS, 263, 589

Hasegawa, T. I., Herbst, E., & Leung, C. M. 1992, ApJS, 82, 167

Hatchell, J. 2003, A&A., 403, L25

Hébrard, G. 2006, in Astronomical Society of the Pacific Conference Series, Vol. 348, Astrophysics in the Far Ultraviolet: Five Years of Discovery with FUSE, ed. G. Sonneborn, H. W. Moos, & B.-G. Andersson, 47

Heiles, C., McCullough, P. R., & Glassgold, A. E. 1993, ApJS, 89, 271

Heinzeller, D., Nomura, H., Walsh, C., & Millar, T. J. 2011a, Astrophys. J, 731, 115

Heinzeller, D., Nomura, H., Walsh, C., & Millar, T. J. 2011b, ApJ, 731, 115

Henning, T. & Meeus, G. 2011, Dust Processing and Mineralogy in Protoplanetary Accretion Disks, ed. P. J. V. Garcia, 114–148

Herbst, E. 1982, A&A., 111, 76

Herbst, E. 1985, ApJ, 291, 226

Herbst, E., Adams, N. G., Smith, D., & Defrees, D. J. 1987, ApJ, 312, 351

Herbst, E. & Klemperer, W. 1973, ApJ, 185, 505

Herbst, E., Terzieva, R., & Talbi, D. 2000, MNRAS, 311, 869

Herbst, E. & van Dishoeck, E. F. 2009, Ann. Rev. Astron. Astrophys., 47, 427

Herczeg, G. J., Karska, A., Bruderer, S., et al. 2012, A&A., 540, A84

Hersant, F., Wakelam, V., Dutrey, A., Guilloteau, S., & Herbst, E. 2009, A&A., 493, L49

Hidaka, H., Watanabe, M., Kouchi, A., & Watanabe, N. 2009, ApJ, 702, 291

Hiraoka, K., Mochizuki, N., & Wada, A. 2006, in American Institute of Physics Conference Series, Vol. 855, Astrochemistry - From Laboratory Studies to Astronomical Observations, ed. R. I. Kaiser, P. Bernath, Y. Osamura, S. Petrie, & A. M. Mebel , 86–99

Hirota, T., Ikeda, M., & Yamamoto, S. 2001, ApJ, 547, 814

Hirota, T., Ikeda, M., & Yamamoto, S. 2003, ApJ, 594, 859

Ho, P. T. P. & Townes, C. H. 1983, Ann. Rev. Astron. Astrophys., 21, 239

Hogerheijde, M. R., Bergin, E. A., Brinch, C., et al. 2011, Science, 334, 338

Honvault, P., Jorfi, M., González-Lezana, T., Faure, A., & Pagani, L. 2011, Physical Review Letters, 107, 023201

Hoover, R. B. 2006, Biogeosciences Discussions, 3, 23

Horn, A., Møllendal, H., Sekiguchi, O., et al. 2004, ApJ, 611, 605

Hornekær, L., Baurichter, A., Petrunin, V. V., Field, D., & Luntz, A. C. 2003, Science, 302, 1943

Howard, A. W. 2013, Science, 340, 572

Hugo, E., Asvany, O., & Schlemmer, S. 2009, J. Chem. Phys., 130, 164302

Hutsemékers, D., Manfroid, J., Jehin, E., Zucconi, J.-M., & Arpigny, C. 2008, A&A., 490, L31

Ilgner, M., Henning, T., Markwick, A. J., & Millar, T. J. 2004, A&A., 415, 643

Ilgner, M. & Nelson, R. P. 2006, A&A., 445, 223

Indriolo, N., Geballe, T. R., Oka, T., & McCall, B. J. 2007, ApJ, 671, 1736

Indriolo, N. & McCall, B. J. 2012, ApJ, 745, 91

Izidoro, A., de Souza Torres, K., Winter, O. C., & Haghighipour, N. 2013, ApJ, 767, 54

Jacq, T., Walmsley, C. M., Henkel, C., et al. 1990, A&A., 228, 447

Jacquet, E. & Robert, F. 2013, Icarus, 223, 722

Javaux, E. J. & Dehant, V. 2010, A&A Rev., 18, 383

Jensen, M. J., Bilodeau, R. C., Safvan, C. P., et al. 2000, ApJ, 543, 764

Jørgensen, J. K. & van Dishoeck, E. F. 2010, ApJ Lett., 725, L172

Juhász, A., Bouwman, J., Henning, T., et al. 2010, ApJ, 721, 431

Kaeufl, H.-U., Ballester, P., Biereichel, P., et al. 2004, in Society of Photo-Optical Instrumentation Engineers (SPIE) Conference Series, Vol. 5492, Society of Photo-Optical Instrumentation Engineers (SPIE) Conference Series, ed. A. F. M. Moorwood & M. Iye, 1218–1227

Kalvans, J. & Shmeld, I. 2011, in IAU Symposium, Vol. 280, IAU Symposium, 212P

Kasting, J. F., Whitmire, D. P., & Reynolds, R. T. 1993, Icarus, 101, 108

Katz, N., Furman, I., Biham, O., Pirronello, V., & Vidali, G. 1999, ApJ, 522, 305

Kawakita, H. & Kobayashi, H. 2009, ApJ, 693, 388

Kelley, M. S., Woodward, C. E., Harker, D. E., et al. 2006, Astrophys. J, 651, 1256

Kenyon, S. J. & Luu, J. X. 1998, AJ, 115, 2136

Kerridge, J. F. 1985, Geochimica et Cosmochimica Acta, 49, 1707

Kessler, J. E., Blake, G. A., & Qi, C. 2003, in SFChem 2002: Chemistry as a Diagnostic of Star Formation, ed. C. L. Curry & M. Fich, 188

Kokoouline, V. & Greene, C. H. 2003a, Physical Review Letters, 90, 133201

Kokoouline, V. & Greene, C. H. 2003b, Phys. Rev. A, 68, 012703

Kokoouline, V., Greene, C. H., & Esry, B. D. 2001, Nature, 412, 891

Kreckel, H., Motsch, M., Mikosch, J., et al. 2005, Physical Review Letters, 95, 263201

Kreckel, H., Novotný, O., Crabtree, K. N., et al. 2010, Phys. Rev. A, 82, 042715

Kristensen, L. E., Visser, R., van Dishoeck, E. F., et al. 2010, A&A., 521, L30

Kuan, Y.-J., Chuang, H.-E., Charnley, S., & Huang, H.-C. 2008, in COSPAR, Plenary Meeting, Vol. 37, HDCO in Comet C/2002 T7 (LINEAR), 1640

Laas, J. C., Garrod, R. T., Herbst, E., & Widicus Weaver, S. L. 2011, ApJ, 728, 71

Lacour, S., André, M. K., Sonnentrucker, P., et al. 2005, A&A., 430, 967

Larsson, M. 1995, Reports on Progress in Physics, 58, 1267

Larsson, M. 2000, in Phil. Trans. R. Soc. Lond. A, Vol. 358, Astronomy, physics and chemistry of H^+_3, 2433–2444

Larsson, M., Danared, H., Larson, A., et al. 1997, Phys. Rev. Lett., 79, 395

Launhardt, R., Nutter, D., Ward-Thompson, D., et al. 2010, ApJS, 188, 139

Launhardt, R., Stutz, A. M., Schmiedeke, A., et al. 2013, A&A., 551, A98

Lécluse, C. & Robert, F. 1994, Geochim. Cosmochim. Acta, 58, 2927

Lecuyer, C., Gillet, P., & Robert, F. 1998, Chemical Geology, 145, 249

Lee, H.-H., Herbst, E., Pineau des Forets, G., Roueff, E., & Le Bourlot, J. 1996, A&A., 311, 690

Lee, H.-H., Roueff, E., Pineau des Forets, G., et al. 1998a, A&A., 334, 1047

Lee, H.-H., Roueff, E., Pineau des Forets, G., et al. 1998b, A&A., 334, 1047

Leger, A., Jura, M., & Omont, A. 1985, Astron. Astrophys, 144, 147

Lellouch, E., Bézard, B., Fouchet, T., et al. 2001, A&A., 370, 610

Lindsay, C. M. & McCall, B. J. 2001, Journal of Molecular Spectroscopy, 210, 60

Linsky, J. L. 2003, Space Sci. Rev., 106, 49

Lipshtat, A. & Biham, O. 2004, Physical Review Letters, 93, 170601

Lis, D. C., Biver, N., Bockelée-Morvan, D., et al. 2013, ApJ Lett., 774, L3

Lis, D. C., Gerin, M., Phillips, T. G., & Motte, F. 2002a, ApJ, 569, 322

Lis, D. C., Roueff, E., Gerin, M., et al. 2002b, ApJ Lett., 571, L55

Liszt, H. S. 2006, Royal Society of London Philosophical Transactions Series A, 364, 3049

Liu, F., Parise, B., Kristensen, L., et al. 2011, A&A., 527, A19

Loinard, L., Castets, A., Ceccarelli, C., et al. 2003, in SFChem 2002: Chemistry as a Diagnostic of Star Formation, ed. C. L. Curry & M. Fich, 351

Loinard, L., Castets, A., Ceccarelli, C., et al. 2002, Planet. Space Sci., 50, 1205

Loren, R. B. & Wootten, A. 1985, ApJ, 299, 947

Luine, J. A. & Dunn, G. H. 1985, ApJ Lett., 299, L67

MacLeod, J. M., Avery, L. W., & Broten, N. W. 1981, ApJ Lett., 251, L33

Mangum, J. G., Plambeck, R. L., & Wootten, A. 1991, ApJ, 369, 169

Marcelino, N., Cernicharo, J., Roueff, E., Gerin, M., & Mauersberger, R. 2005, ApJ, 620, 308

Maret, S., Faure, A., Scifoni, E., & Wiesenfeld, L. 2009, MNRAS, 399, 425

Margulès, L., Huet, T. R., Demaison, J., et al. 2010, ApJ, 714, 1120

Markwick, A. J., Charnley, S. B., Butner, H. M., & Millar, T. J. 2005, ApJ Lett., 627, L117

Markwick, A. J., Millar, T. J., & Charnley, S. B. 2002, A&A., 381, 560

Marty, B. 2012, Earth and Planetary Science Letters, 313, 56

Marty, B., Alexander, C. M. O., & Raymond, S. N. 2012, ArXiv e-prints

Masset, F. & Snellgrove, M. 2001, MNRAS, 320, L55

Mayor, M. & Queloz, D. 1995, Nature, 378, 355

McCall, B. J., Geballe, T. R., Hinkle, K. H., & Oka, T. 1998, Science, 279, 1910

McCall, B. J., Hinkle, K. H., Geballe, T. R., et al. 2002, ApJ, 567, 391

McCall, B. J., Huneycutt, A. J., Saykally, R. J., et al. 2004, Phys. Rev. A, 70, 052716

McCall, B. J., Huneycutt, A. J., Saykally, R. J., et al. 2003, Nature, 422, 500

McElroy, D., Walsh, C., Markwick, A. J., et al. 2013a, A&A., 550, A36

McElroy, D., Walsh, C., Markwick, A. J., et al. 2013b, A&A., 550, A36

McKee, C. F. & Ostriker, E. C. 2007, Ann. Rev. Astron. Astrophys., 45, 565

McKellar, A. 1940, PASP, 52, 187

Meeus, G., Pinte, C., Woitke, P., et al. 2010, A&A., 518, L124

Meier, R., Owen, T. C., Matthews, H. E., et al. 1998, Science, 279, 842

Miettinen, O., Harju, J., Haikala, L. K., & Juvela, M. 2012, A&A., 538, A137

Miettinen, O., Harju, J., Haikala, L. K., Kainulainen, J., & Johansson, L. E. B. 2009, A&A., 500, 845

Millar, T. J., Bennett, A., & Herbst, E. 1989, ApJ, 340, 906

Millar, T. J., Defrees, D. J., McLean, A. D., & Herbst, E. 1988, A&A., 194, 250

Millar, T. J., Farquhar, P. R. A., & Willacy, K. 1997, A&AS, 121, 139

Min, M., Dullemond, C. P., Kama, M., & Dominik, C. 2011, Icarus, 212, 416

Minowa, H., Satake, M., Hirota, T., et al. 1997, ApJ Lett., 491, L63

Morbidelli, A., Chambers, J., Lunine, J. I., et al. 2000, Meteoritics and Planetary Science, 35, 1309

Morbidelli, A. & Crida, A. 2007, Icarus, 191, 158

Morbidelli, A., Levison, H. F., Tsiganis, K., & Gomes, R. 2005, Nature, 435, 462

Morbidelli, A., Lunine, J. I., O'Brien, D. P., Raymond, S. N., & Walsh, K. J. 2012, Annual Review of Earth and Planetary Sciences, 40, 251

Morfill, G. E. & Voelk, H. J. 1984, ApJ, 287, 371

Mottram, J. C., van Dishoeck, E. F., Schmalzl, M., et al. 2013, ArXiv e-prints

Müller, H. S. P., Schlöder, F., Stutzki, J., & Winnewisser, G. 2005, Journal of Molecular Structure, 742, 215

Müller, H. S. P., Thorwirth, S., Roth, D. A., & Winnewisser, G. 2001, A&A., 370, L49

Mumma, M. J., Weaver, H. A., & Larson, H. P. 1987, Astron. Astrophys, 187, 419

Nagaoka, A., Watanabe, N., & Kouchi, A. 2005, ApJ Lett., 624, L29

Nagasawa, M., Thommes, E. W., Kenyon, S. J., Bromley, B. C., & Lin, D. N. C. 2007, Protostars and Planets V, 639

Najita, J. R., Ádámkovics, M., & Glassgold, A. E. 2011, ApJ, 743, 147

Najita, J. R., Carr, J. S., Pontoppidan, K. M., et al. 2013, ApJ, 766, 134

Nakagawa, Y., Nakazawa, K., & Hayashi, C. 1981, Icarus, 45, 517

Natta, A. 2008, Physica Scripta Volume T, 130, 014014

Natta, A., Testi, L., Calvet, N., et al. 2007, Protostars and Planets V, 767

Nielbock, M., Launhardt, R., Steinacker, J., et al. 2012, A&A., 547, A11

Öberg, K. I., Garrod, R. T., van Dishoeck, E. F., & Linnartz, H. 2009a, A&A., 504, 891

Öberg, K. I., Qi, C., Wilner, D. J., & Hogerheijde, M. R. 2012, ApJ, 749, 162

Öberg, K. I., van Dishoeck, E. F., & Linnartz, H. 2009b, A&A., 496, 281

Oka, T. 2004, Journal of Molecular Spectroscopy, 228, 635

Okumura, M., McCall, B. J., & Geballe, T. R. 2013, The Journal of Physical Chemistry A, 117, 9305

Okuzumi, S. & Hirose, S. 2012, ApJ Lett., 753, L8

Okuzumi, S., Tanaka, H., & Sakagami, M.-a. 2009, ApJ, 707, 1247

Oort, J. H. 1950, Bull. Astron. Inst. Netherlands, 11, 91

Oró, J. 1961, Nature, 190, 389

Owen, T., Bar-Nun, A., & Kleinfeld, I. 1992, Nature, 358, 43

Pagani, L., Vastel, C., Hugo, E., et al. 2009a, A&A., 494, 623

Pagani, L., Vastel, C., Hugo, E., et al. 2009b, A&A., 494, 623

Parise, B., Belloche, A., Du, F., Güsten, R., & Menten, K. M. 2011, A&A., 526, A31

Parise, B., Castets, A., Herbst, E., et al. 2004, A&A., 416, 159

Parise, B., Caux, E., Castets, A., et al. 2005, A&A., 431, 547

Parise, B., Ceccarelli, C., Tielens, A. G. G. M., et al. 2006, A&A., 453, 949

Parise, B., Ceccarelli, C., Tielens, A. G. G. M., et al. 2002, A&A., 393, L49

Parise, B., Du, F., Liu, F.-C., et al. 2012, A&A., 542, L5

Parise, B., Leurini, S., Schilke, P., Roueff, E., & Thorwirth, S. 2007, in Molecules in Space and Laboratory

Parise, B., Leurini, S., Schilke, P., et al. 2009, A&A., 508, 737

Parise, B., Simon, T., Caux, E., et al. 2003, A&A., 410, 897

Perets, H. B. & Biham, O. 2006, MNRAS, 365, 801

Perets, H. B., Biham, O., Manicó, G., et al. 2005, ApJ, 627, 850

Pérez, L. M., Carpenter, J. M., Chandler, C. J., et al. 2012, Astrophys. J. Lett, 760, L17

Perryman, M. A. C., de Boer, K. S., Gilmore, G., et al. 2001, A&A., 369, 339

Persson, M. V., Jørgensen, J. K., & van Dishoeck, E. F. 2013, A&A., 549, L3

Petrignani, A., Altevogt, S., Berg, M. H., et al. 2011, Phys. Rev. A, 83, 032711

Phillips, T. G., Jefferts, K. B., & Wannier, P. G. 1973, Astrophys. Lett., 15, 17

Pierens, A. & Nelson, R. P. 2008, A&A., 482, 333

Pilbratt, G. L., Riedinger, J. R., Passvogel, T., et al. 2010, A&A., 518, L1

Pontoppidan, K. M., Blake, G. A., van Dishoeck, E. F., et al. 2008, Astrophys. J, 684, 1323

Pontoppidan, K. M., Dullemond, C. P., van Dishoeck, E. F., et al. 2005, ApJ, 622, 463

Pontoppidan, K. M., Salyk, C., Blake, G. A., et al. 2010, Astrophys. J, 720, 887

Prasad, S. S. & Huntress, Jr., W. T. 1980a, ApJS, 43, 1

Prasad, S. S. & Huntress, Jr., W. T. 1980b, ApJ, 239, 151

Qi, C., Wilner, D. J., Aikawa, Y., Blake, G. A., & Hogerheijde, M. R. 2008, ApJ, 681, 1396

Quack, M. 1977, Molecular Physics, 34, 477

Rachford, B. L., Snow, T. P., Destree, J. D., et al. 2009, ApJS, 180, 125

Rachford, B. L., Snow, T. P., Tumlinson, J., et al. 2002, ApJ, 577, 221

Rathborne, J. M., Jackson, J. M., Zhang, Q., & Simon, R. 2008, ApJ, 689, 1141

Raymond, S. N. 2008, in IAU Symposium, Vol. 249, IAU Symposium, ed. Y.-S. Sun, S. Ferraz-Mello, & J.-L. Zhou, 233–250

Raymond, S. N., O'Brien, D. P., Morbidelli, A., & Kaib, N. A. 2009, Icarus, 203, 644

Ricci, L., Testi, L., Natta, A., & Brooks, K. J. 2010, A&A., 521, A66

Rimmer, P. B., Herbst, E., Morata, O., & Roueff, E. 2012, A&A., 537, A7

Riviere-Marichalar, P., Ménard, F., Thi, W. F., et al. 2012, A&A., 538, L3

Robert, F. 2003, Space Sci. Rev., 106, 87

Robert, F. 2011, Nature Geoscience, 4, 74

Robert, F. & Epstein, S. 1982, Geochimica et Cosmochimica Acta, 46, 81

Robert, F., Gautier, D., & Dubrulle, B. 2000, Space Sci. Rev., 92, 201

Roberts, H. 2005, in IAU Symposium, Vol. 231, Astrochemistry: Recent Successes and Current Challenges, ed. D. C. Lis, G. A. Blake, & E. Herbst, 27–36

Roberts, H., Herbst, E., & Millar, T. J. 2003, ApJ Lett., 591, L41

Roberts, H., Herbst, E., & Millar, T. J. 2004, A&A., 424, 905

Roberts, H. & Millar, T. J. 2000a, A&A., 364, 780

Roberts, H. & Millar, T. J. 2000b, A&A., 361, 388

Roberts, H. & Millar, T. J. 2006, Royal Society of London Philosophical Transactions Series A, 364, 3063

Roberts, H. & Millar, T. J. 2007, A&A., 471, 849

Rodgers, S. D. & Millar, T. J. 1996, MNRAS, 280, 1046

Rodmann, J., Henning, T., Chandler, C. J., Mundy, L. G., & Wilner, D. J. 2006, A&A., 446, 211

Rodón, J. A., Beuther, H., Megeath, S. T., & van der Tak, F. F. S. 2008, A&A., 490, 213

Rogers, A. E. E., Dudevoir, K. A., & Bania, T. M. 2007, AJ, 133, 1625

Roueff, E. & Gerin, M. 2003, Space Sci. Rev., 106, 61

Roueff, E., Lis, D. C., van der Tak, F. F. S., Gerin, M., & Goldsmith, P. F. 2005, A&A., 438, 585

Roueff, E., Tiné, S., Coudert, L. H., et al. 2000, A&A., 354, L63

Rowe, B. R. & Marquette, J. B. 1987, Int. J. Masspectrom. Ion Process., 80, 239

Ruzmaikina, T. V., Khatuncev, I. V., & Konkina, T. V. 1993, in Lunar and Planetary Institute Science Conference Abstracts, Vol. 24, 1225–1226

Saal, A. E., Hauri, E. H., Van Orman, J. A., & Rutherford, M. J. 2013, Science, 340, 1317

Saito, S., Ozeki, H., Ohishi, M., & Yamamoto, S. 2000, ApJ, 535, 227

Sakai, N., Sakai, T., Hirota, T., & Yamamoto, S. 2009, ApJ, 702, 1025

Sarrasin, E., Abdallah, D. B., Wernli, M., et al. 2010, MNRAS, 404, 518

Schilke, P., Walmsley, C. M., Pineau Des Forets, G., et al. 1992, A&A., 256, 595

Schloerb, F. P., Snell, R. L., Langer, W. D., & Young, J. S. 1981, ApJ Lett., 251, L37

Schräpler, R. & Henning, T. 2004, ApJ, 614, 960

Seager, S. & Deming, D. 2010, Ann. Rev. Astron. Astrophys., 48, 631

Sellgren, K., Uchida, K. I., & Werner, M. W. 2007, ApJ, 659, 1338

Sellgren, K., Werner, M. W., Ingalls, J. G., et al. 2010, ApJ Lett., 722, L54

Semenov, D. 2010, ArXiv e-prints, 1011.4770

Semenov, D., Hersant, F., Wakelam, V., et al. 2010a, Astron. Astrophys, 522, A42

Semenov, D., Hersant, F., Wakelam, V., et al. 2010b, A&A., 522, A42

Semenov, D., Hersant, F., Wakelam, V., et al. 2010c, A&A., 522, A42

Semenov, D. & Wiebe, D. 2011, ApJS, 196, 25

Semenov, D., Wiebe, D., & Henning, T. 2006, ApJ Lett., 647, L57

Shah, R. Y. & Wootten, A. 2001, ApJ, 554, 933

Shakura, N. I. & Sunyaev, R. A. 1973, A&A., 24, 337

Shinnaka, Y., Kawakita, H., Kobayashi, H., Boice, D. C., & Martinez, S. E. 2012, Astrophys. J, 749, 101

Sicilia-Aguilar, A., Hartmann, L., Calvet, N., et al. 2006, ApJ, 638, 897

Sidhu, K. S., Miller, S., & Tennyson, J. 1992, A&A., 255, 453

Sipilä, O., Caselli, P., & Harju, J. 2013a, ArXiv e-prints

Sipilä, O., Caselli, P., & Harju, J. 2013b, A&A., 554, A92

Sipilä, O., Caselli, P., & Harju, J. 2013c, A&A., 554, A92

Sipilä, O., Hugo, E., Harju, J., et al. 2010, A&A., 509, A98

Smith, A. M. 1973, ApJ Lett., 179, L11

Smith, D., Adams, N. G., & Alge, E. 1982a, J. Chem. Phys., 77, 1261

Smith, D., Adams, N. G., & Alge, E. 1982b, ApJ, 263, 123

Smith, I. W. M. 2008, Low Temperatures and Cold Molecules

Smith, I. W. M. 2011, Ann. Rev. Astron. Astrophys., 49, 29

Smith, I. W. M. & Rowe, R. 2000, Acc. Chem. Res., 33, 261

Smith, M. A. 1998, International Reviews in Physical Chemistry, 17, 35

Snow, T. P. & McCall, B. J. 2006a, Ann. Rev. Astron. Astrophys., 44, 367

Snow, T. P. & McCall, B. J. 2006b, Ann. Rev. Astron. Astrophys., 44, 367

Snow, T. P., Ross, T. L., Destree, J. D., et al. 2008, ApJ, 688, 1124

Snyder, L. E., Buhl, D., Zuckerman, B., & Palmer, P. 1969, Physical Review Letters, 22, 679

Spitzer, L., Drake, J. F., Jenkins, E. B., et al. 1973, ApJ Lett., 181, L116

Stancil, P. C., Lepp, S., & Dalgarno, A. 1998, ApJ, 509, 1

Stark, R., Sandell, G., Beck, S. C., et al. 2004, ApJ, 608, 341

Stark, R., van der Tak, F. F. S., & van Dishoeck, E. F. 1999, ApJ Lett., 521, L67

Stern, S. A. & Colwell, J. E. 1997, AJ, 114, 841

Sundstrom, G., Mowat, J. R., Danared, H., et al. 1994, Science, 263, 785

Suzuki, H. 1987, in IAU Symposium, Vol. 120, Astrochemistry, ed. M. S. Vardya & S. P. Tarafdar, 199

Talukdar, R. K. & Ravishankara, A. R. 1996, Chemical Physics Letters, 253, 177

Taquet, V., Ceccarelli, C., & Kahane, C. 2012a, ApJ Lett., 748, L3

Taquet, V., Ceccarelli, C., & Kahane, C. 2012b, A&A., 538, A42

Taquet, V., López-Sepulcre, A., Ceccarelli, C., et al. 2013a, ApJ Lett., 768, L29

Taquet, V., Peters, P. S., Kahane, C., et al. 2013b, A&A., 550, A127

Teanby, N. A., Irwin, P. G. J., de Kok, R., et al. 2009, Icarus, 202, 620

Teixeira, T. C., Devlin, J. P., Buch, V., & Emerson, J. P. 1999, A&A., 347, L19

Teske, J. K., Najita, J. R., Carr, J. S., et al. 2011, Astrophys. J, 734, 27

Testi, L., Natta, A., Shepherd, D. S., & Wilner, D. J. 2003, Astron. Astrophys, 403, 323

Thi, W.-F., Woitke, P., & Kamp, I. 2010, MNRAS, 407, 232

Tilling, I., Woitke, P., Meeus, G., et al. 2012, A&A., 538, A20

Tiné, S., Roueff, E., Falgarone, E., Gerin, M., & Pineau des Forêts, G. 2000, A&A., 356, 1039

Tom, B. A., Zhaunerchyk, V., Wiczer, M. B., et al. 2009, J. Chem. Phys., 130, 031101

Tscharnuter, W. M. & Gail, H.-P. 2007, A&A., 463, 369

Tsiganis, K., Gomes, R., Morbidelli, A., & Levison, H. F. 2005, Nature, 435, 459

Turner, B. E. 1990, ApJ Lett., 362, L29

Turner, B. E. 2001, ApJS, 136, 579

Turner, B. E. & Zuckerman, B. 1978, ApJ Lett., 225, L75

Turner, N. J., Sano, T., & Dziourkevitch, N. 2007, ApJ, 659, 729

Ubach, C., Maddison, S. T., Wright, C. M., et al. 2012, MNRAS, 425, 3137

van Boekel, R., Min, M., Leinert, C., et al. 2004, Nature, 432, 479

van Boekel, R., Min, M., Waters, L. B. F. M., et al. 2005, A&A., 437, 189

van der Tak, F., Herpin, F., & Wyrowski, F. 2011, in EAS Publications Series, Vol. 52, EAS Publications Series, ed. M. Röllig, R. Simon, V. Ossenkopf, & J. Stutzki, 201–204

van der Tak, F. F. S. 2006, Royal Society of London Philosophical Transactions Series A, 364, 3101

van der Tak, F. F. S., Black, J. H., Schöier, F. L., Jansen, D. J., & van Dishoeck, E. F. 2007, A&A., 468, 627

van der Tak, F. F. S., Müller, H. S. P., Harding, M. E., & Gauss, J. 2009, A&A., 507, 347

van der Tak, F. F. S., Schilke, P., Müller, H. S. P., et al. 2002, A&A., 388, L53

van der Tak, F. F. S. & van Dishoeck, E. F. 2000, A&A., 358, L79

van Dishoeck, E. F. 1987, in IAU Symposium, Vol. 120, Astrochemistry, ed. M. S. Vardya & S. P. Tarafdar, 51–63

van Dishoeck, E. F. 2009, Astrochemistry of Dense Protostellar and Protoplanetary Environments, ed. Thronson, H. A., Stiavelli, M., & Tielens, A., 187

van Dishoeck, E. F., Blake, G. A., Jansen, D. J., & Groesbeck, T. D. 1995, ApJ, 447, 760

van Dishoeck, E. F., Jonkheid, B., & van Hemert, M. C. 2006, Faraday Discussions, 133, 231

van Dishoeck, E. F., Kristensen, L. E., Benz, A. O., et al. 2011, PASP, 123, 138

van Dishoeck, E. F., Thi, W., & van Zadelhoff, G. 2003, A&A., 400, L1

Varju, J., Hejduk, M., Dohnal, P., et al. 2011, Physical Review Letters, 106, 203201

Vastel, C. 2007, in SF2A-2007: Proceedings of the Annual meeting of the French Society of Astronomy and Astrophysics, ed. J. Bouvier, A. Chalabaev, & C. Charbonnel, 266

Vastel, C., Caselli, P., Ceccarelli, C., et al. 2012, A&A., 547, A33

Vastel, C., Caselli, P., Ceccarelli, C., et al. 2006a, ApJ, 645, 1198

Vastel, C., Phillips, T. G., Caselli, P., Ceccarelli, C., & Pagani, L. 2006b, Royal Society of London Philosophical Transactions Series A, 364, 3081

Vastel, C., Phillips, T. G., & Yoshida, H. 2004, ApJ Lett., 606, L127

Vasyunin, A. I. & Herbst, E. 2013a, ApJ, 762, 86

Vasyunin, A. I. & Herbst, E. 2013b, ApJ, 769, 34

Vasyunin, A. I., Semenov, D., Henning, T., et al. 2008a, ApJ, 672, 629

Vasyunin, A. I., Semenov, D., Henning, T., et al. 2008b, ApJ, 672, 629

Vasyunin, A. I., Sobolev, A. M., Wiebe, D. S., & Semenov, D. A. 2004, Astronomy Letters, 30, 566

Vasyunin, A. I., Wiebe, D. S., Birnstiel, T., et al. 2011, ApJ, 727, 76

Vasyunina, T., Linz, H., Henning, T., et al. 2009, A&A., 499, 149

Vasyunina, T., Vasyunin, A. I., Herbst, E., & Linz, H. 2012, ApJ, 751, 105

Vidali, G. 2013, Chemical Reviews

Villanueva, G. L., Mumma, M. J., Bonev, B. P., et al. 2009, ApJ Lett., 690, L5

Villanueva, G. L., Mumma, M. J., Disanti, M. A., et al. 2011, Icarus, 216, 227

Visser, R., Doty, S. D., & van Dishoeck, E. F. 2011, A&A., 534, A132

Visser, R., Jørgensen, J. K., Kristensen, L. E., van Dishoeck, E. F., & Bergin, E. A. 2013, ApJ, 769, 19

Visser, R., van Dishoeck, E. F., Doty, S. D., & Dullemond, C. P. 2009, A&A., 495, 881

Volk, K. & Malhotra, R. 2008, The Astrophysical Journal, 687, 714

Wakelam, V., Herbst, E., Le Bourlot, J., et al. 2010a, A&A., 517, A21

Wakelam, V., Herbst, E., & Selsis, F. 2006a, A&A., 451, 551

Wakelam, V., Herbst, E., Selsis, F., & Massacrier, G. 2006b, A&A., 459, 813

Wakelam, V., Selsis, F., Herbst, E., & Caselli, P. 2005, A&A., 444, 883

Wakelam, V., Smith, I. W. M., Herbst, E., et al. 2010b, Space Sci. Rev., 156, 13

Walmsley, C. M., Flower, D. R., & Pineau des Forêts, G. 2004a, A&A., 418, 1035

Walmsley, C. M., Flower, D. R., & Pineau des Forêts, G. 2004b, A&A., 418, 1035

Walsh, K. J., Morbidelli, A., Raymond, S. N., O'Brien, D. P., & Mandell, A. M. 2011, Nature, 475, 206

Walsh, K. J., Morbidelli, A., Raymond, S. N., O'Brien, D. P., & Mandell, A. M. 2012, Meteoritics and Planetary Science, 47, 1941

Watanabe, N. 2005, in IAU Symposium, Vol. 231, Astrochemistry: Recent Successes and Current Challenges, ed. D. C. Lis, G. A. Blake, & E. Herbst, 415–426

Watson, W. D. 1976, Rev. Mod. Phys., 48, 513

Weaver, H. A., A'Hearn, M. F., Arpigny, C., et al. 2008, LPI Contributions, 1405, 8216

Webber, W. R. 1998, ApJ, 506, 329

Wehrstedt, M. & Gail, H.-P. 2002, A&A., 385, 181

Weissman, P. R. 1999, Space Sci. Rev., 90, 301

Werner, M. W., Uchida, K. I., Sellgren, K., et al. 2004, ApJS, 154, 309

Willacy, K. 2007, ApJ, 660, 441

Willacy, K., Langer, W., Allen, M., & Bryden, G. 2006, ApJ, 644, 1202

Willacy, K. & Woods, P. M. 2009, ApJ, 703, 479

Wilson, R. W., Jefferts, K. B., & Penzias, A. A. 1970, ApJ Lett., 161, L43

Windmark, F., Birnstiel, T., Güttler, C., et al. 2012, A&A., 540, A73

Woitke, P., Kamp, I., & Thi, W.-F. 2009, A&A., 501, 383

Woodall, J., Agúndez, M., Markwick-Kemper, A. J., & Millar, T. J. 2007, A&A., 466, 1197

Woodward, C. E., Kelley, M. S., Bockelée-Morvan, D., & Gehrz, R. D. 2007, Astrophys. J, 671, 1065

Wootten, A. 1987, in IAU Symposium, Vol. 120, Astrochemistry, ed. M. S. Vardya & S. P. Tarafdar, 311–318

Wozniakiewicz, P. J., Kearsley, A. T., Ishii, H. A., et al. 2012, Meteoritics and Planetary Science, 47, 660

Yang, L., Ciesla, F. J., & Alexander, M. O. 2013, Icarus, 226, 256

Zinnecker, H. & Yorke, H. W. 2007, Ann. Rev. Astron. Astrophys., 45, 481

"Challenge yourself with something you know you could never do, and what you will find is that you can overcome anything."

— Anonymous

ACKNOWLEDGMENTS

The work presented in this thesis has benefited greatly from both the scientific and social atmosphere in Heidelberg, as well as that presented from my colleagues around the world, and in the final written words of this work I wish to acknowledge every one who have contributed to the work that I present here and for making my PhD such a educational and cheerful time.

Let me start by thanking my advisors, Prof. Thomas Henning and Dr. Dmitry Semenov, who have been of great help to me throughout my PhD. Their expertise and insights into the field of Astronomy has been a great inspiration and their passion for the field has been really contagious. I am also grateful to my co-authors and colleagues: Anton Vasyunin, Eric Herbst, Holger Kreckel, Nick Indriolo, Kyle Crabtree, Thomas Gerner, Ewine van Dishoeck, Joseph Mottram, Markus Schmalzl, Catherine Walsh, Ruud Visser and Lars Kristensen. I have learnt a lot from our discussions and your insights over the years.

I also wish to extend thanks to all my colleagues at MPIA, past and present, and the non-scientific staff for their help in all practical matters at the institute. I have enjoyed the atmosphere in my office(s) at the MPIA and although I might have spent more time away traveling than at my desk I am thankful for the friendly company of my office-mates, past and present: Maren Mohler, Yu-Yen Chang, Simon Bihr, Ronald Läsker, Nils Lippok, Robert Singh and Alex Büdenbender.

Many thanks to the IMPRS coordinator Christian Fendt. I am happy to have been part of the IMPRS, and a big thank you to my colleagues of the 6th IMPRS generation, the years have gone by so fast for all of us! I am in debt to Thomas Gerner for his help with translating my German Zusammenfassung and Richard Teague for taking his time to read through my introduction and improving the English. I am also thankful to Thomas Henning, Ralf Klessen, Kees Dullemond and Andreas Wolf in my thesis committee, and extra thanks to Kees Dullemond in my IMPRS committee.

It has been a pleasure to be part of the ITN programme "LASSIE" and I wish to thank the coordinators for the effort they have put into organizing meetings, conferences and more importantly for bringing us, as LASSIE members, together all over Europe. Thereby I also wish to acknowledge the financial support that funded this project through the European Community's Seventh Framework Programme [FP7/2007-2013] under grant agreement no. 238258.

To my colleagues in LASSIE: I am thankful for all the memories, laughs and joyful times that we have experienced together as we together have explored the corners of Europe. I hope that our paths will cross sometime soon again! Special thanks to Thanja Lamberts (you are, to me, considered an honorary

LASSIE!), Gleb Fedoseev, Irene San Jose, as well as other colleagues at the Sterrewacht, for making my three month visit in Leiden most pleasurable.

Life is not enjoyable without a bit of fantasy and adventure, and I am proud to have been part of the group of adventurers who explored the arid world of Athas and the group of gamers who contended for world domination in Civilization, raced in Formula 1 to be number one, throwing fireballs and slaying dragons, in all the games that we have played over the years. Special thanks goes to Fredrik Windmark for bringing us together with his endless imagination that made our adventures in Athas so exciting and his undying love for boardgames.

Jag vill till sist, och främst, tacka min underbara familj för ert stöd och uppmuntran genom detta äventyr. Det har varit många tuffa år men att alltid kunna komma hem till er i vackra Vargön har bidragit stort till var jag är idag. Tack för att ni alltid funnits där! Borta bra men hemma bäst.